VERIFICATION OF INTENSITY MODULATED RADIATION THERAPY BEAMS USING A TISSUE EQUIVALENT PLASTIC SCINTILLATOR DOSIMETRY SYSTEM

by

MARTIN PETER PETRIC

B.Sc., McMaster University, 1999
M.Sc., McGill University, 2001

A THESIS SUBMITTED IN PARTIAL FULFILLMENT OF THE
REQUIREMENTS FOR THE DEGREE OF

DOCTOR OF PHILOSOPHY

in

THE FACULTY OF GRADUATE STUDIES
(Physics and Astronomy)

THE UNIVERSITY OF BRITISH COLUMBIA
July 2006

Abstract

This thesis describes the development and implementation of a novel method for the dosimetric verification of intensity modulated radiation therapy (IMRT) fields with several advantages over current techniques. Through the use of a tissue equivalent plastic scintillator sheet viewed by a charge-coupled device (CCD) camera, this method provides a truly tissue equivalent dosimetry system capable of efficiently and accurately performing field-by-field verification of IMRT plans.

This work was motivated by an initial study comparing two IMRT treatment planning systems. The clinical functionality of BrainLAB's BrainSCAN and Varian's Helios IMRT treatment planning systems were compared in terms of implementation and commissioning, dose optimization, and plan assessment. Implementation and commissioning revealed differences in the beam data required to characterize the beam prior to use with the BrainSCAN system requiring higher resolution data compared to Helios. This difference was found to impact on the ability of the systems to accurately calculate dose for highly modulated fields, with BrainSCAN being more successful than Helios. The dose optimization and plan assessment comparisons revealed that while both systems use considerably different optimization algorithms and user-control interfaces, they are both capable of producing substantially equivalent dose plans.

The extensive use of dosimetric verification techniques in the IMRT treatment planning comparison study motivated the development and implementation of a novel IMRT dosimetric verification system. The system consists of a water-filled phantom with a tissue equivalent plastic scintillator sheet built into the top surface. Scintillation light is reflected by a plastic mirror within the phantom towards a viewing window where it is captured using a CCD camera. Optical photon spread is removed using a micro-louvre optical collimator and by deconvolving a glare kernel

from the raw images. Characterization of this new dosimetric verification system indicates excellent dose response and spatial linearity, high spatial resolution, and good signal uniformity and reproducibility. Dosimetric results from square fields, dynamic wedged fields, and a 7-field head and neck IMRT treatment plan indicate good agreement with film dosimetry distributions. Efficiency analysis of the system reveals a 50% reduction in time requirements for field-by-field verification of a 7-field IMRT treatment plan compared to film dosimetry.

Table of Contents

Abstract ..... **ii**
Table of Contents ..... **iv**
List of Tables ..... **ix**
List of Figures ..... **xi**
List of Abbreviations ..... **xxiii**
Acknowledgments ..... **xxiv**
Chapter 1 Introduction **1**
1.1 Radiation Therapy 1
1.1.1 Historical Background 2
1.1.2 Tumour and Healthy Tissue Response 3
1.1.3 Treatment planning 5
1.1.3.1 Evaluating Treatment Plans 5
1.1.3.2 Advances in Imaging 7
1.2 Dose Deposition 7
1.2.1 Kerma and Absorbed Dose 7
1.2.2 Photon Interactions with Matter 10
1.2.3 Electron Energy Transfer – Stopping Power 13
1.2.4 Čerenkov Radiation 14
1.2.5 Pencil Beam Dose Deposition Model 15
1.3 General Dose Delivery Techniques – Multiple Fields 16
1.4 Field Shaping 18
1.4.1 Multileaf Collimator 19
1.5 Intensity Modulated Radiation Therapy 21
1.5.1 Plan Optimization 22

1.5.2 Delivery 24
1.5.3 Intensity and Fluence 26
1.6 IMRT Dose Verification 26
1.6.1 Evaluating Dose Verification Measurements 27
1.6.2 IMRT Dosimetric Verification Systems Requirements 29
1.6.3 Current IMRT Dosimetric Verification Systems 31
1.6.3.1 Ionization Chamber and Diode Detector Arrays 31
1.6.3.2 Gel Dosimetry 33
1.6.3.3 Film Dosimetry 34
1.6.3.4 Electronic Portal Imaging Devices 36
1.7 Thesis Objectives 38
1.7.1 An Evaluation of Two Treatment Planning Systems for IMRT 38
1.7.2 A Tissue Equivalent Plastic Scintillator IMRT Verification System 39
1.7.3 System Characterization and Testing 39
1.7.4 System Evaluation 39
Chapter 2 An Evaluation of Two Treatment Planning Systems for IMRT 40
2.1 Method and Materials 40
2.1.1 Implementation and Commissioning 41
2.1.2 Effects of Commissioning Data Resolution 43
2.1.2.1 Radiographic Film Dosimetry 43
2.1.3 Optimization Parameters and System Functionality 44
2.1.4 Plan Assessment 45
2.1.5 Efficiency 49
2.2 Results 50
2.2.1 Implementation and Commissioning 50
2.2.2 Effects of Commissioning Data Resolution 51
2.2.3 Optimization Parameters and System Functionality 53
2.2.4 Plan Assessment 54

2.2.5 Efficiency 60
2.3 Discussion 61
Chapter 3 A Tissue Equivalent Plastic Scintillator IMRT Verification System. 65
3.1 Plastic Scintillators 65
3.1.1 Organic Scintillator Theory 65
3.1.2 Plastic Scintillator Properties 68
3.1.3 Plastic Scintillator Based Dosimetry Systems 70
3.2 System Design 73
3.2.1 Phantom Design 74
3.2.1.1 Scintillator Sheet Preparation 77
3.2.1.2 Micro-Louvre Optical Collimator 81
3.2.2 Imaging System Setup 86
3.3 Data Acquisition and Processing 89
3.3.1 System Setup 89
3.3.2 Image Acquisition and Summation 92
3.3.3 Subtraction of Dark Current 94
3.3.4 Deblurring 94
3.3.5 Flood Field Correction 97
3.3.6 Light Intensity to Dose Conversion 98
Chapter 4 System Characterization and Testing 99
4.1 Method and Materials 99
4.1.1 Dose Linearity 99
4.1.2 Dose Rate Dependence and Short-Term Reproducibility 100
4.1.3 Spatial Linearity and Effective Pixel Size 100
4.1.4 Čerenkov Signal Contribution 101
4.1.5 Signal Uniformity and Long-Term Reproducibility 101
4.1.6 Verification of Simple Static and Dynamic Wedged Fields 102
4.2 Results 102

4.2.1 Dose Linearity 102
4.2.2 Dose Rate Dependence and Short-Term Reproducibility 103
4.2.3 Spatial Linearity and Effective Pixel Size 104
4.2.4 Čerenkov Signal Contribution 105
4.2.5 Signal Uniformity and Long-Term Reproducibility 107
4.2.6 Verification of Simple Static and Dynamic Wedged Fields 108
4.2.6.1 Simple Static Square Fields 108
4.2.6.2 Dynamic Wedged Fields 112
4.3 Discussion 117
4.3.1 Dose Linearity 117
4.3.2 Dose Rate Dependence and Short-Term Reproducibility 117
4.3.3 Spatial Linearity and Effective Pixel Size 118
4.3.4 Čerenkov Signal Contribution 119
4.3.5 Signal Uniformity and Long-Term Reproducibility 120
4.3.6 Verification of Simple Static and Dynamic Wedged Fields 121
Chapter 5 System Evaluation 123
5.1 Method and Materials 123
5.1.1 Dosimetric Comparison 123
5.1.2 System Efficiency 124
5.1.3 High Spatial Frequency IMRT Field 124
5.2 Results 125
5.2.1 Dosimetric Comparison 125
5.2.2 System Efficiency 130
5.2.3 High Spatial Frequency IMRT Field 132
5.3 Discussion 137
5.3.1 Dosimetric Comparison 137
5.3.2 System Efficiency 138
5.3.3 High Spatial Frequency IMRT Field 140

Chapter 6 Conclusion **142**
6.1 Conclusion 142
6.2 Future Work 144
Bibliography **149**
Appendix A: 7-Field IMRT Results **161**

List of Tables

Table 1.1: Physical properties of various tissue equivalent materials in comparison to soft tissue 30

Table 2.1: Commissioning beam data requirements for the Varian Helios and BrainLAB BrainSCAN treatment planning systems 41

Table 2.2: Normal tissue constraints as a percentage of prescribed dose for comparison of treatment planning systems 49

Table 2.3: Properties of the masked γ map distributions comparing calculated distributions to film measured distribution. 53

Table 2.4: PTV dose volume statistics for three cases as a function of prescription dose (Rx) 56

Table 2.5: Ratio of monitor units required to deliver IMRT plans compared to conventional conformal plan 61

Table 3.1: Important physical properties of the tissue equivalent plastic scintillator detection screen used in the system. 77

Table 3.2: Results from sanding investigation showing the effect of sandpaper grit on scintillator light output and radiation distribution blurring. Results for each grit are averaged over 5 irradiations. Zero grit indicates the smooth, cast scintillator surface prior to any sanding. 80

Table 3.3: Region-of-interest mean intensity for verification system with and without presence of micro-louvre optical collimator film for identical 25 cm × 25 cm open square fields. 86

Table 3.4: Reduction of dark current as a result of moving control and capture computer into the treatment room. 89

Table 4.1: Dose rate dependence of verification system. Region-of-interest comprised a 1 cm × 1 cm square centered at the field isocenter. Error values indicate standard deviations over 10 trials at each dose rate. 104

Table 4.2: Region-of-interest analysis for 25 cm × 25 cm square field. Percent Čerenkov contribution has been calculated using total signal intensity as measured using central ROI of image acquired with scintillator detection sheet in place (value = 591.22). 106

Table 4.3: Contribution of Čerenkov signal to total light signal for square fields ranging in size from 5 cm × 5 cm to 25 cm × 25 cm. 107

Table 4.4: Summary of percent dose difference and gamma factor maps for simple square fields. 112

Table 4.5: Summary of percent dose difference and gamma factor maps for wedges in the x- and y-directions. 117

Table 5.1: Summary of percent dose difference and gamma factor maps for all fields from 7-field IMRT plan. 129

Table 5.2: Time requirements for field-by-field dose verification of a 7-field IMRT plan using film dosimetry and scintillator dosimetry system. 130

Table 5.3: Setup sub-task requirements for scintillator dosimetry system. Shaded times indicate sub-tasks that are likely unaffected by prototype status of system. 131

Table 5.4: Predicted time requirements for field-by-field dose verification of a 7-field IMRT plan using film dosimetry and commercial implementation of scintillator dosimetry system. 131

Table 5.5: Summary of percent dose difference and gamma factor maps for high spatial frequency IMRT field. 137

List of Figures

Figure 1.1: Sigmoidal dose-response curves for tumour control and normal tissue response. A classical, more favourable representation is displayed in (a) while (b) shows a more realistic, less favourable representation. 4

Figure 1.2: Evaluation methods for assessing three-dimensional radiation treatment plans include (a) isodose displays, (b) three-dimensional dose surfaces and (c) dose-volume histograms. 6

Figure 1.3: (a) Schematic diagram illustrating number of electrons liberated from medium as a function of depth as well as the depth of subsequent energy absorption by the medium. (b) Kerma (dashed line) and absorbed dose (solid line) as a function of depth in medium. Adapted from [9]. 9

Figure 1.4: Schematic diagram illustrating the three primary photon interactions which contribute to dose deposition in radiation therapy: (a) photo-electric effect, (b) Compton scattering and (c) pair production..... 11

Figure 1.5: Predominance of the three main forms of photon interaction with matter as a function of incident photon energy and atomic number of medium. The lines show the values of Z and photon energy for which the two neighboring effects are equal. Adapted from [11]..... 12

Figure 1.6: Percent depth dose curve in water for a single, square, 10 cm × 10 cm photon beam with an energy of 6 MV. The maximum dose, which occurs at a depth of 1.5 cm, has been normalized to 100%. 16

Figure 1.7: Dose distribution for a multiple radiation field treatment. In this case, four fields are used to treat a prostate tumour thus improving the uniformity of the lethal dose delivered to the target and sparing the surrounding normal tissue by spreading the dose out over a larger volume. 17

Figure 1.8: Front- (a) and side-view (b) schematic diagrams illustrating design of modern linear accelerator treatment units. The high energy photon source is capable of rotating around a fixed point in space known as the isocenter..... 18

Figure 1.9: Simple beam shaping for external radiation therapy can be carried out using the secondary collimator located in the head of the linac to match outer edges of the rectangular treatment field to the outermost extend of the target (a). The field may be further shaped to conform to the exact shape of the target by using shaped alloy blocks (b)..... 19

Figure 1.10: Modern beam shaping is performed using multileaf collimator devices (a) which are incorporated into the head of linear accelerator treatment units. Definition of the beam is carried out by moving the attenuating leaves into the radiation field to match the outer contour of the target (b)..... 20

Figure 1.11: Intensity modulation can be accomplished through the use of beam modifiers such as (a) physical wedges and (b) compensator blocks which are typically used to account for irregular skin surface contours. 21

Figure 1.12: In IMRT each field aperture is divided up into an array of pixels each of which has an associated beamlet projecting through the patient volume. The dose deposited in any voxel is affected by all beamlets intersecting it (e.g. the dose in voxel V_m is affected by the beamlets A_n and B_n)..... 22

Figure 1.13: Examples of intensity modulated fields. Higher intensity beamlets (pixels) are represented in black while low intensity beamlets are represented by white. Lines indicate target contour as shaped using MLC and crosshair indicates location of isocenter..... 24

Figure 1.14: Generation of a simple intensity modulated field through delivery of several uniquely shaped sub-fields. The total photon fluence (i.e. intensity) at any point is equal to the sum of all overlapping sub-fields at that point. In this case, darker shading represents higher intensities. 25

Figure 1.15: Commonly used methods for evaluating dose verification results include (a) one-dimensional dose profile comparisons, (b) two-dimensional dose difference maps, and (c) gamma factor analysis. 29
Figure 1.16: A simple, thimble ionization chamber commonly used in radiation therapy dosimetry 32
Figure 1.17: Schematic diagram of a typical p-n diode detector. A reverse bias potential across the p-n junction causes the creation of a depletion region. 33
Figure 1.18: Cross section of a radiographic film. A thin acetate or polyester base is coated with an emulsion consisting of silver halide crystals embedded in a gelatin base. 35
Figure 1.19: Schematic diagram of a typical video-based electronic portal imaging device. 37
Figure 2.1: CT image set for Case #1 showing (a) axial, (b) coronal, and (c) sagittal views of planning target volume and its anatomical relationship with organs-at-risk 46
Figure 2.2: CT image set for Case #2 showing (a) axial, (b) coronal, and (c) sagittal views of planning target volume and anatomical relationship with brainstem and spinal cord. 47
Figure 2.3: CT image set for Case #3 showing (a) axial, (b) coronal, and (c) sagittal views of planning target volume and anatomical relationship with bladder and rectum. 48
Figure 2.4: Comparison of measured and calculated fluence distributions from a selected intensity modulated field. The top panel shows (a) the film measurement, (b) the BrainSCAN calculated distribution, and (c) the Eclipse calculated distribution. The two lower panels show profiles through the three distributions horizontally (d) and vertically (e). The location of these profiles is indicated by the white cross-hair on the film measurement distribution. 51

Figure 2.5: Two dimensional gamma maps comparing film measured distributions to BrainSCAN (a) and Eclipse (b) calculated distributions. 52
Figure 2.6: Planning comparison for Case #1 using a benchmark conformal plan and 7-field IMRT plans for BrainSCAN and Helios. Calculated dose volume histograms for the PTV un-normalized (a) and normalized at 99% coverage of the PTV (b). Calculated dose volume histograms for the left (c) and right (d) parotid glands with all three plans. The asterisks on the dose volume histograms indicate the restraint values used for optimization. 55
Figure 2.7: Planning comparison for Case #2 using a benchmark conformal plan and 7-field IMRT plans for BrainSCAN and Helios. Calculated un-normalized (a) and normalized (b) dose volume histograms for the PTV. Calculated dose volume histograms for the brainstem (c) and spinal cord (d) with all three plans. The asterisks on the dose volume histograms indicate the restraint values used for optimization. 57
Figure 2.8: Planning comparison for Case #3 using a benchmark conformal plan and 5-field IMRT plans for BrainSCAN and Helios. Calculated un-normalized (a) and normalized (b) dose volume histograms for the PTV. Calculated dose volume histograms for the bladder (c) and rectum (d) with all three plans. The asterisks on the dose volume histograms indicate the constraint values used for optimization. 58
Figure 2.9: Case #2 BrainSCAN calculated dose volume histograms for (a) the PTV, (b) all tissue outside the PTV (Normal Tissue), and (c) the brainstem for the four calculations considering the PTV Only and the organs-at-risk as a High, Normal and Low priority. 59
Figure 2.10: Case #2 BrainSCAN calculated dose volume histograms for (a) the PTV, (b) all tissue outside the PTV (Normal Tissue) and (c) the brainstem taking into consideration a volume of risk defined immediately outside the PTV and designated Normal Tissue Expansion (NTE). The four curves in each plot are for

the calculations considering the OARs only, the NTE with a maximum dose constraint of 20% and 50% of the isocenter dose and the combination of the organs-at-risk and the NTE at the 50% level. 60
Figure 3.1: Electronic energy levels of an organic molecule possessing a π-electron structure. Adapted from [42] 67
Figure 3.2: Mass energy-absorption coefficients for water, polystyrene and tissue equivalent plastic scintillator for monoenergetic photons ranging from 10 keV to 20 MeV. Plotted using data from [82]. 69
Figure 3.3: Mass collision stopping power for water, polystyrene and tissue equivalent plastic scintillator for monoenergetic electrons ranging from 10 keV to 25 MeV. Plotted using data from [83]. 69
Figure 3.4: Tissue equivalent plastic scintillator small-volume, point detector system. A small active volume plastic scintillator is optically coupled to a photomultiplier tube that detects scintillation light. A 'background' fiber optic light guide and PMT are used to detect the Čerenkov light contribution. Adapted from [84]. 70
Figure 3.5: Tissue equivalent plastic scintillator two-dimensional dose measurement system. A CCD video camera captures light emitted from a sheet of plastic scintillator fixed in a water-filled Plexiglas cylinder. The sheet is irradiated using coplanar IMRT treatment beams with the beam axis parallel to the plane of the scintillating sheet. Isocenter of the IMRT plan is indicated by the *. Adapted from [89]. 72
Figure 3.6: Schematic representation of IMRT verification system: (a) phantom outer box with CCD camera capturing light reflected out of viewing window; (b) inner wedge insert with Lucite mirror at 45° to scintillator sheet 73
Figure 3.7: Orientation of IMRT verification system with respect to treatment unit. The system is oriented so that the treatment beam is orthogonal to the scintillator sheet of the phantom thus allowing measurement of beam's-eye-view doses. 74

Figure 3.8: Machining diagram for verification system phantom showing (a) side, (b) front and (c) top perspectives. All non-labeled walls consist of opaque black Lucite. All dimensions are given in centimeters..... 75
Figure 3.9: Prototype of IMRT verification system phantom. Tissue equivalent plastic scintillator sheet is shown at the top while the clear, viewing window is to the right. Small filling hole is used to fill the inner cavity with water to complete tissue equivalence of the phantom..... 76
Figure 3.10: Initial state of tissue equivalent plastic scintillator sheet following casting. Top and bottom surfaces are smooth and clear while edges are rough and translucent from cutting of sheet to specified dimensions..... 78
Figure 3.11: Summation images from sanding investigation for (a) no sanding (i.e. smooth, cast surface) and (b) sanding using 220 grit sandpaper. Also illustrated are the square, 1 cm × 1 cm, region-of-interest (ROI) and the horizontal profiles used for analysis of the images..... 79
Figure 3.12: Example light intensity distributions measured using the initial prototype phantom described above for (a) an 10 cm × 10 cm open square field and (b) a 25 cm × 25 cm open square field..... 82
Figure 3.13: Origin of spatially variant cross-talk phenomenon. A high energy photon at point A produces scintillation light which is emitted directly towards the CCD camera (dashed line) as well as towards the point B for higher emission angles (solid line). If these visible photons reaching point B reflect off the scintillator back towards the CCD camera (dotted line) they will be indistinguishable from scintillation photons emitted from a high energy photon interaction at point B. Adapted from [95]..... 83
Figure 3.14: Placement and orientation of the micro-louvre optical collimator film in the verification phantom. Micro-louvre optical collimator is fixed directly below scintillation screen with collimation strips perpendicular to the y-direction..... 84

Figure 3.15: Effects of micro-louvre optical collimator film on images acquired using verification system for (a) 10 cm × 10 cm open square field and (b) 25 cm × 25 cm open square field. 85
Figure 3.16: Normalized intensity profiles across 25 cm × 25 cm open square field with and without presence of micro-louvre optical collimator film in (a) the x-direction and (b) the y-direction. 85
Figure 3.17: Spectral response characteristics of Hitachi KP-M1 monochrome CCD camera. The camera used in this work was fitted with an infrared (IR) cut filter. Adapted from [99]..... 87
Figure 3.18: Dark current or background images using verification system (a) prior to and (b) after local positioning of control and capture computer in linear accelerator treatment vault..... 88
Figure 3.19: Image of linear accelerator field verification light for a 10 cm × 10 cm field acquired using CCD camera. Crosshair marks position of isocenter while edge separation can be used to determine image scaling factor. Image mottle is the result of mottle on thin translucent projection sheet..... 90
Figure 3.20: Placement of tissue equivalent scatter material around phantom to ensure full scatter conditions during dose measurement. 91
Figure 3.21: Prototype dose verification system setup for measurements at a depth of 10 cm. This photograph shows positioning of the dose verification system under the linear accelerator with tissue equivalent scatter material for full scatter conditions in place and 10 cm of Solid Water for measurement at depth. 92
Figure 3.22: Image acquisition control visual interface used to control CCD camera during system setup and data acquisition..... 93
Figure 3.23: Central profiles through optimized blurring kernel described in equation 3.7 in the x-direction (a) and the y-direction (b)..... 96
Figure 3.24: Profiles across original, blurred distribution, de-blurred distribution, and treatment planning system (TPS) calculated distribution for a 2 cm × 2 cm square

field showing effects of deconvolution of optimized kernel in the x-direction (a) and the y-direction (b). 97
Figure 3.25: A typical light intensity / dose calibration curve used for final conversion of light intensity value to dose. 98
Figure 4.1: Sample square 10 cm ×10 cm field illustrating positioning of 1 cm × 1 cm square region-of-interest centered around isocenter. 100
Figure 4.2: Pixel intensity of the system with respect to field size and dose delivered. The solid line represents a linear fit of the average response of all fields. 103
Figure 4.3: Acquired image field size in pixels with respect to physical field size in centimeters as shaped by the collimator jaws. Data is shown for both the x-direction and the y-direction. 105
Figure 4.4: Čerenkov signal contribution images for (a) 10 cm × 10 cm square field and (b) 25 cm × 25 cm square field acquired using phantom with scintillation detector sheet replaced with Lucite sheet. The central region-of-interest as well as the gradient regions-of-interest used for analysis of the Čerenkov contribution are also shown in (b). 106
Figure 4.5: Dependence of Čerenkov signal on the dose deposited at the detection plane. All measurements were acquired using a 5 cm × 5 cm square field. The solid line represents a linear fit of the data. 107
Figure 4.6: Average region-of-interest pixel intensity as a function of time. Data has been normalized such that the average observed response over the 180 day period is equal to unity. 108
Figure 4.7: Relative dose distributions for simple static fields. Results are shown for the 5 cm × 5 cm square field measured using (a) scintillator based verification system and (b) 2-D film dosimetry and for the 10 cm × 10 cm square field measured using (c) scintillator based verification system and (d) 2-D film dosimetry. Crosshairs indicate positions of 1-D profiles shown in Figure 4.8.. 109

Figure 4.8: Profiles across measured relative dose distributions for both scintillator based verification system and film dosimetry for 5 cm × 5 cm square field in (a) x-direction and (b) y-direction and for 10 cm × 10 cm square field in (c) x-direction and (d) y-direction. Point ionization chamber measurements are illustrated with asterisks..... 110

Figure 4.9: Percent dose difference and gamma factor maps for simple static field data acquired using scintillator verification system and 2-D film dosimetry. The 5 cm × 5 cm square field percent dose difference map is shown in (a) while the gamma factor map for this field is shown in (b). The 10 cm × 10 cm square field percent dose difference map is shown in (c) while the gamma factor map for this field is shown in (d). 111

Figure 4.10: Relative dose distributions for a wedged field in the y-direction measured using (a) scintillator based verification system and (b) 2-D film dosimetry. Crosshairs indicate positions of 1-D profiles shown in Figure 4.11.113

Figure 4.11: Profiles across measured relative dose distributions for wedged field in y-direction for both scintillator based verification system and film dosimetry in (a) x-direction and (b) y-direction. Point ionization chamber measurements are illustrated with asterisks..... 114

Figure 4.12: Relative dose distributions for a wedged field in the x-direction measured using (a) scintillator based verification system and (b) 2-D film dosimetry. Crosshairs indicate positions of 1-D profiles shown in Figure 4.13.114

Figure 4.13: Profiles across measured relative dose distributions for wedged field in x-direction for both scintillator based verification system and film dosimetry in (a) x-direction and (b) y-direction. Point ionization chamber measurements are illustrated with asterisks..... 115

Figure 4.14: Percent dose difference and gamma factor maps for dynamic wedged field data acquired using scintillator verification system and 2-D film dosimetry. The percent dose difference map for the wedged field in the y-direction is shown

in (a) while the gamma factor map for this field is shown in (b). The percent dose difference map for the wedged field in the x-direction is shown in (c) while the gamma factor map for this field is shown in (d). 116

Figure 5.1: Dosimetric comparison results for field number 5 of the 7-field IMRT treatment plan. Dose distributions measured using (a) scintillator dosimetry system and (b) film dosimetry are shown with crosshairs indicating positions of 1-D profiles. Profiles in the x- and y-directions are shown in (c) and (d) respectively. Percent dose difference (e) and gamma factor (f) maps are also shown for these dose distributions. 126

Figure 5.2: Dosimetric comparison results for field number 7 of the 7-field IMRT treatment plan. Dose distributions measured using (a) scintillator dosimetry system and (b) film dosimetry are shown with crosshairs indicating positions of 1-D profiles. Profiles in the x- and y-directions are shown in (c) and (d) respectively. Percent dose difference (e) and gamma factor (f) maps are also shown for these dose distributions. 127

Figure 5.3: Relative dose distributions for high spatial frequency IMRT field. Measured distributions acquired using the scintillator dosimetry system (a) and film dosimetry (b) are shown in addition to predicted distributions calculated by the Eclipse (c) and BrainSCAN (d) treatment planning systems. Crosshairs indicate positions of 1-D profiles shown in Figure 5.4. 132

Figure 5.4: Profiles across measured and planned relative dose distributions for the high spatial frequency IMRT field. Profiles through the measured distributions are compared to profiles through the BrainSCAN calculated distribution in (a) the x-direction and (b) the y-direction. Profiles through the measured distributions are compared to profiles through the Eclipse calculated distribution in (c) the x-direction and (d) the y-direction. Point ionization chamber measurements are illustrated with asterisks. 134

Figure 5.5: Percent dose difference maps comparing scintillator measured distribution with (a) film measured distribution, (b) Eclipse calculated distribution, and (c) BrainSCAN calculated distribution..... 135
Figure 5.6: Gamma factor maps comparing scintillator measured distribution with (a) film measured distribution, (b) Eclipse calculated distribution, and (c) BrainSCAN calculated distribution. 136
Figure 6.1: Schematic representation of an anthropomorphic cumulative dosimetry phantom using the prototype IMRT verification system described in this work.146
Figure 6.2: Schematic diagram of alternative tissue equivalent plastic scintillator dosimetry system with reflecting mirror placed outside of water cavity..... 147
Figure 6.3: Anthropomorphic, cumulative version of alternative tissue equivalent plastic scintillator dosimetry system. 148
Figure A.1: Dosimetric comparison results for field number 1 of the 7-field IMRT treatment plan. Dose distributions measured using (a) scintillator dosimetry system and (b) film dosimetry are shown with crosshairs indicating positions of 1-D profiles. Profiles in the x- and y-directions are shown in (c) and (d) respectively. Percent dose difference (e) and gamma factor (f) maps are also shown for these dose distributions. 161
Figure A.2: Dosimetric comparison results for field number 2 of the 7-field IMRT treatment plan. Dose distributions measured using (a) scintillator dosimetry system and (b) film dosimetry are shown with crosshairs indicating positions of 1-D profiles. Profiles in the x- and y-directions are shown in (c) and (d) respectively. Percent dose difference (e) and gamma factor (f) maps are also shown for these dose distributions. 162
Figure A.3: Dosimetric comparison results for field number 3 of the 7-field IMRT treatment plan. Dose distributions measured using (a) scintillator dosimetry system and (b) film dosimetry are shown with crosshairs indicating positions of 1-D profiles. Profiles in the x- and y-directions are shown in (c) and (d)

respectively. Percent dose difference (e) and gamma factor (f) maps are also shown for these dose distributions. 163
Figure A.4: Dosimetric comparison results for field number 4 of the 7-field IMRT treatment plan. Dose distributions measured using (a) scintillator dosimetry system and (b) film dosimetry are shown with crosshairs indicating positions of 1-D profiles. Profiles in the x- and y-directions are shown in (c) and (d) respectively. Percent dose difference (e) and gamma factor (f) maps are also shown for these dose distributions. 164
Figure A.5: Dosimetric comparison results for field number 6 of the 7-field IMRT treatment plan. Dose distributions measured using (a) scintillator dosimetry system and (b) film dosimetry are shown with crosshairs indicating positions of 1-D profiles. Profiles in the x- and y-directions are shown in (c) and (d) respectively. Percent dose difference (e) and gamma factor (f) maps are also shown for these dose distributions. 165

List of Abbreviations

BEV	beam's-eye-view
CCD	charge-coupled device
CPU	central processing unit
CT	computed tomography
DSK	dose spread kernel
DTA	distance-to-agreement
DVH	dose-volume histogram
EDR2	extended dose range 2
EPID	electronic portal imaging device
FFT	fast Fourier transform
FWHM	full width at half maximum
IMRT	intensity modulated radiation therapy
IR	infrared
MLC	multi-leaf collimator
MU	monitor unit
MRI	magnetic resonance imaging
NTE	normal tissue expansion
OAR	organ-at-risk
PDD	percent depth dose
PET	positron emission tomography
PMT	photomultiplier tube
PSF	point spread function
PTV	planning target volume
RAM	random access memory
RDF	relative dose factor
ROI	region-of-interest
SAD	source-to-axis distance
SNR	signal-to-noise ratio
SPECT	single photon emission computed tomography
SSD	source-to-surface distance
TPS	treatment planning system

Acknowledgments

I would like to thank Dr. Brenda Clark for her supervision during the course of this thesis. Her encouragement, advice, and guidance were greatly appreciated. I would also like to thank my co-supervisor, Dr. James Robar, for his continued support and feedback and especially for providing the inspiration for this work.

My supervisory committee of Dr. Alex MacKay, Dr. Vesna Sossi, and Dr. Jonn Wu have contributed useful critical discussions during the course of this work.

I would like to acknowledge the financial support I have received from the Natural Sciences and Engineering Research Council of Canada (NSERC), the University of British Columbia, and the BC Cancer Agency for which I am grateful.

I would like to express my gratitude to all the physicists and staff members at the Vancouver Cancer Centre. Special thanks go to Rodger Sabey and the electronics staff for helping to bring my CCD camera to life and to Cameron Shorey and Colin Potter for turning my back-of-the-envelope schematics into a working phantom. I am also indebted to the physics assistants, Ron Horwood, Vince Strgar, Vince LaPointe, and Joe Cortese, for offering their time and expertise in the evenings when I was performing my measurements.

I would also like to convey my warmest thanks to my fellow students, Alanah Bergman, Nick Chng, Jongmin Cho, Tony Mestrovic, Marie-Pierre Milette, Moira Schmuland, and Miao Zhang, for providing a stimulating and fun environment to work in and for much needed coffee and lunch breaks. I'd especially like to thank Karl Otto for being a friend and a mentor throughout my time in Vancouver.

My fondest appreciation go to my entire extended family especially my father and mother, Martin and Naomi, my sisters, Cathy and Elizabeth, my brother-in-laws, John and Alex, and my nephews, Justin and Stephen, for their unwavering love and support throughout my very long student-life.

Lastly and most importantly, I would like to thank my wife, Marie-Laure, for her love, patience, support, and understanding It is hard to imagine completing this work without her at my side.

Chapter 1

INTRODUCTION

The goal of radiation therapy for the treatment of cancer is to deliver a highly localized lethal dose of ionizing radiation to the cancerous tumour while sparing the surrounding healthy tissue. Attempts to maximize the dose to the tumour while at the same time minimizing the dose to the surrounding normal tissue have led to the development of complex treatment techniques that result in highly structured dose distributions. Although these radiation delivery techniques have the potential to provide a high degree of control over the 3-dimensional radiation dose distribution delivered to a target, they also pose several problems from a quality assurance perspective with the highly structured dose distributions requiring high resolution verification prior to the beginning of each treatment regime. While several dose verification systems have been developed to meet this need, all such systems have inherent disadvantages which cause them to fall short of the requirements for an "ideal" dose verification system. It is the goal of this thesis to develop and implement a novel method for dosimetric verification of complex dose distributions that has several advantages over current techniques and fulfills all requirements for an "ideal" dose verification system.

1.1 Radiation Therapy

Cancer is a group of diseases characterized by unregulated division of mutated host cells leading to the growth and spread of tumour masses. In 2005, it is estimated that 149 000 Canadians will be diagnosed with cancer and that 69 500 Canadians will die of cancer [1]. Based on current incidence rates, 38% of Canadian women and 44% of Canadian men will develop cancer during their lifetimes and approximately one in four Canadians will die from cancer [1]. Approximately half of all people diagnosed with cancer are treated with some form of radiation, either alone or in combination with other types of cancer treatment such as surgery or chemotherapy [2].

The use of ionizing radiation to treat cancer is termed *radiation therapy*. In radiation therapy a lethal dose of ionizing radiation is delivered to a defined *planning target volume* (PTV), while minimizing the dose to the surrounding healthy tissue and *organs-at-risk* (OARs). The planning target volume includes the cancerous tumour as well as margins to account for both microscopic spread of the disease and target positioning variability. Via both direct and indirect ionizations, the delivered radiation causes molecular damage in DNA and other critical cell components which leads to cell death in the cancerous cells [3]. The overall goal of radiation therapy can be either to eradicate the disease through tumour ablation (curative) or to minimize disease symptoms and alleviate suffering through tumour shrinkage (palliative).

1.1.1 Historical Background

Radiation therapy has been used for the treatment of cancer and other diseases for more than 100 years. As early as 1896, just one year after the discovery of x-rays by Wilhelm Conrad Roentgen, it was realized that ionizing radiation could be used for therapeutic as well as diagnostic purposes [4]. The first report of a patient being cured by radiation therapy was in 1899 [5].

These early uses of radiation therapy were performed on very shallow or surface malignancies such as carcinomas of the skin using low energy cathode ray tubes. Brachytherapy, the use of sealed radioactive sources in radiation therapy, was first performed in 1910 [6]. While initially used for surface application as well, use of sealed sources for interstitial and inter-cavity treatments soon followed thus expanding the types and locations of disease that could be treated with radiation therapy. Further expansion of use was gained through advances in x-ray tube design. By 1922, x-rays tubes with peak energies of 200 keV were available allowing for the treatment of more deeply seated diseases. The 1920s and 1930s also bore witness to a number of famous experiments investigating the radiobiological basis of radiation therapy. These experiments eventually led to the realization that delivering multiple daily treatments to the same treatment site (termed *fractionation*) had several radiobiological advantages over single delivery treatments [7]. The application of fractionation to a wide range of treatment sites eventually formed the basis for modern clinical radiation therapy treatment regimes. The 1940s saw the advent of higher energy

particle accelerators with the Van de Graaf generator providing the first ever megavoltage x-ray treatment device. This evolution to megavoltage energy treatments was a significant step forward considering greater than 50% of all cancers are present in anatomy with a thickness amenable to 1 MeV photons [8]. The introduction of cobalt-60 teletherapy treatment units in 1951 provided an economical, simple and reliable means for delivering megavoltage radiation therapy. With its relatively high specific activity, an average photon energy of 1.25 MeV and a half-life of 5.261 years, cobalt-60 teletherapy units quickly became the most popular devices used for radiation therapy. While still in limited use today, cobalt-60 teletherapy has been replaced as the work-horse of radiation therapy by the linear accelerator (commonly termed *linac*). With typical photon beam energies ranging from 4 MV to 25 MV, today, the vast majority of radiation treatments are delivered using this technology.

1.1.2 Tumour and Healthy Tissue Response

With few exceptions, cancerous tumours are generally not directly accessible by treatment devices and are typically located in close proximity to normal healthy tissue. As such, tumour eradication usually involves radiation beams traversing normal tissue with the consequence of killing normal cells and causing complications as a result of treatment. Due to these circumstances, an understanding of the response to radiation of both tumour and healthy tissue is critical in radiation therapy. Based on *in vitro* experimental data, the models of tumour and healthy tissue response are characterized by sigmoidal dose-response curves such as those displayed in Figure 1.1 [3]. As the dose increases, a threshold dose is reached where tumour eradication commences (approximately 30 Gy in Figure 1.1(a)). Immediately beyond this dose, the tumour response increases sharply as the number of cancerous cells killed swells. This increase is then observed to taper off and the slope of the curve becomes shallower as the 100% response is approached asymptotically. Also displayed in this figure is the response curve for normal tissue. Figure 1.1(a) displays the normal tissue response curve to the right of the tumour response curve in a classical, more favourable representation of a treatment situation. In this representation, the normal tissue is less sensitive to radiation compared to the tumour and choice of the optimum radiation delivery dose to maximize tumour control and minimize normal tissue damage is fairly easy. For Figure 1.1(a) a dose of

50 Gy will result in greater than 95% probability of tumour control with less than 5% chance of normal tissue complications.

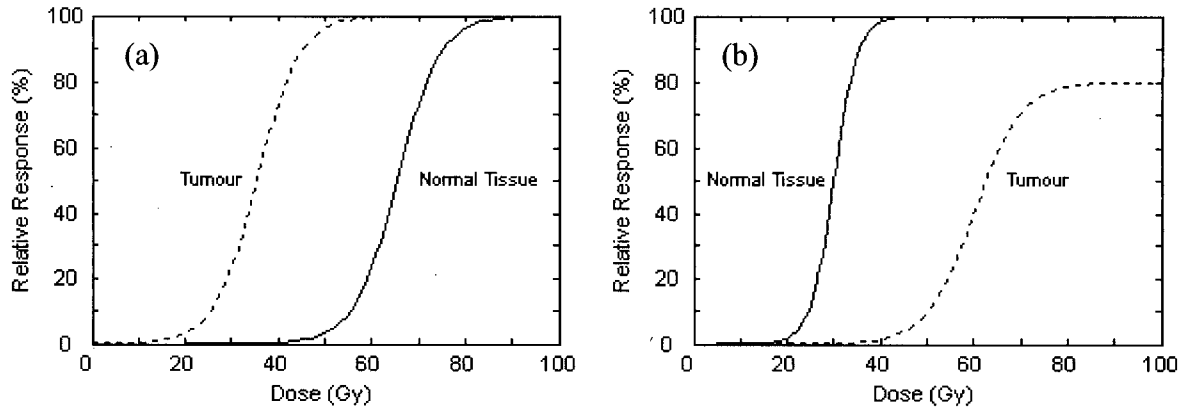

Figure 1.1: Sigmoidal dose-response curves for tumour control and normal tissue response. A classical, more favourable representation is displayed in (a) while (b) shows a more realistic, less favourable representation.

While the classical representation displayed in Figure 1.1(a) is representative of certain dose response curves generated in *in vitro* laboratory settings, it should be noted that very few complete dose response curves have been determined for real clinical situations. Furthermore, the limited data available for such situations indicates considerable deviations from the classical representation. A more clinically realistic dose response representation is displayed in Figure 1.1(b). Although the dose response curves are similar in shape in this figure, several characteristics of this representation make it less favourable compared to the classical representation. Most noticeably, the normal tissue response curve is to the left of the tumour response curve indicating that the normal tissue is more sensitive to radiation in this case. This may be due to a combination of factors including the type of tissue (e.g. differentiation of cells) and physiological condition (e.g. degree of oxygenation). The tumour response curve also has a shallower slope compared to the normal tissue response curve as a result of heterogeneity of tumour cells throughout the tumour volume. Finally, the tumour response curve never reaches 100% due to the presence of microscopic or metastatic spread of the disease beyond the primary tumour site. The model displayed in Figure 1.1(b) poses a considerable problem as the normal tissue response limits the delivery of a lethal dose to the tumour. Effective treatment of the tumour in such a case is therefore dependent

on the implementation of methods capable of avoiding the normal tissue at risk i.e. minimizing dose to normal tissue while maximizing dose to tumour.

1.1.3 Treatment planning

Treatment planning refers to the process of determining the optimal treatment configuration to ensure the goal of the treatment, whether palliative or curative, while minimizing the probability of normal tissue complications. An integral part of this process is the calculation of the distribution of dose that results from a single or multiple beams entering the patient from different directions. In most treatment planning methods, beam geometries are altered in an iterative process to optimize the calculated dose distribution to match the prescription of the radiation oncologist. This type of treatment planning is referred to as *forward planning*. Dose calculation methods have evolved considerably over the past 50 years primarily as a result of the introduction and advancement of computers. Early computers used for radiation dose calculation in the 1960s made use of two-dimensional universal atlases of isodose distributions to predict the contribution from individual treatment beams [9]. Today, computer technology has advanced to the point where complex and computationally difficult techniques of dose calculation (see section 1.2.5) can be used to calculate the three-dimensional dose distribution based on the individual subtleties of each patient's anatomy.

1.1.3.1 Evaluating Treatment Plans

Throughout the treatment planning process it is necessary for the treatment plan to be continuously evaluated. This evaluation is necessary to observe the effect of the iterative changes made to the plan as it is being optimized and to ensure the final plan meets the objectives set in the radiation oncologist's prescription. Methods of assessing three-dimensional treatment plans include two-dimensional isodose displays, three-dimensional dose surfaces and dose-volume histograms (DVHs). All three of these modalities for evaluating treatment plans are illustrated in Figure 1.2. The DVH displayed in this figure is a differential dose-volume histogram showing the percent volume of the target or organ receiving a given amount of radiation or more. Each of the evaluation methods shown in Figure 1.2 have their inherent advantages and disadvantages. For instance, isodose lines and surface displays give detailed information about the physical locations of doses but give no

information summarizing target volume coverage or organ-at-risk sparing. On the other hand, dose-volume histograms provide a clear summary of the volumes irradiated to different doses but give no information about where doses occur within each organ. In most cases, several evaluation methods are used in concert to assess a treatment plan thus overcoming the shortcomings of each individual method.

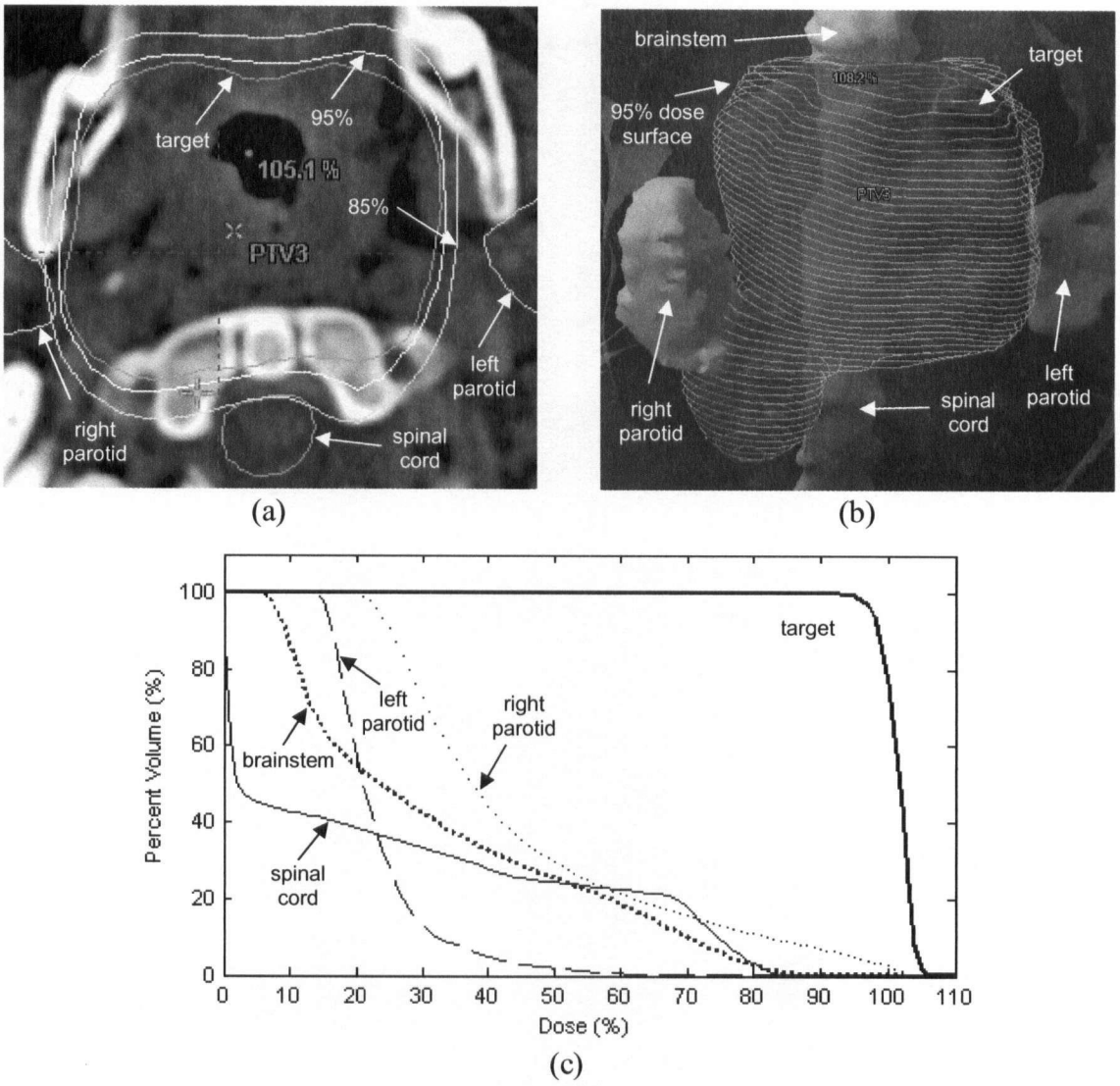

Figure 1.2: Evaluation methods for assessing three-dimensional radiation treatment plans include (a) isodose displays, (b) three-dimensional dose surfaces and (c) dose-volume histograms.

1.1.3.2 Advances in Imaging

Accurate determination of the delivered dose distribution and successful treatment of the disease site are obviously dependent on the ability to accurately localize both the disease and the surrounding normal tissue. In early radiation therapy, radiation oncologists were limited to using conventional 2-dimensional radiography and surface palpation thus causing large uncertainties in target localization. This situation changed dramatically with the introduction of x-ray computed tomography (CT) in the early 1970s [10]. CT imaging uses numerous radiographic projections acquired at various angles around the patient to reconstruct a 3-dimensional image volume representing the physical density of the inside of the patient. This image volume can be readily used by radiation oncologists to precisely identify the location and size of disease as well as normal tissue. With further advances in CT imaging in addition to the advent of other imaging modalities including magnetic resonance imaging (MRI), single photon emission computed tomography (SPECT) and positron emission tomography (PET), today's radiation oncologist is able to access a plethora of information to aid in the accurate localization of disease.

1.2 Dose Deposition

An understanding of the process of dose deposition is critical in radiation therapy. Although several different types of ionizing radiation (e.g. electrons, protons, etc.) may be used to deliver a lethal dose to a disease site, this thesis will deal primarily with the use of high energy photons. Photons fall into a subcategory of ionizing radiation termed *indirectly ionizing radiation* due to their lack of an electronic charge. Unlike *directly ionizing radiation* (charged particles) which produce ionizations through Coulombic interactions as they pass through matter, uncharged, indirectly ionizing particles such as photons liberate charged particles (electrons) in matter. The subsequent ionization of the matter is carried out by these liberated particles.

1.2.1 Kerma and Absorbed Dose

As a result of the two stage process in the ionization of matter by indirectly ionizing radiation such as photons, dose deposition also occurs in two stages. The transfer of energy in the first

stage, as the photon sets electrons into motion, is termed *kerma* (kinetic energy released in the medium) and is defined as:

$$K = \frac{dE_{tr}}{dm} \tag{1.1}$$

where E_{tr} is the kinetic energy transferred from photons to electrons in a volume element with mass dm. The absorption of energy from the electron to the medium is termed absorbed dose and is defined as:

$$D = \frac{dE_{ab}}{dm} \tag{1.2}$$

where E_{ab} is the energy imparted to a mass dm. Kerma and absorbed dose both have units of Gray (Gy) where 1 Gray is equal to 1 joule per kilogram (J/kg).

These two stages of dose deposition do not take place in the same location in the medium as the result of electron propagation (i.e. electrons traveling between the location where they were liberated and the location where they finally deposit the last of their kinetic energy). This phenomenon is illustrated in Figure 1.3. In Figure 1.3(a) the location of the liberation (denoted by *) and number of electrons liberated is shown together with the location where these electrons deposit their kinetic energy (denoted by points making up arrows). When photons enter the medium (from the left side), they liberate electrons which travel predominantly in a forward direction relative to the beam. As the beam penetrates further into the medium fewer electrons are liberated due to attenuation of the beam. This causes the kerma in Figure 1.3(b) to progressively decrease with depth in the medium. The absorbed dose curve in this figure has a more complicated shape. Near the surface of the medium where the photon beam enters very little absorbed dose is observed since very few electrons are absorbed in this region. This region, where more electrons are liberated than absorbed, is referred to as the *build-up region*. Beyond the build-up region, the absorbed dose is observed to pass the kerma as more electrons set in motion "upstream" are absorbed than electrons are liberated as a result of attenuation of the photon beam by the medium.

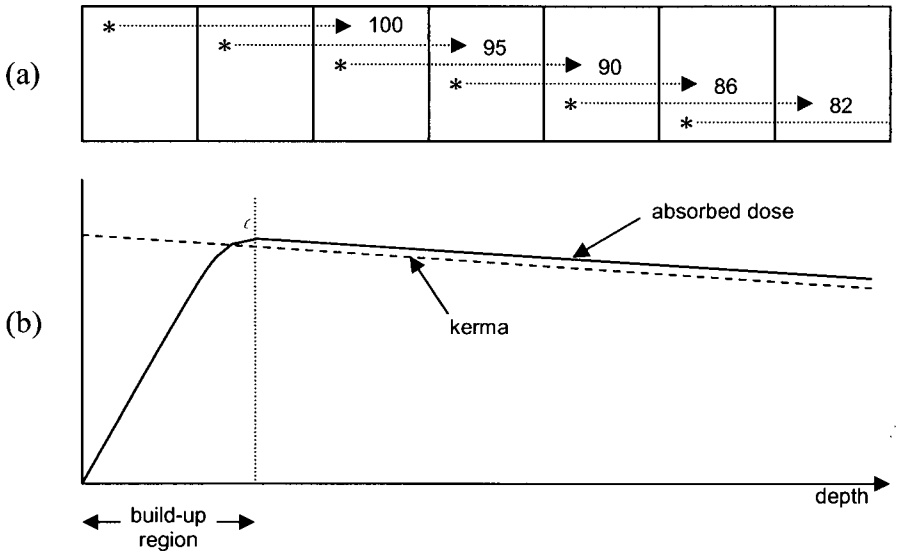

Figure 1.3: (a) Schematic diagram illustrating number of electrons liberated from medium as a function of depth as well as the depth of subsequent energy absorption by the medium. (b) Kerma (dashed line) and absorbed dose (solid line) as a function of depth in medium. Adapted from [9].

The depth in material is not the only factor upon which the dose deposition is dependent. Other factors affecting the dose deposited include the beam energy, the composition of the medium, the distance of the medium from the beam source, as well as the size and shape of the beam aperture. The complex dependence of the dose on such factors, complicates the discussion of how much dose should be delivered by a given beam (i.e. dose must be specified at a certain point in space together with all affecting factors). To simplify this, an arbitrary unit termed the *monitor unit* has been devised. Linear accelerator beams are calibrated such that they deliver a known dose under a set of reference conditions for each monitor unit (MU) of radiation delivered. This monitor unit is defined by a set amount of charge collected in the monitor ionization chamber located in the head of the linac. For instance, a certain radiation therapy clinic may choose to calibrate its linac beams such that the delivery of 1 MU of radiation corresponds to 1 cGy of dose to a point 100 cm from the radiation source at a depth of dose maximum in water for a square beam with dimensions 10 cm × 10 cm. With this calibration in place, all radiation prescriptions can be translated to monitor units prior to delivery thus simplifying matters greatly.

1.2.2 Photon Interactions with Matter

In the 0 to 25 MeV photon energy range used in radiation therapy, there are six primary interactions with matter: Rayleigh scattering, photo-electric effect, Compton scatter, pair production, triplet production and photodisintegration. Of these six interactions, triplet production and photodisintegration have very low probabilities for this energy range and Rayleigh scattering is a coherent, elastic process which does not contribute to the dose. Consequently the most important photon interactions in radiation therapy are the photo-electric effect, Compton scatter and pair production.

The photo-electric effect refers to the interaction of an incident photon with a bound atomic electron in the medium. This process is illustrated in Figure 1.4(a). In this interaction, the entire energy of the incident photon is absorbed by the bound electron which is ejected from the atom leaving a vacancy in one of the inner orbitals of the atom. For an incident photon with energy $h\nu$, the kinetic energy of the ejected photo-electron is given by:

$$E_{e^-} = h\nu - E_b \tag{1.3}$$

where E_b is the electron binding energy. The probability of a photo-electric interaction occurring varies approximately as the inverse cube of the incident photon energy with local probability maxima when the energy is slightly above the binding energy of the electron. The probability also varies with the atomic number of the target medium cubed.

Compton scattering involves the interaction of an incident photon with a loosely bound or free electron as illustrated in Figure 1.4(b). In this interaction, the photon is scattered by the electron and some of the energy of the incident photon is transferred to the recoil electron as kinetic energy, E_{e^-}. The resultant kinetic energy of the Compton electron is thus simply:

$$E_{e^-} = h\nu - h\nu' \tag{1.4}$$

where $h\nu'$ is the energy of the scattered photon which is in turn dependent on both the incident photon energy and the photon scattering angle [6]. The probability of Compton scattering is inversely proportional to the incident photon energy and independent of the atomic number of the medium.

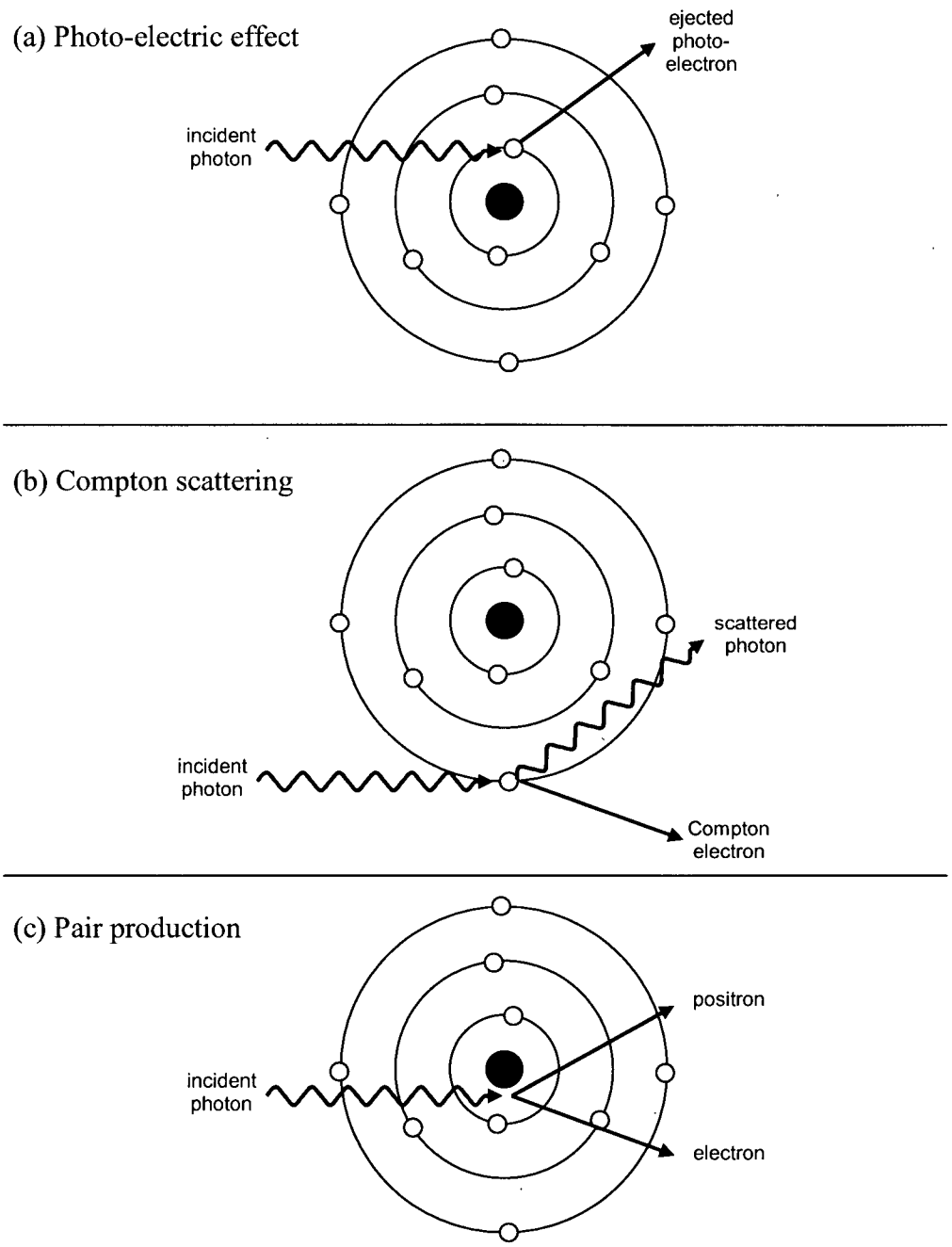

Figure 1.4: Schematic diagram illustrating the three primary photon interactions which contribute to dose deposition in radiation therapy: (a) photo-electric effect, (b) Compton scattering and (c) pair production.

Pair production is a process that occurs when the incident photon energy is greater than 1.022 MeV. In this process, illustrated in Figure 1.4(c), the incident photon interacts

with the electromagnetic field of the nucleus of an atom causing the photon to be completely absorbed and replaced by an electron-positron pair. Since both the electron and the positron have rest mass energies of m_e = 511 keV/c^2, the threshold energy of the incident photon is $2m_e$ or 1.022 MeV. Incident photon energy in excess of this threshold energy is transferred to the electron and positron as kinetic energy:

$$E_{trans} = h\nu - 2m_e \tag{1.5}$$

The most probable distribution of this transferred kinetic energy is an equal sharing between the electron and positron. The probability of pair production occurring varies exponentially with the incident photon energy and as the square of the atomic number of the medium.

The predominant photon interaction will depend on both incident photon energy and atomic number, as illustrated in Figure 1.5. In radiation therapy, the interaction media (i.e. human tissue) is generally composed of low atomic number (Z) materials with Z < 10. Considering this, together with the typical photon beam energies used of 0 to 25 MeV, it is apparent from Figure 1.5 that Compton scattering is the most predominant photon interaction in radiation therapy applications.

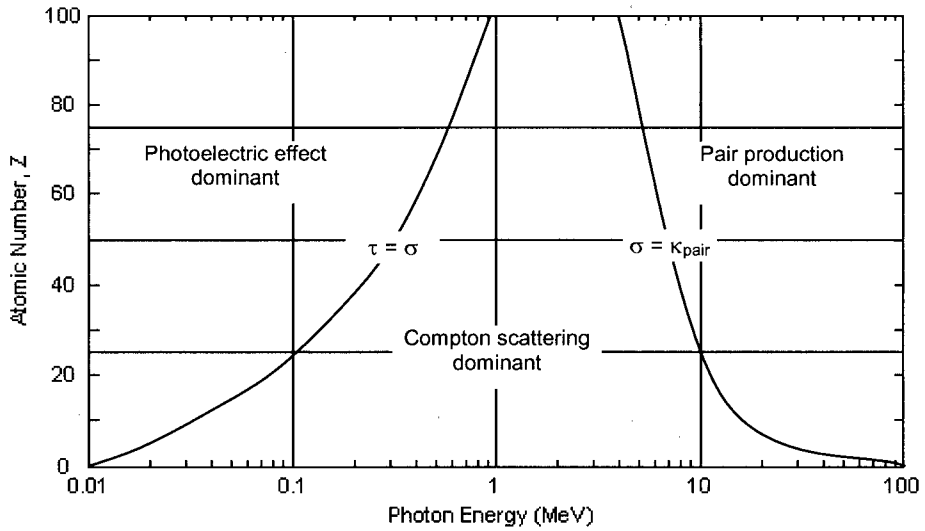

Figure 1.5: Predominance of the three main forms of photon interaction with matter as a function of incident photon energy and atomic number of medium. The lines show the values of Z and photon energy for which the two neighboring effects are equal. Adapted from [11].

1.2.3 Electron Energy Transfer – Stopping Power

The three above mentioned primary photon interactions with matter all transfer energy to electrons in the medium in the form of kinetic energy thus setting the electrons in motion. Propagation of these electrons causes the downstream deposition of dose as described in section 1.2.1. The process of energy transfer between the electrons set in motion and the medium is primarily through Coulombic interactions between the electric field of these moving electrons and the electric field of either electrons or atomic nuclei in the medium.

Interactions involving electrons in the medium result in ionizations along the initial electron's trajectory and are thus termed *ionizational losses*. The rate of energy loss per unit length of material as a result of these interactions is characterized by the ionizational stopping power *dE/dx*, where E is the kinetic energy of the initial energetic electron and x is the length traversed. The mass ionizational stopping power for electrons is obtained by dividing *dE/dx* by the density of the material, ρ:

$$S_{ion} = \frac{1}{\rho}\frac{dE}{dx} = 2\pi r_0^2 N_e \frac{\mu_0}{\beta^2}\left[\ln\frac{E^2(E+2\mu_0)}{2\mu_0 I^2} + \frac{E^2/8-(2E+\mu_0)\mu_0 \ln 2}{(E+\mu_0)^2} + 1 - \beta^2 - \delta\right] \quad (1.6)$$

where:

r_0 = classical electron radius

N_e = number of electrons per gram of medium

μ_0 = $m_e c^2$

β = v/c = incident electron relative velocity

I = mean atomic ionization potential

δ = density correction

This expression gives the energy loss per unit thickness of material and has units of $MeV \cdot cm^2/g$.

Interactions involving atomic nuclei in the medium result in *radiative loss* of energy through bremsstrahlung processes that result in emission of photons. The mass radiative stopping power for electrons is given by:

$$S_{rad} = 4r_0^2 \frac{N_e Z E}{137}\left[\ln\frac{2(E+\mu_0)}{\mu_0} - \frac{1}{3}\right] \quad (1.7)$$

1.2.4 Čerenkov Radiation

Another process through which energetic electrons can lose energy is through the emission of Čerenkov radiation. Čerenkov emission occurs when a charged particle passes through any medium in which the phase velocity of light is less than the particle velocity (i.e. $\beta n > 1$ where n is the refractive index of the medium). These conditions occur when high-speed charged particles pass into a transparent dielectric [11]. While the velocity of the particle is unaltered (except, of course, for the previously described ionizational and radiative losses), the electric field associated with the particle's charge and the magnetic field associated with the motion of this charge are propagated with a phase velocity of only c/n. As the particle "runs away" from a slower-moving portion of its own electromagnetic field, a electromagnetic wave front is formed. The number of quanta emitted is inversely proportional to the square of the wavelength and therefore shorter wavelengths are preferred and Čerenkov radiation appears as bluish-white light. The threshold particle energy required to generate Čerenkov radiation is given by:

$$E_{th} = m_0 c^2 \left(-1 + \sqrt{1 + \frac{1}{n^2 - 1}} \right) \tag{1.8}$$

while the number of photons emitted within a spectral region defined by λ_1 and λ_2 is given by:

$$N = 2\pi d\alpha \left(\frac{1}{\lambda_2} - \frac{1}{\lambda_1} \right) \left(1 - \frac{1}{n^2 \beta^2} \right) \tag{1.9}$$

where d is the depth of medium traversed and α is the fine structure constant. These photons are emitted in an anisotropic fashion with the direction of emission being characterized by a cone spreading out at the Čerenkov angle:

$$\kappa = \arccos\left(\frac{1}{n\beta} \right) \tag{1.10}$$

from the direction of the interacting particle. Although an important consideration in several types of specialized dosimetric devices, Čerenkov radiation is typically not a concern in everyday radiation therapy where the interacting media are in general not transparent.

1.2.5 Pencil Beam Dose Deposition Model

As described earlier, the calculation of the dose deposition from multiple treatment beams is an integral part of the treatment planning process. Currently, this calculation is carried out by computerized treatment planning systems (TPS). These treatment planning systems allow for the "placement" of multiple beams incident upon the patient anatomy (as represented by a CT image set) and subsequent calculation of the resultant dose distribution. Achieving an acceptable treatment plan typically requires several iterations to determine an optimal beam configuration. Due to the iterative nature of this treatment planning process, it is imperative that the calculation of the dose deposition be as efficient as possible. To this end, several simplified dose deposition models have been devised [12]. One such model, which has been implemented in several commercially available treatment planning systems, considers the photon beam as a series of infinitely thin pencil beams [13, 14]. In this *pencil beam* model, the dose resulting from a single pencil beam is assumed to be a symmetric function referred to as the dose spread kernel (DSK) [15]. This dose contributes in a cumulative fashion to the dose from each of the multiple pencil beams making up the radiation field. Since each pencil beam is infinitely small, the summation of all beams to arrive at the cumulative dose can be described as a convolution:

$$D(x,y,d) = \Phi(x,y) \otimes DSK(x,y) = \int_{-\infty}^{\infty}\int_{-\infty}^{\infty} \Phi(a,b)DSK(x-a,y-b,d)dadb \qquad (1.11)$$

where Φ is the input photon fluence and $\otimes$ denotes convolution. By making use of fast Fourier transforms (FFT), this model enables efficient calculation of dose distributions for use in the treatment planning process. In early implementations of this method, the DSK were obtained through Monte Carlo simulations [13, 14]. While having the advantage of being based on the physics of photon and electron interactions, the application of these DSK were not straightforward since they necessitated information on the energy spectrum and primary fluence of the photon beam as a function of off-axis position. To overcome these complications, methods for deriving the DSK from measured photon beam data were suggested [15, 16]. Several recent commercial treatment planning systems make use of this method for generating dose spread kernels used in the calculation of dose.

1.3 General Dose Delivery Techniques – Multiple Fields

There are several techniques available to accomplish the radiation therapy goal of maximizing the lethal dose to the target while minimizing the dose to the surrounding normal tissue. The oldest and most simple technique for external radiation therapy is to use multiple intersecting radiation fields. Figure 1.6 shows the percent depth dose (PDD) curve (i.e. the dose as a function of depth) for a single, square, 10 cm × 10 cm photon beam with a typical radiation therapy energy of 6 MV. As expected, this curve has the same general shape as the dose curve in Figure 1.3(b) with the dose maximum occurring after the build-up region (at a depth of 1.5 cm for this beam energy) after which depth the dose decreases steadily. For this single beam, the relatively shallow depth of the dose maximum (d_{max}) combined with the steady drop off in dose beyond makes delivery of a uniform lethal dose to a target while sparing the surrounding tissue inappropriate for most disease locations.

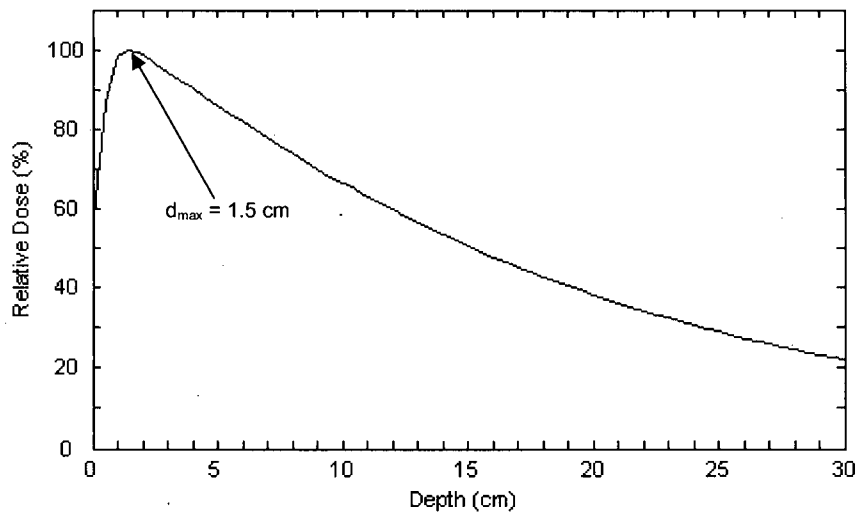

Figure 1.6: Percent depth dose curve in water for a single, square, 10 cm × 10 cm photon beam with an energy of 6 MV. The maximum dose, which occurs at a depth of 1.5 cm, has been normalized to 100%.

Figure 1.7 displays the dose distributions obtained through the use of multiple radiation fields. For the prostate cancer case shown, four intersecting fields are used to deliver the prescribed dose with the point of intersection of these fields located inside the target volume. As shown in the figure, this technique has improved the uniformity of the dose delivered to

the target while reducing the peripheral doses around the patient, thus sparing the surrounding normal tissue.

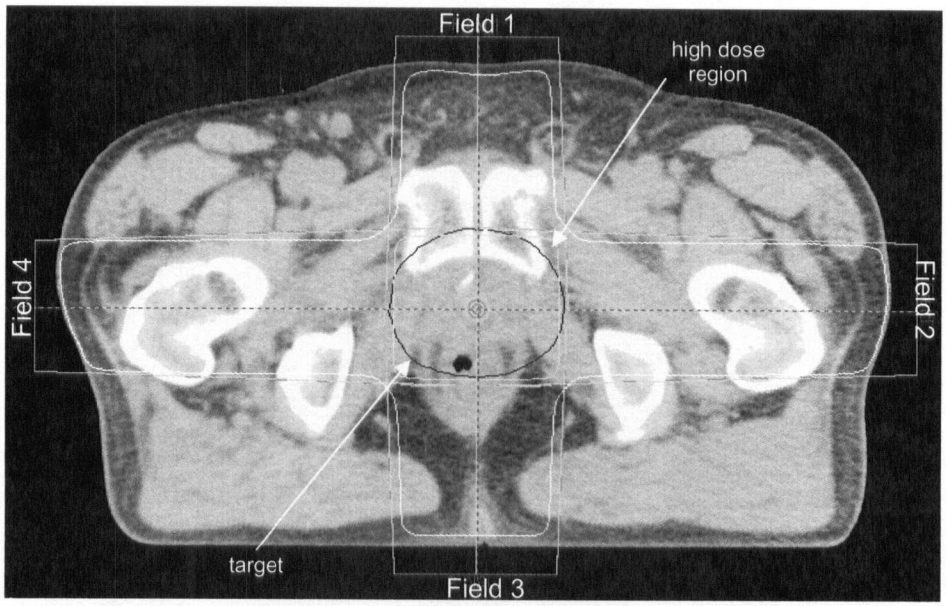

Figure 1.7: Dose distribution for a multiple radiation field treatment. In this case, four fields are used to treat a prostate tumour thus improving the uniformity of the lethal dose delivered to the target and sparing the surrounding normal tissue by spreading the dose out over a larger volume.

Selection of the number of beams used as well as the relative directions of these beams is a manual, iterative, treatment planning process which often depends on clinical experience. Although computerized techniques for determining the optimal beam number and direction have been investigated [17, 18], none have achieved clinical implementation.

Treatment using multiple radiation fields is facilitated by the design of modern linear accelerators. A schematic diagram of one such unit is displayed in Figure 1.8. As shown in this figure, the high energy photon source in these units is mounted on a gantry that is capable of rotating 360° around a fixed point in space termed the *isocenter*. As such the distance from the source to the isocenter is fixed (typically at 100 cm).

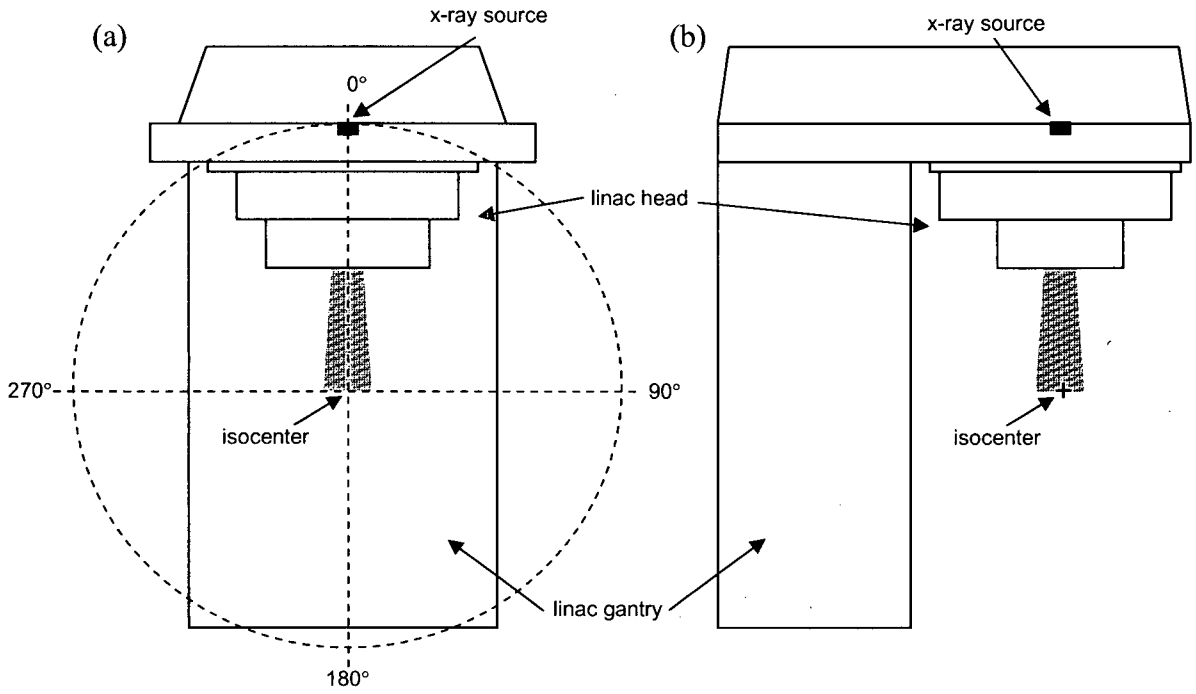

Figure 1.8: Front- (a) and side-view (b) schematic diagrams illustrating design of modern linear accelerator treatment units. The high energy photon source is capable of rotating around a fixed point in space known as the isocenter.

1.4 Field Shaping

Another obvious way to maximize the lethal dose to the target and spare the surrounding normal tissue is to shape the aperture of the radiation treatment beam to match the outer contour of the target volume. Treatments using these shaped beams are termed *conformal radiation therapy*. Several types of beam shaping exist in external beam conformal radiation therapy. The simplest method to shape the beam is to use the secondary collimator in the head of the linac. This collimator consists of four large blocks of tungsten (located just before the beam exit port) which can be moved in and out to define the outer edges of the radiation field. On modern linacs, each block, or *jaw*, can be moved independently to form square and rectangular apertures of varying sizes. A schematic diagram illustrating the secondary collimator and its use for field shaping is displayed in Figure 1.9(a). While the secondary collimator may be used to form rectangular fields with the same maximum dimensions as the target, the complex, irregular shape of most targets calls for a further degree of beam shaping which may be carried out through the use of alloy blocks. Alloy

blocks (see schematic diagram in Figure 1.9(b)) consist of patient and field specific blocks molded from a low melting point attenuating metal (i.e. Cerrobend) to shape the beam to match the outer contour of the target. The blocks are placed below the secondary collimator jaws before treatment of each field. Although capable of closely conforming the radiation field aperture to the shape of the target, alloy blocks have several disadvantages. Fabrication of blocks takes several hours and requires handling of Cerrobend which is a toxic material [19]. In addition, blocks are typically very heavy and must be mounted on the linac head by hand thus putting radiation therapists at risk of lifting injuries and putting patients at risk from accidentally dropped blocks. Finally, the necessity to change blocks before treatment of each field adds considerably to the time required to perform a treatment.

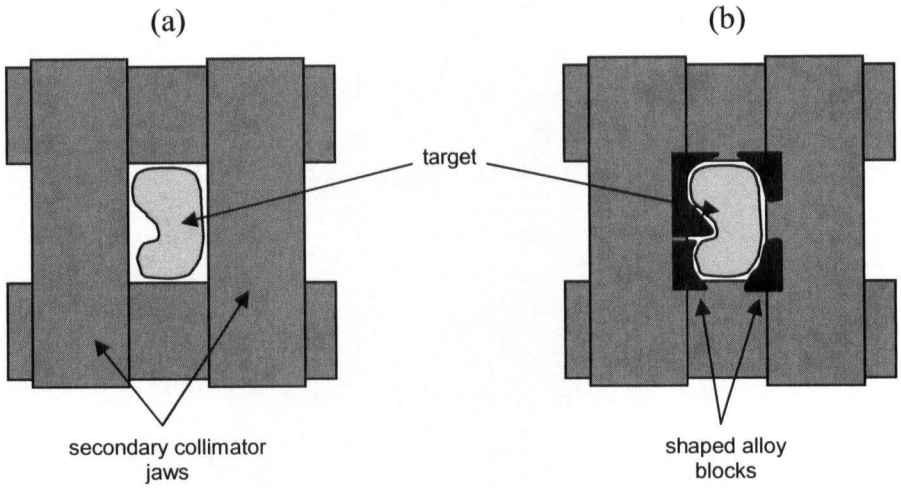

Figure 1.9: Simple beam shaping for external radiation therapy can be carried out using the secondary collimator located in the head of the linac to match outer edges of the rectangular treatment field to the outermost extend of the target (a). The field may be further shaped to conform to the exact shape of the target by using shaped alloy blocks (b).

1.4.1 Multileaf Collimator

To overcome the disadvantages of using alloy blocks, modern linear accelerators are equipped with devices called multileaf collimators (MLCs). MLCs consist of a series of attenuating, tungsten vanes (or leaves) that move parallel to one another in to and out of the radiation field. By positioning each leaf at the edge of the desired radiation aperture shape, the radiation beam can be shaped in a segmental manner to match the approximate

continuous contour of the target. Field definition using multileaf collimators is illustrated in Figure 1.10. The movement of each leaf is facilitated by a computer controlled motor and is independent of the motion of the adjacent leaves. This computer control means that fields may be changes without the need to enter the treatment room.

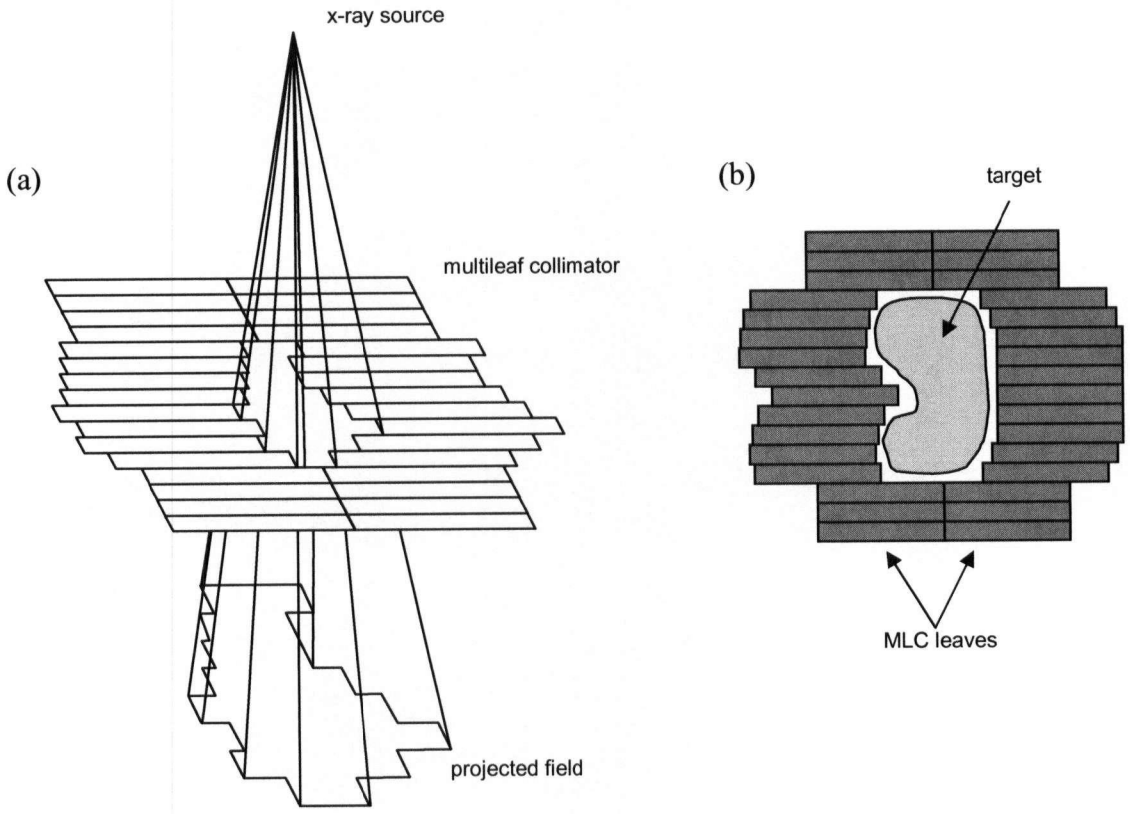

Figure 1.10: Modern beam shaping is performed using multileaf collimator devices (a) which are incorporated into the head of linear accelerator treatment units. Definition of the beam is carried out by moving the attenuating leaves into the radiation field to match the outer contour of the target (b).

MLCs can be mounted directly below the secondary collimator jaws inside the linac head (Varian linear accelerators) or they can replace one set of the collimator jaws completely thus decreasing the size and weight of the linac head (Siemens and Elekta linear accelerators). Typical MLC leaf widths vary from 3 mm to 1 cm (size of leaf width projection at isocenter).

1.5 Intensity Modulated Radiation Therapy

Another technique used to achieve the goals of radiation therapy in more complicated treatment cases is to modulate the intensity of the radiation beam across each field. In its simplest form this intensity modulation can be performed by placing variably attenuating beam modifiers in the beam path. These beam modifiers include physical wedges and compensator blocks and are typically used to reestablish a uniform beam when entering an irregular skin surface contour [9, 20]. Figure 1.11 illustrates the use of beam modifiers in such cases.

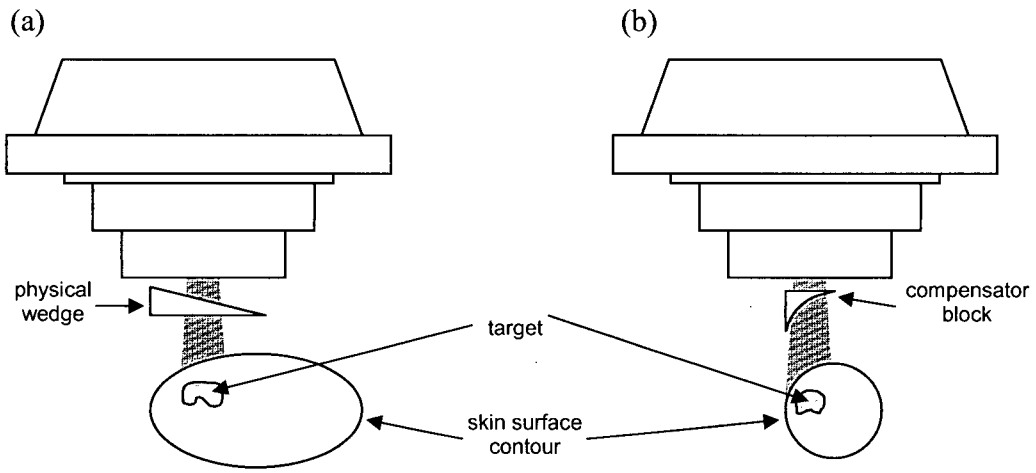

Figure 1.11: Intensity modulation can be accomplished through the use of beam modifiers such as (a) physical wedges and (b) compensator blocks which are typically used to account for irregular skin surface contours.

While the use of beam modifiers is in essence a method of modulating the intensity of the radiation beam, these techniques are still referred to as conventional beam intensity radiation therapy since they do not take into account the geometry of the target volume or surrounding organs-at-risk [19]. *Intensity modulated radiation therapy* (IMRT) refers to a specialized, new modality in which the incident photon beams are purposely modulated to improve the total, cumulative dose distribution produced by many fields. IMRT provides increased flexibility in the dose distributions that can be generated thereby offering the potential for improved target coverage and increased normal tissue sparing.

1.5.1 Plan Optimization

As described above, the two-dimensional field intensities in IMRT are modulated such that the cumulative dose distribution produced by many fields provides uniform coverage of the target with the lethal prescription dose while minimizing dose to surrounding normal tissue. While obviously a very beneficial tool in radiation therapy, IMRT poses several challenges specifically for the treatment planning process. In IMRT each field aperture is divided into a two-dimensional array of "picture elements" or *pixels*. Each pixel also has associated with it a projection or *beamlet* that extends through the patient as illustrated in Figure 1.12.

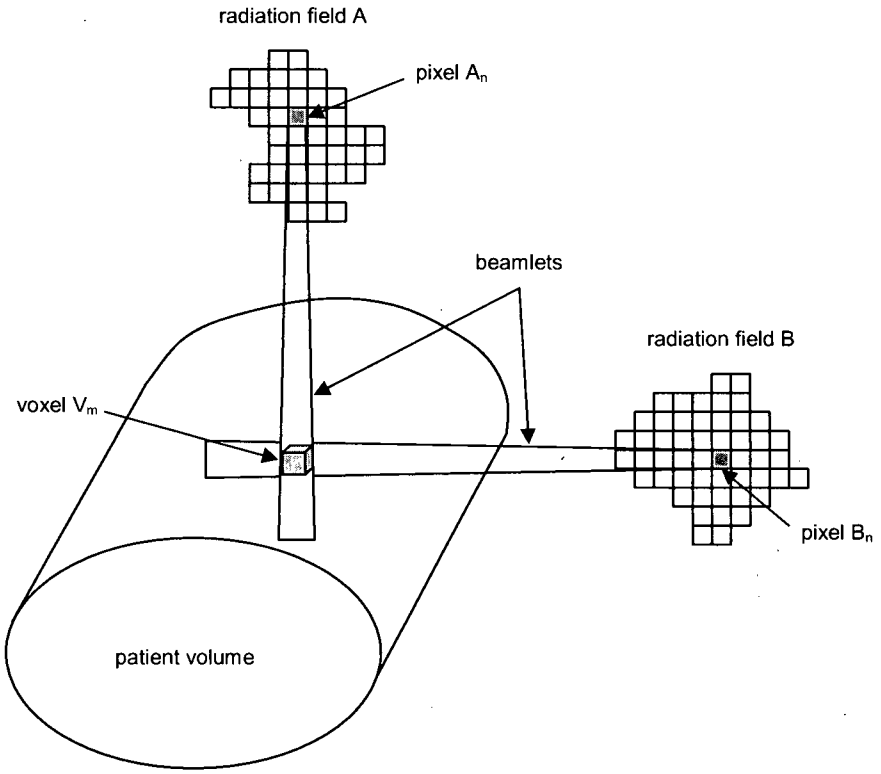

Figure 1.12: In IMRT each field aperture is divided up into an array of pixels each of which has an associated beamlet projecting through the patient volume. The dose deposited in any voxel is affected by all beamlets intersecting it (e.g. the dose in voxel V_m is affected by the beamlets A_n and B_n).

Since IMRT treatments use multiple beam configurations, the dose deposited at a given "volume element" or *voxel* in the patient is affected by the intensity of all beamlets (and hence pixels) that intersect it. This is also illustrated in Figure 1.12 where voxel, V_m, is

observed to be affected by beamlets from both incident radiation beams, A_n and B_n. Typical IMRT treatment plans use between five and nine incident radiation beams [17] with pixel dimensions on the order of 5 mm [21]. The subsequent large number of pixels that can be modified in terms of intensity causes the number of combinations and permutations to be overwhelmingly large for conventional, iterative, forward planning [22]. As a result, optimization of IMRT treatment plans requires *inverse planning*.

IMRT inverse planning is an inverse, automated process where the required dose distribution over the target and surrounding normal structures is specified and an optimization algorithm calculates a two-dimensional intensity pattern for each field to achieve that specification. Most inverse planning algorithms use an iterative method in which thousands of intensity patterns are generated and evaluated before arriving at a solution that satisfies the input criteria [22]. For each arrangement, a single value cost function, usually defined in terms of irradiation of normal tissue and loss of dose homogeneity over the target, is assessed. At each iteration, the algorithm attempts to reduce this cost function to a minimum. A number of approaches have been developed to define and efficiently minimize cost functions for inverse treatment planning [23-27]. In most inverse planning systems, cost functions are based on objectives set by the user. These objectives may include single dose values, a set of dose-volume points or fully flexible dose-volume histograms. The IMRT treatment plan is optimized to fulfill these objectives. Examples of intensity modulated radiation fields are displayed in Figure 1.13.

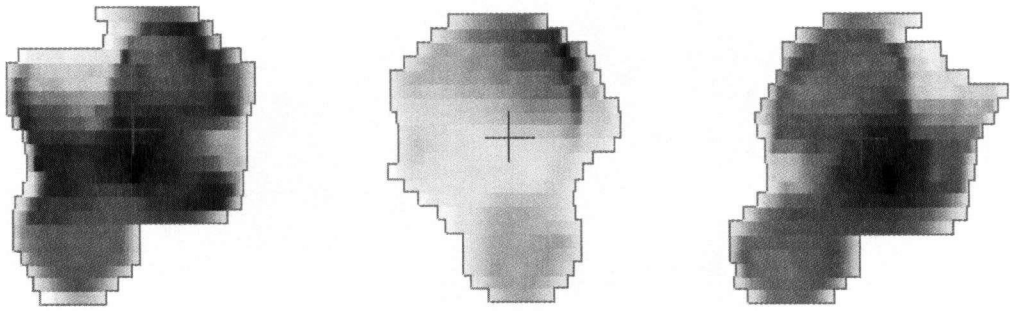

Figure 1.13: Examples of intensity modulated fields. Higher intensity beamlets (pixels) are represented in black while low intensity beamlets are represented by white. Lines indicate target contour as shaped using MLC and crosshair indicates location of isocenter.

1.5.2 Delivery

Once the optimum intensity modulated fields have been determined by the inverse planning system, the next step is to determine how to deliver each field to the patient. The most common method used to generate linear accelerator based IMRT fields is through the use of multiple MLC fields [28]. In this method, each intensity modulated field is decomposed into several uniquely shaped sub-fields all of which cumulatively sum to produce the desired intensity modulation. This technique is illustrated schematically in Figure 1.14. As displayed in this figure, locations where more of the sub-fields overlap receive more intensity compared to locations where fewer sub-fields overlap which in turn receive more intensity compared to locations where just one sub-field is present. By using an adequate number of sub-fields, this method is capable of generating arbitrary intensity maps.

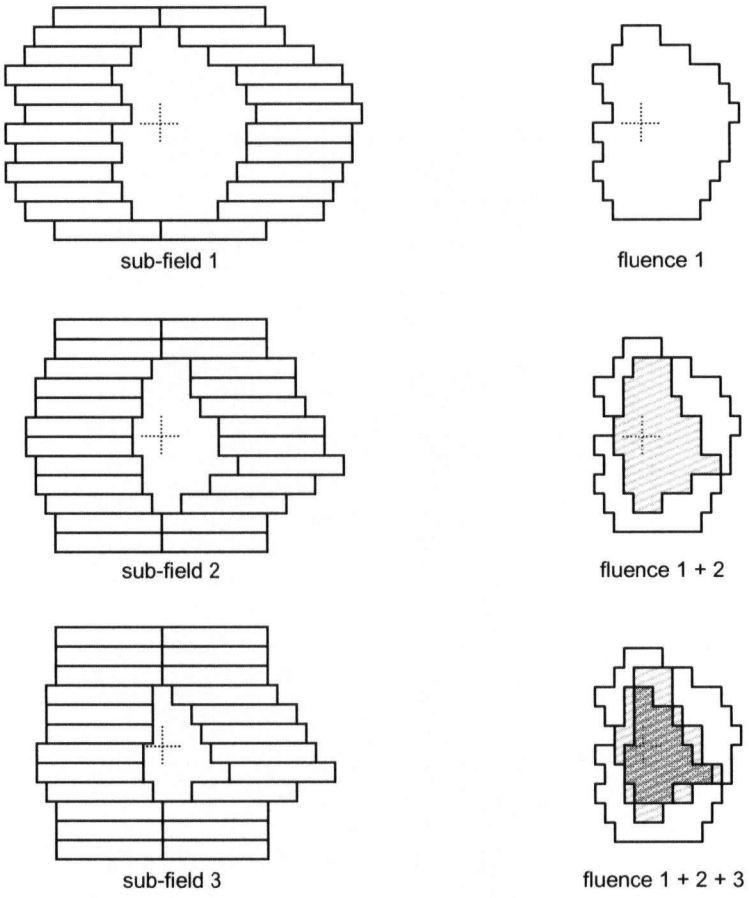

Figure 1.14: Generation of a simple intensity modulated field through delivery of several uniquely shaped sub-fields. The total photon fluence (i.e. intensity) at any point is equal to the sum of all overlapping sub-fields at that point. In this case, darker shading represents higher intensities.

Once the shapes of the necessary sub-fields have been determined, delivery of the intensity modulated field is straightforward using the multileaf collimator. The shapes for all sub-fields are loaded into the MLC control computer such that after delivery of each sub-field the MLC leaves immediately move into the position for the next field. This capability makes total delivery time short enough for clinical use. The sequential delivery of sub-fields to produce the intensity modulation is termed the *step-and-shoot* technique [29]. An alternative for delivering the intensity modulated field is to use a *dynamic* technique [30, 31]. Dynamic techniques deliver the intensity modulated field with the MLC leaves moving continuously throughout delivery by dividing the field into a large number of continuously

varying sub-fields. In this case, the speed of each leaf as well as the dose rate of the linear accelerator are precisely monitored and controlled to ensure accurate delivery.

1.5.3 Intensity and Fluence

When making use of MLC techniques for delivery of intensity modulated fields the terms *fluence* and *intensity* are often used interchangeably. Intensity is defined as the energy, E, passing through unit area, a, per unit time, t:

$$I = \frac{dE}{dadt} \tag{1.12}$$

whereas fluence is defined as the number of photons, N, passed through a unit area, a:

$$\Phi = \frac{dN}{da} \tag{1.13}$$

For MLC based IMRT delivery techniques it can be assumed that the photon energy spectrum remains constant throughout delivery of the field and thus the total energy flux is equal to the number of photons per unit area multiplied by the energy per photon (i.e. energy, E, is directly proportional to the number of photons, N). While this assumption accounts for the numerators in equations 1.12 and 1.13, the time expression in the denominator of equation 1.12 still causes a discrepancy when using fluence and intensity interchangeably in terms of modulation. This discrepancy is a result of the original, inappropriate naming of "intensity modulated radiation therapy". In IMRT, it is the cumulative energy delivered across each field which is of interest and not the rate of deposition of this energy. As the cumulative energy delivered is directly proportional to the total number of photons delivered, a more appropriate name for this technique would have been "fluence modulated radiation therapy". In keeping with the standard terminology used in the field of radiation therapy, henceforth, intensity modulation and fluence modulation will refer to the same process.

1.6 IMRT Dose Verification

Although IMRT has the potential to provide a high degree of control over the three-dimensional radiation dose distribution delivered to a target, it also poses several challenges from a quality assurance standpoint. The complex radiation fluence maps used in IMRT (such as those displayed in Figure 1.13) call for verification of the dose distribution prior to the beginning of each treatment regime [21, 32, 33]. These verification measurements should

include checks of the dose deposited by each field individually (termed *field-by-field measurements*) as well as cumulative measurement of the distribution from all fields. The common technique to carry out these verification measurements is to create a series of "phantom" or "hybrid" plans [34]. This technique is performed by applying the MLC segments, leaf trajectories and MU for each field, as derived from the final patient calculation, to a CT image set of a standard phantom (i.e. an anthropomorphic representation of a patient comprised of a material radiologically equivalent to water) and then recalculating the final deliverable dose distributions to the phantom. These distributions are then compared to measurements acquired using the phantom irradiated according to the phantom plan. Since the shapes of the calculation and measurement phantom are identical, the use of a phantom with a shape different from that of the patient is accounted for and the measured doses should agree with calculation. Observed discrepancies using this technique are thus a result of errors in the transcription of IMRT delivery parameters, leaf sequences and MU calculations or mechanical errors during delivery. This hybrid method can be applied to both field-by-field and cumulative dose distribution measurements. Typical dose and spatial tolerances for such verification measurements are 3% dose difference and 3 mm distance. Discrepancies outside these tolerances are typically deemed unacceptable.

1.6.1 Evaluating Dose Verification Measurements

Once dose verification measurements have been performed, there are several methods available to evaluate discrepancies between the calculated and measured dose distributions. These methods include overlaying isodose distributions, dose profile analysis, dose difference maps, distance-to-agreement (DTA) maps, and gamma factor analysis. While a commonly used technique for comparing distributions, the superposition of isodose distributions is inherently qualitative and as such tends to highlight areas of significant disagreement while leaving areas with smaller discrepancies to be evaluated according to the user's past experience. The use of one-dimensional dose profiles through distributions to compare measured and calculated results enables the user to more quantitatively assess the situation. An example of a dose profile comparison is displayed in Figure 1.15(a). In this technique, the user can qualitatively inspect the profiles for areas of large discrepancies while also given the opportunity to evaluate the magnitude of the discrepancies by observing the y-

axis (i.e. dose values). Quantitative methods which display discrepancies in two-dimensions include dose difference and distance-to-agreement maps. Dose difference maps, such as the one displayed in Figure 1.15(b), are created by subtracting the calculated distribution from the measured distribution. These maps are often displayed in absolute values to facilitate viewing. While very useful for comparisons in low dose gradient regions, dose difference maps have the inherent problem of over-exaggerating the effect of spatial discrepancies in high dose gradient regions such as field edges. In these regions, even very small spatial misalignments of the calculated and measured distributions can lead to very large disagreements in dose. This effect is readily observed at the edges of the field in Figure 1.15(b). Measurement of spatial misalignments between distributions is the basis of distance-to-agreement maps. These maps are created by calculating the distance between a measured data point and the nearest point in the calculated distribution that exhibits the same dose. Unfortunately, DTA maps have the opposite problem to dose difference maps. While useful in comparisons of high dose gradient regions, DTA maps are overly sensitive to low gradient regions where small dosimetric offsets can lead to large DTA values.

Recently, composite analysis methods have been introduced which make use of both dose difference and distance measurements. The most popular of these techniques is the gamma (γ) factor analysis method purposed by Low *et al.* [35]. This method makes use of a set of pass-fail criteria for both dose difference and distance (typically 3% dose difference and 3 mm distance). The dose difference, ΔD, and distance, d, are divided by these criteria respectively and the results are added in quadrature:

$$\gamma_{x,y} = \left\{ \sqrt{\left(\frac{d_{i,j}}{d_{crit}}\right)^2 + \left(\frac{\Delta D_{i,j}}{\Delta D_{crit}}\right)^2} \right\}_{\min i,j} \tag{1.14}$$

The resultant gamma factor map represents points where the criteria are met with values ≤ 1. An example of a gamma factor map is displayed in Figure 1.15(c). As is typical with gamma factor maps, a greyscale colour-map has been chosen with all values meeting the criteria displayed in black. In general, multiple methods are used to evaluate the data from dose verification measurements. Medical physicists use these methods in concert to decide whether a measured distribution is suitably similar to the calculated distribution for treatment to proceed.

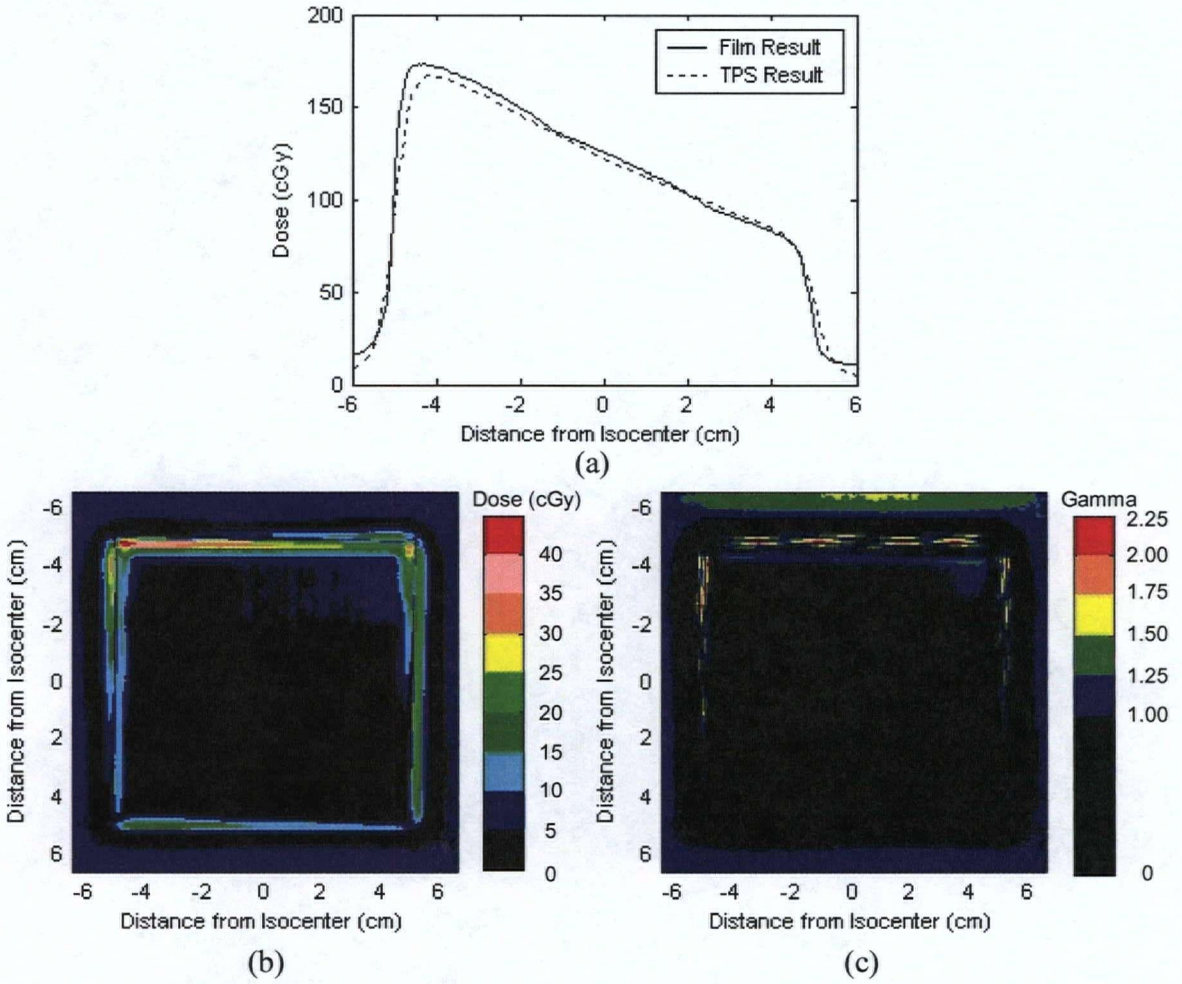

Figure 1.15: Commonly used methods for evaluating dose verification results include (a) one-dimensional dose profile comparisons, (b) two-dimensional dose difference maps, and (c) gamma factor analysis.

1.6.2 IMRT Dosimetric Verification Systems Requirements

Ideally, the measurement modality used for IMRT dosimetric verifications should provide a high resolution measurement of the dose deposited in the tissue equivalent phantom volume while at the same time being not overly labour-intensive. The required resolution for such verification should be less than the dose grid spacing in the treatment planning system being used. Typically this spacing varies from 1 mm to 2.5 mm for IMRT treatment planning systems.

The use of a tissue equivalent measurement medium is the only way to ensure the dose measured is truly representative of the dose that will be eventually deposited in the patient. For the photon energies used in radiation therapy, water is considered to be equivalent to soft tissue [6]. The reason for this can be readily observed in Table 1.1 which lists the physical characteristics relevant to high energy dose deposition for soft tissues and water.

Table 1.1: Physical properties of various tissue equivalent materials in comparison to soft tissue

	Mass Density (g/cm^3)	**Electron Density ($/cm^3$)**	**Effective Z**
Muscle	1.04	3.31×10^{23}	7.64
Fat	0.92	3.34×10^{23}	6.46
Water	1.00	3.34×10^{23}	7.51
Solid Water	1.03	3.34×10^{23}	7.54
Polystyrene	1.04	3.24×10^{23}	5.69
Lucite	1.16	3.24×10^{23}	6.48

The similarities between water and both muscle and fat in terms of mass and electron density as well as effective atomic number are evident. Also listed in this table are the characteristics of three commonly used dosimetric materials. "Solid Water" is the commercial name for an epoxy-resin based composite specifically engineered for use in high energy radiation therapy dosimetric measurements [36]. This material provides a convenient, albeit expensive, alternative to using cumbersome water tanks whose contents must be filled and emptied to adjust for measurement depth during routine dosimetry checks. Solid Water slabs are available in a wide range of sizes and thicknesses for easy stacking to adjust depth of measurement. In terms of dosimetric accuracy, Solid Water has been shown capable of achieving results within ± 1% of measurements in water [36, 37]. The final two materials listed in Table 1.1 are cheaper alternatives to Solid Water. Polystyrene and Lucite are readily available in a wide range of sizes and shapes and can be machined using tools found in a standard machine shop. While studies have shown that the dosimetric accuracy of measurements in these materials may deviate from measurements in water by as much as 3%,

their cost and ability to be machined to form customized anthropomorphic shapes has resulted in them being the most frequently used materials in commercial dosimetry phantoms.

Other important requirements for an IMRT dosimetric verification system are ease of use and reusability of the system for multiple measurements. With IMRT treatments becoming increasingly popular for a wide range of disease sites, it is imperative that IMRT dosimetric verification be a simple and efficient process. In many clinics, the use of clinical treatment units during regular treatment hours means that IMRT dose verification must be carried out on evenings or weekends. Streamlining the verification process by eliminating the use of labour-intensive and time consuming processes involved therefore translates into a saving of clinic resources. In terms of reusability, an ideal measurement system would be capable of performing all measurements needed for verification without the need to replace the measurement media thus saving time (required to enter the treatment room and make the replacement) and reducing cost (for new replacement media). Additionally, a dose verification system should be capable of acquiring data for both the field-by-field verifications as well as the cumulative dose distribution verification.

1.6.3 Current IMRT Dosimetric Verification Systems

Currently, there are several techniques which are actively used for performing IMRT dosimetric verification in clinical settings. These techniques include using ionization chamber and diode detector arrays, gel dosimetry, radiographic film dosimetry, and electronic portal imaging device based dosimetry. While each of these techniques have inherent advantages for performing dosimetric verification of IMRT treatments, currently no single dosimeter fulfills all the requirements discussed above.

1.6.3.1 Ionization Chamber and Diode Detector Arrays

Ionization chambers and diode detectors are both point detectors. Although several different types of ionization chambers exist with varying operational details, their general operating principles are all similar and may be explained using a simple, thimble ionization chamber as an example. A schematic diagram of this device is given in Figure 1.16. It consists of a cylindrical chamber (typically < 6 mm in diameter and < 3 cm in length) encompassing a volume of gas (typically air). The chamber wall consists of either air- or water-equivalent

material and the inner wall is lined with a thin conducting material. In the center of the chamber is a thin, insulated, collecting electrode. When in operation, a voltage is applied between the thin conducting wall lining and this central electrode. When the ionization chamber is placed in a radiation beam, ions are created in the chamber gas. These ions are collected by the anode and the resulting current is measured using an electrometer. Ionization chamber measurements can be related to absolute dose measurements through the use of standard protocols and a factor traceable to a national standards laboratory. They provide point dose measurements which are cumulative over the chamber volume. While useful in providing point dose checks of IMRT distributions, full IMRT dosimetric verification requires at least two-dimensional measurement. IMRT quality assurance devices have been developed which make use of arrays of small ionization chambers [38, 39]. These devices are advantageous in being very easy to use with a completely reusable detector media. Unfortunately, they do not meet the required spatial resolution necessary for IMRT dosimetric verification with detector sizes on the order to 0.5 cm. Furthermore, the detection media are typically not tissue equivalent due to the presence of readout electronics.

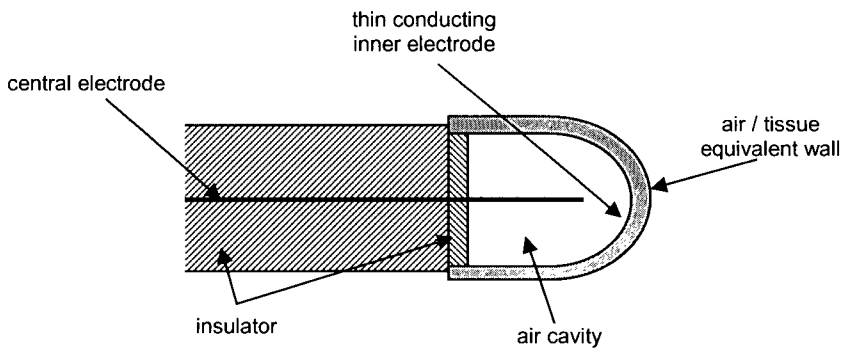

Figure 1.16: A simple, thimble ionization chamber commonly used in radiation therapy dosimetry.

Diode detector arrays have also been developed for use in IMRT quality assurance [40, 41]. These detectors are made of semiconductor materials such as silicon which has been doped with impurities to form "p-" and "n-type" silicon [42]. The p-type silicon is so-called because it contains an excess of holes and is therefore an electron acceptor. Conversely, the n-type silicon has an excess of electrons and is therefore an electron donor. When a reverse bias potential is placed across the p-n junction between the n- and p-type

silicon, an enhanced depletion region is created as a net negative space charge builds on the p-side and a net positive space charge builds on the n-side. This effect is illustrated in Figure 1.17. The accumulated space charge creates an electric field which stops the diffusion of charge carriers inherent in the materials. When this electronic configuration is placed in a radiation beam, ionizations lead to the formation of electron-hole pairs in the depletion region. As a result of the bias, the electrons and holes are swept to the n- and p-sides of the junction, respectively, thus creating a current which can ultimately be related to the absorbed dose. Diode detectors are advantageous in their relative ease of use as well as their small sizes (typically < 1 mm). Unfortunately, diodes tend to be quite susceptible to radiation damage and thus require frequent adjustment of their relative output and eventual replacement [42]. Furthermore, the electronics necessary for readout of diode arrays cause these devices to be non-tissue equivalent and the practicality of reading out each individual diode greatly limits the number of diodes used in these devices thus limiting their inherent resolution.

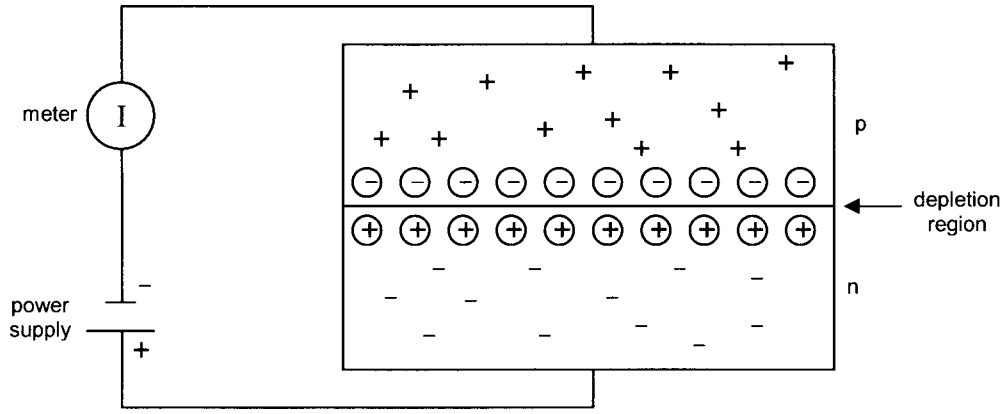

Figure 1.17: Schematic diagram of a typical p-n diode detector. A reverse bias potential across the p-n junction causes the creation of a depletion region.

1.6.3.2 Gel Dosimetry

The most commonly used gel dosimeters are Fricke and polyacrylamide gels [43]. Both of these dosimeters are based on radiation induced chemical changes in molecules which have been spatially fixed in a matrix of gelatin or agarose. In Fricke gel dosimeters ferrous ions (Fe^{2+}) are oxidized into ferric ions (Fe^{3+}) whose concentration can be related to absorbed

dose. In polyacrylamide gels, radiation causes the polymerization of acrylamide and N,N' methylene-bis-acrylamide into long cross-linked macromolecules [44]. In both cases, gels are prepared in a laboratory and poured into the desired phantom where they are allowed to set. Once set, the gel filled phantom is irradiated and dose distribution information is read out using an imaging modality such as MRI [45, 46], x-ray CT [47] or optical CT [48].

Advantages of gel dosimetry include tissue equivalent measurement media, a high spatial resolution (on the order to 1 to 2 mm depending on readout modality), and the fact that these systems provide three-dimensional dose distribution measurements. The main drawbacks of gel dosimetry systems are the time, labour and facilities necessary to support such a dosimetry program. As mentioned, gel dosimetry requires a use of a laboratory for (often arduous) preparation of the gels. Depending on the type of gel dosimeter used, this preparation may necessitate air-tight glove boxes. The need for a suitable readout modality may also pose problems in clinical settings where MRI and x-ray CT resources may be limited. Finally, the requirement of a reusable detection medium is not fulfilled by gel dosimetry. For each verification procedure, a newly filled gel phantom is necessary.

1.6.3.3 Film Dosimetry

Film is widely used in IMRT quality assurance as a two-dimensional dosimeter. Although several types of film are available for film dosimetry, the most common is radiographic film. Radiographic film consists of an emulsion of silver halide crystals in a gelatin matrix coated on both sides of a thin polyester or cellulose acetate base [49]. A cross section of this structure is displayed in the schematic diagram in Figure 1.18. When irradiated, ionization of the emulsion atoms results in the release of electrons which are eventually captured at trapping centers within the silver halide grains. The trapping process sensitizes the grains by causing lattice defects and a latent image is built up of such grains. Upon development of the film, silver ions are converted to atomic silver at the sensitized grains while un-sensitized grains are removed. Variations in the density of silver on the film produce variations in optical density which can be measured and correlated to absorbed dose through use of a calibration curve.

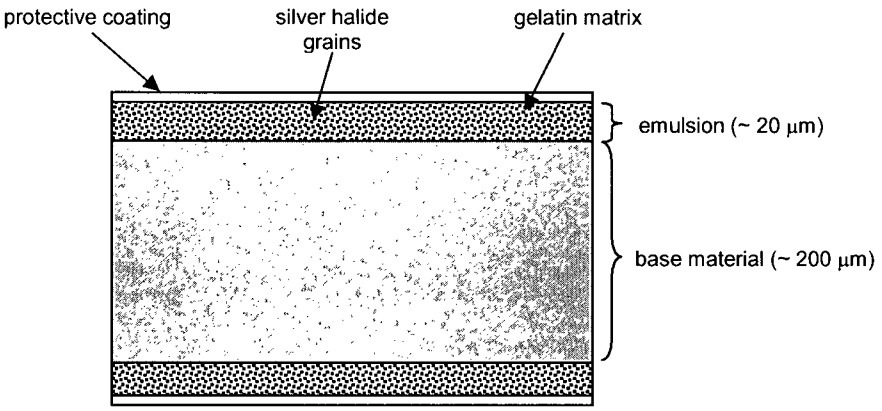

Figure 1.18: Cross section of a radiographic film. A thin acetate or polyester base is coated with an emulsion consisting of silver halide crystals embedded in a gelatin base.

The sub-millimeter spatial resolution of film systems are typically dependent on the modality used to *digitize* the film to a digital file format and as such fulfills the resolution requirements necessary for IMRT dosimetric verification. Early attempts at performing film dosimetry encountered issues with sensitivity of the film. Typical radiographic films used in radiology and radiation therapy departments of the time were optimized for delivery of low doses of ionizing radiation to maximize image contrast for diagnostic x-ray imaging or port verification imaging. Delivery of high doses inherent to radiation therapy treatments to these types of film resulted in poor dose contrast or signal saturation. The introduction of new film types with lower silver halide content resolved these problems [50]. Kodak's extended dose range 2 (EDR2) film (Eastman Kodak Inc., USA) is one such film which is widely used for radiation therapy dose verification [51-54].

The tissue equivalence of film is an interesting topic. While film's silver halide emulsion is high Z (atomic number of Ag = 47), the fact that this layer is so thin (as illustrated in Figure 1.18) causes the difference in dose deposition downstream from a piece of film to be negligible from the dose deposition with no film present [55]. Unfortunately this does not apply for the dose deposition in the film emulsion itself where the presence of high Z elements causes an over-response to low energy photons due to an increase in photoelectric interactions [56]. Recent studies have shown this problem to be minimal in extended dose range film types where the silver halide content is lower and virtually negligible in film dosimetry when calibration curves are acquired using small radiation fields

[57]. Consequently, several dosimetry systems based on radiographic film have emerged including three-dimensional measurement phantoms [55, 58].

The main disadvantages to film dosimetry are the time and labour required for the loading and unloading of films in a dark room (radiographic film is also very sensitive to optical wavelengths), film processing and subsequent digitization of the developed films before dose information can be obtained. Additionally, film is not a reusable measurement media therefore necessitating a constant supply of fresh films. Finally, the dependence of film dosimetry on film processors leaves this technique susceptible to artifacts caused by operational problems with film processor units [59]. Appearance of such artifacts in dosimetry films (particularly calibration films) can quickly render a full set of film dosimetry measurements completely useless.

1.6.3.4 Electronic Portal Imaging Devices

Electronic portal imaging devices (EPIDs) were originally developed to replace film-based megavoltage radiography treatment verification systems. The goal of megavoltage radiography treatment verification is to use the megavoltage treatment beam to perform radiographic imaging on the patient during treatment. Verification images are used to ensure correct positioning of the patient in the radiation field through the localization of bony landmarks in reference to field edges. The use of radiographic film for megavoltage imaging carries with it several of the disadvantages mentioned in the previous section. EPIDs use electronic detection arrays placed on the exit side of the patient to replace film-based port beam imaging. These devices are physically attached to the gantry of the linac at source-to-axis distances ranging from 105 cm to 180 cm and can usually be retracted or removed to facilitate treatment setup.

There are three main categories of electronic portal imaging devices in clinical use today: scanning liquid ionization chamber EPIDs, video-based EPIDs and flat panel EPIDs. Scanning liquid ionization chamber EPIDs typically consist of 256 strip formed electrodes oriented perpendicular to 256 high voltage electrodes to form a mesh like structure [60]. This structure is then submerged in a fluid that serves as the ionization medium during irradiation thus forming a 256 $\times$ 256 matrix of ionization chambers. While this device provides a compact detector array its major limitation is its poor conversion efficiency as a

result of its systematic, electrode-by-electrode, scanning readout. A schematic diagram of a typical video-based EPID is displayed in Figure 1.19. These devices use video cameras to capture the visible light emitted from scintillation-based x-ray detectors (scintillation detectors are described in detail in section 3.1). These detectors are viewed through a 45° mirror to avoid direct irradiation of the radio-sensitive video camera. Advantages of video-based EPIDs include the potential for real-time monitoring of patient setup as well relatively large detection areas and high resolution images. Unfortunately, these devices suffer from low light collection efficiency with typically only 0.1% to 0.01% of the light emitted reaching the video camera [61].

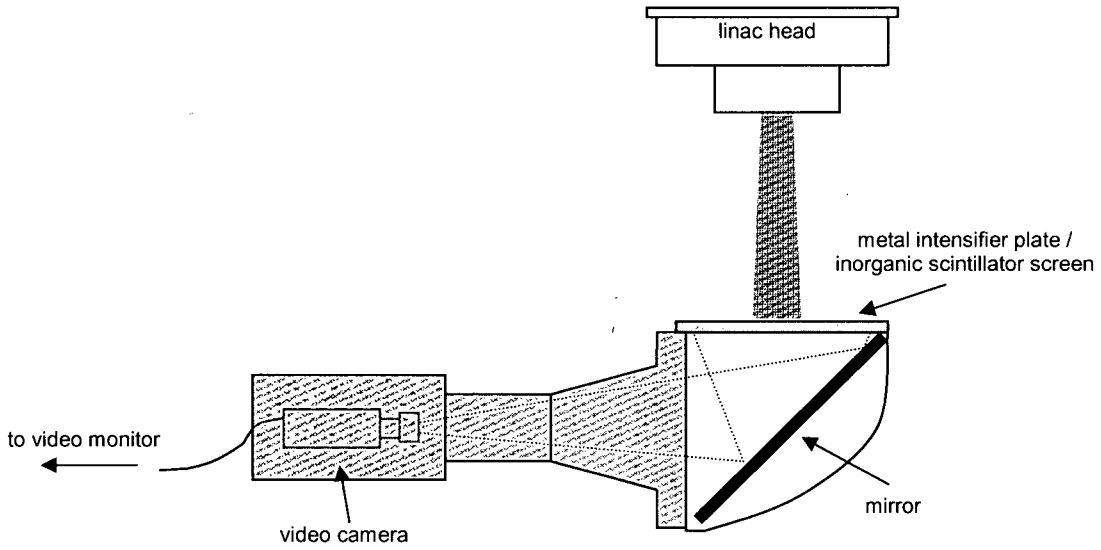

Figure 1.19: Schematic diagram of a typical video-based electronic portal imaging device.

Flat panel EPIDs are the most recent technological development in megavoltage radiography. Like video-based EPIDs, these devices consist of a scintillation-based x-ray detector which emits visible light upon irradiation. In flat panel EPIDs, however, the collection of this light is performed using solid state photodiodes placed directly below the x-ray detector. These photodiodes are most commonly made of amorphous silicon which has been formed into a two-dimensional matrix of thin film transistors. The compact size of flat panel EPIDs together with their high conversion efficiency and high spatial resolution have caused most linear accelerator vendors to move towards the use of these devices in place of both scanning liquid ionization chamber and video-based EPIDs.

While originally developed for megavoltage imaging during treatment of the patient, a great deal of research has been carried out towards using EPIDs to perform IMRT dosimetric verification measurements [62-65] before the start of treatment. In contrast to film and gel dosimetry, EPID systems provide fast, directly digital data on IMRT dose distributions using a reusable detector which is already mounted on the linac gantry thus greatly reducing setup time. In terms of spatial resolution, EPID acquired dose distributions fulfill the requirements of IMRT dosimetric verification with resolutions < 1 mm. The major disadvantage to performing IMRT dosimetric verification using EPIDs is their lack of a water equivalent measurement medium. Having been optimized for megavoltage image contrast, EPIDs typically contain several high Z components such as copper intensifier plates, inorganic scintillating layers, and readout electronics. The presence of these materials has been shown to cause increased sensitivity to scattered low energy photons and increased photoelectric interactions within the measurement region which can lead to significant deviations between the dose measured and the dose deposited in the patient [62, 66]. This, combined with the inability of many of these systems to be placed between adequate build-up and backscatter material, make in-phantom dosimetric results an impossibility for current EPID systems.

1.7 Thesis Objectives

The primary objective of this thesis is the development and implementation of a novel method for the dosimetric verification of IMRT fields that has several advantages over current techniques. This work was motivated by an initial study which compared two treatment planning systems for IMRT.

1.7.1 An Evaluation of Two Treatment Planning Systems for IMRT

This study, detailed in Chapter 2, compared the clinical functionality of two commercial treatment planning systems for intensity modulated radiation therapy with the aim of identifying practical and technical issues. The study considered implementation and commissioning, dose optimization, and plan assessment. Both systems were commissioned for the same 6 MV photon beam equipped with a high resolution multileaf collimator. The software was applied to three test plans having identical imaging and contour data. Analysis

considered three dimensional axial dose distributions, dose volume histograms and monitor unit calculations. In addition to yielding several important results, the extensive use of IMRT verification techniques throughout this study served as the motivation behind the main objective of this thesis, namely the design, development, and implementation of a novel IMRT dosimetric verification system.

1.7.2 A Tissue Equivalent Plastic Scintillator IMRT Verification System

Motivated by the dosimetric verification measurements acquired during the IMRT treatment planning system comparison described in Chapter 2, a new system for dosimetric IMRT treatment verification is proposed. This system is based on a tissue equivalent plastic scintillator material. A tissue equivalent phantom was designed and constructed around a sheet of this scintillator. Scintillation light emitted from the material is directed towards a high resolution charge-coupled device (CCD) video camera where images of the light distribution are captured and stored digitally on a personal computer. Following image processing and application of a light-intensity/dose calibration curve, a two-dimensional beam's-eye-view (BEV) dose distribution is obtained. Chapter 3 details the design and construction of the system as well as the steps involved in data acquisition and processing.

1.7.3 System Characterization and Testing

In Chapter 4, a series of experiments that serve to characterize and test the new dosimetric verification system is presented. These experiments include evaluation of the system's dose linearity, dose rate dependence and short-term stability, spatial linearity and effective pixel size, signal uniformity and long-term reproducibility. The dosimetric accuracy of the system was also tested using both static and dynamic fields whose dose distributions are accurately known.

1.7.4 System Evaluation

Final system evaluation is performed in Chapter 5 by using the new system to perform field-by-field verification of a 7-field IMRT plan. The verification process was directly compared to a standard, clinical film dosimetry verification process. Data analysis included dosimetric comparisons using one-dimensional dose profiles, two-dimensional percentage dose difference maps and gamma factor analysis.

Chapter 2

AN EVALUATION OF TWO TREATMENT PLANNING SYSTEMS FOR IMRT

The degree of success achieved by the treatment planning optimization process in IMRT is largely dependent on the cost function used by the optimization algorithm (which in turn depends on the structures and dose constraints defined by the user) and the algorithm used for minimization itself. While several studies have been carried out to evaluate the various optimization algorithms available [67-69], two recent studies have compared commercial IMRT planning systems. A study by Fogliata *et al.* [70] compared the inverse planning algorithms used by three commercial systems. While thorough in its analysis of dosimetric outcome, this study excluded all user considerations such as user interfaces, optimization efficiency, and plan design and evaluation tools. A study by Mayo and Urie [71] proposes the use of a systematic benchmark method for comparison and presents results from two commercial systems using two different multileaf collimator/beam combinations applied to a carefully designed phantom. The BC Cancer Agency, Vancouver Cancer Centre has two treatment planning systems capable of inverse planning and will shortly be implementing IMRT for treatments of the head and neck region. This study was undertaken to survey the differences between the two systems in terms of user interface and functionality. Both systems were commissioned for the same MLC/beam combination and were applied to three typical patient CT image data sets. Results from this study were published in the Journal of Applied Clinical Medical Physics [72] and presented at two scientific conferences [73, 74].

2.1 Method and Materials

This investigation assessed the BrainSCAN v.5.2 (BrainLAB AG, Germany) and Helios (Eclipse v.7.1.31, Varian Medical Systems Inc., USA) IMRT planning systems. The BrainSCAN treatment planning system includes both the inverse IMRT planning software

and the forward planning software (i.e. forward calculation of dose distributions) whereas Helios represents only the inverse IMRT planning software component of the Eclipse forward treatment planning system. The optimization algorithm employed by BrainSCAN is the dynamically penalized likelihood method [24] while Helios uses a gradient method [26]. Using a 6 MV photon beam (CL21EX, Varian Medical Systems Inc., USA) equipped with a 5 mm, high resolution multileaf collimator (Millennium 120 leaf, Varian Medical Systems Inc., USA) these systems were compared in terms of commissioning and implementation, system functionality, and quality of final plans.

2.1.1 Implementation and Commissioning

Both planning systems required specific beam commissioning data before use. Commissioning was performed for dynamic IMRT delivery for both systems. A summary of the data required is displayed in Table 2.1.

Table 2.1: Commissioning beam data requirements for the Varian Helios and BrainLAB BrainSCAN treatment planning systems

Parameter	BrainSCAN	Helios
Nominal Linac Output	Low resolution	
Percent Depth Dose	1 mm depth resolution	5 mm depth resolution
Transverse Profiles	0.5 mm resolution	2.5 mm resolution
Diagonal Profiles	0.5 mm resolution	2.5 mm resolution
Relative Dose Factors	10 mm × 10 mm minimum field size	20 mm × 20 mm minimum field size
MLC Transmission Factor	Low resolution	
MLC Leaf Gap	Low resolution	

Differences in the measurement resolutions required by each system necessitated the use of different detector types. Specifically, BrainSCAN's requirement for high resolution percentage depth dose, relative dose factor (RDF), and transverse and radial profile measurements were fulfilled by using detectors with small active volumes. These measurements were performed using an NAC009 miniature thimble ion chamber with an

ionization volume of 0.007 cm^3 (2 mm central electrode, 6.3 mm outside diameter, 3 mm length) as well as diode detectors. For Helios, these same measurements were performed using an IC10 ionization chamber (Scanditronix Wellhofer AG, Germany) with an volume of 0.13 cm^3. For both systems, the low resolution measurements shown in Table 2.1 were acquired using a Capintec PR-06C ionization chamber (Capintec Inc., USA) with an ionization volume of 0.65 cm^3.

All measurements in this study were performed using the linear accelerator in service mode. Nominal linac output measurements were performed using the TG-51 protocol for clinical reference dosimetry [75]. These measurements were performed at a source-to-surface distance of 100 cm and a depth of 5 cm in a small water tank (30 cm × 30 cm × 35 cm) using a calibrated standard ionization chamber. Collimator jaws and the MLC were matched to define a 10 cm × 10 cm square field. A similar setup was used to measure the MLC transmission factor. For this measurement, the MLC jaws were closed completely with a 5 cm offset. The MLC leaf gap was measured using the same apparatus but with a SSD of 98 cm and at a depth of 2 cm. With the collimator jaws set at 10 cm × 10 cm, a series of sliding, MLC defined gaps of varying size were delivered. By plotting the gap sizes versus the measured dose, the MLC leaf gap was obtained by extrapolating to zero dose [76]. The remaining commissioning parameter measurements, namely PDDs, RDFs, and transverse and diagonal profiles, were performed using a large water tank (48 cm × 48 cm × 41 cm).

Following beam commissioning, the output of each system was validated using both 2D film dosimetry and point checks using standard ionization chambers. These validation measurements were performed using IMRT treatment plans for a sample prostate case. Both systems were used independently to create 5-field IMRT plans for this sample case. Field-by-field distributions as well as composite distributions were verified using absolute film dosimetry and ionization chamber point checks in low dose gradient regions. Details of the film dosimetry measurements can be found in section 2.1.2.1.

Comparisons with respect to commissioning and implementation were based on complexity and time required for beam data acquisition, processing of this data and compilation of the data file necessary for input into the planning software.

2.1.2 Effects of Commissioning Data Resolution

The differences in the spatial resolution of the commissioning data requested by both systems prompted an investigation into the effect of these differences on system output. This investigation was carried out using a method similar to that used in a study by Arnfield *et al.* [77] which explored the use of high resolution film dosimetry to improve IMRT dose calculations. In this study, also using Varian's Eclipse treatment planning system, Arnfield *et al.* showed that commissioning data acquired using standard methods, in this case a standard ionization chamber with a volume of 0.13 cm^3, can lead to inaccuracies in dose of up to 20% for IMRT fields with high spatial frequency characteristics. In order to compare BrainSCAN and Helios in this respect the calculated dose distributions from both systems for an IMRT field with high spatial frequency characteristics were compared with the measured dose distribution for this field acquired using absolute film dosimetry.

The comparison was made possible by the ability of the Eclipse treatment planning system to import dynamic MLC files. As a result of this functionality, a high spatial frequency field was selected from a BrainSCAN IMRT plan to perform the comparison. The dynamic MLC file for this field was imported into Eclipse where a forward calculation yielded the predicted dose distribution on a Solid Water phantom CT set. The dose distribution in a plane perpendicular to the field at a depth of 5 cm was calculated with a resolution of 1.25 mm and exported using DICOM RT. The corresponding distribution (also perpendicular to the field and at a depth of 5 cm) was obtained from BrainSCAN using the *Export Dose Map for Individual Beams* function in BrainSCAN. The resolution of the BrainSCAN distribution was 1 mm. Absolute film dosimetry was employed to measure the dose distribution. This film-measured distribution was quantitatively compared to both the Eclipse and BrainSCAN calculated distributions using both one-dimensional dose profiles and two-dimensional gamma factor analysis. The pass/fail criteria for the gamma analysis was a dose difference of 3% of the prescription dose and a distance criterion of 3 mm.

2.1.2.1 Radiographic Film Dosimetry

Film dosimetry measurements were carried out using Kodak EDR2 film (Eastman Kodak Inc., USA) placed perpendicular to beam central axis at 5 cm depth in a light-tight Solid Water cassette (Gammex RMI Inc., USA). This cassette consists of two 2 cm-thick solid

water slabs sealed along three edges with nylon screws and a rubber O-ring. To minimize the occurrence of air gaps, the film was removed from its envelope and paper liner and inserted into the cassette under safelight. Film calibration was performed using percent depth dose measurements on the same phantom with the film parallel to the beam central axis. These PDD measurements were delivered at a source-to-surface distance of 98.5 cm with a 5 cm × 5 cm field size in order to minimize the effects of low energy scattered photons on the film response [57]. To minimize possible variations due to film processing conditions, all films were developed at the same time, approximately 12 hours after the irradiation of the last film [78], using a Kodak X-Omat RP processor (Eastman Kodak Inc., USA) for which the throughput is very high and quality assurance is performed daily. All films were digitized using a VIDAR VXR-16 Dosimetry Pro film scanner (Vidar Systems Corp., USA) and conversion to absolute dose was performed using previously verified in-house film dosimetry software [55].

2.1.3 Optimization Parameters and System Functionality

Although both Helios and BrainSCAN make use of dose volume histograms in the objective functions to be achieved in plan optimization, the different optimization routines employed by the systems require somewhat different formats for the input parameters to guide the formation of each plan. Both systems required user defined calculation grid sizes, fluence map smoothing, and hot beamlet restrictions. These common parameters were found to have minimal impact on the optimization results in both systems. The only input parameter found to have a significant impact on the results was BrainSCAN's *Normal Tissue Expansion* option (NTE). *Normal Tissue Expansion* allows BrainSCAN users to specify constraints on the tissue surrounding the planning target volume by defining a structure enclosing the volume given by two margins around the PTV. The first margin specified around the PTV, which has a minimum value of twice the selected PTV grid size, allows for a volume of tissue immediately surrounding the PTV where no restrictions are placed to allow a dose fall-off from the PTV. The second margin gives the distance from the PTV for the extent of the calculation and there is an option to make this the outer patient contour. The volume defined between these two margins becomes a structure on which a restriction may be placed to force the algorithm to reduce the dose surrounding the PTV within a defined distance. The effect

of using NTE on optimization results was systematically investigated following the plan assessment portion of this study.

Following the setting of input parameters, Helios and BrainSCAN differ significantly in terms of system functionality. Both systems have inherent tools and options that are advantageous to the user once the optimization process has begun. Throughout the course of the study functionality of each system was systematically explored and a qualitative comparison performed.

2.1.4 Plan Assessment

To assess the output plans from both systems, three patients treated previously with three-dimensional conformal radiation therapy were selected, two with head and neck cancer and one with prostate cancer since these are the two most frequently treated sites with IMRT. The choice of sample patients was made to assess and illustrate the ability of the planning systems to accommodate different target/normal tissue combinations. Case #1 was selected to assess the ability to provide parotid sparing for a nasopharynx treatment. CT images from this case together with contours indicating the target and organs-at-risk are displayed in Figure 2.1. The figure shows the relatively complex shape of the PTV and the position of the parotid glands.

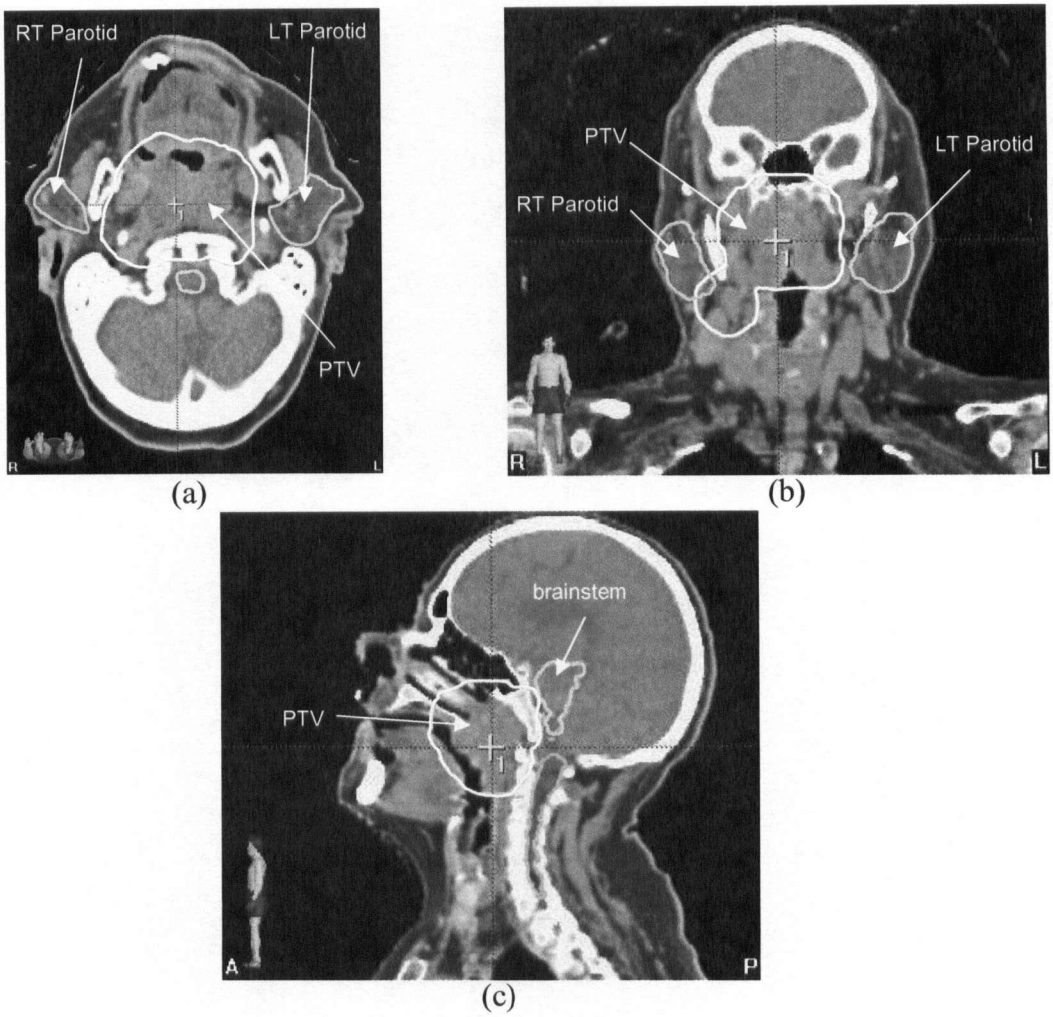

Figure 2.1: CT image set for Case #1 showing (a) axial, (b) coronal, and (c) sagittal views of planning target volume and its anatomical relationship with organs-at-risk.

Case #2 was selected, having a relatively large, complex planning target volume which could not be covered using conventional conformal planning, to assess the ability of IMRT to obtain target coverage. The CT image set for Case #2 is displayed in Figure 2.2. The PTV in this case is a complex horseshoe shape wrapping around both the brainstem and the spinal cord.

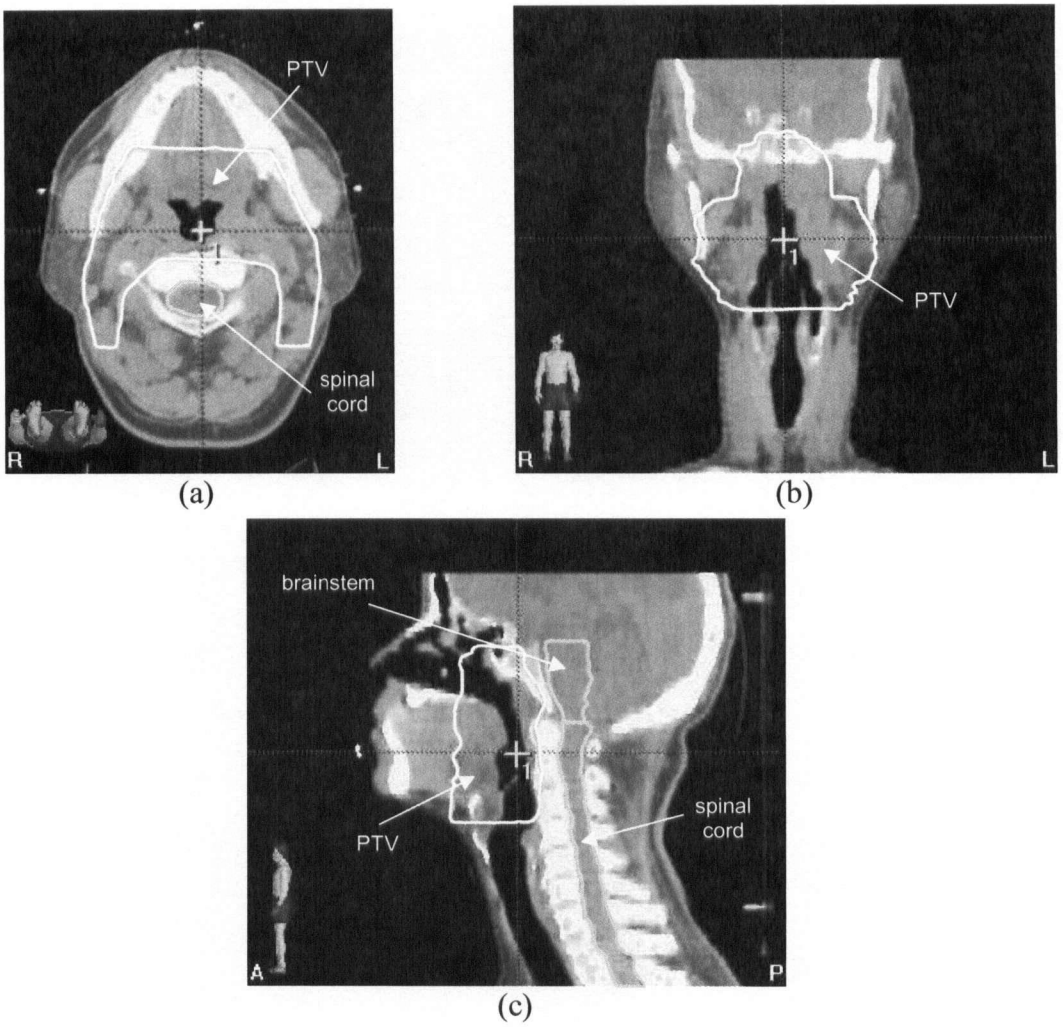

Figure 2.2: CT image set for Case #2 showing (a) axial, (b) coronal, and (c) sagittal views of planning target volume and anatomical relationship with brainstem and spinal cord.

Case #3 required the sparing of an organ-at-risk directly in contact with the PTV. This case, a prostate plan with both bladder and rectum considered as OARs, is displayed in Figure 2.3.

Image sets together with target and OAR contours for the patients were entered into both planning systems using DICOM transfer protocols. To establish benchmark parameters, a conformal plan giving the best possible dose distribution using conventional techniques was done by an experienced planner for each patient. DVH data from these plans were used to establish initial dose constraints for optimization.

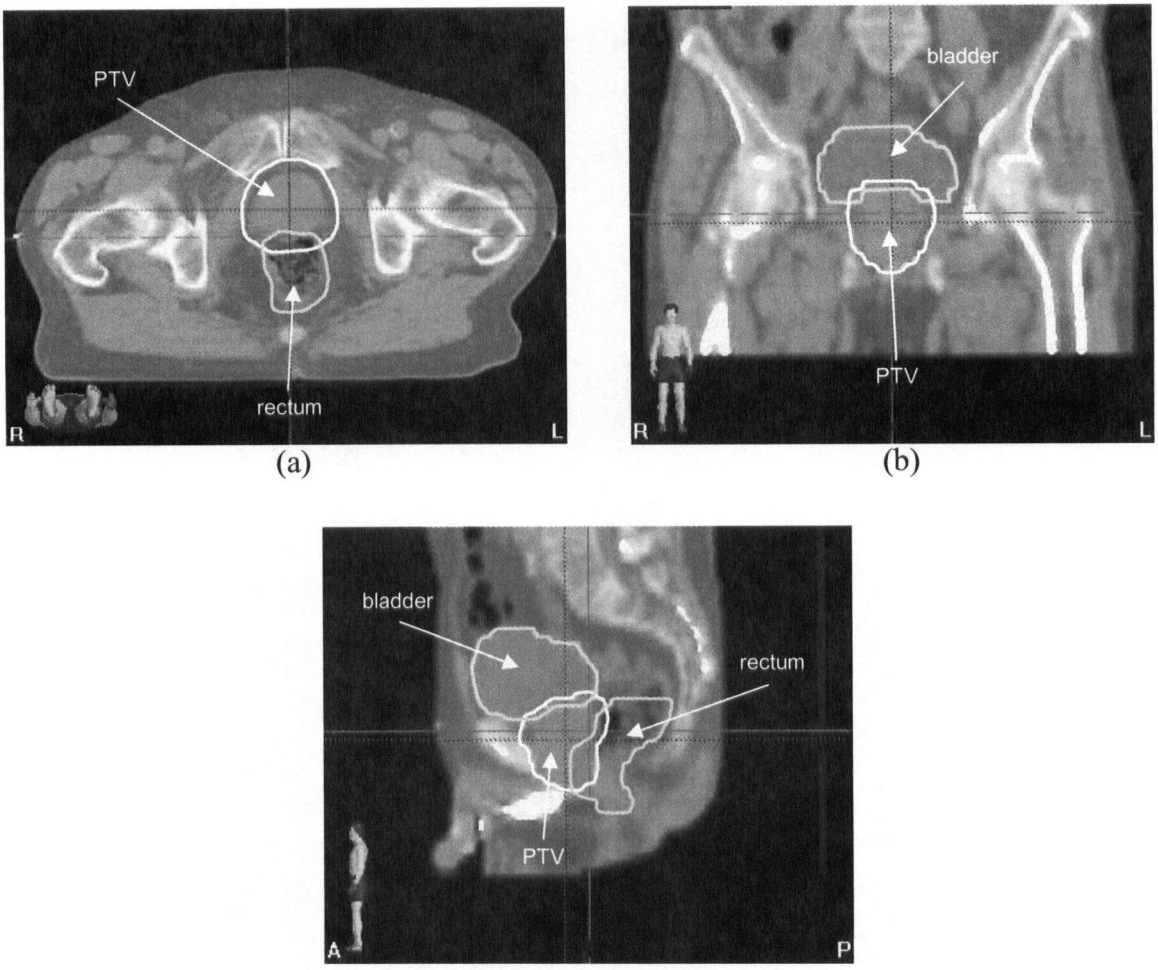

Figure 2.3: CT image set for Case #3 showing (a) axial, (b) coronal, and (c) sagittal views of planning target volume and anatomical relationship with bladder and rectum.

The quality of an IMRT plan is determined by the parameters chosen for the optimization, specifically the target dose coverage, target dose homogeneity, and OAR sparing. For all cases, the PTV constraints were set to require that 100% of the PTV received a dose of 95%. In BrainSCAN, the second PTV constraint was in the form of a "Desired Dose" which was set to 100%. The BrainSCAN algorithm inherently tries to provide a homogenous dose distribution over the PTV at this dose. For Helios, the second PTV constraint was a maximum dose which was set to 105%, giving a dose variation across the PTV of 10%.

While the target dose homogeneity can generally be clearly specified, OAR constraints are not as easily defined, the general principle being that the lower the dose the

better the plan. Most planning systems used for IMRT require the user to gain familiarity with the response of the system to the input parameter variation to obtain optimal results. To ensure that this study was as objective as possible, the planning systems were assessed with identical OAR constraints.

The OAR constraint values for this study were developed in a two stage process as follows. Each system was run with an initial set of constraints and these values were adjusted independently as required to obtain an optimized dose distribution based on both target and organ-at-risk DVHs. The resulting set of constraints for the two systems were then compared, a final set derived using the best of both systems, and these constraints were used, without further modification, to calculate the dose distribution for assessment (Table 2.2). The plans output from both systems were then assessed in terms of axial doses, DVHs and number of monitor units.

Table 2.2: Normal tissue constraints as a percentage of prescribed dose for comparison of treatment planning systems

Case #	Organ-at-Risk	Volume (%)	Dose (%)
1	Brainstem	0, 30, 50	83, 42, 20
	Spinal Cord	0, 40	83, 15
	Left Parotid	10, 50, 67	30, 20, 15
	Right Parotid	10, 50, 67	80, 35, 28
2	Brainstem	0, 5, 25, 50	50, 35, 20, 10
	Spinal Cord	0, 5, 25, 50	70, 60, 20, 5
3	Rectum	0, 15, 25, 50	100, 95, 80, 40
	Bladder	0, 10, 25, 50	100, 75, 35, 5

2.1.5 Efficiency

Analysis of the required monitor units was performed by determining the ratio of the MUs for each IMRT plan to the MUs required by the corresponding three-dimensional conformal benchmark plan. All dynamic MLC fields from both planning systems consisted of 28 segments.

2.2 Results

2.2.1 Implementation and Commissioning

The beam data required by both BrainSCAN and Helios were similar. Both systems required measurements of the nominal linac output, PDDs at various field sizes, transverse and diagonal beam profiles at various depths, RDFs, MLC transmission and effective leaf gap measurements. As mentioned previously, a key difference between the systems with respect to commissioning is the required measurement resolution. As displayed in Table 2.1, BrainSCAN requires PDD measurements with a depth resolution of 1 mm (this requirement is relaxed to 5 mm resolution for depths over 50 mm), transverse and radial profile measurements with 0.5 mm resolution and RDF data for field sizes as small as 10 mm × 10 mm. In contrast, the resolution required by Helios is 5 mm for PDD measurements and 2.5 mm for transverse and radial profiles while Helios RDF measurements require data for a minimum field size of 20 mm × 20 mm. The similarity of the data required by both systems caused the time requirements for commissioning to be virtually identical. Although BrainSCAN's smaller minimum field size requirement for RDFs necessitates more measurements, this increase was found to be negligible in terms of commissioning time. In terms of commissioning complexity, the only difference between the systems is BrainSCAN's requirement for a high resolution mini-ionization chamber. In order to increase confidence in the small field measurements acquired with this chamber a series of "spot check" measurements were performed using a photon diode detector. Diode measurements agreed with mini-ionization chamber measurements within 0.5%.

Analysis of beam data and compilation of the data file varied between the systems. The BrainSCAN system required that all data be sent to BrainLAB for verification, conversion of radial profiles to radial factors, and compilation of the data into a collimator file that can be directly read by the treatment planning system. This process took approximately 2 days from the time the data was sent to BrainLAB to the receipt of the collimator file. For Helios, beam data was compiled, in house, into a file readable by the planning system. This compilation took approximately 1 day.

Output measurements using film dosimetry and ionization chamber point checks indicated acceptable agreement for the sample prostate IMRT plans from both systems.

Maximum dose discrepancies were well below 5% for both field-by-field measurements and composite distributions.

2.2.2 Effects of Commissioning Data Resolution

The calculated and film-measured dose distributions for the selected high spatial frequency IMRT field are displayed in Figure 2.4.

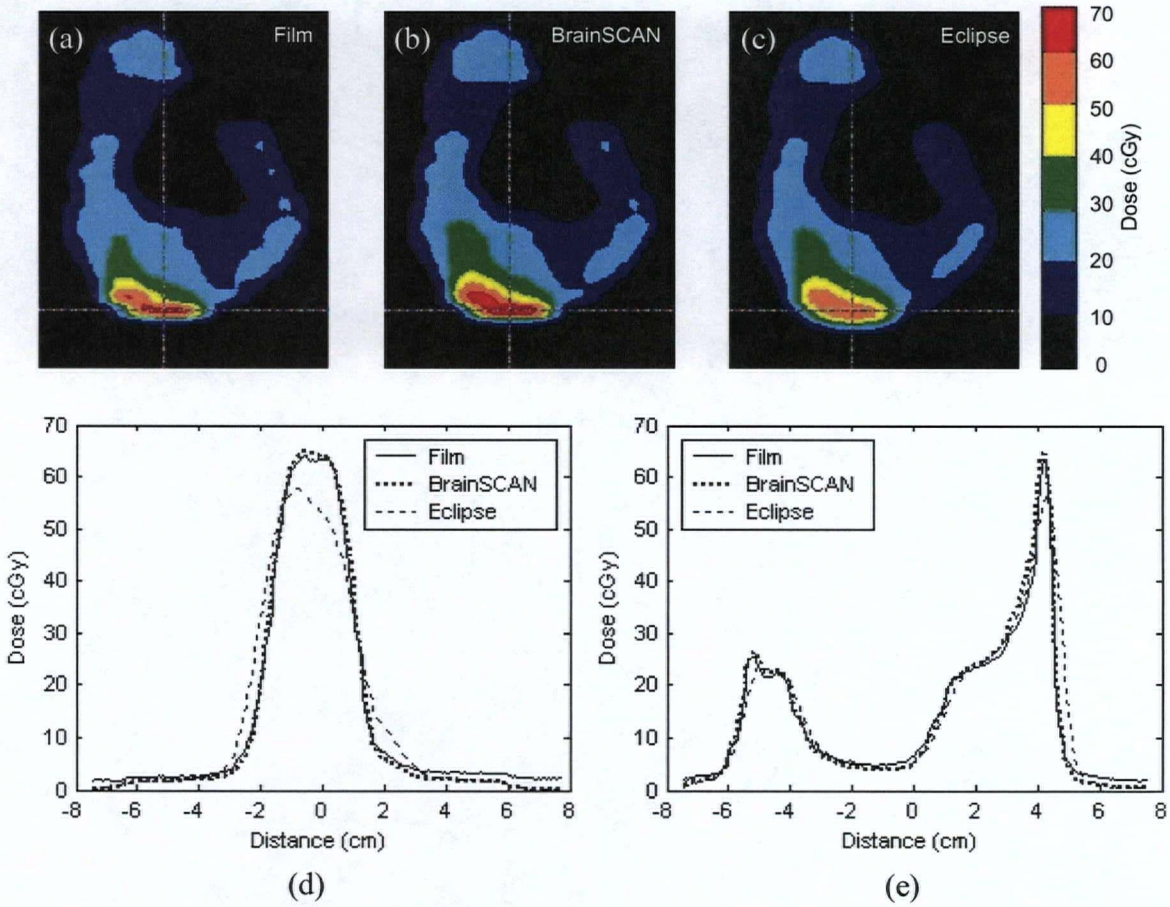

Figure 2.4: Comparison of measured and calculated fluence distributions from a selected intensity modulated field. The top panel shows (a) the film measurement, (b) the BrainSCAN calculated distribution, and (c) the Eclipse calculated distribution. The two lower panels show profiles through the three distributions horizontally (d) and vertically (e). The location of these profiles is indicated by the white cross-hair on the film measurement distribution.

Also displayed in this figure are 1D dose profiles through the high spatial frequency region of the field. From these profiles it is apparent that there is a difference between the distributions produced by BrainSCAN and Eclipse. The x and y profiles for the BrainSCAN system show acceptable agreement with the measured data in both low and high spatial frequency regions. In contrast, the profiles from the Eclipse distribution show acceptable agreement with measurement in low spatial frequency regions while discrepancies are apparent for high spatial frequency areas. At the intersection point of these 2 profiles, marked by the cross hair in Figure 2.4(a) (x = -0.32 cm, y = 4.19 cm), the percent dose difference from the measured distribution for BrainSCAN was 1.86% while Eclipse showed a 13.32% dose difference. Results of the 2D gamma factor analysis are displayed in Figure 2.5. The low gamma values in these maps indicate that both BrainSCAN and Eclipse show acceptable agreement with the measured data over most of the dose distribution. As expected, the highest gamma values are found in the vicinity of the high spatial frequency region of the field. This high-gamma value region is noticeably larger for the Eclipse calculated distribution.

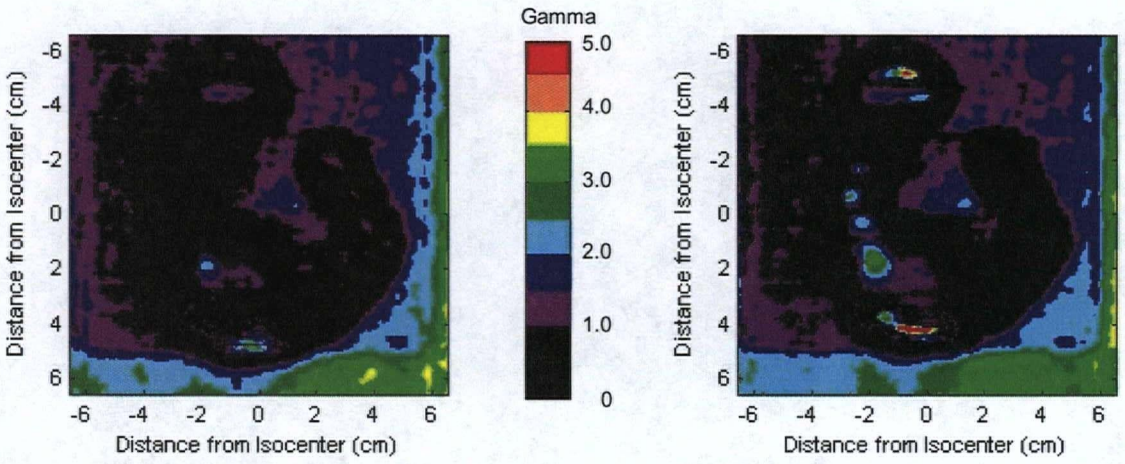

Figure 2.5: Two dimensional gamma maps comparing film measured distributions to BrainSCAN (a) and Eclipse (b) calculated distributions.

The sum of all gamma values, $\sum \gamma(i,j)$, as well as the mean and max gamma values for both gamma factor maps are displayed in Table 2.3 further highlighting the dosimetric

discrepancies of the Eclipse calculated distribution. Statistical analysis of the gamma maps was performed on a region defined by the open field plus a 1 cm margin in all directions.

Table 2.3: Properties of the masked γ map distributions comparing calculated distributions to film measured distribution.

	BrainSCAN	**Eclipse**
$\Sigma \gamma$ (i,j)	25354	29739
Mean γ (i,j)	0.71	0.83
Max γ (i,j)	3.46	9.04
Percent γ (i,j) $\geq$ 1.0	46.0	49.4

2.2.3 Optimization Parameters and System Functionality

Input parameters used to guide the optimization were found to have minimal impact on the optimization results with the exception of BrainSCAN's *Normal Tissue Expansion* option. Results indicating the effect of the NTE are shown in the following section.

Once the input parameters are set and the optimization process has begun, BrainSCAN and Eclipse differ significantly in their functionality. The BrainSCAN system calculates four separate plans with different priority on the dose to the organs-at-risk. Once all calculation parameters have been chosen by the user, the BrainSCAN system automatically calculates four IMRT plans labeled: *PTV Only*, *OAR Low*, *OAR Normal* and *OAR High*. The *PTV Only* plan is optimized to produce a uniform dose distribution over the volume of the PTV with no consideration for the dose to the organs-at-risk. *OAR Low, OAR Normal* and *OAR High* plans are optimized with varying priorities placed on the dose to the organs-at-risk. Once the fluence patterns have been optimized, the dose distributions are calculated and the user is presented with an interface which allows comparison of any two of the plans. The optimal plan is selected based on dose distributions and the DVHs.

In contrast, once optimization has begun in the Helios system the user has the ability to interactively adjust the constraint parameters, and thus the objective functions, while the optimization process is being performed. This allows points on the DVHs to be modified in real-time during optimization. For example, if the system was observed during optimization to be struggling to achieve a particular important constraint for one of the OARs, the

constraints of the other OARs may be adjusted or relaxed until an optimal compromise is achieved. This functionality combined with the ability to re-enter and continue optimization at a later time gives the user direct control over the progression of the optimization.

The two systems also differ in the flexibility offered to define arbitrarily shaped DVHs. Both systems are convenient in that they allow for general DVHs to be saved to a library for repeated use. In BrainSCAN each DVH is defined using a fixed number of points on a dose-volume plot. The target DVH is defined by a desired dose, set to 100%, and a single point to define coverage of the PTV at a particular dose level. Helios offers the additional option of defining both upper and lower dose limits for the target DVH. The DVHs for the organs-at-risk in BrainSCAN are defined by 4 points on the curves. These points define the upper limits for the resultant DVHs for these organs. In Helios, DVHs can be defined by an arbitrary number of points or by a continuous line drawn by the user. As in BrainSCAN, OAR points define the upper limits for the resultant DVHs for these organs. A unique feature to Helios is the definition of a priority for each point making up the DVH curves for OARs and the PTV. These priorities indicate the relative importance placed on each constraint point and thus provide additional control over the direction of the optimization. In BrainSCAN, the user has the option of adjusting the priority of each organ-at-risk relative to the others by specifying *OAR Guardian* values. These values are used to specify the priority of all the DVH points for a given organ but do not distinguish between individual constraint points on the same DVH.

Neither system optimizes gantry or couch angles. BrainSCAN, however, does offer automatic optimization of the collimator angles prior to entering the inverse planning process.

2.2.4 Plan Assessment

The optimized dose distributions obtained independently from each system prior to derivation of the final set of optimization constraints were observed to be very similar with no large differences in DVH points between the systems. In all three clinical cases, the final constraints were composed of an equal number of DVH points from the distributions produced by both systems.

Results for Case #1 are shown in Figure 2.6. The benchmark conformal plan for this case was composed of one anterior and two lateral wedged fields while both IMRT plans consisted of 7 uniformly spaced coplanar beams. The DVH plots illustrate that while neither system produced a plan with PTV coverage as uniform as the conformal plan, both systems were able to achieve substantial sparing of both parotid glands. In addition to displaying the un-normalized DVH plots for the PTV, this figure also shows the dose volume histograms for the PTV normalized at 99% coverage. Dose volume statistics for the PTV in all three cases are displayed in Table 2.4.

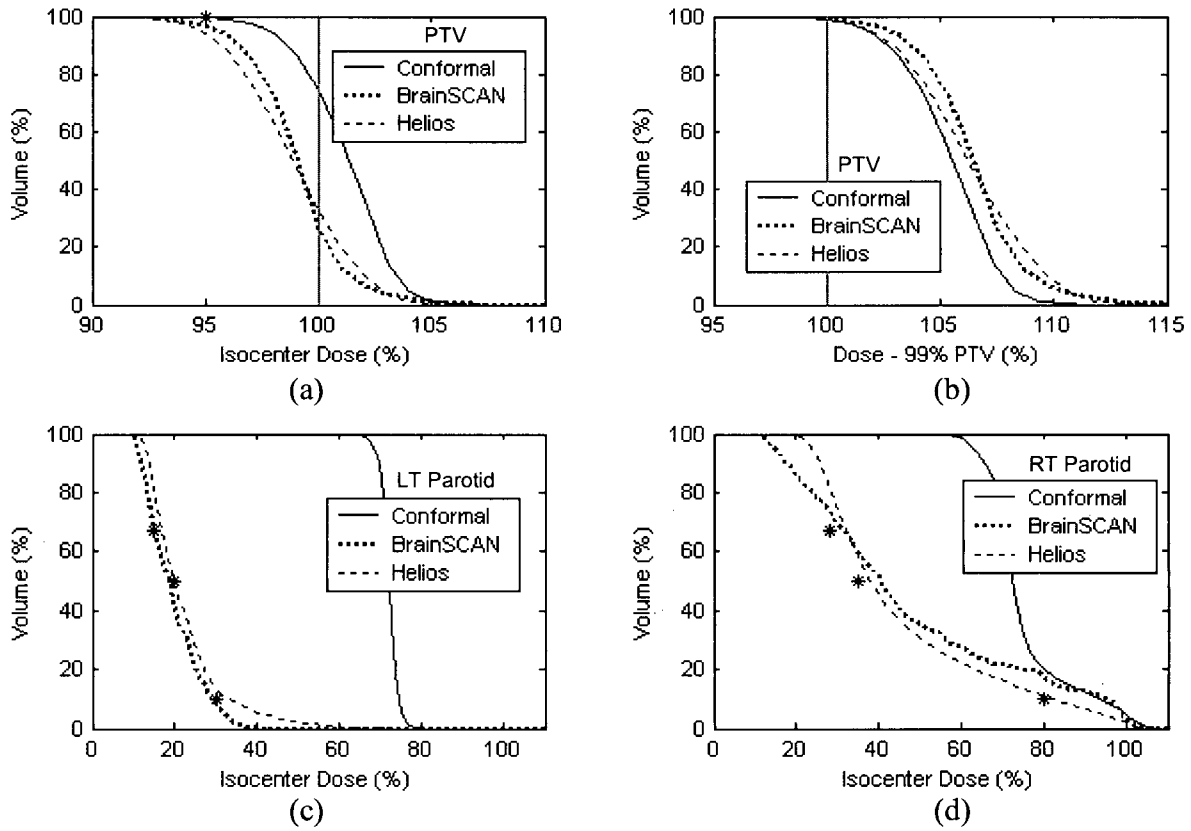

Figure 2.6: Planning comparison for Case #1 using a benchmark conformal plan and 7-field IMRT plans for BrainSCAN and Helios. Calculated dose volume histograms for the PTV un-normalized (a) and normalized at 99% coverage of the PTV (b). Calculated dose volume histograms for the left (c) and right (d) parotid glands with all three plans. The asterisks on the dose volume histograms indicate the restraint values used for optimization.

Table 2.4: PTV dose volume statistics for three cases as a function of prescription dose (Rx)

	CASE 1		CASE 2		CASE 3	
	BrainSCAN	**Helios**	**BrainSCAN**	**Helios**	**BrainSCAN**	**Helios**
%Vol Covered by Rx Dose	96.9	94.5	94.6	90.8	96.4	97.0
PTV Min (% of Rx Dose)	85	87	85	86	76	86
PTV Max (% of Rx Dose)	107	107	111	106	107	105

Planning comparison results for Case #2 are displayed in Figure 2.7. The benchmark conformal plan for Case #2 was composed of two lateral fixed fields plus two anterio-lateral 105° conformal arcs while the IMRT plans again consisted of 7 uniformly spaced coplanar beams. The DVH plots show that the conformal plan does not provide coverage of the PTV until a dose of approximately 80% of the isocenter dose. Both BrainSCAN and Helios were able to achieve coverage of the PTV by approximately 90% of the isocenter dose with no increase in maximum dose, with BrainSCAN giving a slightly more homogeneous dose (95% to 5% volume change over a 7% variation in dose for BrainSCAN compared to an 11% dose change for Helios). Both IMRT plans also show improvement in dose to the brainstem and spinal cord over the conformal plan with Helios giving a slightly lower dose to the spinal cord in the lower dose range.

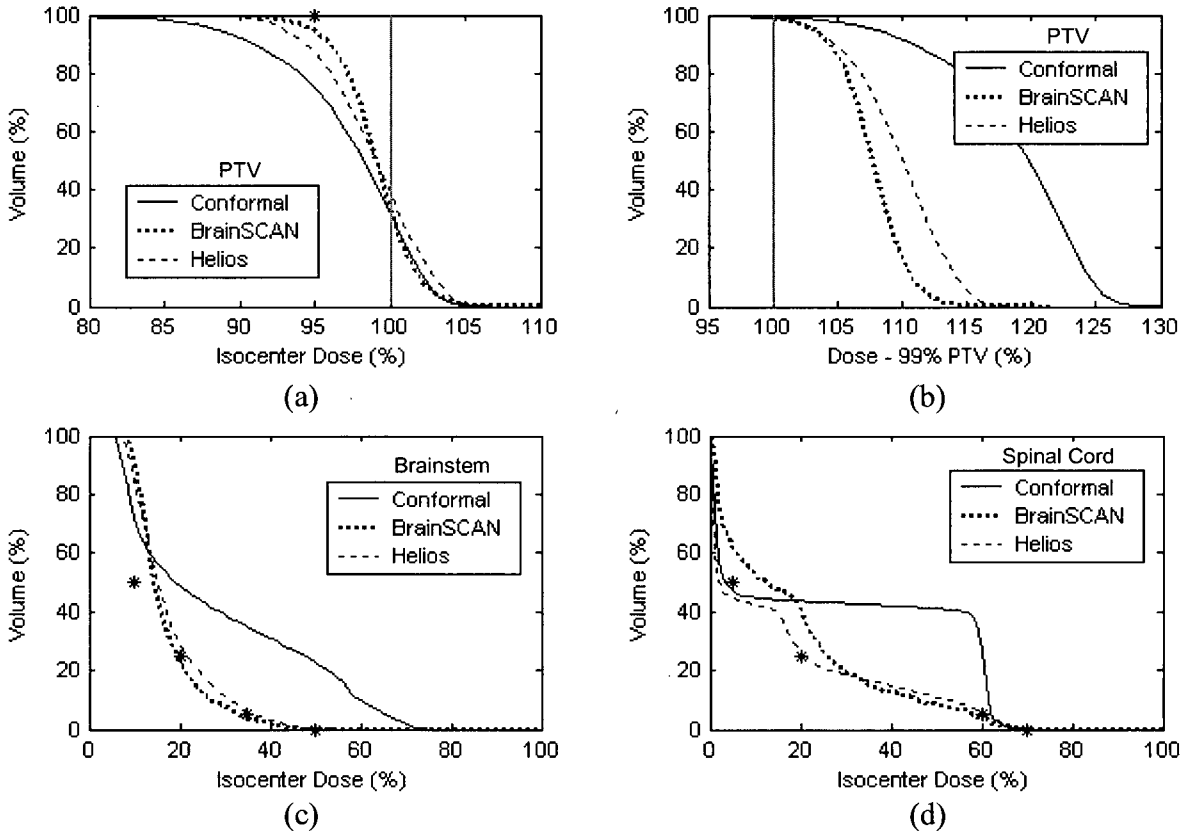

Figure 2.7: Planning comparison for Case #2 using a benchmark conformal plan and 7-field IMRT plans for BrainSCAN and Helios. Calculated un-normalized (a) and normalized (b) dose volume histograms for the PTV. Calculated dose volume histograms for the brainstem (c) and spinal cord (d) with all three plans. The asterisks on the dose volume histograms indicate the restraint values used for optimization.

Figure 2.8 shows the results for Case #3. The benchmark conformal plan for this case was a four field box while the IMRT plans were composed of 5 uniformly spaced coplanar beams. The PTV DVHs shown in this figure illustrate small differences in the three plans. When normalized to the isodose value enclosing 99% of the PTV, it can be seen that the BrainSCAN plan gives increased dose inhomogeneity throughout the PTV with a corresponding small advantage to the rectal dose, mostly at the lower dose values. The bladder dose remains virtually the same in all cases.

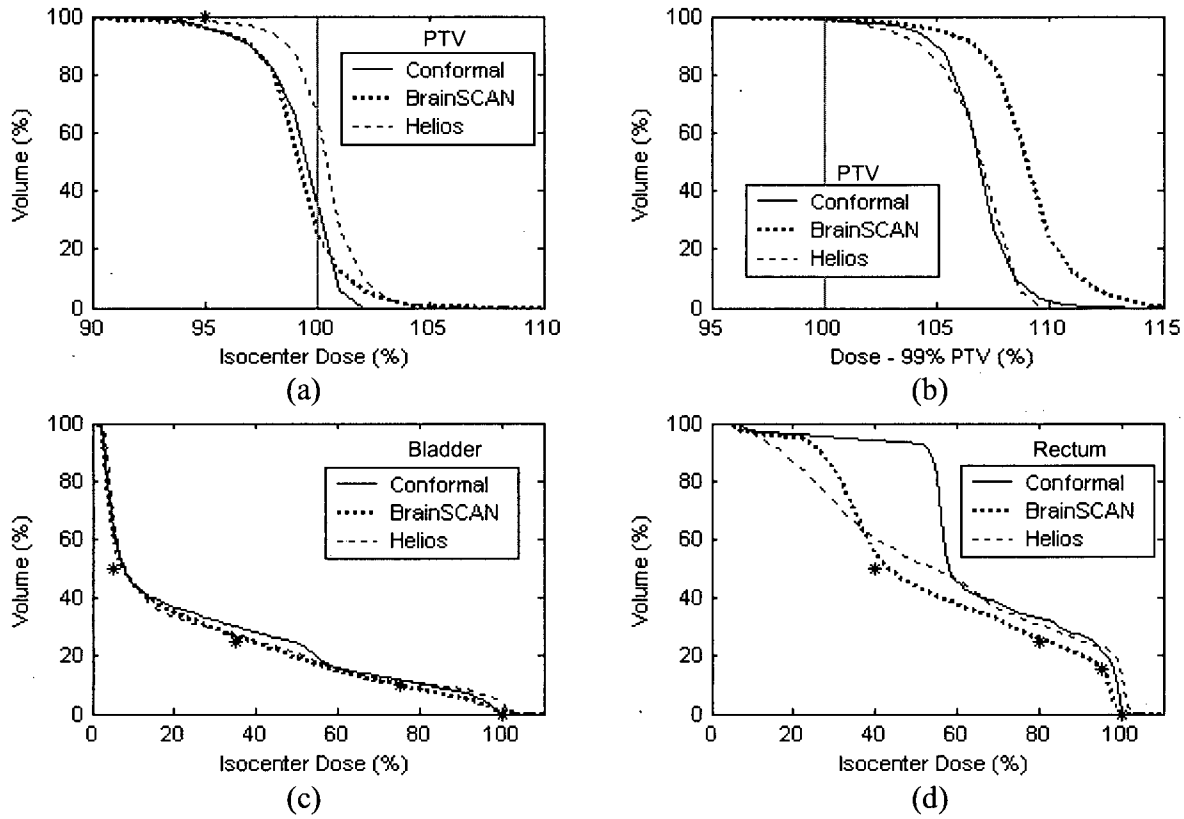

Figure 2.8: Planning comparison for Case #3 using a benchmark conformal plan and 5-field IMRT plans for BrainSCAN and Helios. Calculated un-normalized (a) and normalized (b) dose volume histograms for the PTV. Calculated dose volume histograms for the bladder (c) and rectum (d) with all three plans. The asterisks on the dose volume histograms indicate the constraint values used for optimization.

A comparison of the results of the four plans displayed by BrainSCAN after each optimization for Case #2 is shown in Figure 2.9. Figure 2.9(a), showing the results for the PTV, illustrates that while the *PTV Only* option provides the best dose homogeneity, not surprisingly the addition of the normal tissue and sensitive structure information will degrade this coverage. Clearly the addition of a constraint considering all tissue outside the PTV, designated "Normal Tissue" and shown in the Figure 2.9(b), provides for successive tissue sparing outside the PTV. From Figure 2.9(c) showing the brainstem results, it can be seen that three of the four dose constraints are met with the OAR Normal result.

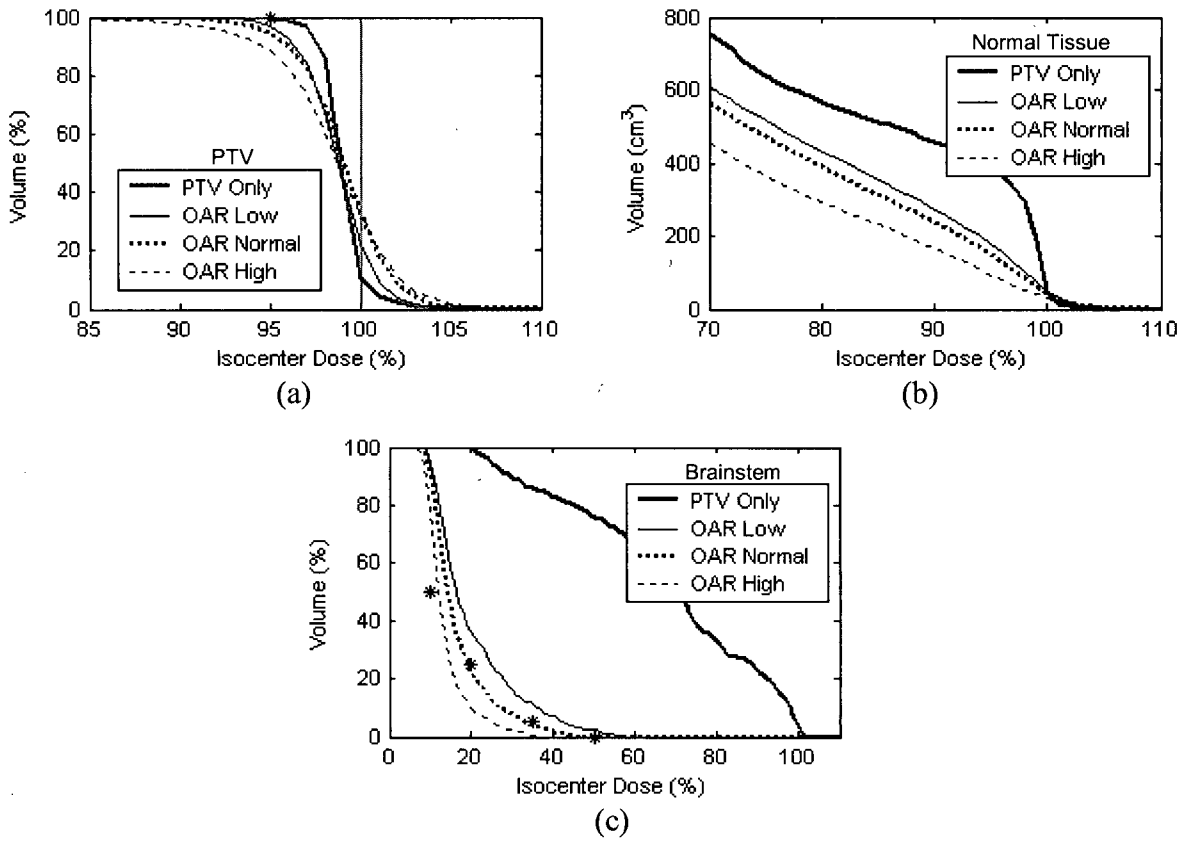

Figure 2.9: Case #2 BrainSCAN calculated dose volume histograms for (a) the PTV, (b) all tissue outside the PTV (Normal Tissue), and (c) the brainstem for the four calculations considering the PTV Only and the organs-at-risk as a High, Normal and Low priority.

The use of the *Normal Tissue Expansion* (NTE) option adds further flexibility, as illustrated in Figure 2.10. For this analysis, an NTE was defined around the PTV extending from 8 mm to 48 mm from the PTV forming an annular volume-at-risk with a width of 4 cm. The PTV DVHs shown in the top panel indicate that restricting the maximum dose to this NTE to 20% of the isocenter dose degraded the dose homogeneity and coverage of the PTV. Adding an NTE restriction with a dose maximum of 50% to the calculation including the OARs was almost equivalent to the calculation without the NTE. Considering the normal tissue shown in Figure 2.10(b), the addition of the NTE provides tissue sparing. Figure 2.10(c) showing the brainstem DVHs shows clearly that the definition of an NTE alone will not provide appropriate structure specific dose sparing.

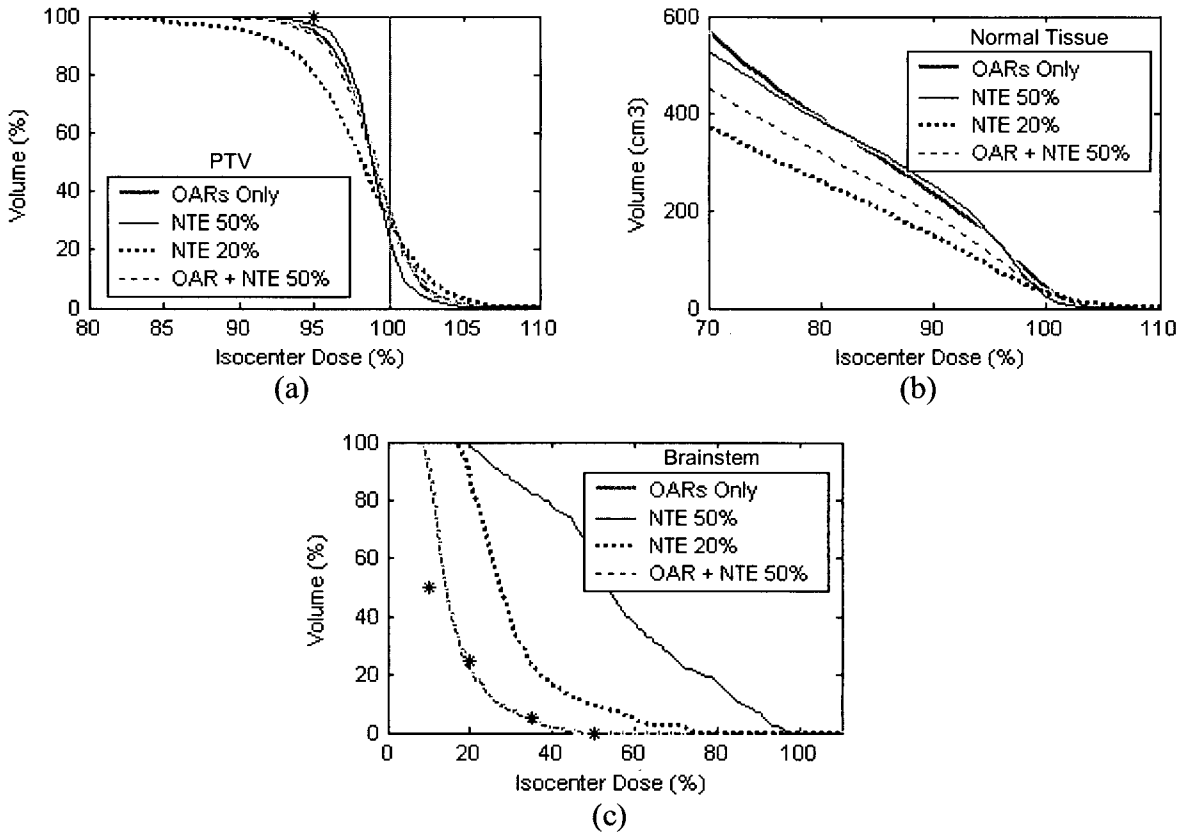

Figure 2.10: Case #2 BrainSCAN calculated dose volume histograms for (a) the PTV, (b) all tissue outside the PTV (Normal Tissue) and (c) the brainstem taking into consideration a volume of risk defined immediately outside the PTV and designated Normal Tissue Expansion (NTE). The four curves in each plot are for the calculations considering the OARs only, the NTE with a maximum dose constraint of 20% and 50% of the isocenter dose and the combination of the organs-at-risk and the NTE at the 50% level.

2.2.5 Efficiency

Results from the efficiency analysis are displayed in Table 2.5. Using BrainSCAN, the increase in required MUs was higher than that for Helios for Case #1 with the two systems showing comparable results for the other cases.

Table 2.5: Ratio of monitor units required to deliver IMRT plans compared to conventional conformal plan

Case	BrainSCAN	Helios
1	2.4	1.7
2	1.7	1.6
3	2.4	2.4
Average	**2.2**	**1.8**

2.3 Discussion

In terms of implementation and commissioning, dose optimization, and plan assessment, no substantial differences in performance were demonstrated between the BrainSCAN and Helios planning systems. Results indicated that both systems can produce substantially equivalent dose plans in terms of target coverage and normal tissue sparing.

Implementation and commissioning of the systems were found to be comparable in terms of complexity and time involved. Acquisition of high resolution data for BrainSCAN added only marginally to the overall time required for beam data acquisition. While the requirement to send the commissioning data to BrainLAB added an extra day to the overall commissioning of the BrainSCAN system, it also eliminated the workload of having to compile the beam data file.

While comparable in terms of output plans, BrainSCAN and Helios both have advantages and disadvantages over each other in terms of functionality. While both systems have adequate input mechanisms for dose constraints, the BrainSCAN system presents the user with four plans for each optimization from which to choose the optimal. The *PTV Only* option is rarely clinically viable (except for performing 3D electronic compensation) and is done to provide the basis of the subsequent optimization which includes the OAR constraints. However, the presentation of three calculated plans with slightly different relative constraint weighting provides a quick assessment of the value of making changes in the optimization parameters. This was found to be useful in speeding up the software learning process.

Alternatively, Helios offers the option of editing DVH parameters during calculation thus providing immediate interactive input during the optimization. This feature adds

substantial flexibility, provides a good learning tool and may reduce the overall time for optimization where adequate information for the definition of the constraints is not available *a priori*.

Analysis of the PTV curves shown in Figure 2.6 through Figure 2.8 illustrate one of the difficulties of IMRT planning. With identical constraints set in each case, clearly, there is a frequent requirement for a (small) renormalization of the dose distribution after optimization as the "optimized" plans do not consistently reach the goals set for the PTV. For example, of the three IMRT plans, only the Helios plan in Figure 2.8 provides coverage of the PTV at the 95% dose level. There is also a corresponding differing ability of the systems to reach the dose constraints set for the organs-at-risk with each system failing to reach a particular constraint in one case or another.

While the analysis of the commissioning requirements of both systems revealed no significant differences in terms of complexity and time requirements, the portion of this study investigating the effects of the differences in commissioning data resolution revealed an inadequacy in the Eclipse treatment planning system. Verification measurements on the sample prostate case used during early commissioning revealed no discrepancies larger than 5%. This validation was performed on a typical prostate case with significantly less complex fields compared to the head and neck cases used in the later comparisons. Serious discrepancies as large as 13% were observed when a field with high spatial frequency was analyzed. The large discrepancies observed for this field indicates that the resolution of the commissioning data required by Eclipse is inadequate for dose calculations of high resolution IMRT fields. This problem is directly related to the pencil beam kernels used to calculate the dose distributions. These kernels are derived from commissioning data and can be affected by the spatial resolution capabilities of the measuring device used [79]. While studies have shown that dose calculations using kernels derived from standard (low resolution) ionization chamber data are accurate for conventional planning scenarios [80], this is not the case for all IMRT fields. IMRT fields can contain highly modulated intensity regions that will be affected by low resolution pencil beam kernels [77]. The profiles for the Eclipse distribution in Figure 2.4 clearly illustrate these effects. These profiles are in good agreement with the film measured profiles except in highly modulated regions. In the horizontal profile, Eclipse not only underestimates the dose of the high intensity peak by over 13% but also

overestimates the horizontal spread of dose at the sides of the peak. The BrainSCAN distribution is in good agreement throughout this profile. In the vertical profile the narrow peak on the right is again underestimated by the Eclipse system whereas BrainSCAN is successful in its dose calculation. For the double peak on the left side of this plot BrainSCAN slightly overestimates the dose but is successful in distinguishing the two peaks. Eclipse on the other hand is unable to separate the peaks. Although this inadequacy of the Eclipse treatment planning system may have a direct impact on the treatment of IMRT plans, it should be noted that this is inherently a problem with the Eclipse forward planning calculation and not with the Helios inverse planning software. While correction of this problem by directly entering higher resolution data into Eclipse is not possible due to a minimum resolution capability of 2.5 mm, studies have shown that these inaccuracies can be reduced by using high resolution film dosimetry to measure the penumbra region of transverse profile commissioning data [77] or through direct pencil beam kernel optimization [81]. Additionally, the clinical impact of this inadequacy is yet to be determined and it should be reiterated that this effect is only apparent for highly modulated fields. The high resolution field used to ascertain the effects of the commissioning data resolution was specifically chosen as being the most highly modulated field produced in the DVH comparison.

It has been demonstrated that both BrainSCAN and Helios have inherent advantages for IMRT planning. Both inverse planning systems are capable of producing substantially equivalent dose plans in terms of target coverage and normal tissue sparing. Several insignificant differences between the systems exist in terms of implementation and commissioning, dose optimization and plan assessment. One difference brought to light by this comparison was the inadequacy of Eclipse treatment planning system to accurately calculate dose for highly modulated fields. Although this study did not evaluate the clinical impact of this inadequacy, IMRT quality assurance generally has a large impact on time and resources and discrepancies between calculations and measurements for highly modulated fields will most certainly be problematic.

Throughout this study IMRT dosimetric verification measurements were performed using plans from both Helios and BrainSCAN. These verification measurements, which included a five field prostate plan in addition to the measurements investigating the effects of

commissioning data resolution, were carried out using two-dimensional radiographic film dosimetry. In theory, these measurements required a minimum of 17 films to be loaded, exposed, unloaded, and processed (5 prostate fields × 2 planning systems + 3 calibration films + 1 high resolution field + 3 calibration films). In reality, however, several of the film verification measurements had to be repeated as the result of either experimenter or film processor errors. The most common experimenter error encountered was neglecting to set the collimator jaws to the settings prescribed by the planning systems. Although this type of error could have been avoided by delivering the IMRT fields with the linear accelerator in treatment mode where interlocks would have alerted the experimenter to the error, service mode was the preferred delivery mode due to its efficiency and flexibility. Film processor errors encountered included processor temperature artifacts in the form of vertical smearing as well as film roller artifacts. The time and labour spent performing dosimetric IMRT verification during this study prompted the research which is this main objective of this thesis, namely the design, development, and implementation of an easier to use and more efficient novel IMRT dosimetric verification system. The remainder of this thesis is devoted to this endeavour.

Chapter 3

A TISSUE EQUIVALENT PLASTIC SCINTILLATOR IMRT VERIFICATION SYSTEM

Quality assurance of IMRT would be best supported by a rapid, easy to use, high resolution, tissue equivalent dosimetry system. In this work, we introduce a prototype dose verification system that fulfills these requirements. Our dosimetry system is based on an organic tissue equivalent plastic scintillator material.

3.1 Plastic Scintillators

Scintillators are materials that convert energy absorbed from incident ionizing radiation into visible wavelength photons which are subsequently emitted by the material. The use of scintillators for radiation detection is very widespread particularly in the field of medical physics with scintillator detectors being used extensively in x-ray CT, PET and SPECT imaging as well as in digital radiography and portal imaging systems. The majority of these scintillation detectors make use of inorganic scintillator materials. Inorganic scintillators differ from organic scintillators in several ways. The scintillation mechanism in inorganic scintillators is dependent on energy states determined by the crystal lattice of the scintillator material. It thus follows that inorganic scintillators are comprised of crystalline materials (most commonly alkali halide crystals) and as such are typically made up of high Z elements. Additionally, inorganic scintillators tend to have slower response times, higher light outputs and better response linearity compared to organic scintillators.

3.1.1 Organic Scintillator Theory

The plastic scintillator material used in this work is a type of organic scintillator. The scintillation mechanism in organic scintillators differs quite markedly from that of

inorganic scintillators. In organic scintillators, this process arises from transitions in the energy level structure of a single molecule. The majority of organic scintillators are based on organic molecules possessing certain symmetry properties which give rise to what is known as a *π-electron structure*. The electronic energy level diagram of a π-electron structure molecule is shown in Figure 3.1. This diagram shows a series of singlet energy states on the left and a series of triplet energy states on the right with vibrational states of the molecule indicated as dashed lines. The spacing of the vibrational states is typically on the order of 0.15 eV. Since this spacing is large compared with average thermal energies (~0.025 eV), at room temperature nearly all molecules are found in the S_0 state. Upon irradiation of the material, a portion of the energy deposited as dose is absorbed by the organic scintillator molecules. This energy excites the electron configurations of the molecules into the upper singlet states as indicated by the upward arrows in Figure 3.1. The higher singlet states excited in this absorption are quickly de-excited through radiationless internal conversion to the S_1 state. These internal conversion de-excitations occur on the order of picoseconds resulting in a population of S_1 excited states. It is the de-excitation from the S_1 state to one of the vibrational states of the ground electronic state, S_0, that produces the principle scintillation light emitted by the scintillator. This emission is termed *prompt fluorescence* and is represented in Figure 3.1 by the left-most set of downward arrows. The energy difference between the S_1 and S_0 states is approximately 3 eV for typical organic scintillator molecules corresponding to visible photons with wavelengths between 400 nm and 500 nm (violet and blue light). The speed, or response time, of the prompt fluorescence is characterized by the decay time, τ, such that the prompt fluorescence intensity at a time t is given by:

$$I = I_0 \exp\left[-\frac{t}{\tau}\right] \tag{3.1}$$

where I_0 is the initial intensity. For typical organic scintillators the decay time is on the order of nanoseconds.

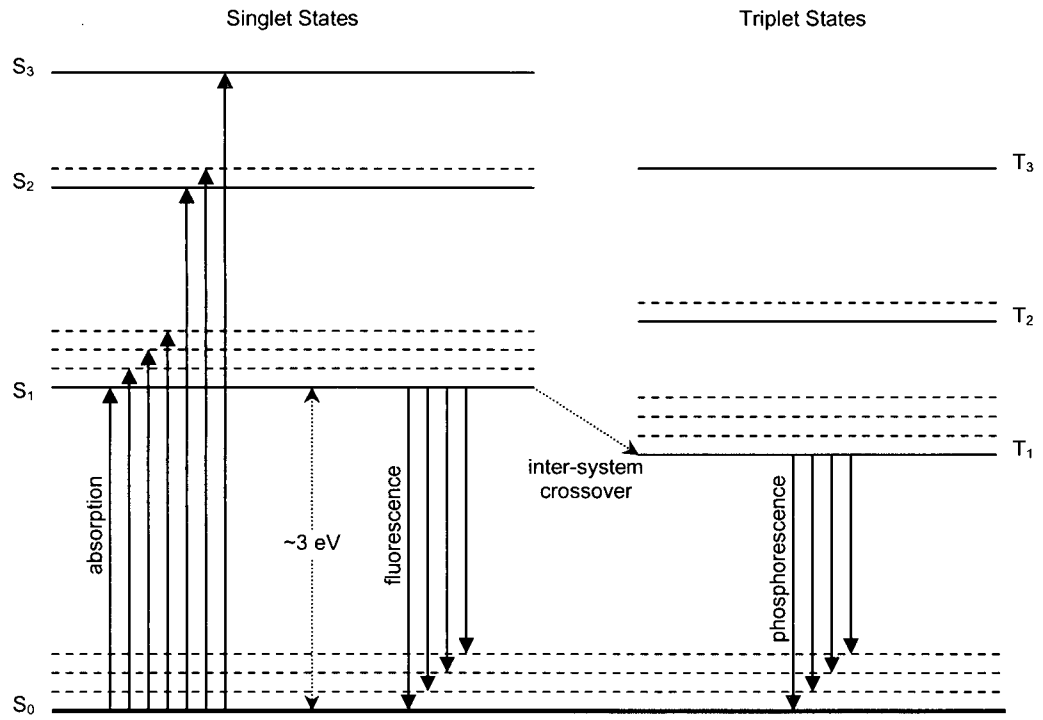

Figure 3.1: Electronic energy levels of an organic molecule possessing a π-electron structure. Adapted from [42].

Although prompt fluorescence makes up the majority of scintillation light emitted from an irradiated organic scintillator, there are other processes that can lead to emission of visible light following irradiation. One such process is *phosphorescence*. Phosphorescence occurs when singlet states are converted to triplet states through a transition called *inter-system crossover*. An example of inter-system crossover from the S_1 state to the T_1 state is shown in Figure 3.1. As indicated in this figure, the energy difference between the triplet and ground states is less than the energy difference between the S_1 and ground states causing de-excitation from the triplet state to correspond to emission of longer wavelength light. Additionally, the lifetime of the first triplet state is characteristically much longer (on the order of milliseconds) than that of the first singlet state thus leading to a slightly delayed light emission following irradiation. Another process leading to the delayed emission of light from scintillators is known as *delayed fluorescence*. In delayed fluorescence, molecules in the triplet T_1 state are excited back to the S_1 state and subsequently de-excite to the ground state. As this de-excitation is

from the S_1 state to one of the vibrational states of S_0, the light emitted is identical in wavelength to prompt fluorescence light.

3.1.2 Plastic Scintillator Properties

In contrast to inorganic scintillators where the scintillation process is dependent on the material's crystalline structure, the organic scintillation process is independent of the physical state of the molecular species. As such, organic scintillators undergo fluorescence as solids, as vapours, or as part of multi-component solutions. Plastic scintillators, like the one used in this work, are formed by dissolving an organic scintillator in a solvent which is subsequently polymerized to form a solid plastic. This plastic is fabricated and can be shaped using methods identical to those used in the fabrication and machining of common plastics like polystyrene and Lucite. Furthermore plastic scintillator material is robust, durable, and relatively inexpensive thus providing a convenient alternative to crystalline scintillation detector media. By selectively choosing the solvent used to form a plastic scintillator it is possible to create an organic scintillation material with physical characteristics comparable to those of biological tissue. Several scintillator manufacturers provide such *tissue equivalent plastic scintillators*. In this case tissue equivalence refers to the fact that dose deposition in these materials is comparable to dose deposition in an equivalent volume of water (water being considered equivalent to soft tissue as described in section 1.6.2). As such, these plastic scintillators have effective Z values and electron and mass densities comparable to those of water. The dose deposition similarities between tissue equivalent plastic scintillator and water are directly illustrated in Figure 3.2 and Figure 3.3. Figure 3.2 shows a plot of the mass-energy absorption coefficients for water, polystyrene and tissue equivalent plastic scintillator as a function of photon energy from 10 keV to 20 MeV. This plot clearly illustrates the close similarity of tissue equivalent plastic scintillator to both water and polystyrene for the energy range used in clinical radiation therapy (1 MeV to 20 MeV). The mass collision stopping power for water, polystyrene and tissue equivalent plastic scintillator are shown in Figure 3.3 as a function of electron energy from 10 keV to 25 MeV. Once again, the close similarities between these materials is observed.

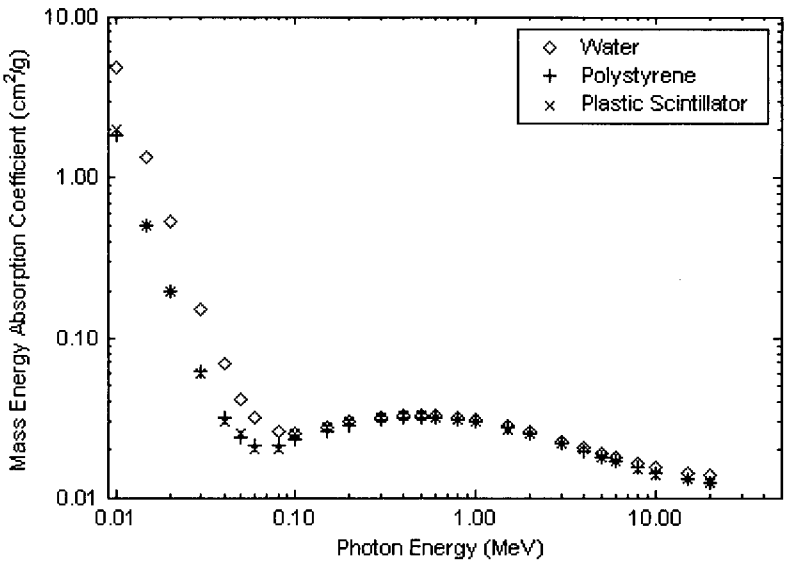

Figure 3.2: Mass energy-absorption coefficients for water, polystyrene and tissue equivalent plastic scintillator for monoenergetic photons ranging from 10 keV to 20 MeV. Plotted using data from [82].

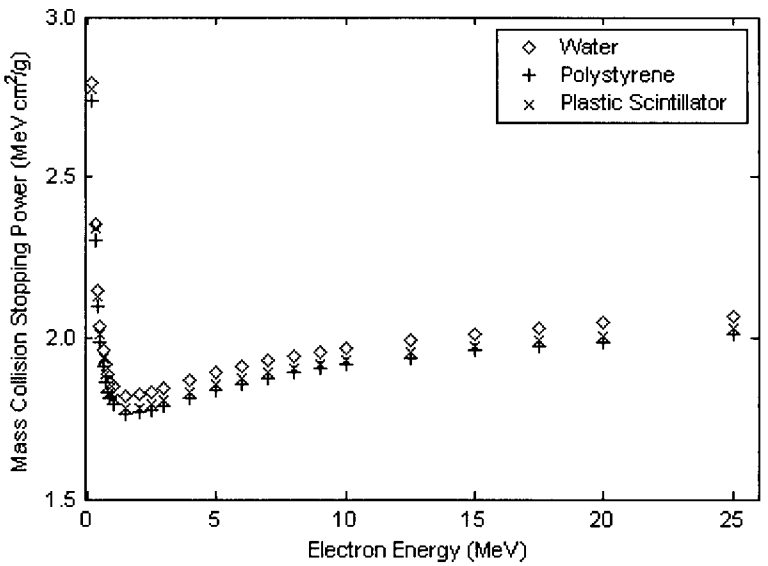

Figure 3.3: Mass collision stopping power for water, polystyrene and tissue equivalent plastic scintillator for monoenergetic electrons ranging from 10 keV to 25 MeV. Plotted using data from [83].

3.1.3 Plastic Scintillator Based Dosimetry Systems

Although the use of tissue equivalent plastic scintillator dosimetry systems is not yet widespread in the field of high energy radiation therapy, several systems have been proposed that make use of this convenient dose measurement medium. The first tissue equivalent plastic scintillator based dosimetry systems purposed were designed as small-volume, point detectors [84-86]. The active detection volume of these systems consisted of a small piece of plastic scintillator material whose volume varied from 1.6 mm^3 to 3.9 mm^3. This active volume was optically coupled using fiber optics to a photomultiplier tube (PMT) or a photodiode. A schematic diagram of one such system is shown in Figure 3.4.

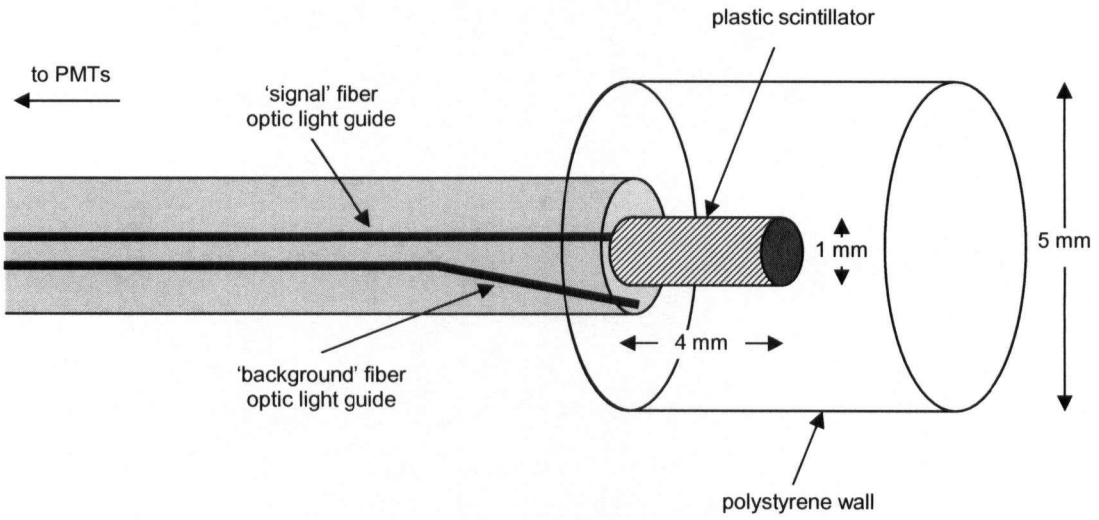

Figure 3.4: Tissue equivalent plastic scintillator small-volume, point detector system. A small active volume plastic scintillator is optically coupled to a photomultiplier tube that detects scintillation light. A 'background' fiber optic light guide and PMT are used to detect the Čerenkov light contribution. Adapted from [84].

In this system a small cylindrical piece of plastic scintillator with a diameter of 1 mm and a length of 4 mm is optically coupled to the 'signal' fiber optic light guide that transmits the emitted scintillation light to the main measurement PMT. A second light guide is also present in the system to correct for the presence of Čerenkov light in the measurement signal. This 'background' fiber optic light guide has the same dimensions as the 'signal' light guide but is optically shielded from the emitted scintillation light. A second PMT is

used to measure the Čerenkov signal from this light guide. The active plastic scintillator detection volume in this system is surrounded by a polystyrene cap that serves to protect the detection medium and to shield it from ambient room light. While useful for small field dosimetry applications (such as stereotactic radiosurgery) or for accurate high dose gradient dose measurements, tissue equivalent plastic scintillator based small-volume, point detectors have not become widespread in the radiation therapy community even in clinics where specialized techniques such as stereotactic radiosurgery are performed. The main reason for this is the relative complexity of such systems compared to competing small-volume, point detectors such as mini-ionization chambers, diode detectors, diamond detectors and MOSFET detectors. All of these alternatives make use of nothing more complicated than simple coaxial or triaxial cables and common electrometers compared to the costly and sensitive fiber optic cables and photomultiplier tubes required by a scintillation based detector. This complexity combined with the limited demand for high resolution, point dosimetry measurement systems has resulted in use of such systems being very limited in the field.

The extension of tissue equivalent plastic scintillator based dosimetry to two-dimensions has been proposed by several groups [87-90]. The first implementation of this extension was performed by Wong *et al.* [87] using a sheet of plastic scintillator positioned vertical along the treatment beam axis. This sheet was placed in water and the light emitted was captured by a CCD video camera. Results from this study were very promising with simple dose distributions being measured with accuracies within 5%. While this study did not investigate the use of the system for IMRT dose verification measurements, it did lead to a further study by Perera *et al.* who investigated the system's usefulness for two-dimensional dose measurement of brachytherapy sources [88]. The first application of a two-dimensional tissue equivalent plastic scintillator dosimetry system for performing IMRT dose verification measurements was performed by Li *et al.* [89]. Using a setup similar to that used by Wong *et al.*, this study demonstrated the applicability of such a system for measuring cumulative IMRT dose distributions in the axial plane. A schematic diagram of the setup used in this study is shown in Figure 3.5. The system consists of a 5 mm thick, circular sheet of plastic scintillator inserted into the waist of a water-filled Plexiglas cylinder with a diameter of 30 cm. The system is

positioned so that the center of the scintillating sheet is at isocenter of the IMRT plan being verified and so that all coplanar beam axes are parallel to the plane of the sheet. A CCD video camera shielded by a light-tight covering is used to capture the light emitted upon irradiation of the system.

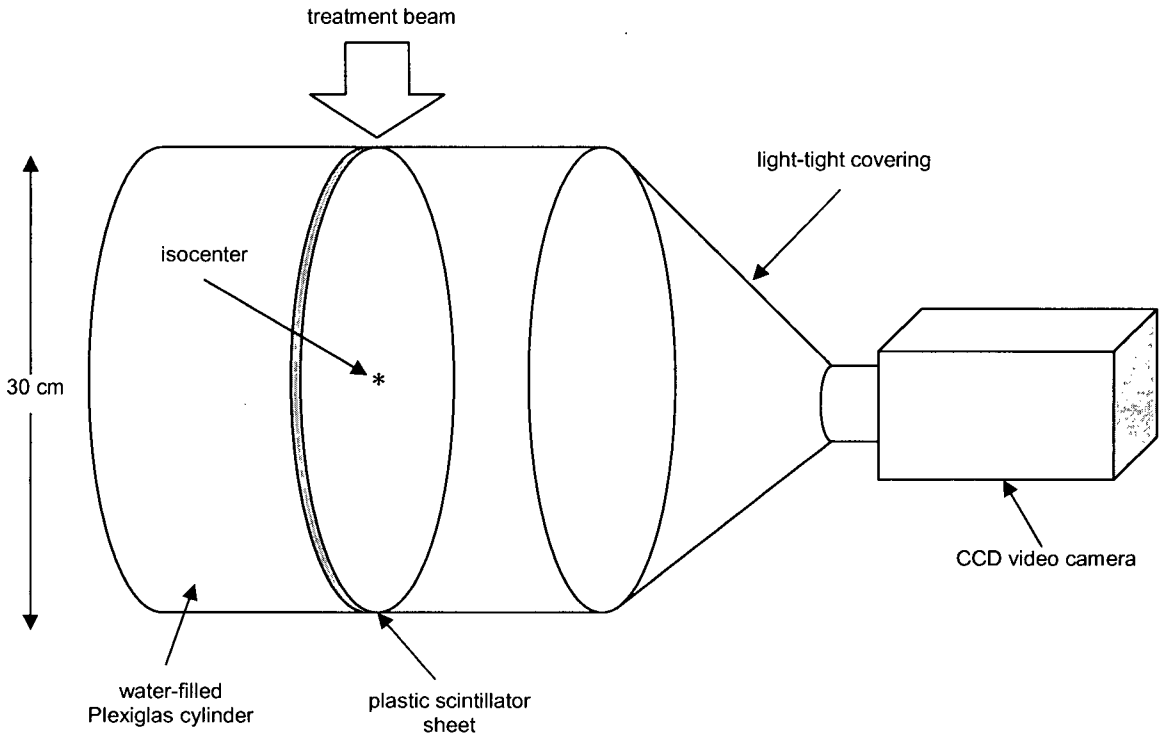

*Figure 3.5: Tissue equivalent plastic scintillator two-dimensional dose measurement system. A CCD video camera captures light emitted from a sheet of plastic scintillator fixed in a water-filled Plexiglas cylinder. The sheet is irradiated using coplanar IMRT treatment beams with the beam axis parallel to the plane of the scintillating sheet. Isocenter of the IMRT plan is indicated by the *. Adapted from [89].*

Results from this study indicate acceptable agreement between measured and calculated dose distributions in the axial plane. While useful for cumulative dose verification of multi-field IMRT plans, this system has several shortcomings. For coplanar IMRT plans where the linear accelerator collimator is oriented at 0°, this system would only measure the dose from one leaf pair. Another major disadvantage of this setup is it's inability to measure dose distributions in the plane perpendicular to the beam central axis. This deficiency is caused by the position of the CCD video camera relative to the scintillation

sheet. This positioning causes the CCD camera to be directly irradiated by treatment beams oriented perpendicular to the scintillation sheet thus leading to radiation damage of the radiosensitive CCD imaging array. As such this system is not capable of performing beam's-eye-view dose verifications of IMRT fields. Beam's-eye-view distributions are the preferred method for performing field-by-field IMRT verification due to the fact that they measure the dose deposited from all contributing MLC leaf pairs [33].

3.2 System Design

The dose verification system developed during this work overcomes several of the shortcomings of previous plastic scintillator based dosimetry systems. By making use of a tissue equivalent mirror to reflect the visible photons from a scintillation sheet orthogonal to the treatment beam, our system is capable of measuring beam's-eye-view two-dimensional dose distributions from individual IMRT fields. A schematic diagram of our prototype dose verification system is displayed in Figure 3.6.

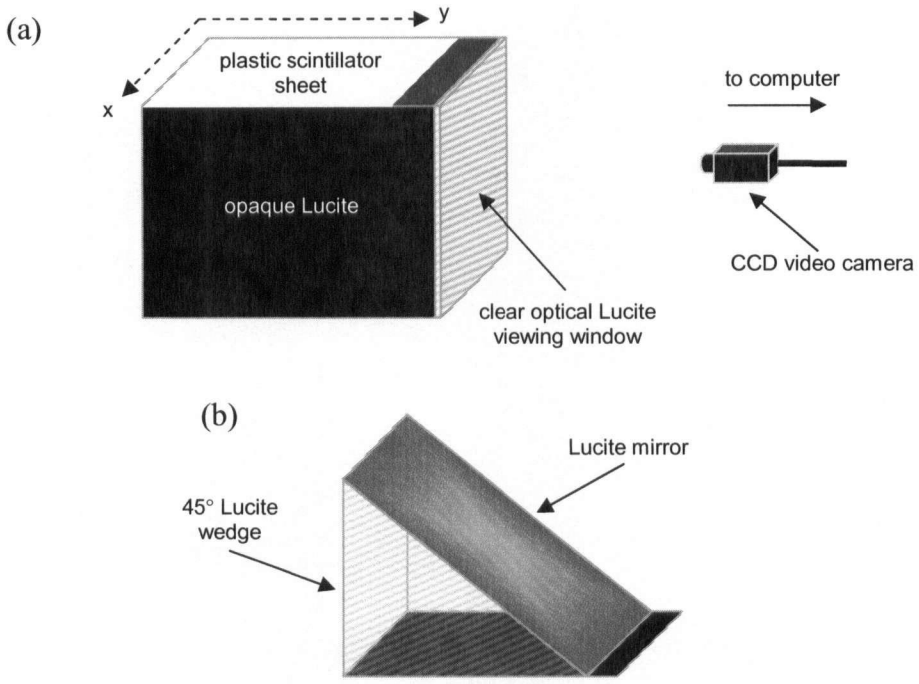

Figure 3.6: Schematic representation of IMRT verification system: (a) phantom outer box with CCD camera capturing light reflected out of viewing window; (b) inner wedge insert with Lucite mirror at 45° to scintillator sheet.

The system consists of two main components: a tissue equivalent phantom and a light capture imaging system. The proposed orientation of the system with respect to the linear accelerator treatment unit is displayed in Figure 3.7. In this orientation the treatment beam is incident orthogonally on the tissue equivalent plastic scintillator detection sheet and the verification system is aligned so that the center of the scintillation sheet is at isocenter. Blocks of tissue equivalent material may be stacked on top of the measurement plane in order to provide beam's-eye-view dose measurements at various depths.

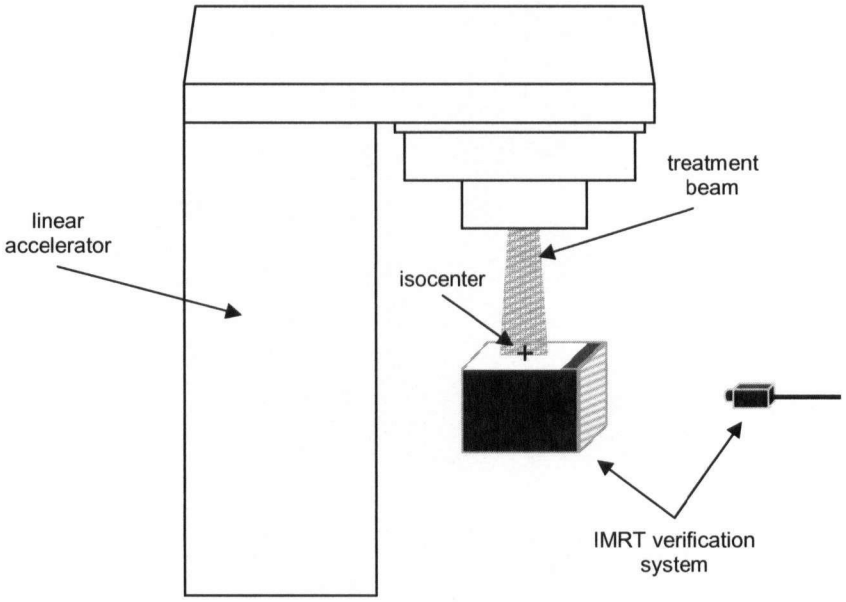

Figure 3.7: Orientation of IMRT verification system with respect to treatment unit. The system is oriented so that the treatment beam is orthogonal to the scintillator sheet of the phantom thus allowing measurement of beam's-eye-view doses.

3.2.1 Phantom Design

The tissue equivalent phantom consists of an outer box made of tissue equivalent materials and an inner insert. The dimensions of the outer box are 17 cm × 17 cm × 22 cm. Of the six walls of the outer box, four are constructed of 10 mm thick, opaque (black) Lucite, one of 10 mm thick, clear, optical quality Lucite, and one of 5 mm thick, tissue equivalent plastic scintillator. Figure 3.6(a) shows the outer box of the phantom. The inner insert of the phantom (displayed in Figure 3.6(b)) consists of a Lucite wedge at a 45° angle. A Lucite, silver coated mirror is mounted onto this wedge such that light

emitted from the scintillator is reflected through 90° out of the clear Lucite wall (viewing window) of the phantom. The insert is fixed inside the outer box and the box is sealed to be water tight. Once sealed, a small hole on the side of the box is used to fill the inner cavity with distilled water to complete the tissue equivalence of the phantom. The physical dimensions of the phantom (shown in Figure 3.8) were dictated by the physical size of the scintillation screen and wall materials in addition to the need for full scatter conditions throughout the detection plane.

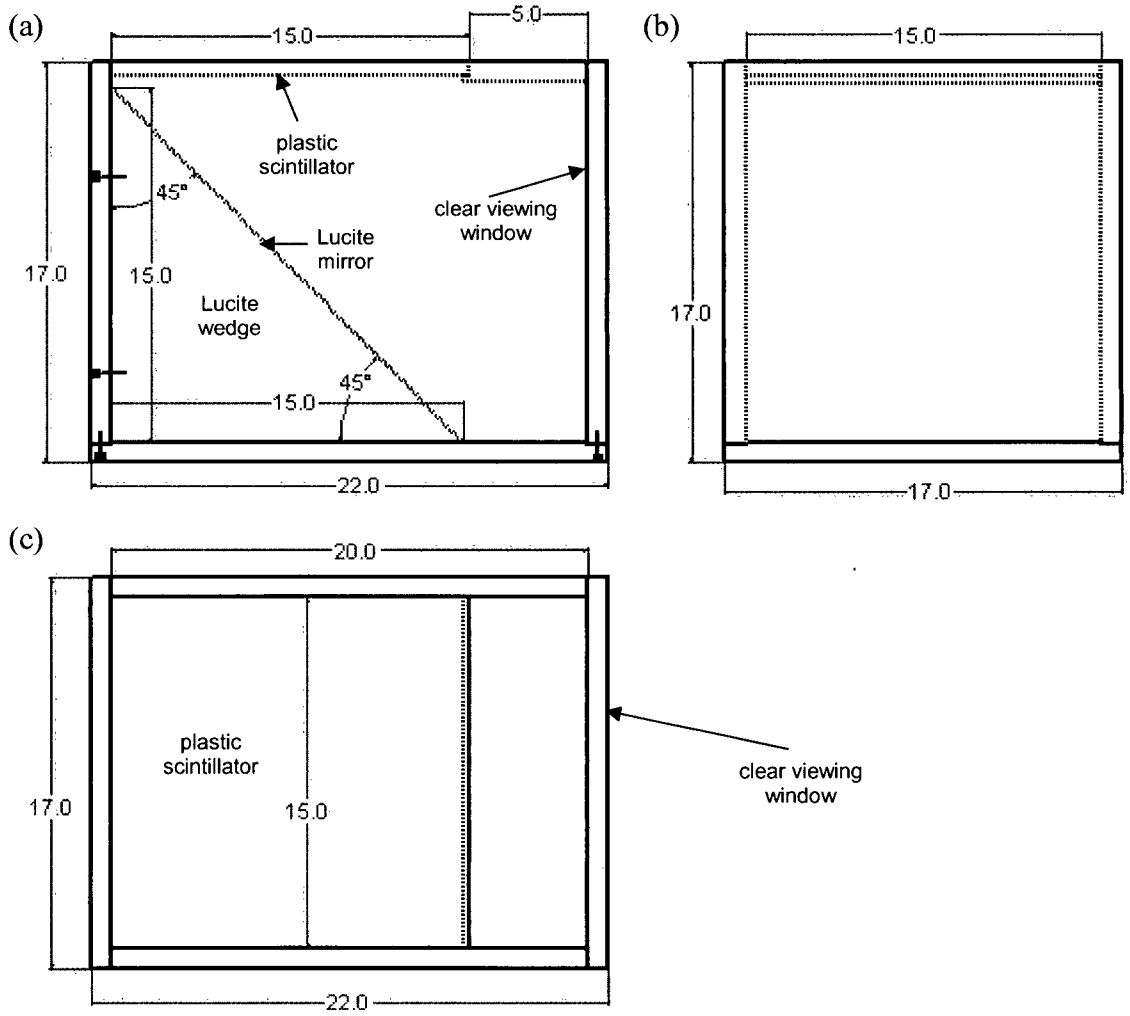

Figure 3.8: Machining diagram for verification system phantom showing (a) side, (b) front and (c) top perspectives. All non-labeled walls consist of opaque black Lucite. All dimensions are given in centimeters.

The scintillation screen measured 15 cm × 15 cm thus accounting for the width of the phantom (15 cm scintillator + 2 outer walls × 1 cm). The height of the phantom was identical to the width since the reflecting mirror is oriented at a 45° angle to both the scintillator and the viewing window as indicated in Figure 3.8(a). The length of the phantom is 5 cm longer than the height and width to ensure full scatter conditions at the end of the scintillator sheet closest to the CCD camera. While full scatter conditions along the other edges of the scintillator are ensured by surrounding the phantom with tissue equivalent blocks, this is not an optimal solution at the viewing window end of the phantom where minimal optical distortion is desired. A photograph of the prototype phantom is displayed in Figure 3.9. While reminiscent of a fluorescent-screen/camera type portal imaging device, this dedicated dosimetry system has the distinct advantage of being completely tissue equivalent thereby providing two-dimensional in-phantom dosimetric results.

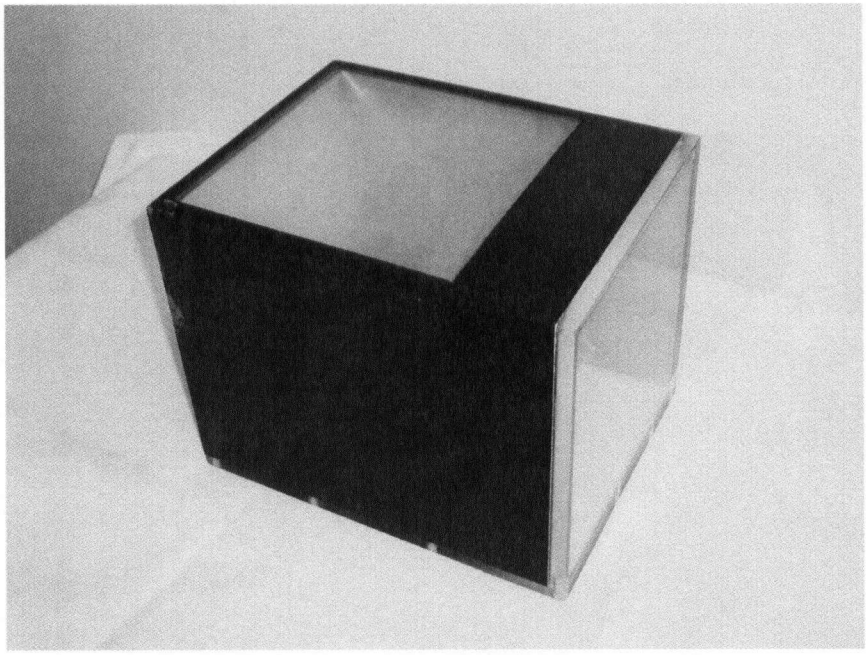

Figure 3.9: Prototype of IMRT verification system phantom. Tissue equivalent plastic scintillator sheet is shown at the top while the clear, viewing window is to the right. Small filling hole is used to fill the inner cavity with water to complete tissue equivalence of the phantom.

3.2.1.1 Scintillator Sheet Preparation

The tissue equivalent plastic scintillator material used in our system is 5 mm thick, EJ-200 plastic scintillator (Eljen Technology, USA). This scintillator material contains no high Z components and has electron and physical densities comparable to those of water. Some of the important physical properties of this material are given in Table 3.1. The square sheet of tissue equivalent plastic scintillator used in the prototype phantom had dimensions of 15 cm by 15 cm thus dictating the maximum measurable field size using this system.

Table 3.1: Important physical properties of the tissue equivalent plastic scintillator detection screen used in the system.

Property	Value
Polymer Base	Polyvinyltoluene
Light Output (% Anthracene)	64
λ of Maximum Emission (nm)	425
Refractive Index	1.58
Decay Time (ns)	2.1
Density (g/cm^3)	1.032
Electron Density ($/cm^3$)	3.37×10^{23}
Effective Z	5.76

Preparation of the scintillator sheet prior to installation in the dosimetry phantom included surface sanding in addition to sanding and painting of the sheet edges. The initial state of the scintillator sheet following casting is shown in Figure 3.10. As illustrated, the large surfaces of the sheet are smooth and clear from the plastic casting process while the sheet edges are rough and translucent as a result of cutting of the sheet to length and width specifications. For the surface of the sheet facing the inside of the phantom (facing the mirror and thus directly viewed by the CCD camera), it is desirable to maximize the light emitted by the scintillator. In this initial state, however, only a small fraction of the scintillation light is emitted from this surface due to internal reflection at the smooth scintillator / water interface. The amount of light emitted can be

increased by sanding the surface to roughen the scintillator / water interface. This technique, commonly used in nuclear science scintillator detector research [91-93], decreases the amount of internal reflection at the light detection interface thus improving the light collection efficiency.

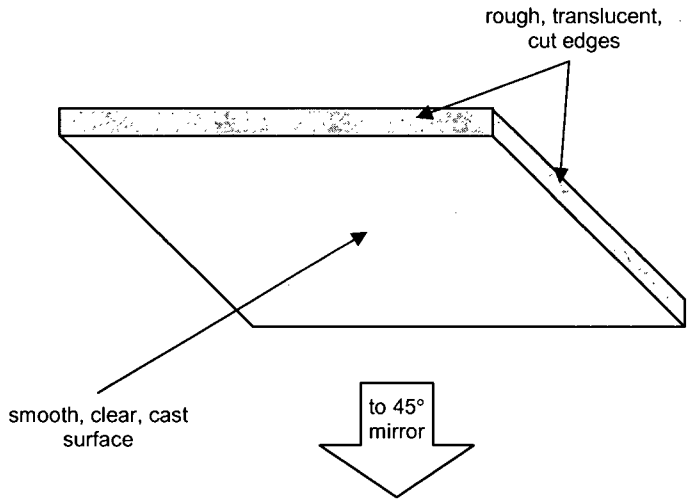

Figure 3.10: Initial state of tissue equivalent plastic scintillator sheet following casting. Top and bottom surfaces are smooth and clear while edges are rough and translucent from cutting of sheet to specified dimensions.

To determine the optimal degree of scintillator sanding to maximize light output a simple investigation was carried out to examine the effect of sandpaper of different "grit" (i.e. roughness) on light output. A small sample sheet of scintillator measuring 6 cm × 6 cm was sanded on one side using pieces of sandpaper of various grit. Following the instructions of the scintillator supplier [94], all sanding was performed using a sanding block and waterproof sandpaper. During use, the sandpaper was repeatedly wet using warm, soapy water. The sample scintillator sheet was sanded using 8 different grits of sandpaper beginning with the lowest grit (most coarse) and proceeding to finer and finer grits. For each grit, the sanded sample was placed in a clear water tank and irradiated edge-on using a square, 3 cm × 3 cm, 6 MV photon beam at a SSD of 100 cm. A total of 5 irradiations were performed each delivering a total of 50 MU at a repetition rate of 600 MU per minute. For each irradiation, scintillation light emitted from the sanded surface was captured using a high resolution, monochrome CCD video camera and a control and

capture computer with a frame-grabber board (equipment details found in section 3.2.2). Summation images were produced by summing the images captured during each irradiation. Examples of these summation images are displayed in Figure 3.11.

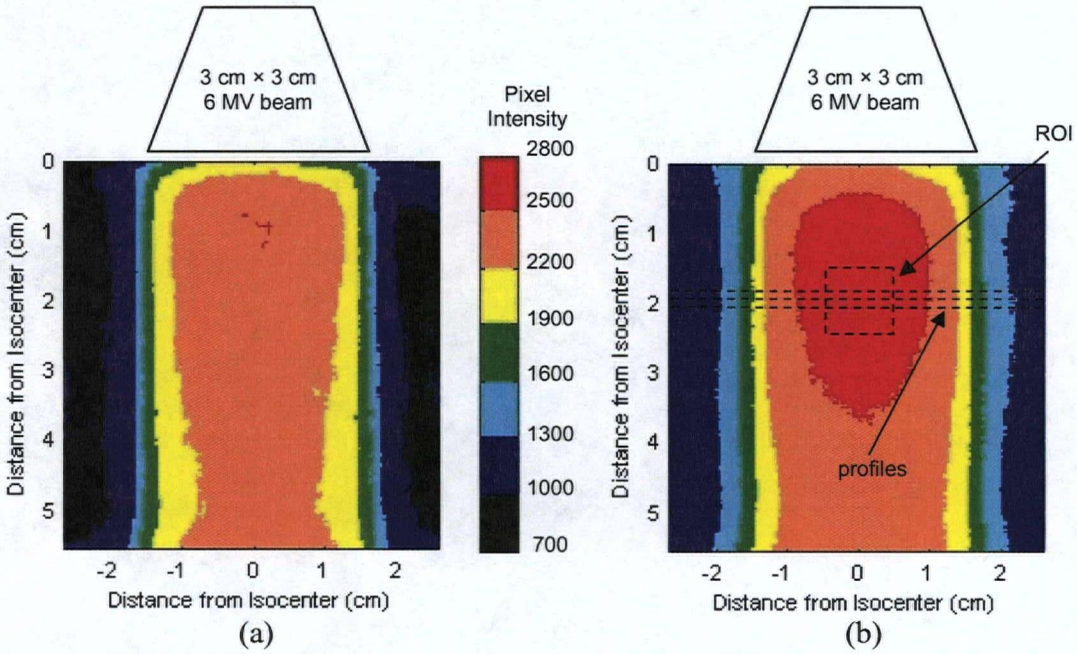

Figure 3.11: Summation images from sanding investigation for (a) no sanding (i.e. smooth, cast surface) and (b) sanding using 220 grit sandpaper. Also illustrated are the square, 1 cm × 1 cm, region-of-interest (ROI) and the horizontal profiles used for analysis of the images.

Summation images were analyzed by defining a square, 1 cm × 1 cm region-of-interest (ROI) centered at a depth of 2.5 cm below the irradiated edge of the scintillator (see Figure 3.11). The mean signal in this ROI was calculated for each summation image. Table 3.2 lists the results from this analysis. The second column represents the mean signal from the ROI averaged over all 5 irradiations at each grit. In addition to investigating the effect of sandpaper grit on the light output, the blurring of the radiation distribution was also examined. Horizontal profiles through the central 5 mm of the ROI were extracted. For each profile, the full width at half of maximum (FWHM) was determined and the average over all profiles calculated. Results from this analysis are also displayed in Table 3.2.

Table 3.2: Results from sanding investigation showing the effect of sandpaper grit on scintillator light output and radiation distribution blurring. Results for each grit are averaged over 5 irradiations. Zero grit indicates the smooth, cast scintillator surface prior to any sanding.

Sandpaper Grit	**ROI Mean Intensity**	**Full Width at Half Max (pixels)**
not sanded	2418.9	78.76
60	2735.1	77.40
120	2738.7	77.40
180	2740.7	77.36
220	2752.1	77.28
320	2694.6	77.00
400	2670.0	77.04
600	2579.6	77.24
1500	2501.1	77.52

As expected, the results displayed in Table 3.2 show an increase of 10% in light output between using the smooth, cast scintillator surface and the surface sanded to 60 grit. As previously described, this increase is due to a drastic decrease in internal reflection at the surface of the scintillator thus allowing more scintillation light to escape and be captured by the camera. The light output is then observed to increase slowly with grit with the maximum scintillator light output occurring for a sandpaper grit of 220. For sandpapers with finer grit than 220, the light output is observed to decrease. This is also expected as the very fine grits have the effect of polishing the scintillator surface thus re-establishing a smooth surface with increased internal reflection. The effect of sandpaper grit on distribution blurring was found to be very small with a maximum variation in FWHM of 1.76 pixels throughout the investigation. Applying the image scaling factor of 0.4 mm per pixel (determined by acquiring an image of a ruler placed directly in front of the

scintillator sheet) the maximum variation of FWHM is 0.7 mm. Although there does seem to be a trend in the FWHM data in Table 3.2 with the blurring being inversely proportional to the light output, the small size of these changes caused them to be only a minor consideration when choosing the optimal sanding for the system of 220 grit.

In addition to sanding the detection surface, preparation of the scintillation sheet also included sanding and painting of the sheet edges. At the edges of the scintillation sheet it is desirable to maximize absorption of emitted scintillation light to avoid reflected light from falsely increasing the signal strength towards the edges of the detection screen. Consequently, scintillator edges were also sanded to 220 grit using the same sanding technique described above. This procedure serves to minimize the internal reflection of light at the edges. Absorption of the emitted light from the edges was achieved by painting each edge with a flat, black, oil-based paint.

Once fully sanded and painted the scintillation sheet was installed into the outer shell of the phantom using a silicon adhesive ensuring the sanded surface faced the 45° mirror. To further increase the light output on this side of the scintillator, a pigment loaded reflective film (Proteus Inc., USA) was placed against the outer surface of the scintillator to reflect light emitted through this surface back towards the CCD camera facing surface. This reflective film is 188 μm thick and consists of calcium carbonate on a polyester backing.

3.2.1.2 Micro-Louvre Optical Collimator

Initial results using the prototype phantom as described above indicated the presence of a spatially variant blurring in the light intensity distributions. Two distributions measured using this setup are displayed in Figure 3.12. The spatially variant blurring is obvious in these distributions with the blur increasing markedly from bottom to top of both images.

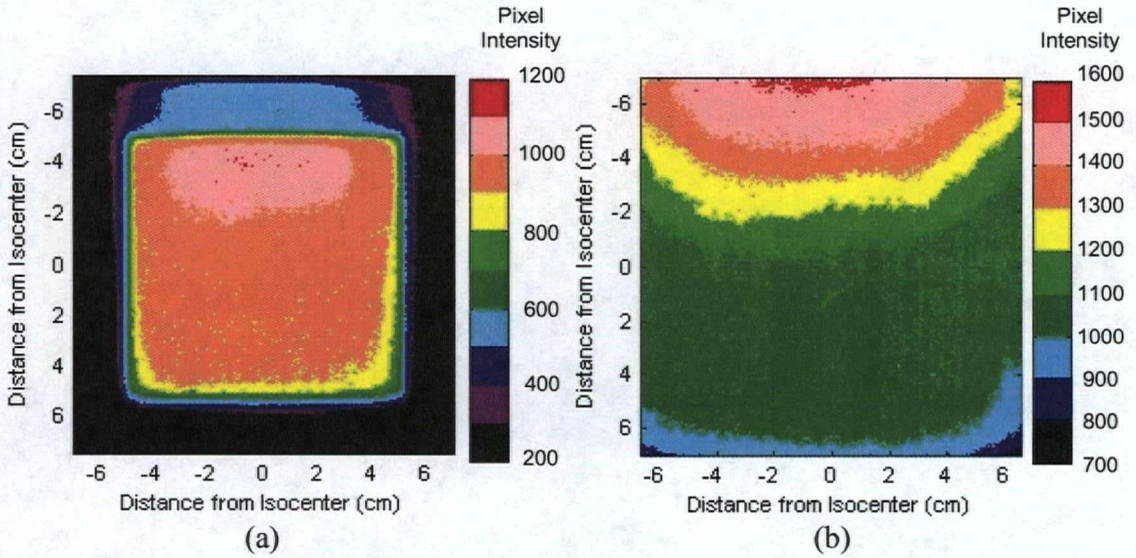

Figure 3.12: Example light intensity distributions measured using the initial prototype phantom described above for (a) an 10 cm × 10 cm open square field and (b) a 25 cm × 25 cm open square field.

This type of spatially variant blurring has been previously observed in electronic portal imaging systems using CCD cameras to view scintillation screens through 45° mirrors [95]. This so called "cross-talk" or "glare" comes about due to multiple reflections of scintillation photons between the mirror and the scintillation sheet. The phenomenon is illustrated in Figure 3.13. In this figure, a high energy photon incident at the point A produces visible scintillation light that is emitted both directly towards the CCD camera (dashed line) and also, for higher emission angles, via the mirror and back onto the scintillation screen at some point B, for example. If the visible photon incident at B then reflects off the scintillation screen directly towards the CCD camera (dotted line), it will be indistinguishable from a visible photon that was originally emitted from B as a result of a high energy photon incident at this point. Multiply-reflected photons such as this give rise to the cross-talk signal. Due to the orientation of the mirror, the cross-talk signal increases as the distance between the mirror and the scintillator screen reduces thus creating a spatially variant blurring in the y-direction (direction indicated in Figure 3.6(a)).

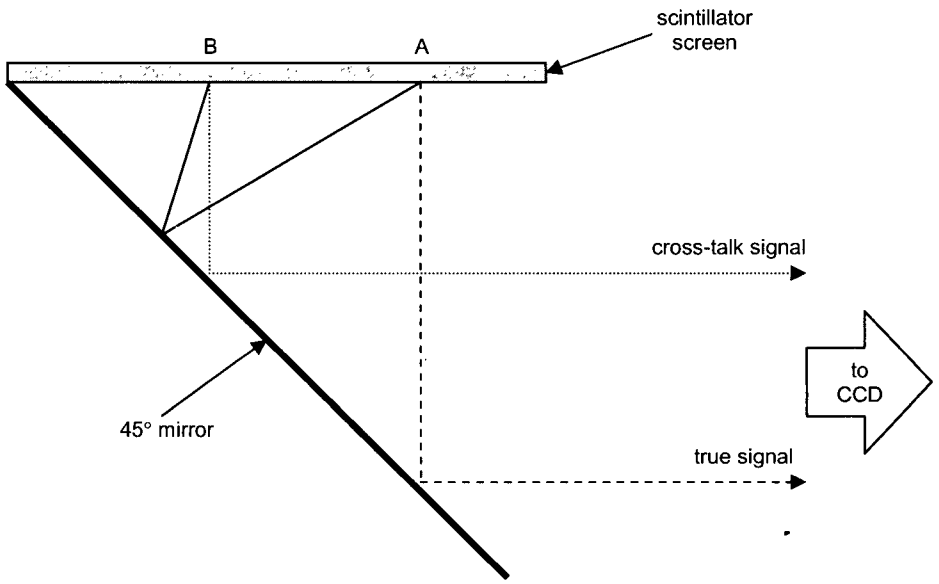

Figure 3.13: Origin of spatially variant cross-talk phenomenon. A high energy photon at point A produces scintillation light which is emitted directly towards the CCD camera (dashed line) as well as towards the point B for higher emission angles (solid line). If these visible photons reaching point B reflect off the scintillator back towards the CCD camera (dotted line) they will be indistinguishable from scintillation photons emitted from a high energy photon interaction at point B. Adapted from [95].

While mathematical methods exist which are capable of removing a spatially variant blur kernel [96-98], these techniques tend to be computationally intensive and the resultant images are typically fraught with processing artifacts. As a result, physical anti-scatter measures were chosen to eliminate the cross-talk. The physical anti-scatter measures consisted of a 1-dimensional optical photon collimator oriented to prevent high-angle scattered light emitted by the scintillation screen from reflecting back onto the screen. Based on previous work by Partridge *et al.* [95], a micro-louvre light control film developed by 3M for use as a "privacy screen" for computer monitors was employed for this purpose (3M Corp., USA). This film consists of a series of thin non-divergent, optically opaque strips embedded in a polycarbonate matrix with a pitch of approximately 0.1 mm. Product data sheets indicate light transmission normal to the film as being approximately 75% with a reduction to 35% at 15° to the surface normal and complete loss of transmission at 30° to normal. The film was placed directly below the

scintillating sheet oriented with the strips running perpendicular to the y-direction in order to optically collimate the scintillation light in the direction of the spatially variant glare (Figure 3.14).

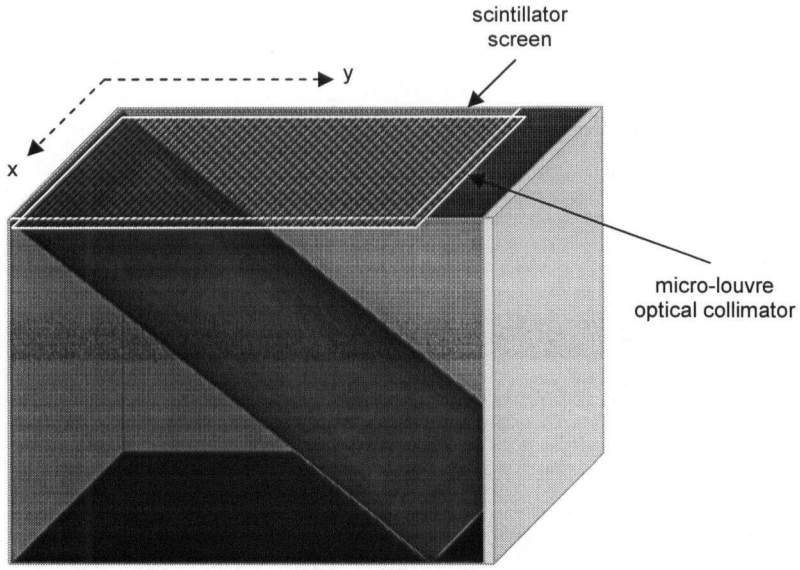

Figure 3.14: Placement and orientation of the micro-louvre optical collimator film in the verification phantom. Micro-louvre optical collimator is fixed directly below scintillation screen with collimation strips perpendicular to the y-direction.

Resultant images using the modified phantom with the micro-louvre in place are displayed in Figure 3.15. This figure shows the same field sizes as those in Figure 3.12 for direct comparison thus displaying the effectiveness of the micro-louvre optical collimator film in eliminating the spatially variant cross talk.

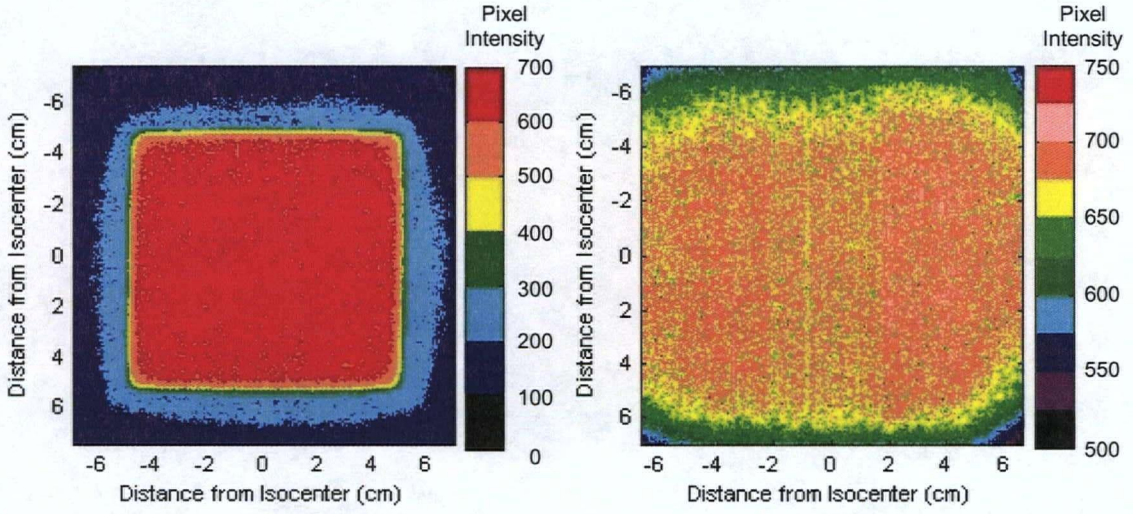

Figure 3.15: Effects of micro-louvre optical collimator film on images acquired using verification system for (a) 10 cm × 10 cm open square field and (b) 25 cm × 25 cm open square field.

This effect is more quantitatively displayed using normalized intensity profiles across the 25 cm × 25 cm open field in Figure 3.16. Clearly the cross talk has been virtually eliminated through use of the anti-scatter measures.

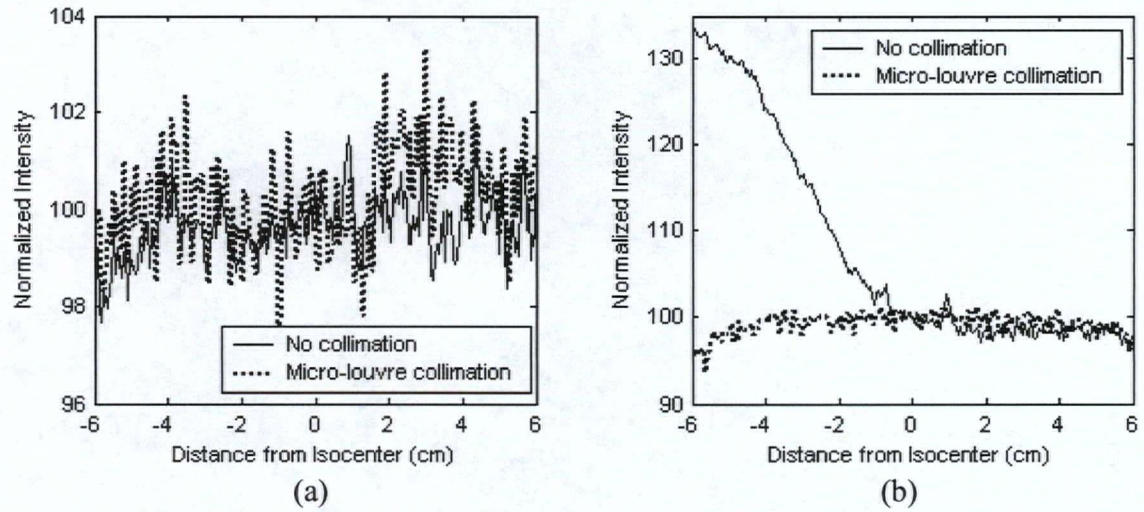

Figure 3.16: Normalized intensity profiles across 25 cm × 25 cm open square field with and without presence of micro-louvre optical collimator film in (a) the x-direction and (b) the y-direction.

The profiles in Figure 3.16 also show an increase in high frequency noise in the data acquired with the micro-louvre optical collimator film in place. This is especially apparent in Figure 3.16(a) with its larger vertical scale. This increase in high spatial frequency variations is the result of a decrease in the signal-to-noise ratio (SNR) of the system that arises from the partial attenuation of the scintillation light by the micro-louvre film. In order to quantify the attenuation of scintillation light by the film measurements of the mean light intensity in a small (1 cm × 1 cm) region-of-interest were acquired both with and without the presence of the micro-louvre film for the same 25 cm × 25 cm open square field. Results of these measurements are displayed in Table 3.3.

Table 3.3: Region-of-interest mean intensity for verification system with and without presence of micro-louvre optical collimator film for identical 25 cm × 25 cm open square fields.

	ROI Mean Intensity
No Micro-Louvre Collimator Film	1088.6
Micro-Louvre Collimator Film	718.2

The results displayed in Table 3.3 clearly show a reduction in the signal when the micro-louvre optical collimator film is employed in the system. This decrease in signal is approximately 35% in the region surrounding isocenter.

3.2.2 Imaging System Setup

The light capture system consists of an 8-bit, high resolution, monochrome CCD video camera (Hitachi KP-M1, Hitachi-Denshi, USA) and a control and capture computer with a high speed frame-grabber board (Matrox Meteor II, Matrox Electronic Systems Ltd., Canada). The spectral response characteristics of the CCD camera are displayed in Figure 3.17. With the infrared (IR) cut filter used throughout this work, the camera has a maximum detection efficiency for wavelengths of 500 nm to 600 nm with the relative sensitivity dropping to 80% at 400 nm [99]. The CCD camera is directed at the clear viewing window of the phantom to capture the reflected scintillation light. The CCD camera is Peltier cooled to 0° C and images are captured at a frame-sampling rate of 25 frames per second. Although capable of acquiring images composed of up to 756 × 581

pixels, the CCD camera signal is digitized to output square images of 288 × 288 pixels in order to facilitate easier and more efficient image storage and processing. Images from the camera are stored directly onto the computer.

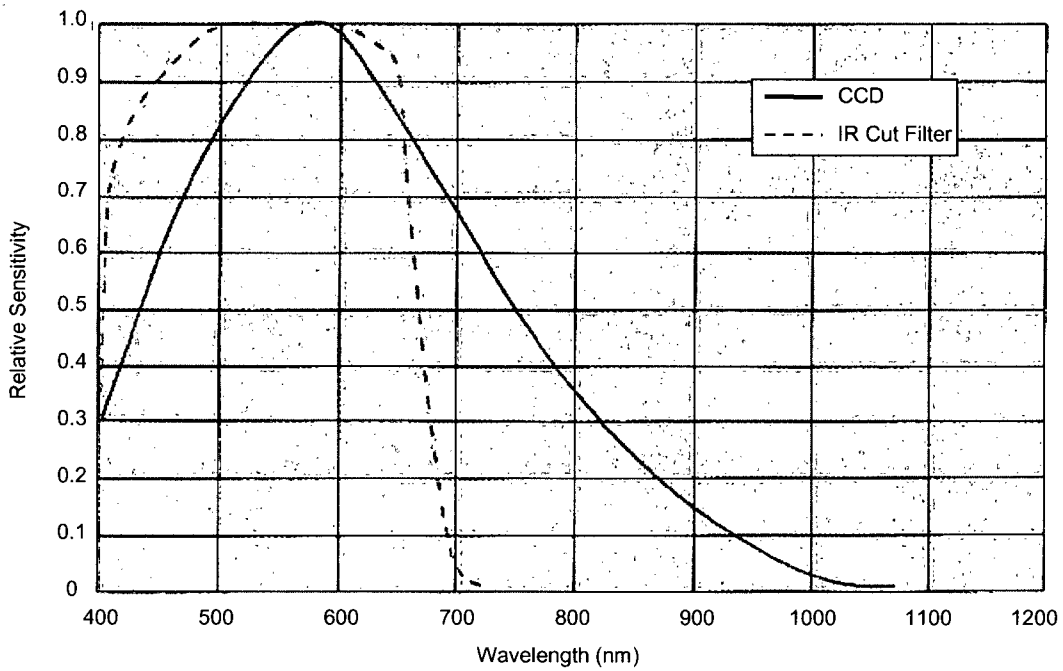

Figure 3.17: Spectral response characteristics of Hitachi KP-M1 monochrome CCD camera. The camera used in this work was fitted with an infrared (IR) cut filter. Adapted from [99].

The placement of the CCD camera in relation to the phantom is shown in Figure 3.6(a). As CCD elements, such as the array present in the CCD camera used in this system, are sensitive to ionizing radiation [100, 101] it is desirable to minimize the radiation exposure of the acquisition camera. This is accomplished in three ways. Firstly, the presence of the 45° mirror to reflect the emitted scintillation light ensures that the CCD camera is never directly irradiated by the primary photon beam. Secondly, the CCD camera is surrounded with 5 mm thick lead shielding to prevent exposure from lower energy scattered photons. Finally, all system testing and measurements were performed using photon beams with energies less than 6 MV to avoid exposure of the CCD element to neutrons produced through photodisintegration.

Initial measurements using the verification system were performed by transferring the video signal from the CCD camera to the capture computer outside the treatment

vault through the use of a 15 m coaxial cable. Although the signal acquired was suitable for proof-of-concept testing, it was soon discovered that this setup yielded results with an unacceptable amount of high frequency noise as a result of signal degradation during the transfer. This noise is clearly observed in dark current or "background" images acquired using the verification system when no high energy photon beam engaged (Figure 3.18(a)). This type of signal degradation is commonly observed when using long extension cables to transfer video signals and can be eliminated through the use of prohibitively expensive shielded cables [102]. To avoid the use of such cables a decision was made to position the control and capture computer local to the CCD camera (inside the treatment vault) and use a short, 1.5 m coaxial cable. In order to minimize radiation damage to the capture computer, the computer was placed at the end of the treatment couch and covered with multiple lead lined vests. A typical dark current image using this local control and capture computer setup is displayed in Figure 3.18(b).

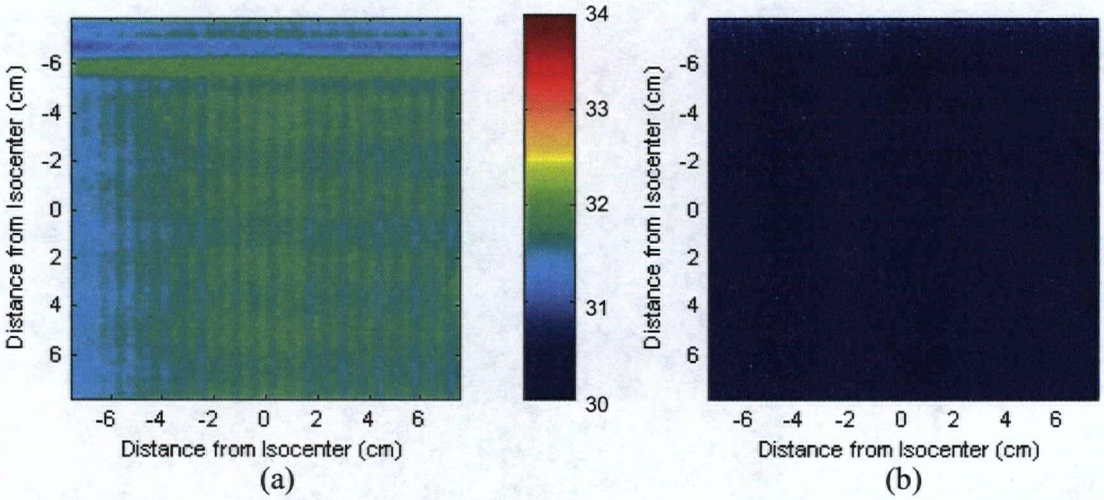

Figure 3.18: Dark current or background images using verification system (a) prior to and (b) after local positioning of control and capture computer in linear accelerator treatment vault.

In order to quantify the reduction of the noise due to this setup, the mean and standard deviation of the background pixel intensity were calculated for each of the images displayed in Figure 3.18. Results of this analysis are displayed in Table 3.4.

Table 3.4: Reduction of dark current as a result of moving control and capture computer into the treatment room.

	Mean Intensity	Standard Deviation
Remote Control and Capture Computer	31.65	0.16
Local Control and Capture Computer	30.32	0.15

These results show a clear improvement when the control and capture computer is placed in the treatment room, local to the CCD camera.

3.3 Data Acquisition and Processing

Once construction of the phantom and finalization of the imaging system was complete for the prototype dose verification system, a procedure for system setup, data acquisition and image processing was devised.

3.3.1 System Setup

Setup of the dose verification system entails positioning of the dosimetry phantom under the treatment beam, surrounding the phantom with tissue equivalent scatter material on all sides, adding the desired amount of tissue equivalent build-up material on top of the detection plane for measurements at depth and finally, masking all sources of visible light within the treatment room to eliminate extraneous signals in our CCD camera acquisitions.

The tissue equivalent dosimetry phantom is positioned under the treatment beam such that beam isocenter is located in the center of the scintillator detection screen with the outer surface of the scintillator at a source-to-surface distance (SSD) of 100 cm. A setup board is used to reproducibly position the CCD camera at a fixed distance from the dosimetry phantom. This distance (44 cm from the front of the phantom viewing window to the camera lens) ensures that the entire scintillator screen surface is imaged by the CCD camera. Once the phantom and CCD camera are in position, the precise location of isocenter on the acquired images as well as the scaling factor between the scintillator screen and the acquired images are determined. Both of these parameters are determined by using the CCD camera to acquire an image of the linear accelerator's field verification

light. This device consists of a light source in the linear accelerator head that mimics the high energy photon source to produce a visible projection of the radiation field that will be delivered. A thin beam alignment crosshair on the beam exit window works in concert with the field verification light to indicate the position of isocenter in the visible projection. With a collimator jaw setting of 10 cm × 10 cm the field verification light was projected onto a thin translucent sheet covering the scintillation screen and an image was acquired using the CCD camera. An example of one such setup image is shown in Figure 3.19.

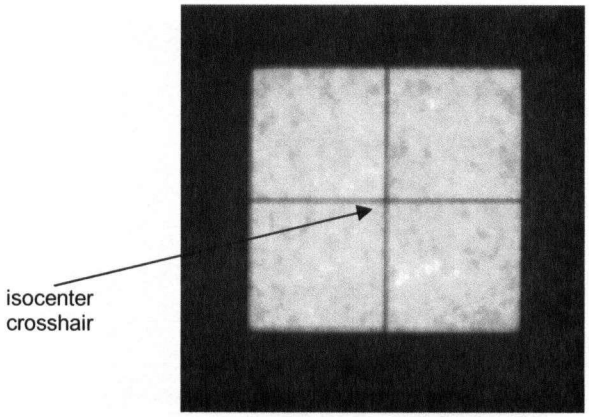

Figure 3.19: Image of linear accelerator field verification light for a 10 cm × 10 cm field acquired using CCD camera. Crosshair marks position of isocenter while edge separation can be used to determine image scaling factor. Image mottle is the result of mottle on thin translucent projection sheet.

The position of the crosshair in images such as this is subsequently used to determine the position of isocenter with respect to the image coordinates. The image scaling factor is determined using the field edge separation. Field edges are localized in both the x- and y-directions by finding the pixels where the intensity drops to 50% of the average light intensity from a central 1 cm × 1 cm ROI. This method of edge localization was validated by comparing the scaling result to that obtained by imaging opaque pieces of film of known dimension with the CCD camera.

To ensure full scatter conditions during dose measurement, the phantom is surrounded by additional tissue equivalent scatter material on the sides and back (opposite side to the viewing window). For this purpose, large 5 cm thick pieces of

Lucite were machined to the appropriate dimensions and positioned as displayed in Figure 3.20.

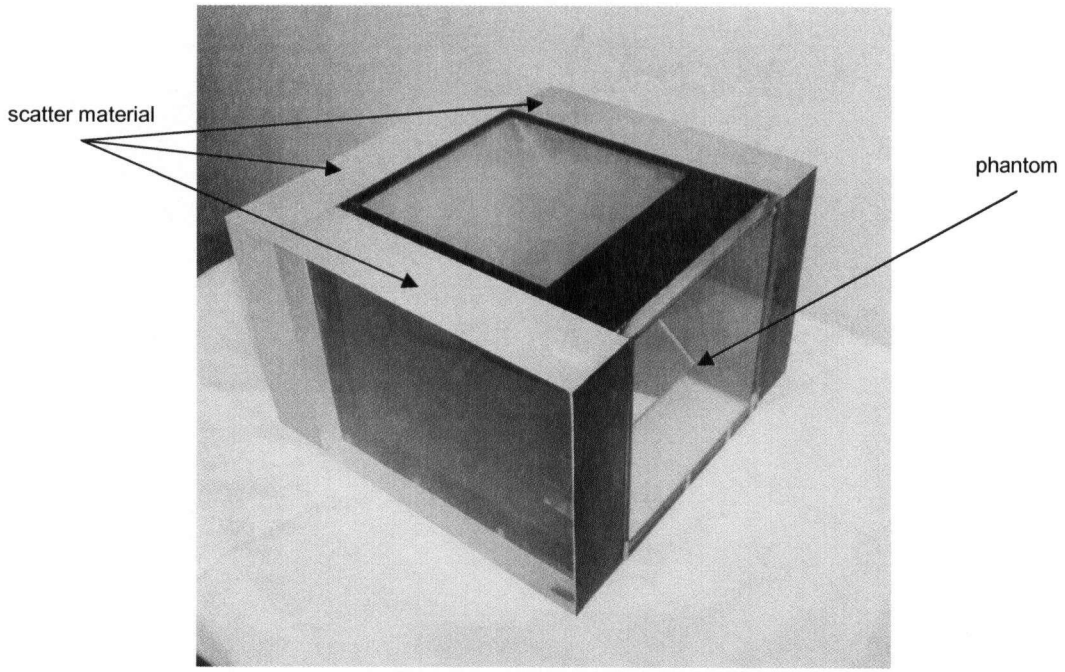

Figure 3.20: Placement of tissue equivalent scatter material around phantom to ensure full scatter conditions during dose measurement.

Additional scatter material is not required beneath the phantom or in front of the viewing window as the design of the phantom inherently provides the necessary scatter material in these directions. Beneath the scintillating sheet is a full 16.5 cm of tissue equivalent scatter material that includes, water, the Lucite mirror and the wedged Lucite mirror support. The phantom has also been designed to include 6 cm of tissue equivalent scatter material adjacent to the scintillator screen on the side with the clear viewing window. This was accomplished by extending the dimensions of the phantom by 5 cm in this direction as previously discussed in section 3.2.1.

Measurement of the dose distribution at arbitrary depths is accomplished by stacking tissue equivalent material on top of the phantom and its surrounding scatter material. Throughout this study, large slabs of Solid Water (Gammex, RMI, USA) of varying thicknesses were stacked on top of the phantom to achieve different measurement depths. A photograph of the dose verification system setup to a depth of 10 cm is shown in Figure 3.21.

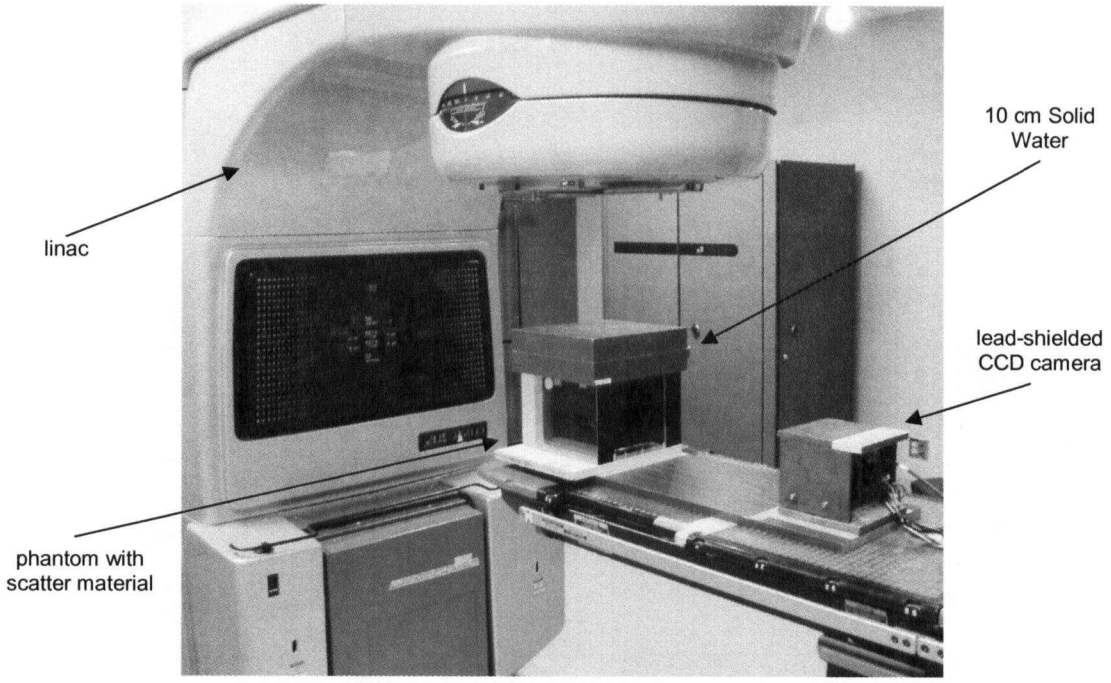

Figure 3.21: Prototype dose verification system setup for measurements at a depth of 10 cm. This photograph shows positioning of the dose verification system under the linear accelerator with tissue equivalent scatter material for full scatter conditions in place and 10 cm of Solid Water for measurement at depth.

The final step in setting up the dose verification system is to eliminate extraneous light sources inside the measurement room. This was accomplished by turning off the room lights as well as all room monitors and covering all illuminated controls and equipment light-emitting diodes with pieces of thin opaque plastic.

3.3.2 Image Acquisition and Summation

Image acquisition was carried out using an acquisition control visual interface programmed in Microsoft Visual Basic 6.0 (Microsoft Corp., USA) using the MIL-Lite Matrox Imaging Library (Matrox Electronic Systems Ltd., Canada). This interface is displayed in Figure 3.22. It has three distinct modes: Apparatus Setup, Background Capture and Data Capture. Apparatus Setup mode features full resolution (756 × 581 pixel) live video feed from the CCD camera to assist the user in aligning the phantom and CCD apparatus. This is the only mode to make use of full resolution images. Both other modes make use of the reduced, 288 × 288 pixel video images by default. The

Background Capture mode is used to acquire background images as well as the field verification light images described in the previous section. This mode captures a set number of seconds of video feed and immediately averages all captured frames to output a mean image. This mode does not allow for control over which captured frames should be used for the averaging and therefore is not suitable for capturing dosimetry data where the pre- and post-beam-on frames should be discarded.

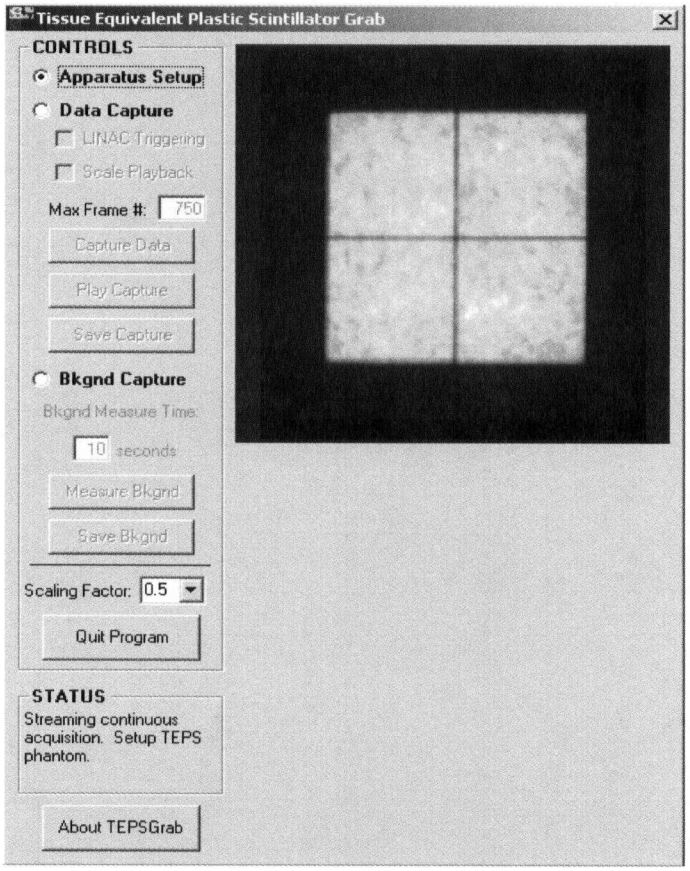

Figure 3.22: Image acquisition control visual interface used to control CCD camera during system setup and data acquisition.

The Data Capture mode is used to capture dosimetry data while the high energy photon beam is engaged. This mode acquires images from the CCD at the maximum frame rate and saves all frames to a binary file format. The user first specifies a maximum frame number which dictates the amount of random access memory (RAM) set aside for frame storage. Once this storage has been allocated and the frame capture starts, the user engages the high energy photon beam. Once the beam has terminated, the user manually

stops frame capture. Beginning frame capture prior to beam-on and terminating it after beam-off is essential for ensuring no scintillation light is missed due to a late CCD start or an early CCD stop.

The first step in the processing of the captured images is to sum the frames captured during radiation beam-on. Due to the data capture procedure described above, it is necessary to discard the pre- and post-beam-on frames in each of the saved binary image files from the dosimetry data capture. This processing step, together with all subsequent processing steps, is accomplished using a graphical user interface developed with MATLAB 6.5 (Mathworks Inc., USA). This program is capable of loading the binary image files and determining which frames correspond to radiation beam-on.

3.3.3 Subtraction of Dark Current

The next step of the image processing involves subtracting the dark current signal or background from the acquired images. A background image is acquired at the beginning of each measurement series. This image is acquired using Background Capture mode with a measurement time of 10 seconds with the treatment beam off. This background image is then loaded into the MATLAB graphical user interface where it is multiplied by the number of frames used to perform the image summation of the dosimetry data. The resultant image is subtracted from the summed dosimetry data image.

3.3.4 Deblurring

In addition to the previously discussed spatially variant blurring (section 3.2.1.2), uniform, spatially invariant blurring is also present in the optical system as light from the scintillating sheet scatters through the water filled cavity, the clear Lucite viewing window, and air on its way to the CCD camera. Since this blur is spatially invariant it can be removed in a comparatively straight forward manner by deconvolving a blurring kernel from the acquired images. While the use of the micro-louvre optical collimator film successfully removes any spatially variant blurring of optical photons, it also poses a difficulty in modeling the remaining spatially invariant blurring kernel. This is because the orientation of the collimator film causes optical blurring in the y-direction to be different from the optical blurring in the x-direction. This difference was accounted for

by fitting the blurring kernel, or point spread function (PSF), with a multiple, elliptical Gaussian blurring kernel of the form:

$$h(i,j) \approx c_1 G_1(i,j) + c_2 G_2(i,j) + c_3 G_3(i,j) + \ldots \tag{3.2}$$

where $G_n(i,j)$ are all normalized elliptical Gaussians of the form:

$$G_n(i,j) = \frac{g_n(i,j)}{\sum_i \sum_j g_n(i,j)} \tag{3.3}$$

where:

$$g_n(i,j) = \exp\left[-\frac{1}{2}\left(\frac{x_i^2}{\sigma_x^2} + \frac{y_j^2}{\sigma_y^2}\right)\right] \tag{3.4}$$

and i and j are the indices of the pixels corresponding to points (x_i,y_j) on the scintillation sheet as defined from a selected origin. The origin for defining this relationship between pixel index and object plane point was chosen to be the isocenter of the high energy photon beam as previously defined using an image of the beam alignment crosshair acquired with the field verification light. The distance of each point from this origin is also already known from the previously defined image scaling factor. Using this optimized kernel, the measured pixel value $P_m(i,j)$ at a point (x_i,y_j) in the scintillator plane can be written as:

$$P_m(i,j) = P_r(i,j) \otimes h(i,j) \tag{3.5}$$

where $P_r(i,j)$ is the real value and $\otimes$ denotes convolution. Fitting of the point spread function was carried out using an unconstrained nonlinear optimization in MATLAB. This optimization made use of a simplex search method [103] to minimize a cost function defined as the summed dose difference between $P_r(i,j)$ and a dose distribution from a clinical treatment planning system (Eclipse v.7.1.31, Varian Medical Systems Inc., USA), P_{calc}, for a standard 10 cm × 10 cm field at a depth of 3 cm and a source-to-axis distance (SAD) of 100 cm:

$$costfunction = \sum_i \sum_j \left| P_{calc}(i,j) - P_r(i,j) \right| \tag{3.6}$$

where $P_r(i,j)$ is calculated using a Wiener filter fast Fourier transform (FFT). The treatment beam used to deliver the above optimization field as well as all other fields in

this study was a 6 MV photon beam from a Varian CL21EX linear accelerator (Varian Medical Systems Inc., USA).

The point spread function determined using this optimization fitting method was found to be a double elliptical Gaussian:

$$h(i,j) = 0.534\frac{e^{-\frac{1}{2}\left(\frac{x_i^2}{3.8^2}+\frac{y_j^2}{3.2^2}\right)}}{1625.5} + 0.466\frac{e^{-\frac{1}{2}\left(\frac{x_i^2}{0.03^2}+\frac{y_j^2}{0.008^2}\right)}}{1.4502} \tag{3.7}$$

where the denominators are normalization factors as represented by the summations in equation 3.3. The x- and y-components of this point spread function are displayed in Figure 3.23 as profiles through the center of the kernel. As expected, this point spread function is asymmetric in the x- and y-directions with the spread of optical photons being dominant in the x-direction (the direction not collimated by the micro-louvre film). Based on this spread function, the effect of blurring can be removed using the proposed deconvolution method.

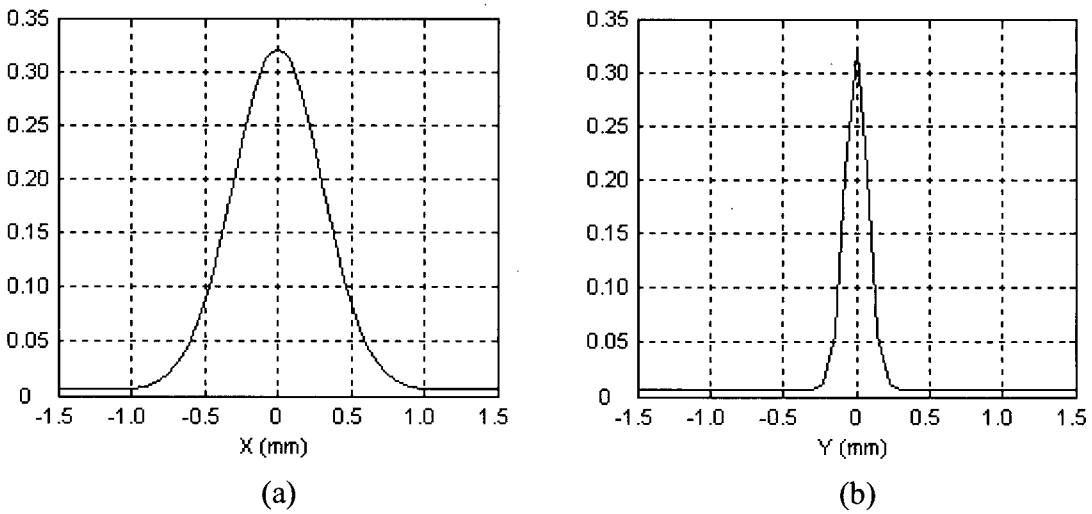

Figure 3.23: Central profiles through optimized blurring kernel described in equation 3.7 in the x-direction (a) and the y-direction (b).

Results from the deconvolution of the optimized blurring kernel from a sample 2 cm × 2 cm square field are displayed in Figure 3.24. The optical blurring as light propagates through the system is apparent in profiles through the original, blurred image in both the x- and y-directions. This blurring is notably reduced in the profiles through the deblurred image. The profiles through the expected distribution as calculated using

the Eclipse treatment planning system are also displayed in Figure 3.24. While comparison of the deblurred and treatment planning system profiles indicate an obvious improvement in the distribution following deconvolution of the optimized blurring kernel, residual discrepancies are apparent in the penumbral shape with the deblurred data having a slightly sharper fall off compared to the treatment planning system data.

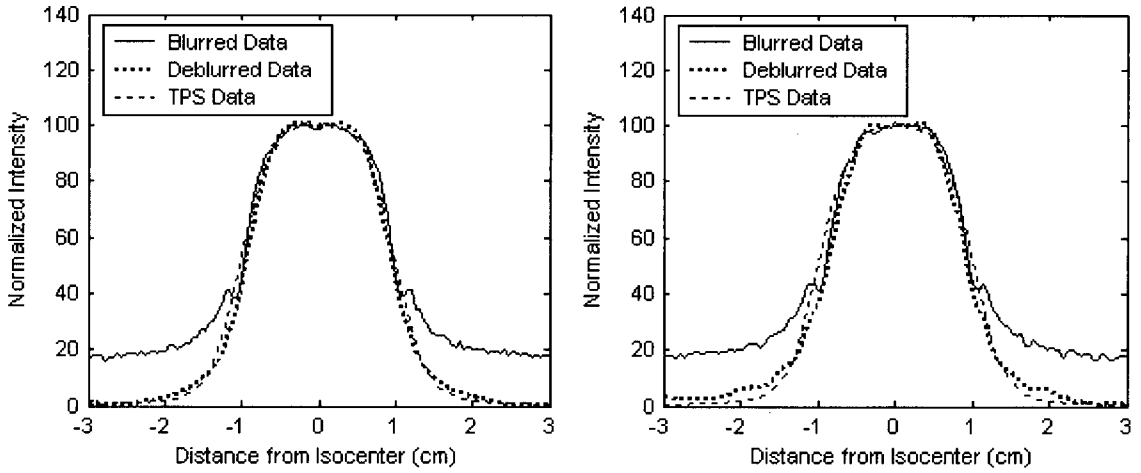

Figure 3.24: Profiles across original, blurred distribution, de-blurred distribution, and treatment planning system (TPS) calculated distribution for a 2 cm × 2 cm square field showing effects of deconvolution of optimized kernel in the x-direction (a) and the y-direction (b).

3.3.5 Flood Field Correction

Following de-blurring, a flood field correction is applied to the image to correct for any intrinsic response inhomogeneities in the scintillating sheet and the CCD camera. This correction was carried out by acquiring an image of a uniform x-ray "flood field". This flood field was delivered using a field size of 25 cm × 25 cm at a depth of 10 cm and an SAD of 100 cm. The flood field image underwent background subtraction and de-blurring as well as modification to account for the known off-axis ratio for a 25 cm × 25 cm open field. This image was then normalized to a small, square 1 cm × 1 cm ROI centered at isocenter.

3.3.6 Light Intensity to Dose Conversion

Converting the light intensity information to dose is accomplished by delivering known radiation doses to the system and observing the signal emitted to determine a light intensity/dose calibration curve. With the scintillation screen oriented orthogonal to the beam at a depth of 3 cm, an SAD of 100 cm a range of MUs from 1 MU to 200 MU were delivered using square, 5 cm × 5 cm fields. Following image processing, the mean signal in a square 1 cm × 1 cm ROI surrounding the isocenter was calculated for each field and plotted against the corresponding dose delivered. The calibration data was fit to a linear function which was used to convert the light intensity distribution map into a dose distribution map. A typical calibration curve used to convert the light intensity distributions to dose is displayed in Figure 3.25.

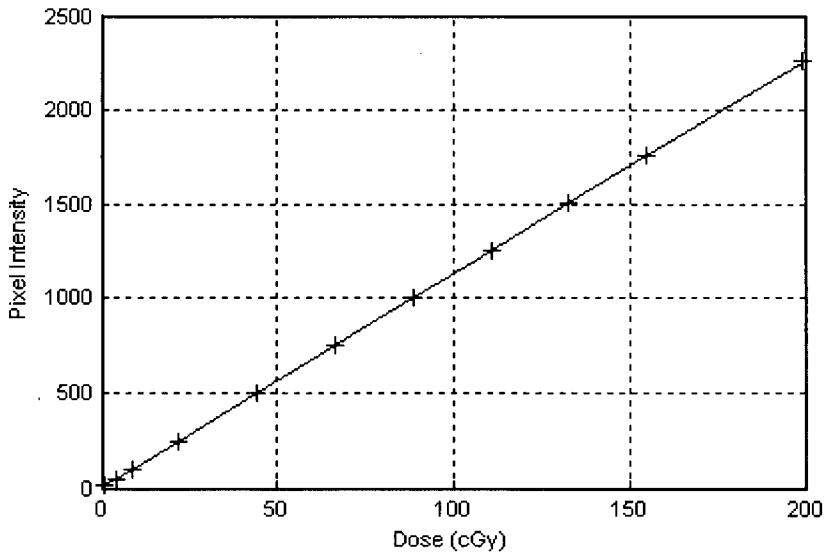

Figure 3.25: A typical light intensity / dose calibration curve used for final conversion of light intensity value to dose.

Chapter 4

SYSTEM CHARACTERIZATION AND TESTING

Once system setup and optimization were complete, the prototype verification system was subject to a number of system characterization tests. These tests included determining the system's dose linearity, dose rate dependence, short-term reproducibility, spatial linearity, effective pixel size, Čerenkov signal contribution, signal uniformity and long-term stability. Following these characterization tests, the system's ability to verify simple static and dynamic treatment fields was evaluated. Results from this study were presented at two scientific conferences [104, 105] and published in the journal Medical Physics [106].

4.1 Method and Materials

All system characterization and testing was performed using a 6 MV photon beam from a Varian CL21EX clinical linear accelerator (Varian Medical Systems Inc., USA). With the exception of the dose rate dependence measurements, all tests were conducted using a repetition rate of 600 MU/minute. The rationale for using this repetition rate is discussed in section 4.3.

4.1.1 Dose Linearity

Dose linearity of the system was examined by constructing dose response curves for a range of different field sizes and monitor units. All measurements were taken at a depth of 3 cm and an SAD of 100 cm. Measurements were acquired for both square and rectangular field sizes ranging from 3 cm × 3 cm to 12 cm × 12 cm and MU ranging from 5 MU to 200 MU. Following image processing, the mean signal in a small, square 1 cm × 1 cm region-of-interest surrounding the isocenter was calculated for each radiation field (Figure 4.1). This average signal was then plotted against the corresponding dose delivered as determined using clinical linear accelerator beam data.

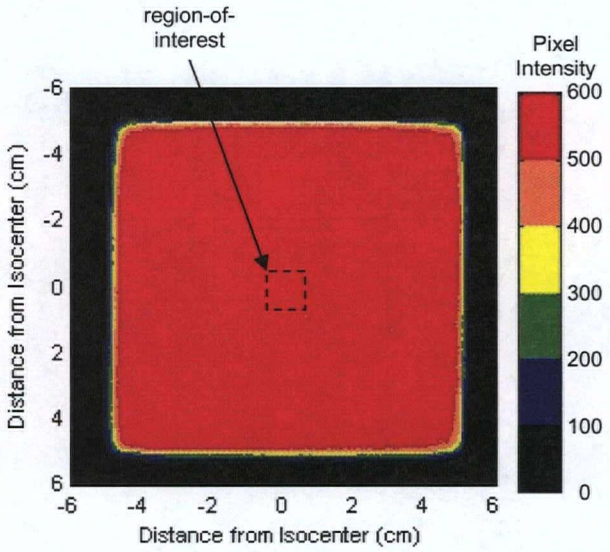

Figure 4.1: Sample square 10 cm ×10 cm field illustrating positioning of 1 cm × 1 cm square region-of-interest centered around isocenter.

4.1.2 Dose Rate Dependence and Short-Term Reproducibility

Dose rate dependence and short-term reproducibility were tested using the same depth and SAD setup as the dose linearity measurements. With a field size of 10 cm × 10 cm, 50 MU were delivered ten times to the system using pulse repetition rates varying from 100 MU/minute to 600 MU/minute. Following image processing, the mean signal in the same 1 cm × 1 cm ROI surrounding the isocenter was calculated for each repetition rate to determine the dose rate response. Short-term reproducibility of the system was determined by observing the variation between the mean signal for different trials at the same dose rate.

4.1.3 Spatial Linearity and Effective Pixel Size

Spatial linearity and effective pixel size were determined using a procedure described by Ma *et al.* [107]. Square fields varying from 1 cm × 1 cm to 12 cm × 12 cm were delivered with 50 MU to the system. Field edges were located in the resultant images by finding the positions where the signal dropped to 50% of the central ROI value. A plot of the field sizes in pixels versus the field sizes in centimeters was constructed to observe spatial linearity of the system. Effective pixel size was calculated by performing a linear fit to this plot and determining the slope.

4.1.4 Čerenkov Signal Contribution

As discussed in sections 1.2.4 and 3.1.3, Čerenkov radiation is a concern in light sensitive dosimetry systems where the measurement media is transparent. In our prototype dosimetry system, possible sources of Čerenkov radiation include the plastic scintillator detection sheet, the water filling the phantom inner cavity, and the clear viewing window facing the CCD camera. To determine the contribution of Čerenkov radiation to the light signal detected by the CCD camera the plastic scintillator detection sheet was removed from the phantom and replaced by a transparent Lucite sheet of identical dimensions. Prior to installation, this piece of Lucite was prepared in the same manner as the plastic scintillator detection sheet including surface and edge sanding and edge painting. With the Lucite sheet installed, the phantom was placed in the treatment beam at an SAD of 100 cm and a depth of 3 cm and 50 MU were delivered to the system using square fields varying from 5 cm × 5 cm to 25 cm × 25 cm. To evaluate the Čerenkov signal contribution, these images were compared to images acquired using an identical setup with the scintillator sheet installed. Comparisons were made by calculating the mean signal in a small, square 1 cm × 1 cm region-of-interest surrounding the isocenter for each field size with and without the scintillation sheet present. To evaluate the dependence of the Čerenkov signal on the dose deposited at the detection plane a series of calibration measurements were also acquired with the Lucite sheet in place of the scintillation screen. Using a 5 cm × 5 cm square field, a range of MUs from 25 MU to 200 MU were delivered to the system. The signal from the central ROI of each acquisition image was then plotted against the corresponding dose delivered to isocenter.

4.1.5 Signal Uniformity and Long-Term Reproducibility

Signal uniformity of the system was characterized by calculating the traditionally defined beam uniformity for a 12 cm × 12 cm square field at 10 cm depth [108]. The distribution acquired with the new scintillator based dosimetry system was corrected to account for non-uniformity in the beam using the treatment planning system calculated distribution and dose variations over 80% of the nominal field size were determined. Long-term signal reproducibility was tested by delivering identical fields to the system and observing the differences in signal over time. Reproducibility measurements were performed 10 times over a 6 month period by delivering 200 MU using field sizes of 25 cm × 25 cm at a depth of 10

cm and an SAD of 100 cm. The mean signal intensity from the same 1 cm × 1 cm ROI surrounding the isocenter was calculated for each measurement to observe signal fluctuations over time.

4.1.6 Verification of Simple Static and Dynamic Wedged Fields

The system's ability to verify simple static fields was evaluated by delivering a set of square fields (5 cm × 5 cm and 10 cm × 10 cm) and comparing the results to 2-D film dosimetry distributions. Similarly, verification of dynamic treatment fields was evaluated by delivering two 8 cm × 8 cm, orthogonal, 60° dynamic wedged fields (Varian Enhanced Dynamic Wedge, Varian Medical Systems Inc., USA) and comparing the results to film distributions. All measurements were delivered using 200 MU at an SAD of 100 cm and a depth of 3 cm. Film dosimetry measurements were carried out using the same techniques described in section 2.1.2.1 (film was placed at a depth of 3 cm in this implementation).

Dose distributions from the new scintillator based verification system and film dosimetry were quantitatively compared using 1D dose profiles, percentage dose difference maps, and 2D gamma factor analysis. Percentage dose difference maps were calculated using absolute dose differences. The pass/fail criteria for the gamma analysis was a dose difference of 3% of the prescription dose and a distance criterion of 3 mm.

Results from the scintillator based system and film dosimetry were also compared to point-by-point measurements acquired using a miniature thimble ionization chamber for these fields. These measurements were acquired in Solid Water using the same miniature chamber described in section 2.1.1 with the same setup parameters used for the scintillator and film verifications. All ionization chamber measurements were normalized to relative doses using the same normalization points used for normalization of the film and scintillator data.

4.2 Results

4.2.1 Dose Linearity

A plot of the pixel intensity for different field sizes versus the dose delivered is displayed in Figure 4.2. The solid line in this figure represents a linear fit of the average response over all field sizes tested. The average pixel intensity is observed to increase linearly with delivered

dose with linear regression analysis yielding a correlation coefficient $r^2 > 0.99$. Inspection of Figure 4.2 indicates no apparent variation of response with field size for field sizes up to 12 cm × 12 cm with variations from the average response being well below 5% for this data.

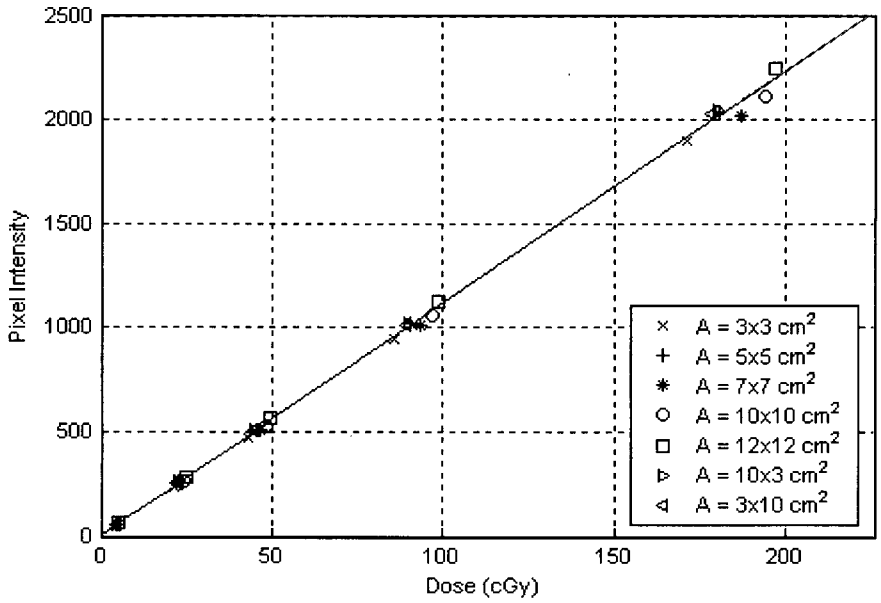

Figure 4.2: Pixel intensity of the system with respect to field size and dose delivered. The solid line represents a linear fit of the average response of all fields.

4.2.2 Dose Rate Dependence and Short-Term Reproducibility

Results from the dose rate dependence and short-term reproducibility tests are displayed in Table 4.1. Errors in this table represent standard deviations over the 10 deliveries at each dose rate. These results indicate a dose rate dependence with a maximum deviation of 19% between dose rates. The system is stable within 1.2% for dose rates of 100 MU/min, 300 MU/min, and 600 MU/min. Variation within the 10 deliveries at each dose rate was found to be small with a maximum deviation of 1.5% indicating the short-term reproducibility of the system.

Table 4.1: Dose rate dependence of verification system. Region-of-interest comprised a 1 cm × 1 cm square centered at the field isocenter. Error values indicate standard deviations over 10 trials at each dose rate.

Dose Rate (MU/minute)	ROI Average Pixel Value
100	574.6 ± 3.2
200	488.3 ± 2.5
300	581.4 ± 3.4
400	522.3 ± 4.2
500	556.6 ± 3.3
600	575.6 ± 1.8

4.2.3 Spatial Linearity and Effective Pixel Size

Results of the spatial linearity and effective pixel size tests are displayed in Figure 4.3. The linear regression analysis performed on data in both x- and y-directions yielded correlation coefficients $r^2 > 0.99$. The effective pixel size was determined from the slopes of the fitted lines. The pixel size in the x-direction was determined to be 0.52 ± 0.01 mm per pixel while the pixel size in the y-direction was determined to be 0.55 ± 0.01 mm per pixel. These values correspond very closely to the expected pixel size of 0.521 mm per pixel as calculated by dividing the size of the scintillation screen (150 mm) by the number of pixels used during image acquisition (288 pixels).

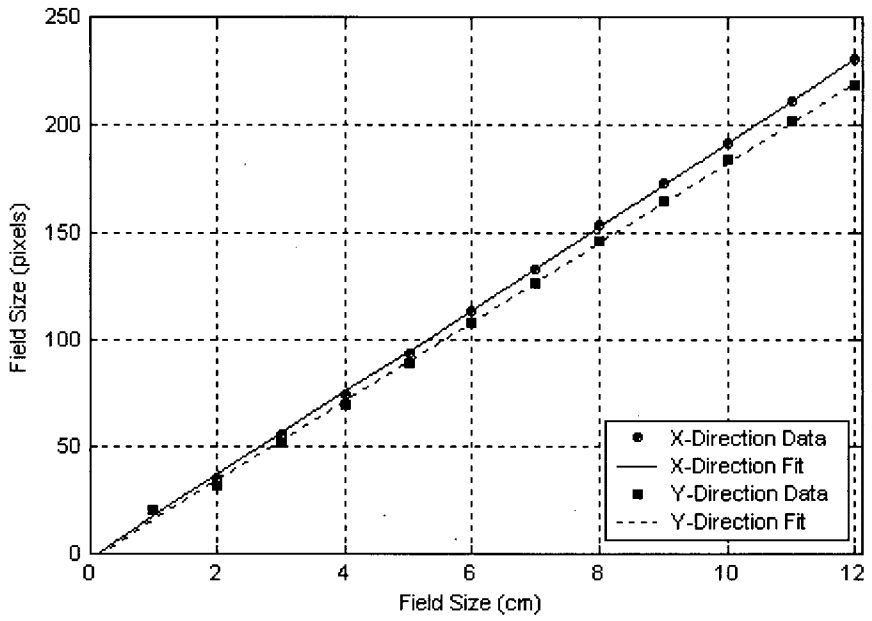

Figure 4.3: Acquired image field size in pixels with respect to physical field size in centimeters as shaped by the collimator jaws. Data is shown for both the x-direction and the y-direction.

4.2.4 Čerenkov Signal Contribution

Images acquired using the phantom with the scintillation sheet replaced with a Lucite sheet are displayed in Figure 4.4 for square fields of 10 cm × 10 cm and 25 cm × 25 cm. The image from the 10 cm × 10 cm field in Figure 4.4(a) shows a widening of the beam towards the bottom of the image. Also apparent in both images is an obvious intensity gradient present from top to bottom (i.e. in the y-direction). Quantification of this gradient was accomplished by determining the average pixel intensities in two square 1 cm × 1 cm regions-of-interest at the top and bottom of the image. These ROIs, along with the central ROI used to quantify the overall Čerenkov contribution, are displayed in Figure 4.4(b). Results from this ROI analysis are displayed in Table 4.2.

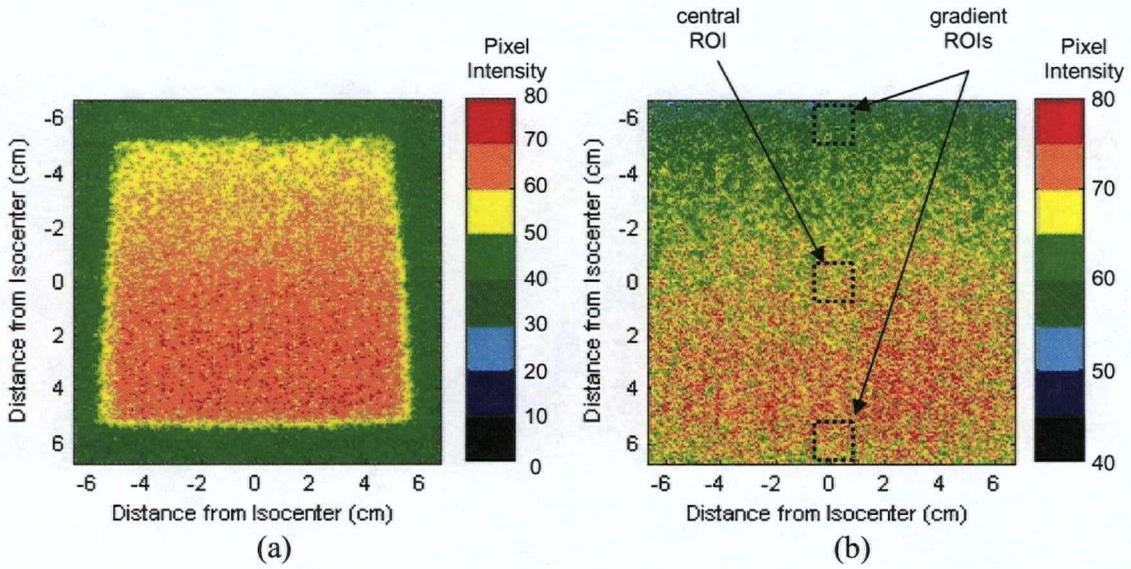

Figure 4.4: Čerenkov signal contribution images for (a) 10 cm × 10 cm square field and (b) 25 cm × 25 cm square field acquired using phantom with scintillation detector sheet replaced with Lucite sheet. The central region-of-interest as well as the gradient regions-of-interest used for analysis of the Čerenkov contribution are also shown in (b).

Table 4.2: Region-of-interest analysis for 25 cm × 25 cm square field. Percent Čerenkov contribution has been calculated using total signal intensity as measured using central ROI of image acquired with scintillator detection sheet in place (value = 591.22).

Region-of-Interest	**Čerenkov Signal Intensity**	**Percent Čerenkov Contribution (%)**
Top	58.08	9.8
Central	68.54	11.6
Bottom	69.75	11.8

This table indicates a 2.0% variation in Čerenkov signal from image bottom to top. Results showing the contribution from Čerenkov radiation for various sized square fields are displayed in Table 4.3. This analysis made use of central regions-of-interest similar to that shown in Figure 4.4(b). The maximum contribution from Čerenkov signal for all field sizes was found to be 11.8%.

Table 4.3: Contribution of Čerenkov signal to total light signal for square fields ranging in size from 5 cm × 5 cm to 25 cm × 25 cm.

Field Size	Čerenkov Signal Intensity	Total Signal Intensity	Percent Čerenkov Contribution (%)
5 cm × 5 cm	59.77	510.31	11.7
8 cm × 8 cm	62.10	525.77	11.8
10 cm × 10 cm	63.56	549.95	11.6
25 cm × 25 cm	68.54	591.22	11.6

Results showing the dependence of the Čerenkov signal on the dose deposited at the detection plane are displayed in Figure 4.5. The solid line in this figure represents a linear fit of the response. The Čerenkov signal is observed to increase linearly with delivered dose with linear regression analysis yielding a correlation coefficient $r^2 > 0.99$.

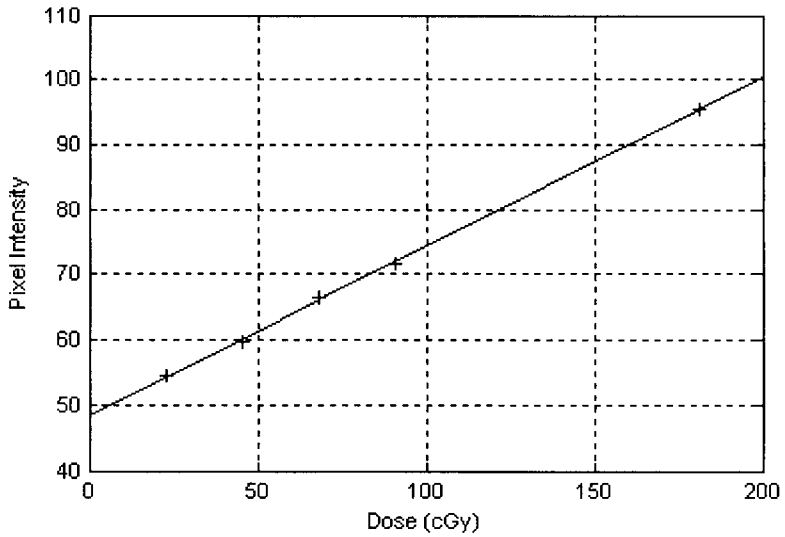

Figure 4.5: Dependence of Čerenkov signal on the dose deposited at the detection plane. All measurements were acquired using a 5 cm × 5 cm square field. The solid line represents a linear fit of the data.

4.2.5 Signal Uniformity and Long-Term Reproducibility

Beam uniformity over 80% of the nominal field size was found to be 7.8% for the distribution acquired using the scintillator based system. No systematic variation in uniformity was observed across the uniformity distribution.

Long-term signal reproducibility data is displayed in Figure 4.6. This data has been normalized to give an average observed response over the testing period equal to unity. Over the 180 day period the system was observed to be stable within 1.7% with no noticeable systematic fluctuations. The standard deviation over all points was found to be less than 1%.

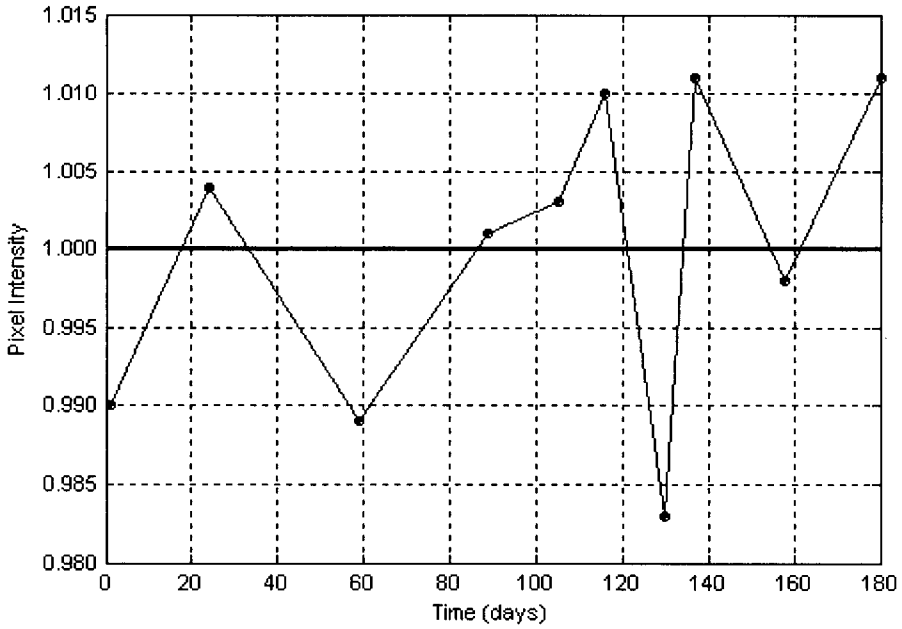

Figure 4.6: Average region-of-interest pixel intensity as a function of time. Data has been normalized such that the average observed response over the 180 day period is equal to unity.

4.2.6 Verification of Simple Static and Dynamic Wedged Fields

4.2.6.1 Simple Static Square Fields

Relative dose distribution maps from film dosimetry and the scintillator based system for the 5 cm × 5 cm and the 10 cm × 10 cm simple static fields are displayed in Figure 4.7. One difference between the film distributions and the distributions acquired using the scintillator system is the increased amount of noise in the scintillator distributions. This noise is manifest by the jagged shape of the isodose levels near the edge of the field.

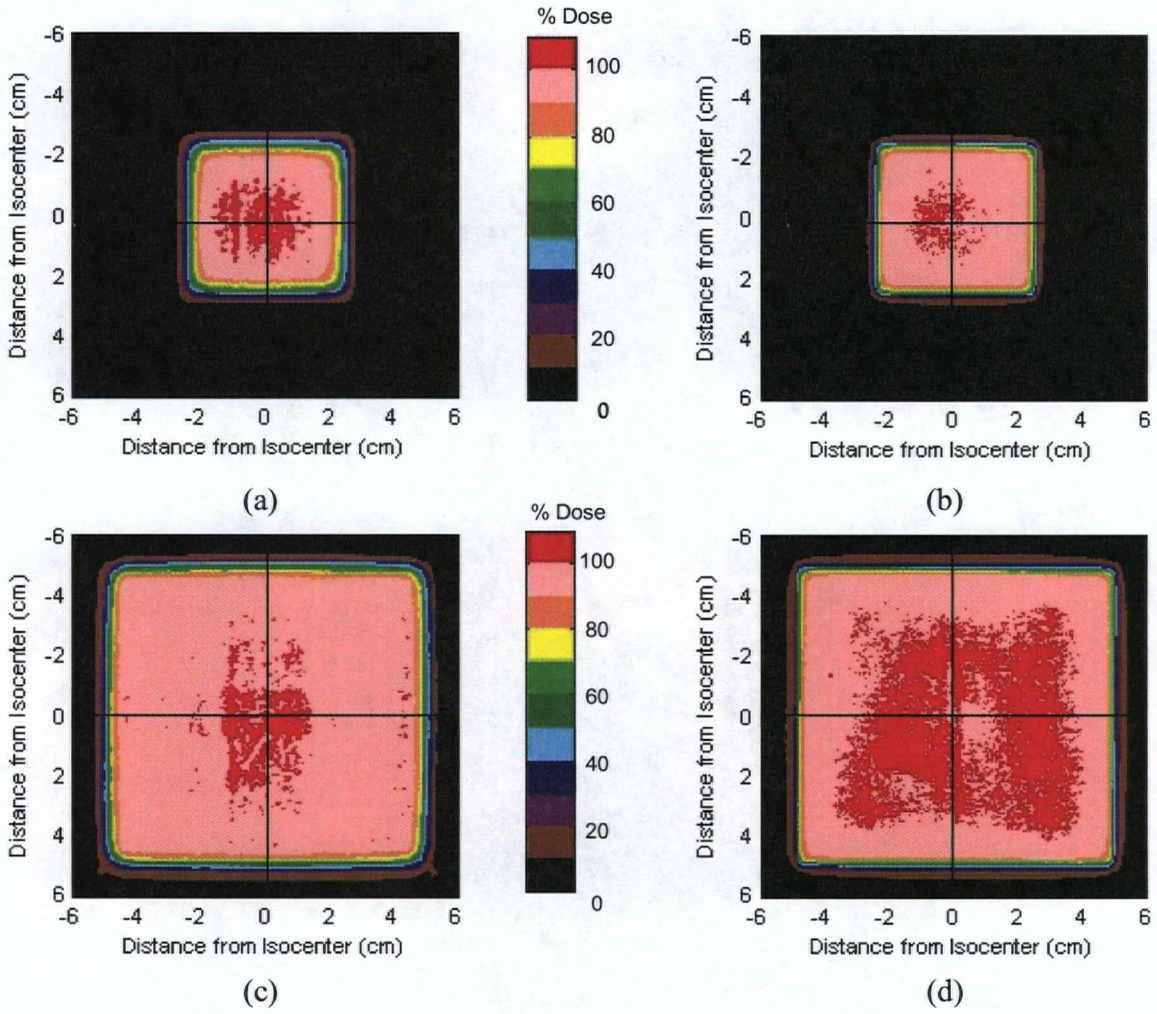

Figure 4.7: Relative dose distributions for simple static fields. Results are shown for the 5 cm × 5 cm square field measured using (a) scintillator based verification system and (b) 2-D film dosimetry and for the 10 cm × 10 cm square field measured using (c) scintillator based verification system and (d) 2-D film dosimetry. Crosshairs indicate positions of 1-D profiles shown in Figure 4.8.

To more quantitatively compare the distributions, profiles were taken along the black crosshairs shown in Figure 4.7. These profiles in both the x- and y-directions are displayed in Figure 4.8. The increased noise observed throughout the scintillator based distributions is clearly apparent in the profiles across the 10 cm × 10 cm square field. Discrepancies between the distributions are also observed in the shape of the penumbra in the profiles. For both field sizes displayed, the film data has a sharper fall off compared to the scintillator data

in both the x- and y-directions. This discrepancy appears to be more intense for the smaller 5 cm × 5 cm square field compared to the larger 10 cm × 10 cm square field.

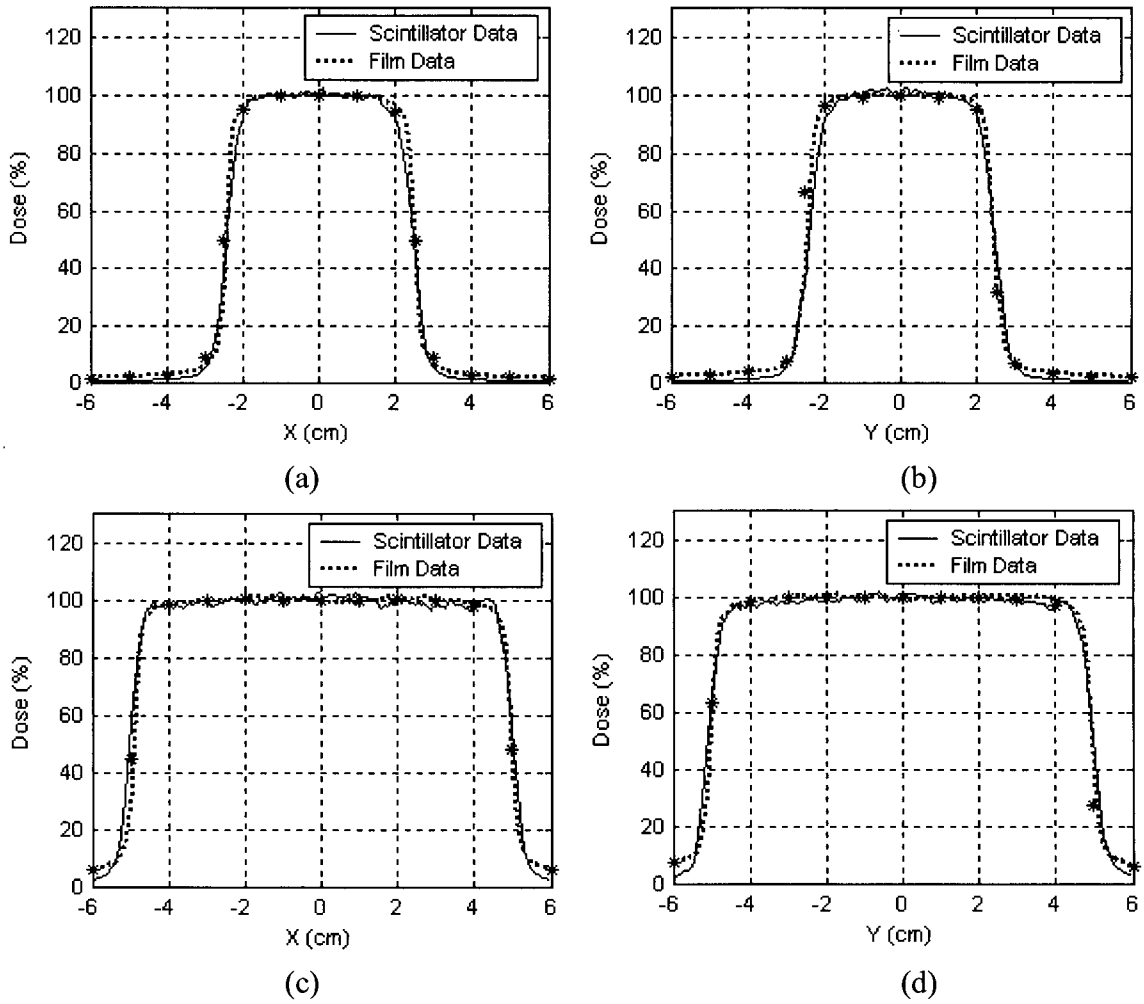

Figure 4.8: Profiles across measured relative dose distributions for both scintillator based verification system and film dosimetry for 5 cm × 5 cm square field in (a) x-direction and (b) y-direction and for 10 cm × 10 cm square field in (c) x-direction and (d) y-direction. Point ionization chamber measurements are illustrated with asterisks.

Also shown in Figure 4.8 are the ionization chamber point dosimetry measurements performed on these fields. For both of these fields, the film data is in closer agreement with the ionization chamber measurements inside the field edges. Outside the field edges film is observed to slightly overestimate the dose compared to ionization chamber measurements while the scintillator based system underestimates the dose in this low-dose region.

Percent dose difference and gamma factor maps comparing the scintillator and film measured distributions are displayed in Figure 4.9 for both the 5 cm × 5 cm and the 10 cm × 10 cm square fields.

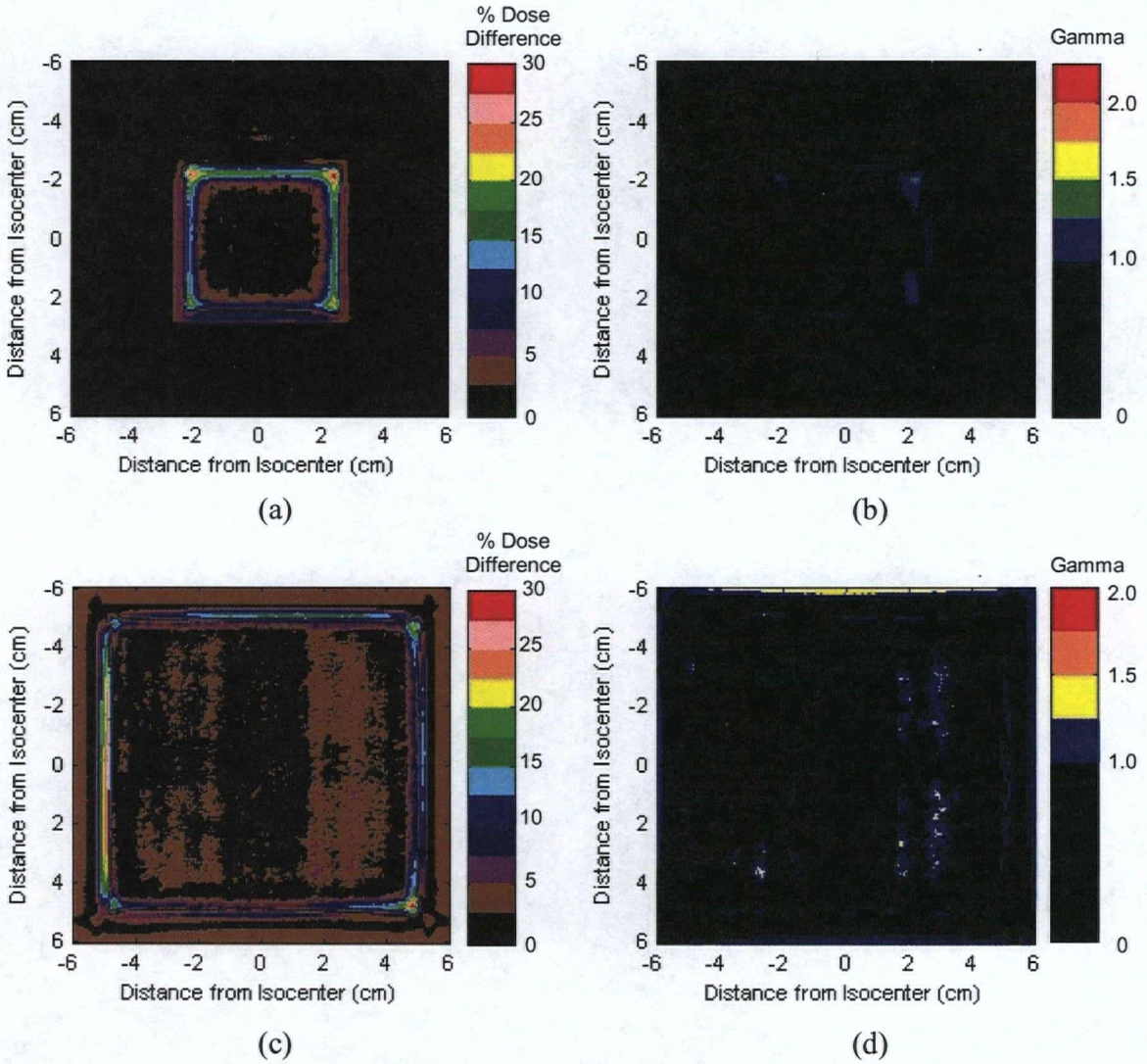

Figure 4.9: Percent dose difference and gamma factor maps for simple static field data acquired using scintillator verification system and 2-D film dosimetry. The 5 cm × 5 cm square field percent dose difference map is shown in (a) while the gamma factor map for this field is shown in (b). The 10 cm × 10 cm square field percent dose difference map is shown in (c) while the gamma factor map for this field is shown in (d).

Percent dose difference maps for both field sizes show dose agreement within 5% over the majority of the field inside the field edges. As expected, dose difference values increase

dramatically as the field edges are approached. Gamma factor maps for both field sizes indicate acceptable agreement over the majority of the distributions. Results from the percent dose difference and gamma factor maps for the simple static fields are summarized in Table 4.4. To take into account the potentially misleading high percent dose difference values close to the field edge, this table displays percent dose difference statistics over 80% of the nominal field size. Gamma factor statistics are given over a region encompassing the nominal field size plus 20%. This region was selected to avoid skewing of the gamma factor statistics that was found to occur when regions far outside the field edges of the gamma factor maps were used for statistical analysis. In these low dose regions, inadequate coverage by the film calibration curve can result in artificially inflated gamma factor values as is indicated in the overestimation of dose compared to ionization chamber measurements.

Table 4.4: Summary of percent dose difference and gamma factor maps for simple square fields.

Field Size	Percent Dose Difference Map (over 80% of nominal field size)			Gamma Factor Map (over nominal field size +20%)		
	Average	Std. Dev.	Max.	Average	Std. Dev.	Max.
5 cm × 5 cm	0.95 %	0.84 %	7.72 %	0.40	0.28	1.84
10 cm × 10 cm	1.02 %	0.98 %	6.59 %	0.41	0.27	1.94

4.2.6.2 Dynamic Wedged Fields

Relative dose distribution maps from film dosimetry and the scintillator based system for the wedged field in the y-direction are displayed in Figure 4.10. Once again there is an increased amount of noise apparent in the scintillator based distribution which is manifest by the jagged shape of the isodose levels. This effect is more clearly observed in the wedged fields compared to the simple square fields as a result of the isodose levels being further spaced apart across the wedged fields. Another variation between the film and scintillator wedged distributions in Figure 4.10 are the small horns which are observable in the scintillator data on both sides of isocenter as the edges of the isodose levels are approached. These horns are not observed in the film distribution.

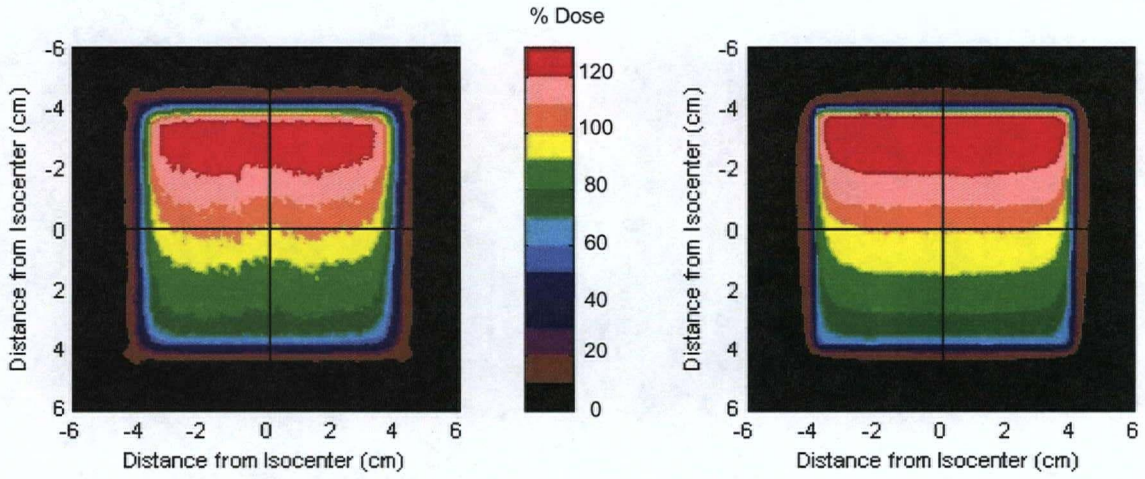

Figure 4.10: Relative dose distributions for a wedged field in the y-direction measured using (a) scintillator based verification system and (b) 2-D film dosimetry. Crosshairs indicate positions of 1-D profiles shown in Figure 4.11.

To more quantitatively compare the distributions, profiles were taken along the black crosshairs shown in Figure 4.10. These profiles in both the x- and y-directions are displayed in Figure 4.11. The off-axis horns observed in Figure 4.10 are observable in the profile in the x-direction in Figure 4.11(a). These horns cause a slight overestimation of the dose on either side of isocenter by approximately 3% with the maximum variation for this profile being 4.2%. In the y-direction, the scintillator data underestimates the dose by approximately 4% over large regions of the profile in Figure 4.11(b) with a maximum deviation of 6.1% inside the field edges. Again, discrepancies are also observed in the shape of the penumbra in the profiles with the film data having a sharper fall off compared to the scintillator data in both the x- and y-directions. Also shown in Figure 4.11 are the ionization chamber point dosimetry measurements performed on this field. Once again, the film data is observed to be in closer agreement with the ionization chamber measurements inside the field edges with a maximum deviation of 2.8%. Outside the field edges film is again observed to overestimate the dose compared to ionization chamber measurements while the scintillator based system underestimates the dose.

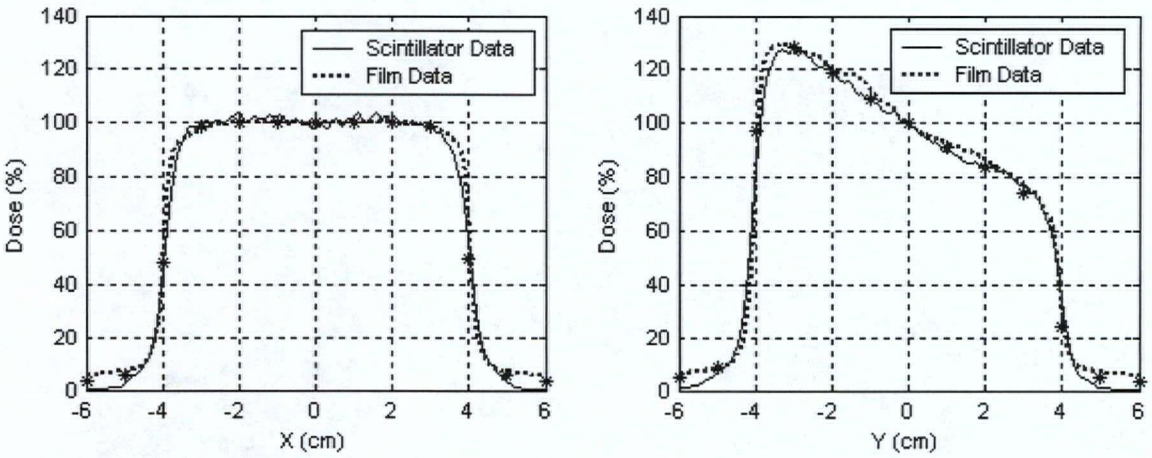

Figure 4.11: Profiles across measured relative dose distributions for wedged field in y-direction for both scintillator based verification system and film dosimetry in (a) x-direction and (b) y-direction. Point ionization chamber measurements are illustrated with asterisks.

Relative dose distribution maps from film dosimetry and the scintillator based system for the wedged field in the x-direction are displayed in Figure 4.12. No horns are immediately apparent in the scintillator distribution for the wedged field in the x-direction.

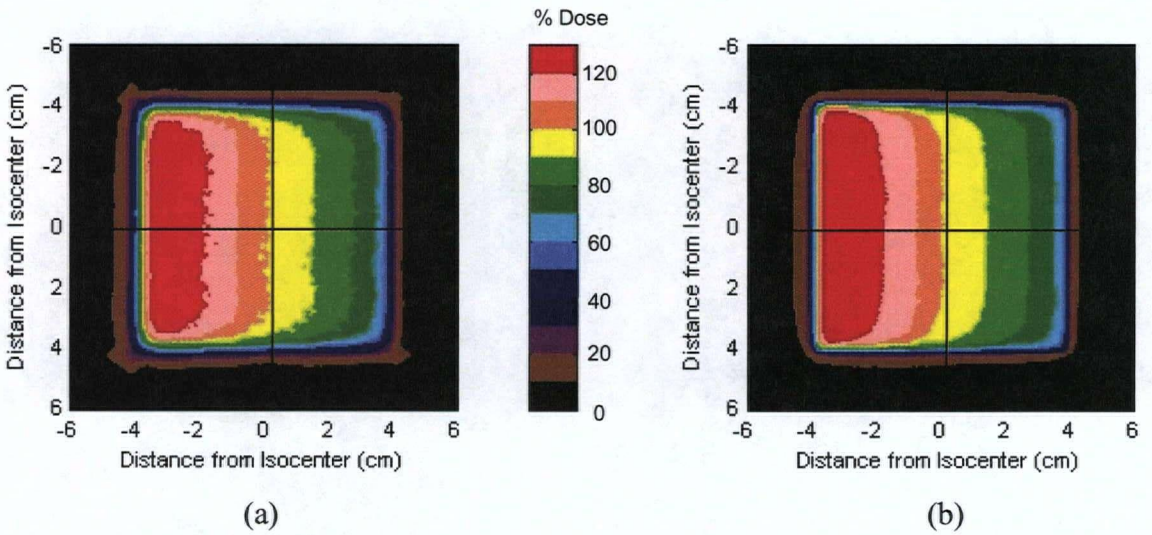

Figure 4.12: Relative dose distributions for a wedged field in the x-direction measured using (a) scintillator based verification system and (b) 2-D film dosimetry. Crosshairs indicate positions of 1-D profiles shown in Figure 4.13.

Profiles in the x- and y-directions through these wedged field distributions are displayed in Figure 4.13. The average dose agreement within the field edges is 1.6% with a maximum deviation of 3.3% in the x-direction and 2.5% with a maximum deviation of 4.3% in the y-direction. Discrepancies in the penumbra region of the distributions are also observed in the profiles in Figure 4.13. Once again, the film data profiles have a slightly sharper fall off compared to the scintillator data profiles in both directions. Ionization chamber point dosimetry measurements in Figure 4.13 again show the film data to be in closer agreement with the ionization chamber measurements inside the field edges with a maximum deviation of 2.6%. Outside the field edges film is observed to overestimate the dose while the scintillator based system underestimates the dose.

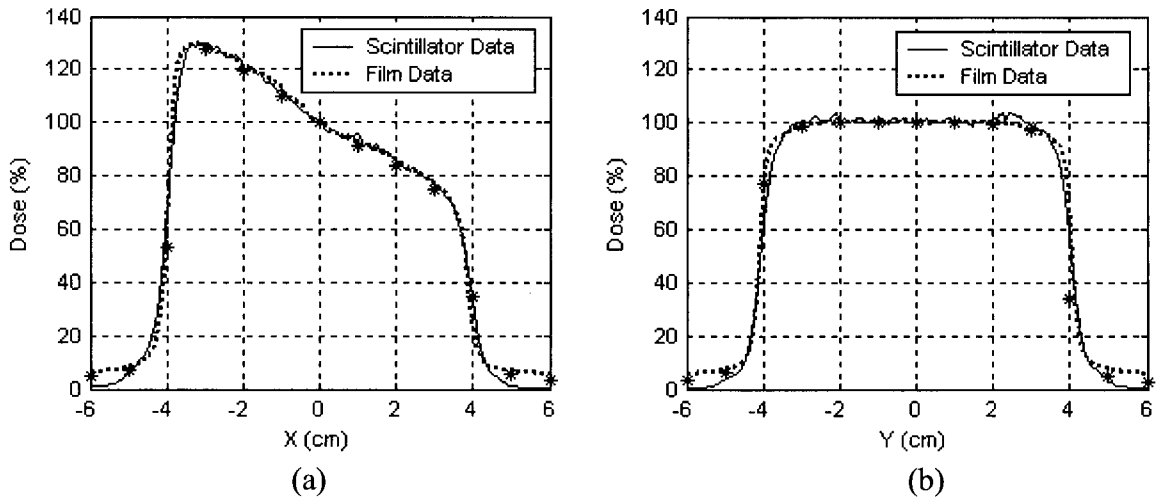

Figure 4.13: Profiles across measured relative dose distributions for wedged field in x-direction for both scintillator based verification system and film dosimetry in (a) x-direction and (b) y-direction. Point ionization chamber measurements are illustrated with asterisks.

Percent dose difference and gamma factor maps comparing the scintillator and film measured distributions are displayed in Figure 4.14 for the dynamic wedged fields in both the y- (Figure 4.14(a) and (b)) and x-directions (Figure 4.14(c) and (d)). Once again, percent dose difference maps for both field sizes show dose agreement within 5% over the majority of the field inside the field edges with dose difference values increasing as the field edges are approached. Gamma factor maps for both field sizes indicate acceptable agreement over the majority of the distributions.

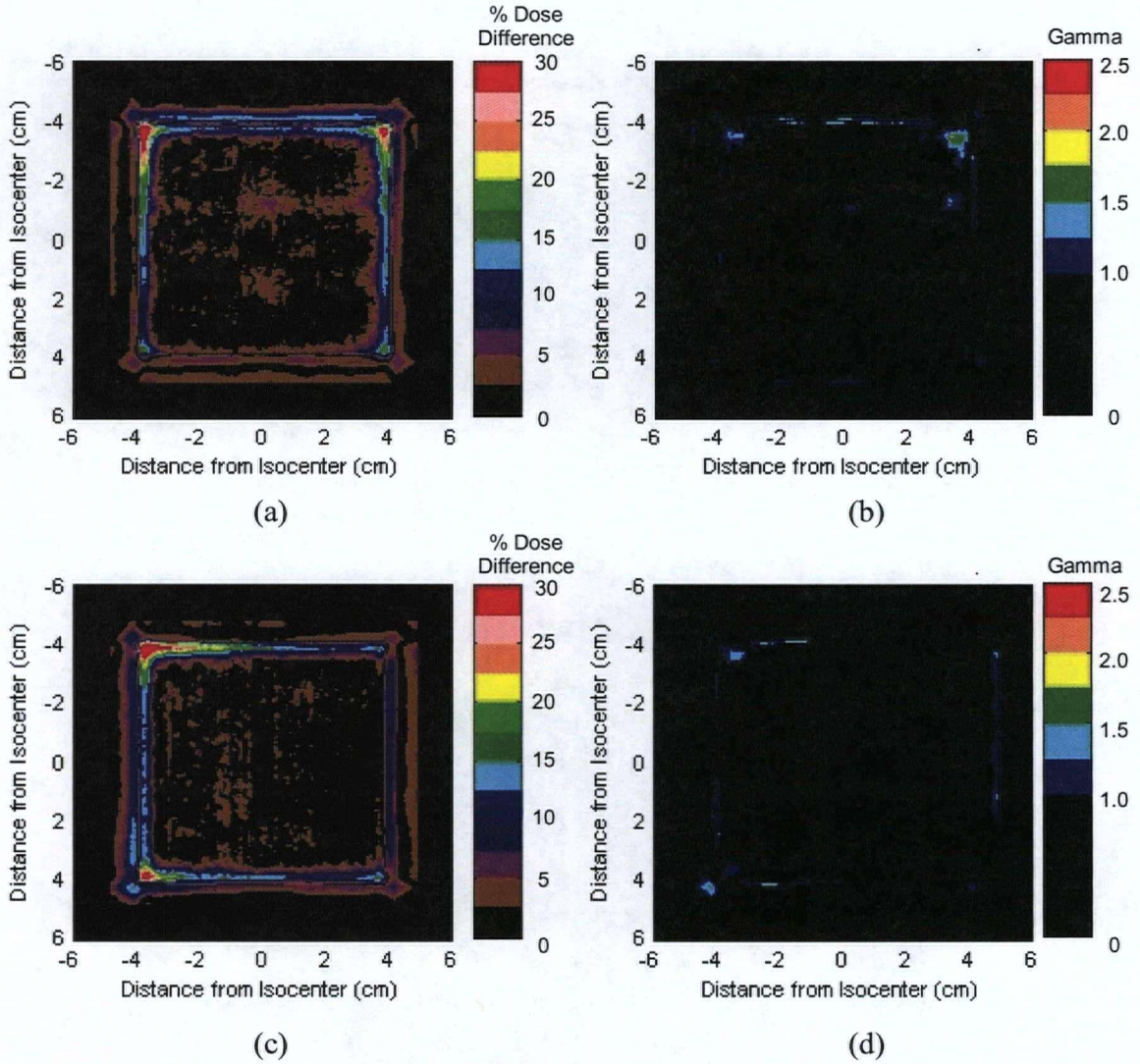

Figure 4.14: Percent dose difference and gamma factor maps for dynamic wedged field data acquired using scintillator verification system and 2-D film dosimetry. The percent dose difference map for the wedged field in the y-direction is shown in (a) while the gamma factor map for this field is shown in (b). The percent dose difference map for the wedged field in the x-direction is shown in (c) while the gamma factor map for this field is shown in (d).

Results from the percent dose difference and gamma factor maps for both wedges are summarized in Table 4.5. Once again, percent dose difference statistics have been calculated over 80% of the nominal field size and gamma factor statistics are given over a region encompassing the nominal field size plus 20%.

Table 4.5: Summary of percent dose difference and gamma factor maps for wedges in the x- and y-directions.

Wedge Direction	Percent Dose Difference Map (over 80% of nominal field size)			Gamma Factor Map (over nominal field size +20%)		
	Average	Std. Dev.	Max.	Average	Std. Dev.	Max.
X-Direction	1.53 %	1.18 %	7.24 %	0.38	0.25	1.82
Y-Direction	1.26 %	0.97 %	7.71 %	0.35	0.24	1.58

4.3 Discussion

4.3.1 Dose Linearity

System characterization results from the prototype system demonstrate the considerable potential of the system. The average pixel intensity was found to increase linearly with delivered dose. The dose response linearity of tissue equivalent organic plastic scintillators has been well documented in previous studies using small volume scintillator detectors read with photo-multiplier tubes [109]. An important consideration for the optical setup utilized in this system is the effect of field size on the system response. Previous investigations of quality assurance using camera based portal imaging systems that make use of similar optical configurations have reported a systematic field size dependence on system response [107, 110, 111]. In a study by Heijmen *et al.* it was determined that this dependence is a direct consequence of the scattering of optical photons as they propagate from the detection screen to the capture camera [110]. This study also showed that the deconvolution of a experimentally determined glare kernel from acquired images virtually eliminated this field size dependence. Our data shows minimal variation of response with field size with variations from the average response being well below 5% thus indicating the overall success of the point spread function used in the deconvolution of the optical glare.

4.3.2 Dose Rate Dependence and Short-Term Reproducibility

A dose rate dependence was observed in the system over a range from 100 MU/minute to 600 MU/minute. This type of dose rate dependence has been previously reported for other quality assurance systems using similar optical setups and frame capture cameras as the result of aliasing of the camera frame rate with the non-periodic pulsed radiation delivery rate

and can complicate attempts at dosimetry specifically when the dose rate is actively changing during beam delivery [111, 112]. Varying dose rates often occur in IMRT beam delivery due to the necessity to allow the MLC leaves to travel to their next designated segment position before delivering the dose for that segment. Signal stability within each dose rate was found to range from 0.3% to 0.8%. This is an expected result since the dose rate for static fields is stable throughout beam delivery. An investigation by Zeidan *et al.*, using a Varian linear accelerator similar to the unit used in this study and a camera based portal imaging device, found the most stable dose rate (with the least aliasing effects) to be 600 MU/minute [111]. This result is in agreement with the intra-dose rate variations observed in Table 4.1 with the 600 MU/minute dose rate having the lowest standard deviation over the 10 trials. Taking these results into consideration, dose rate effects on further dosimetric results were minimized through a two step process. Firstly, all fields were delivered using a dose rate of 600 MU/minute. Secondly, all dynamic field MU values were increased to ensure no dose rate variation during beam delivery. Although the use of a high dose rate (typically IMRT plans at our center are treated at a dose rate of 300 MU/minute) and increased MUs is not ideal for verification of clinical treatment plans where preferably the treatment is verified exactly as it will be carried out on the patient, these modifications not only increased stability of the measurements but were also found to minimize the number of capture frames to be analyzed thus reducing processing time. It should be noted that the dose rate dependence of this system is not an issue for segmental, step-and-shoot delivery techniques where the dose rate is constant for each segment of the delivery. Furthermore, any dose rate effects observed during verification of dynamic delivery techniques could be readily eliminated through the use of a high-speed, integrating camera triggered by the linear accelerator sync signal. By synchronizing image capture with the accelerator's pulsed delivery and integrating the emitted light over the entire delivery, the aliasing effect of the current frame-capture camera would be removed completely. Plans for a next generation prototype of this system including the use of such an image capture setup are discussed further in section 6.2.

4.3.3 Spatial Linearity and Effective Pixel Size

The overall effective pixel size of the system was found to be 0.53 mm per pixel. This is almost a factor of two smaller than the dose grid spacing used in typical, high resolution

calculations by treatment planning systems. The slightly higher effective pixel size in the x-direction is an expected result due to the rectangular pixels of the CCD element used in the camera. This small difference in effective pixel size in the x- and y-directions was accounted for by rescaling the measured distributions prior to comparing then to film and the treatment planning system distributions.

4.3.4 Čerenkov Signal Contribution

Analysis of the Čerenkov signal contribution indicated high levels of Čerenkov light in the signal detected by the CCD camera in our scintillator dosimetry system with an average percent Čerenkov signal contribution over all field sizes of 11.7%. This amount of Čerenkov contamination is high compared to measurements of Čerenkov contamination acquired using small volume plastic scintillator detectors. In a study by Beddar *et al.* [109], the Čerenkov contribution was found to be less than 3% of the light emitted using a cylindrical plastic scintillator detection volume with a diameter of 1 mm and a length of 4 mm irradiated with a 10 MV photon beam. The increased Čerenkov contamination measured in our system is due to the volume of water being irradiated below the scintillation detection sheet. The average depth of water being traversed by the photon beam in our system is approximately 8 cm (at the center of the detection sheet). Fortunately, from equation 1.9, it is apparent that the intensity of Čerenkov radiation emission is proportional to $\left(1-\frac{1}{n^2\beta^2}\right)$ thus indicating a decrease in Čerenkov radiation for media with smaller index of refraction, n. Given the index of refraction of water (n = 1.33) and that of the plastic scintillator used in our system (n = 1.58) and assuming $\beta = 0.8$ for the 6 MV photon beam, the Čerenkov radiation from the water is approximately 3.21 times less intense than the Čerenkov radiation from the scintillation sheet.

Although correction or minimization of Čerenkov radiation is a major concern for small volume scintillation detection systems [113-117], it can be neglected in our 2-dimensional dosimetry system for several reasons. Firstly, the investigation into the dependence of the Čerenkov signal on the dose deposited at the detection plane revealed a linear response as illustrated by the linear fit in Figure 4.5. The linearity of this response indicates the suitability of the Čerenkov radiation for dosimetric purposes. Secondly, our

dosimetry system has been developed such that the angle between the incident radiation field and the detection phantom is fixed (i.e. the radiation beam is always incident on the phantom from the same direction). The dependence of Čerenkov radiation on the angle of the incident high energy radiation (as described in section 1.2.4) is a major concern for small volume scintillator detection systems where the orientation between the detector and the radiation beam can vary widely [114]. Thirdly, the data in Table 4.2 indicates only a 2% variation in the Čerenkov contribution across the 25 cm × 25 cm square field in the y-direction. This variation is a result of the varying depth of water being traversed by the radiation beam before it encounters the Lucite mirror. At the top of the field where the mirror is very close to the detection sheet, very little water is being traversed and the Čerenkov contribution is lower. The contribution is highest at the bottom of the field where the maximum depth of water is being traversed. This small variation across the detection field is corrected for when the flood field correction is applied to the images.

One aspect of the Čerenkov contamination that may adversely affect the dosimetric results of this system is the effect of beam divergence on the Čerenkov signal. Beam divergence is the cause of the widening of the field towards the bottom of the image in Figure 4.4(a). Although this effect has the potential to cause widening of the Čerenkov field size by up to 16% for field sizes approaching the edges of the detection sheet (divergence between SAD = 100 cm and SAD 116 cm), it should be noted that as the beam diverges into the phantom, the depth of water producing Čerenkov radiation decreases thus lowering the signal contribution.

4.3.5 Signal Uniformity and Long-Term Reproducibility

Long-term reproducibility tests indicate that the system is stable within 1.7% over a 6 month period. This result is consistent with previous studies on plastic scintillators which have should them to be relatively insensitive to radiation damage with decreases in detector output of less than 3% for a total accumulated dose of 10^4 Gy [84]. System uniformity was determined to be 7.8% thus failing to meet the typical acceptance criteria of < 3%. This non-uniformity in the scintillator dosimetry system can be attributed to the presence of high frequency noise observed in the acquired images. Further investigation to increase the signal-to-noise ratio in the images is thus warranted to improve system uniformity. One

simple means to increase the signal-to-noise ratio would be to use a CCD camera more closely matched to the spectrum of photons emitted by the scintillation sheet. The present system uses a camera which has a relative sensitivity of 85% at the wavelength of maximum emission of the scintillator sheet (see Table 3.1). Selection of a CCD camera with a maximum sensitivity matched to the maximum emission wavelength for the next implementation of the prototype could therefore increase signal-to-noise by as much as 15%.

4.3.6 Verification of Simple Static and Dynamic Wedged Fields

Results from the dose verification of both the simple static and wedged fields did not meet the typical acceptance criteria of < 3% with observed maximum percent dose differences of up to 7.7%. These discrepancies between the scintillator measured distributions and the film distributions are likely the result of the observed high frequency noise in the scintillator data as well as imperfections in the deconvolution kernel used to remove optical photon blurring from the images. Throughout the characterization of the system, small discrepancies in the optimized blurring kernel were observed. These include the deviation in the penumbral shape of the profiles in Figure 3.24, Figure 4.8, Figure 4.11, and Figure 4.13. In Figure 3.24, the penumbra from the scintillator data was observed to have a sharper fall off compared to the data produced by the treatment planning system. In contrast, Figure 4.8, Figure 4.11 and Figure 4.13 show the penumbra from the film data having a sharper fall off in comparison to the scintillator acquired data. These inconsistencies are most likely due to the use of a treatment planning system distribution to optimize the deconvolution kernel. Penumbral shape discrepancies between film measured data and treatment planning system data have been discussed throughout Chapter 2. One way of improving the optical deconvolution kernel would be to re-optimize using distribution data calculated from a treatment planning system that has been commissioned using high resolution film dosimetry to define the penumbra region. A more direct solution to the discrepancies observed in the derived optical deconvolution kernel used in this study would be to make use of quantitative film dosimetry distributions in the optimization process. These film distributions would have to be calibrated down to low dose levels similar to those found outside the field edges and as such would require use of a more sensitive radiographic film than the type used for the dose comparisons in this study. Additional fine-tuning of the kernel may also be possible by

expanding the optimization to include several different fields of varying size and shape and investigating the comparison metric used in the optimization with the possibility of using more complex cost functions such as summed gamma factors to replace the simple summed dose differences used in this study.

Chapter 5

SYSTEM EVALUATION

Final evaluation of the system was carried out by performing a full, field-by-field, dose verification on an IMRT treatment plan. Dose verification results were quantitatively compared to dose measurements performed using quantitative, 2-D film dosimetry measurements. An additional verification was also performed on the high spatial frequency IMRT field used to examine the effects of commissioning data resolution in Chapter 2. Dose verification results for this field were quantitatively compared to film dosimetry measurements as well as calculated dose distributions from both the Eclipse and BrainSCAN treatment planning systems. Results from this study were presented at a scientific conference [118] and are the subject of a manuscript in preparation [119].

5.1 Method and Materials

Evaluation of the system was performed on a 7-field head and neck IMRT treatment plan for the same patient used as Case #1 in the study evaluating the Eclipse and BrainSCAN treatment planning systems in Chapter 2 (see Figure 2.6). The organs-at-risk in this plan included the spinal cord, the brainstem, and the parotid glands.

5.1.1 Dosimetric Comparison

The tissue equivalent plastic scintillator dosimetry system was used to measure the dose distributions delivered by each field of the 7-field IMRT treatment plan. All fields were delivered using 200 MU with a gantry angle of 0° (i.e. beam's-eye-view) at an SAD of 100 cm and a depth of 3 cm. Following the image processing steps outlined in section 3.3, the measured dose distributions were compared to dose distributions measured using film dosimetry. Film dosimetry measurements were performed using the same techniques described in section 2.1.2.1 except in these measurements the film was placed at a depth of 3 cm. For each field, the film and scintillator distributions were normalized

at the same location. Normalization points in low dose gradient regions were selected such that distributions from all fields had similar dose ranges.

Dose distributions from the tissue equivalent plastic scintillator dosimetry system and film dosimetry were quantitatively compared using 1D dose profiles, percentage dose difference maps, and 2D gamma factor analysis. Percentage dose difference maps were calculated using absolute dose differences and the pass/fail criteria for the gamma analysis was a dose difference of 3% of the normalization point dose and a distance criterion of 3 mm.

Results from the scintillator based system and film dosimetry were again compared to point-by-point measurements acquired using a miniature thimble ionization chamber. These measurements were acquired in Solid Water using the same miniature chamber described in section 2.1.1 with the same setup parameters used for the scintillator and film verifications. All ionization chamber measurements were normalized to relative doses using the same normalization points used for normalization of the film and scintillator data.

5.1.2 System Efficiency

Efficiency of the tissue equivalent plastic scintillator dosimetry system was determined by comparing the time necessary to verify the 7-field IMRT treatment plan using film dosimetry and the new scintillator dosimetry system. For both verification techniques, the time taken for system setup, data acquisition, system takedown, and data post processing was recorded.

5.1.3 High Spatial Frequency IMRT Field

The ability of the tissue equivalent plastic scintillator dosimetry system to successfully verify a high spatial frequency IMRT distribution was determined by verifying the same high spatial frequency IMRT field used to examine the effects of commissioning data resolution in Chapter 2. This field was delivered using 200 MU with a gantry angle of 0° (i.e. beam's-eye-view) at an SAD of 100 cm and a depth of 5 cm. Following image processing, the measured dose distribution for this field was compared to dose distributions measured using film dosimetry as well as the calculated dose distributions

from both the Eclipse and BrainSCAN treatment planning systems. These distributions were compared using 1D dose profiles, percentage dose difference maps, and 2D gamma factor analysis (dose difference criterion = 3% of the normalization point dose and a distance criterion = 3 mm).

5.2 Results

5.2.1 Dosimetric Comparison

Results from the dosimetric comparison of the relative dose distribution maps from film dosimetry and the scintillator based system for two representative fields from the 7-field head and neck IMRT treatment plan are displayed in Figure 5.1 and Figure 5.2. These figures show the relative dose distributions obtained from film dosimetry (a) and using the scintillator dosimetry system (b), profiles across these distributions in the x-direction (c) and the y-direction (d), the percent dose difference map obtained from the distributions (e), and the gamma factor map indicating agreement of the distributions (f). Dosimetric comparison results for the five fields not displayed here can be found in Appendix A.

While the dose distributions in Figure 5.1 and Figure 5.2 are qualitatively quite similar, noticeable differences between the scintillator and film distributions include an increased amount of noise apparent in the jagged shape of the isodose levels of the scintillator distribution. This noise is not as evident as the increase in noise observed across the simpler square and wedged dose distributions in Chapter 4 (section 4.2.6) because of the complex shapes of the isodose lines in the IMRT distributions. Discrepancies observed between the film and scintillator distributions are also apparent in both of these fields. Observation of Figure 5.1(a) and (b), show an obvious discrepancy in the lower right quadrant of the field with the relative dose in the scintillator distribution indicating doses approximately 10% lower than the film distribution. The most obvious discrepancy between Figure 5.2(a) and (b) occurs in the upper left quadrant along the line indicating the position of the horizontal profile. In this region, the scintillator distribution does not detect the small high dose region above 120% that is apparent in the film distribution.

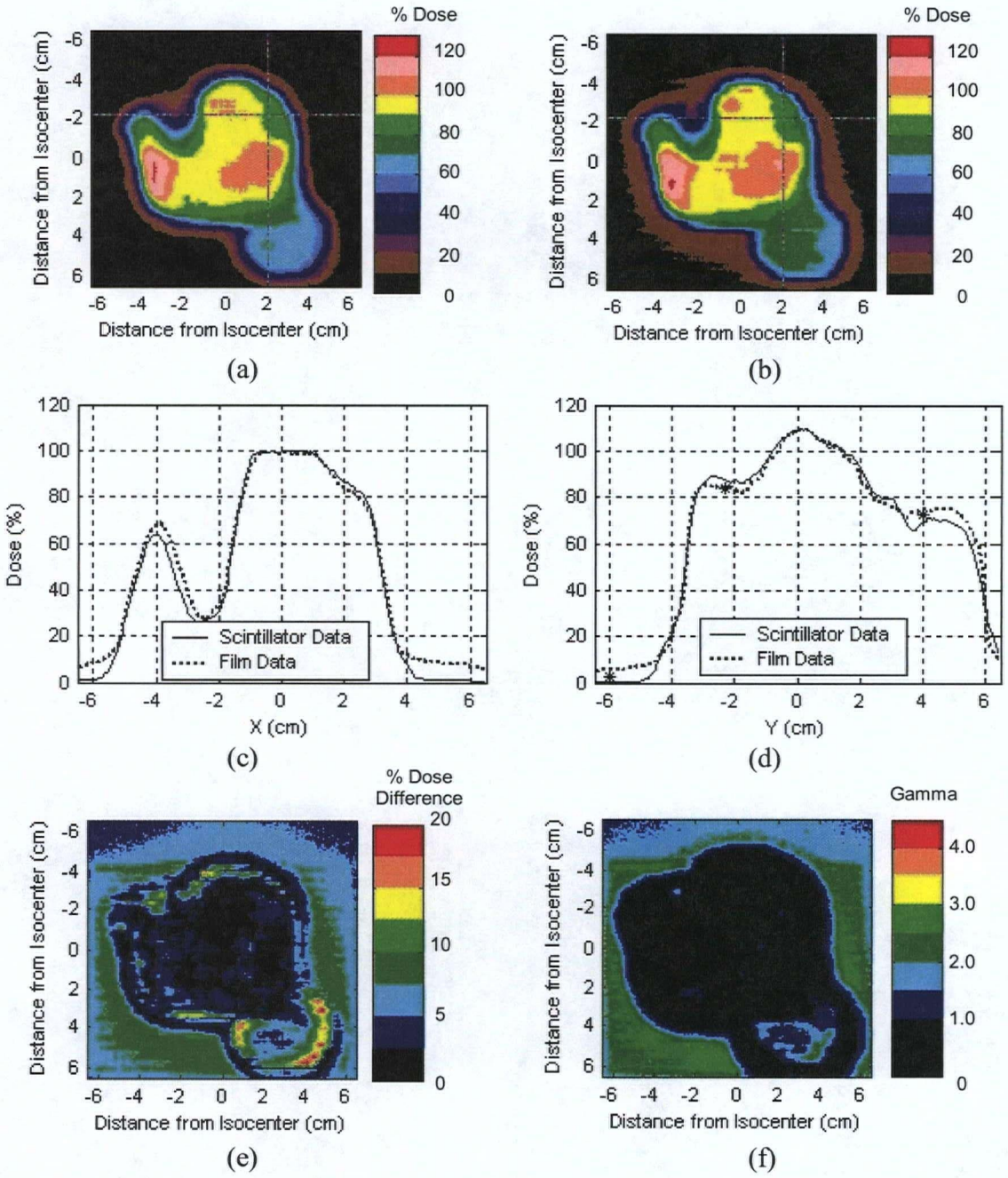

Figure 5.1: Dosimetric comparison results for field number 5 of the 7-field IMRT treatment plan. Dose distributions measured using (a) scintillator dosimetry system and (b) film dosimetry are shown with crosshairs indicating positions of 1-D profiles. Profiles in the x- and y-directions are shown in (c) and (d) respectively. Percent dose difference (e) and gamma factor (f) maps are also shown for these dose distributions.

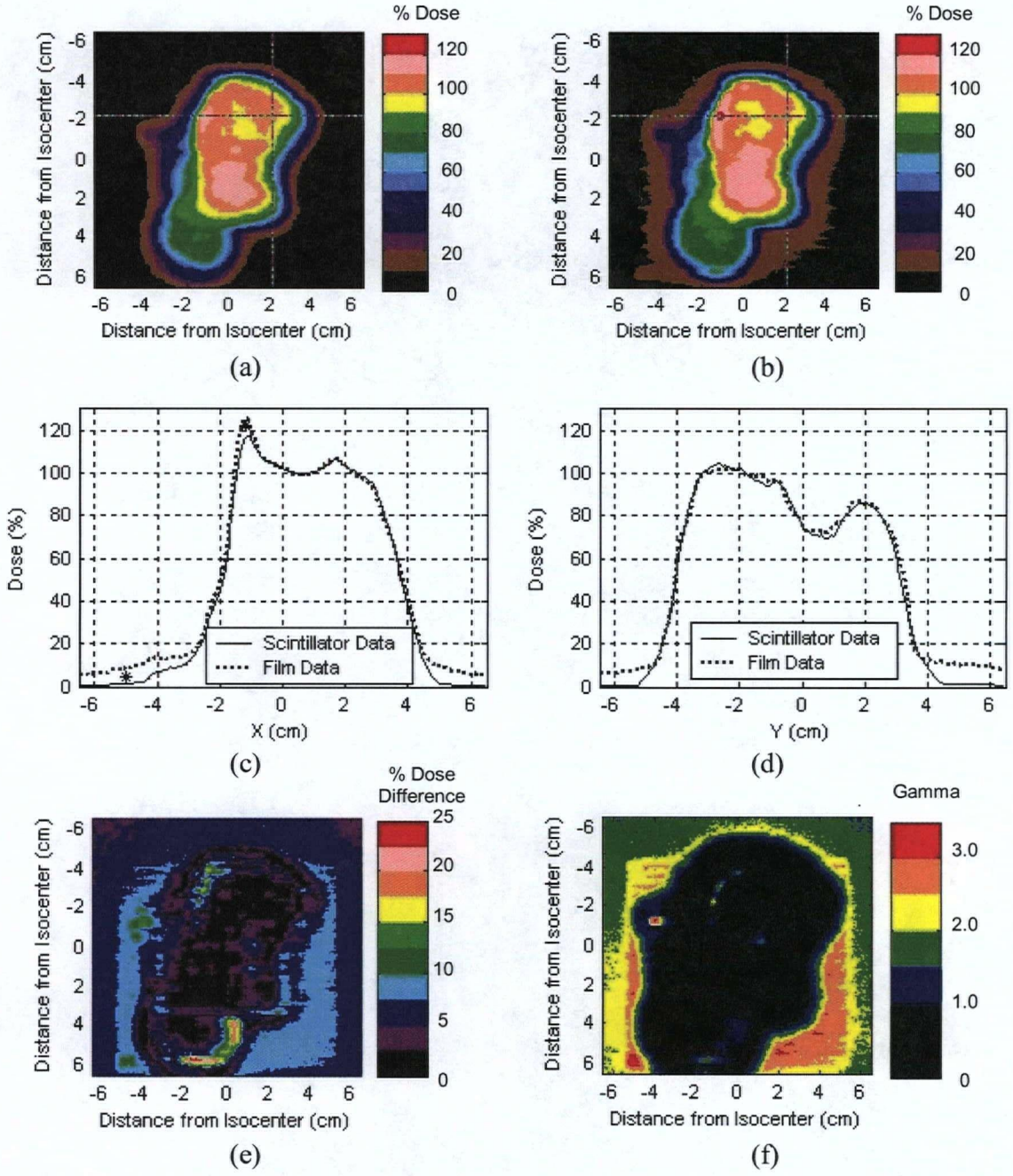

Figure 5.2: Dosimetric comparison results for field number 7 of the 7-field IMRT treatment plan. Dose distributions measured using (a) scintillator dosimetry system and (b) film dosimetry are shown with crosshairs indicating positions of 1-D profiles. Profiles in the x- and y-directions are shown in (c) and (d) respectively. Percent dose difference (e) and gamma factor (f) maps are also shown for these dose distributions.

The profiles displayed in Figure 5.1 and Figure 5.2 indicate good agreement between the film and scintillator distributions. The discrepancies observed in the dose distributions directly are also observed in the profiles with the underestimation of the dose in Figure 5.1(a) being apparent on the right side of the vertical profile through the distributions in Figure 5.1(d). Through examination of this profile, the underestimation is observed to be approximately 5% in this region. The underestimation of the small high dose region in Figure 5.2(a) is clearly seen in the horizontal profile in Figure 5.2(c) with the scintillator underestimating the dose by 7.1%. Additional discrepancies revealed through analysis of profiles include an overestimation by the scintillator distribution of approximately 3% on the left side of the vertical profile in Figure 5.1(d) and an underestimation by the scintillator system of 4.3% on the left side of the horizontal profile in Figure 5.1(c). Also shown in Figure 5.1(d) and Figure 5.2(c) are the ionization chamber point dosimetry measurements performed on these fields as indicated by the asterisks. From these point measurements it is observed that the film data is in agreement with the ionization chamber measurements for the small high dose region in Figure 5.2(c) and on the left and right side of the vertical profile in Figure 5.1(d). Once again, the point ionization chamber measurements outside the field edge indicate an overestimation of the dose by film and an underestimation by the scintillator based system. Analysis of percent dose difference and gamma factor maps in Figure 5.1 and Figure 5.2 indicate reasonable agreement across these IMRT fields. As expected, large percent dose differences are observed along the field edges in both cases. Closer observation of the gamma factor maps in these figures highlights the discrepancies observed in the distribution and profile analysis. Clearly, a large region within the field edge in the lower right quadrant of the gamma map in Figure 5.1(f) does not meet the pass criteria used in this analysis. Similarly, Figure 5.2(f) shows a small but intense region where the pass criteria is not fulfilled in the high dose region underestimated by the scintillator distribution. One point of interest observed in the IMRT dose difference and gamma factor maps is the large number of high valued pixels directly outside the field edges. This is especially apparent in Figure 5.2(f). These high discrepancy regions are a result of MLC leakage as well as leaf tip effects caused by the rounded shape of the MLC leaves used for this delivery. The weak signal caused by these effects is not reliably detected by either film dosimetry

(using the extended dose range film employed here) or the scintillator dosimetry system (low SNR) thus leading to the observed discrepancies.

Results from the percent dose difference and gamma factor maps for all seven fields of the IMRT plan are summarized in Table 5.1. To account for the discussed discrepancies outside the field edge, gamma factor statistics were taken over a region defined by the open field (determined from the dynamic MLC delivery file) plus a 1 cm margin in all directions. Statistics for the percent dose difference maps were determined over a region defined by the open field minus a 1 cm margin in all directions. It should be noted that due to the variable nature of IMRT field distributions this region often includes high dose gradient areas and thus may include high percent dose difference value pixels. This increase is apparent in the maximum values for the percent dose difference maps in Table 5.1.

Table 5.1: Summary of percent dose difference and gamma factor maps for all fields from 7-field IMRT plan.

Field Number	**Percent Dose Difference Map (over open field region – 1 cm)**			**Gamma Factor Map (over open field region + 1 cm)**		
	Average	**Std. Dev.**	**Max.**	**Average**	**Std. Dev.**	**Max.**
1	3.14 %	3.54 %	25.85 %	0.60	0.49	6.61
2	2.96 %	2.59 %	36.55 %	0.66	0.60	4.90
3	4.54 %	2.59 %	17.61 %	0.74	0.50	4.97
4	2.64 %	2.54 %	22.52 %	0.51	0.41	4.47
5	2.81 %	2.67 %	17.17 %	0.58	0.49	4.48
6	2.55 %	2.05 %	26.54 %	0.58	0.41	8.38
7	2.49 %	2.77 %	23.61 %	0.64	0.57	3.16
All Fields	**3.03 %**	**2.80 %**	**36.55 %**	**0.61**	**0.50**	**8.38**
	% of Pixels < 5 %		**81.96 %**	**% of Pixels ≤ 1.0**		**81.96 %**
	% of Pixels < 10 %		**97.29 %**			

5.2.2 System Efficiency

The time requirements for each step of the field-by-field dose verification for both film dosimetry and the scintillator based system are shown in Table 5.2.

Table 5.2: Time requirements for field-by-field dose verification of a 7-field IMRT plan using film dosimetry and scintillator dosimetry system.

Task	Film Dosimetry (minutes)	Scintillator Dosimetry System (minutes)
System Setup	4.5	47.0
Field-by-field Acquisition	49.5	8.5
Calibration	35.0	4.0
Takedown	2.0	14.0
Post Processing to Dose	46.5	24.0
Total	**137.5**	**97.5**

From this table the speed limiting tasks for each system are clearly observed. For film dosimetry the most time consuming process is the acquisition of the field-by-field films combined with the acquisition of the calibration films. These acquisitions include the manual loading and un-loading of film from the solid water phantom under safelight (as discussed in section 2.1.2.1) thus necessitating multiple trips to and from a darkroom located approximately 50 m from the treatment unit. For the current scintillator based system, the most time consuming process is system setup. Due to the prototype nature of this system, setup involved a multitude of specific tasks. These setup sub-tasks are listed in Table 5.3 along with the time required to carry each out. Also indicated in this table (shaded rows) are sub-tasks that are likely unaffected by the prototype status of the present system. These sub-tasks, and the time associated with each, are unlikely to be eliminated or changed following construction of a commercial scintillator based system. Such a commercial implementation would likely include various improvements such as a light tight cover, a fixed phantom/camera orientation and placement, and a dedicated, shielded control and capture computer.

Table 5.3: Setup sub-task requirements for scintillator dosimetry system. Shaded times indicate sub-tasks that are likely unaffected by prototype status of system.

System Setup Sub-Task	Time (minutes)
Block/extinguish all room light sources	4.0
Phantom and camera setup and alignment	6.0
Computer setup	9.0
Computer connection and start-up	5.0
Final setup alignment and light-field acquisition	10.0
Cleaning/polishing of optics and positioning of reflective sheet	4.0
Re-location of computer monitor outside treatment room	6.0
Acquisition of background and flood field images	3.0
Total For Prototype System	**47.0**
Expected Total For Non-Prototype Implementation	**18.0**

Replacing the scintillator system setup time in Table 5.2 with the estimated time for setup of a non-prototype system yields a further savings in time for the scintillator dosimetry system over film dosimetry (Table 5.4).

Table 5.4: Predicted time requirements for field-by-field dose verification of a 7-field IMRT plan using film dosimetry and commercial implementation of scintillator dosimetry system.

Technique	Predicted Time for 7-Field IMRT Verification (minutes)
Film Dosimetry	137.5
Commercial Scintillator Dosimetry System	68.5

5.2.3 High Spatial Frequency IMRT Field

Relative dose distribution maps from film dosimetry and the scintillator based dosimetry system as well as the predicted dose distribution maps from both the Eclipse and BrainSCAN treatment planning systems are displayed in Figure 5.3.

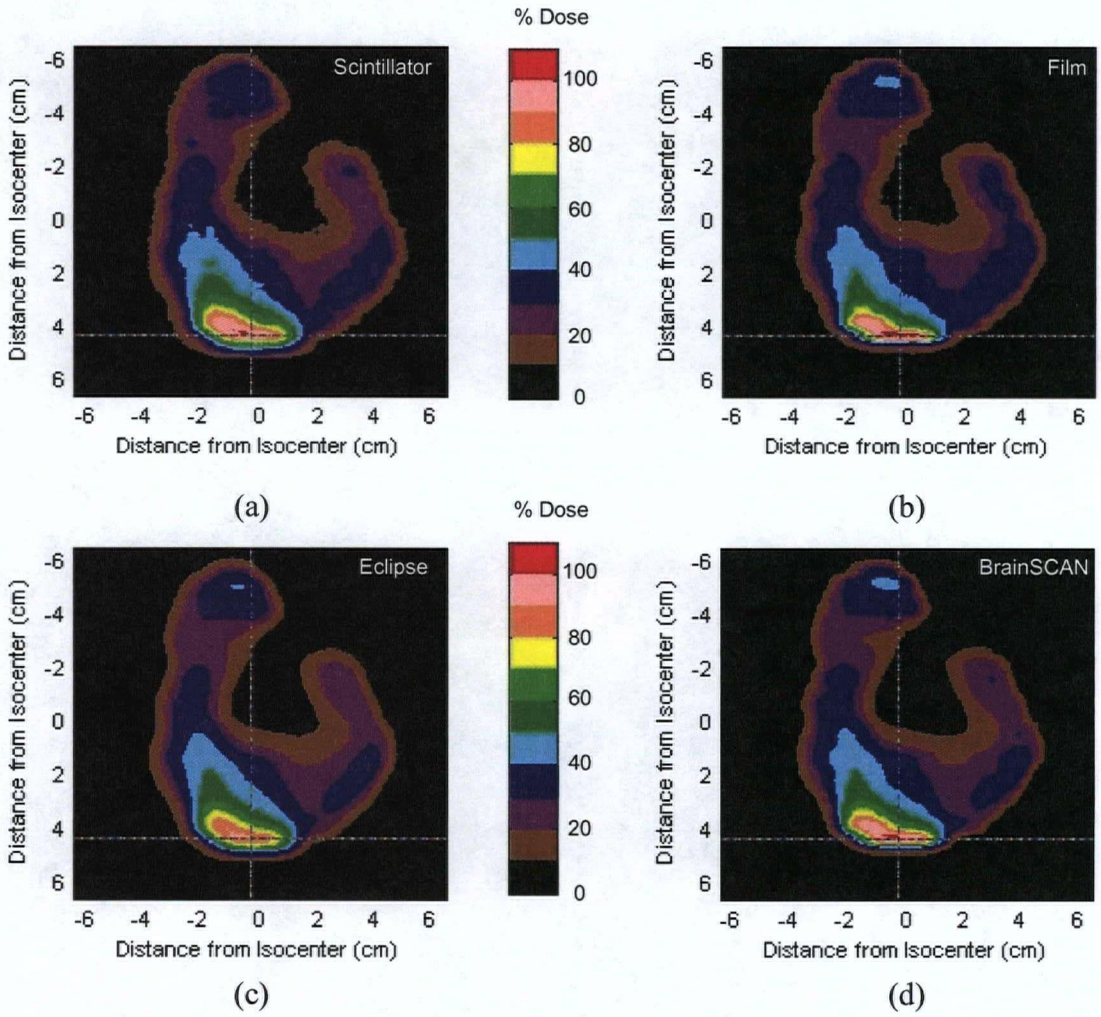

Figure 5.3: Relative dose distributions for high spatial frequency IMRT field. Measured distributions acquired using the scintillator dosimetry system (a) and film dosimetry (b) are shown in addition to predicted distributions calculated by the Eclipse (c) and BrainSCAN (d) treatment planning systems. Crosshairs indicate positions of 1-D profiles shown in Figure 5.4.

While qualitatively similar in many regards, close examination of these distributions reveals several differences. Once again, an increased amount of noise is apparent in the

scintillator distribution in the jagged shape of the isodose lines. Another marked difference between all the distributions and film is the size of the high dose region in the lower part of the field. This high dose region (> 100%) is much larger on the film distribution (Figure 5.3(b)) compared to any of the other distributions. The BrainSCAN distribution in Figure 5.3(d) shows a slightly smaller high dose region while the scintillator distribution in Figure 5.3(a) is observed to have still smaller a region with doses greater than 100%. Finally, the Eclipse distribution in Figure 5.3(c) shows no pixels with doses greater than 100%. Profiles across the high spatial frequency distributions in Figure 5.3 in the x- and y-directions are displayed in Figure 5.4. The positions of these profiles are identical to the positions of the profiles taken across this same high spatial frequency field in section 2.2.2 (see Figure 2.4). For easier viewing, measured profiles from film dosimetry and the scintillator based system are compared to BrainSCAN treatment planning system profiles in Figure 5.4(a) and (b) while measured profiles are compared to Eclipse treatment planning system profiles in Figure 5.4(c) and (d). Examining the profiles from the two treatment planning systems in comparison to film indicates agreement similar to that observed in section 2.2.2 as expected. Slight changes in the relative height of the profiles have occurred as a result of normalization process. These changes include the BrainSCAN profile peak in Figure 5.4(a) being slightly lower than the film peak compared to the opposite occurrence in Figure 2.4. Regardless of these small changes, the BrainSCAN profiles in Figure 5.4(a) and (b) are once again observed to closely follow to the film profiles. In Figure 5.4(c) and (d) it is again observed that the Eclipse profiles deviate markedly from the film profiles. Specifically, the Eclipse profiles fall short of the film profiles and overestimate the spread in the high spatial frequency regions of the field. Analysis of the scintillator profiles in Figure 5.4 indicates similarities to both the film and the Eclipse profiles. In Figure 5.4(c) and (d), the scintillator profiles are observed to fall only 6.8% lower than the film profiles in the high dose region compared to a discrepancy of -13.4% for Eclipse. In addition to this high spatial frequency region, the scintillator system also resolves the two small peaks on the left side of the vertical profile in Figure 5.4(d) while Eclipse is unable to separate the peaks. The scintillator profiles are observed to be similar to the Eclipse profiles in the spread of the high dose peak in Figure 5.4(c) and (d).

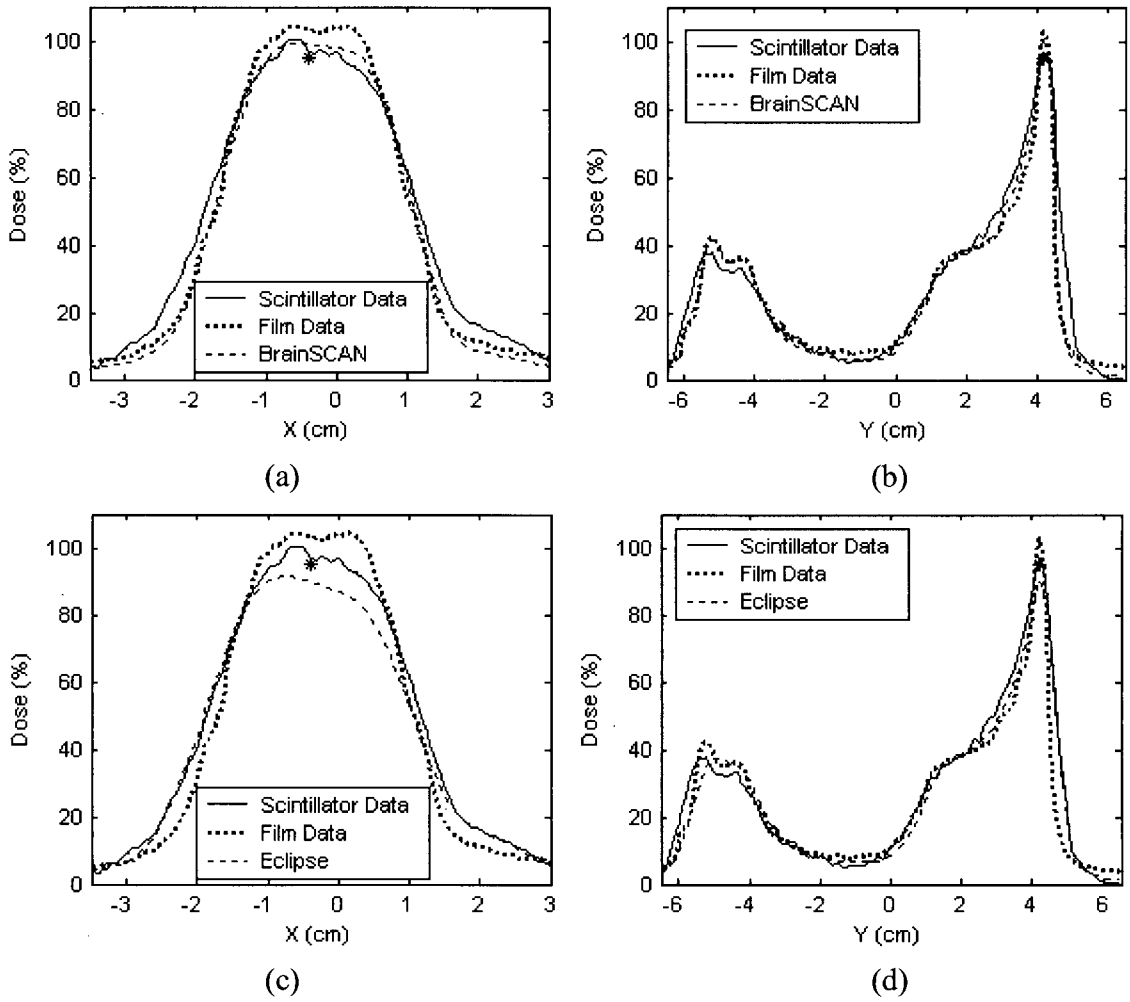

Figure 5.4: Profiles across measured and planned relative dose distributions for the high spatial frequency IMRT field. Profiles through the measured distributions are compared to profiles through the BrainSCAN calculated distribution in (a) the x-direction and (b) the y-direction. Profiles through the measured distributions are compared to profiles through the Eclipse calculated distribution in (c) the x-direction and (d) the y-direction. Point ionization chamber measurements are illustrated with asterisks.

Also shown in Figure 5.4 is a point dose ionization chamber measurement for this field in the center of the high dose region. This small volume ionization chamber measurement is observed to agree most closely to the BrainSCAN data. This agreement is to be expected considering that the BrainSCAN system was commissioned using small volume

ionization chamber data similar to that shown here. The apparent overestimation of the film data at this point is likely due to volume averaging of the dose over this very high spatial frequency dose region as previously discussed in section 2.3.

Percent dose difference maps comparing the distribution measured using the scintillator based system with the distributions from film and both treatment planning systems are displayed in Figure 5.5.

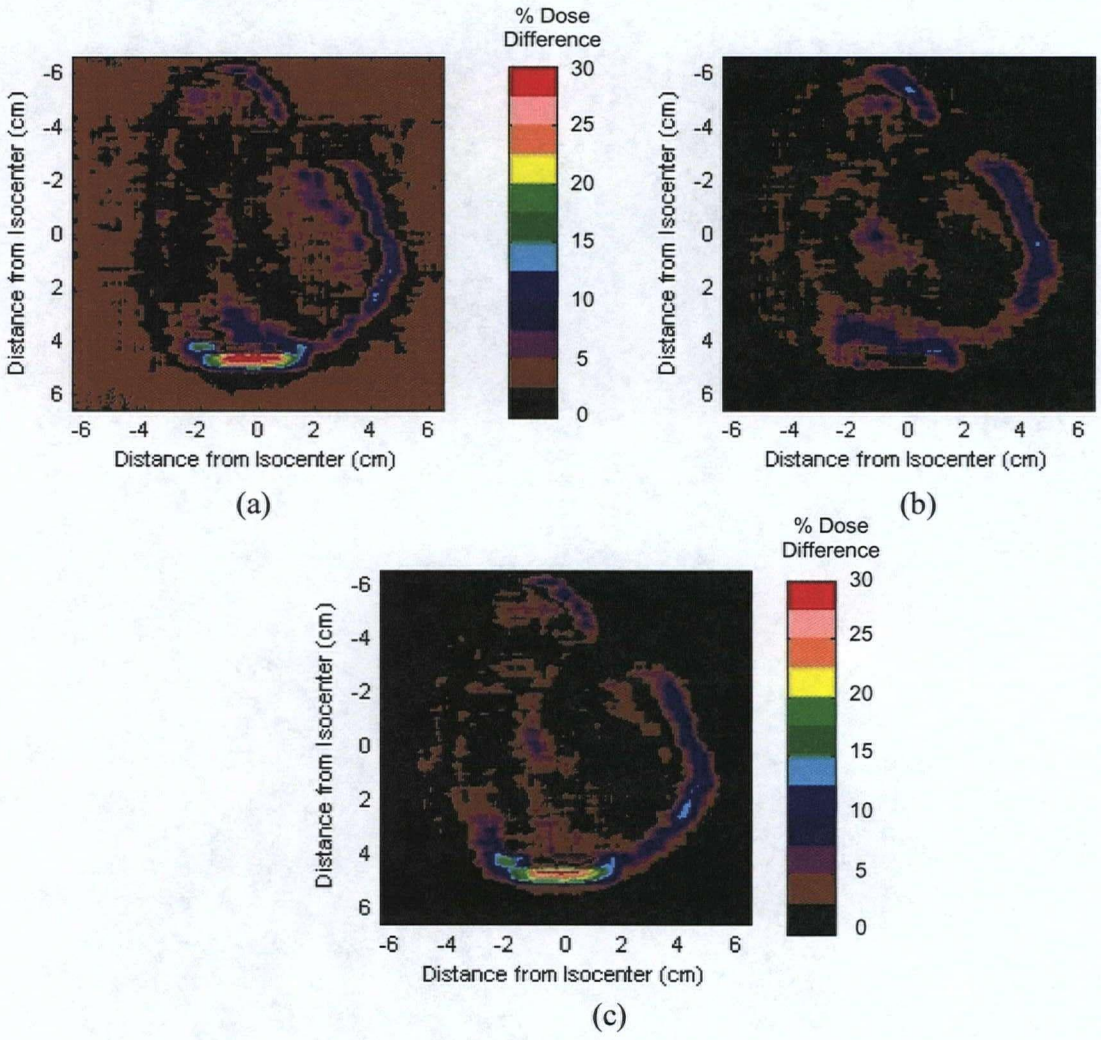

Figure 5.5: Percent dose difference maps comparing scintillator measured distribution with (a) film measured distribution, (b) Eclipse calculated distribution, and (c) BrainSCAN calculated distribution.

As expected the percent dose difference maps for film and BrainSCAN are very similar. As usual, the field edges show large percent dose differences. The area surrounding the

high dose/high spatial frequency region in the lower part of the field shows the largest percent dose differences as a result of the relatively large dose gradient in this region. Comparing Figure 5.5(b) to the other maps indicates that the scintillator distribution agrees more closely with the Eclipse distribution compared to BrainSCAN and film.

Gamma factor maps comparing the distribution measured using the scintillator based system with the distributions from film and both treatment planning systems are displayed in Figure 5.6.

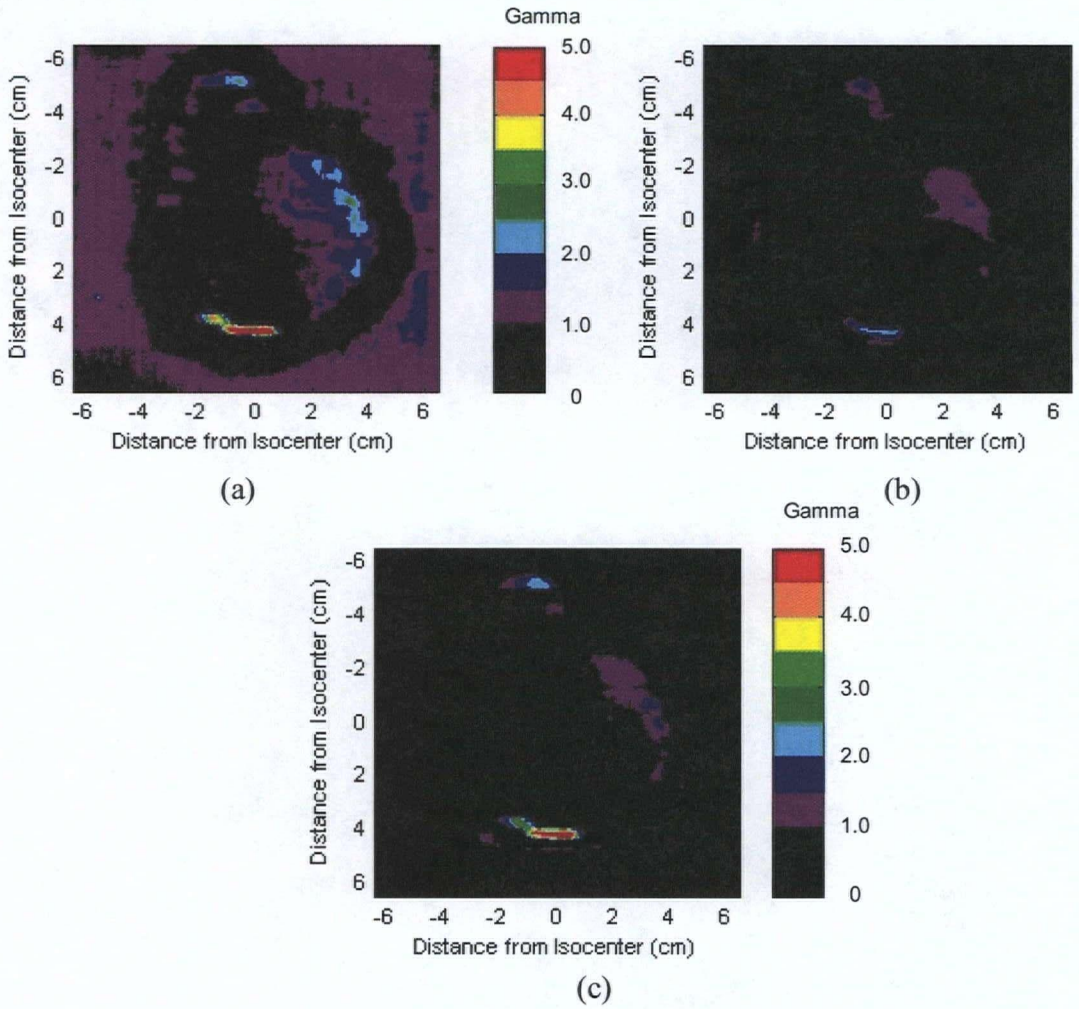

Figure 5.6: Gamma factor maps comparing scintillator measured distribution with (a) film measured distribution, (b) Eclipse calculated distribution, and (c) BrainSCAN calculated distribution.

These gamma maps indicate the closest agreement between the scintillator distribution and the Eclipse distribution. The worst agreement is between the scintillator distribution

and the film distribution. As expected, the region with the lowest number of pixels fulfilling the gamma criteria was the high spatial frequency region in the lower part of the field. Results from the percent dose difference and gamma factor maps in Figure 5.5 and Figure 5.6 are summarized in Table 5.5. Once again, these statistics were taken over a region defined by the open field plus a 1 cm margin in all directions.

Table 5.5: Summary of percent dose difference and gamma factor maps for high spatial frequency IMRT field.

Scintillator System vs.	Percent Dose Difference Map (over open field region – 1 cm)			Gamma Factor Map (over open field region + 1 cm)		
	Average	Std. Dev.	Max.	Average	Std. Dev.	Max.
Film	4.27 %	3.53 %	35.31 %	0.75	0.60	7.16
Eclipse	2.68 %	2.46 %	14.68 %	0.43	0.31	2.72
Brain-SCAN	2.93 %	3.49 %	30.74 %	0.46	0.45	5.40

5.3 Discussion

5.3.1 Dosimetric Comparison

Results from the dosimetric comparison for the 7-field IMRT treatment plan clearly demonstrate the potential of this system with an average dose difference between scintillator measured and film measured distributions of approximately 3% over all fields. The large maximum percent dose differences found in Table 5.1 reveal a common problem when attempting to summarize IMRT dose difference maps using statistics. The modulation of intensity across individual IMRT fields makes choice of a suitable region for performing statistics difficult. This was not the case for the simple square fields verified in Chapter 4 where the high dose gradient regions were all located along the edge of the field. To alleviate this problem, additional statistics have been provided for all of the fields. These statistics indicate that approximately 82% of all pixels used in the

analysis were found to have dose differences of less than 5% while 97% were found to have dose differences of less than 10%. Analysis of the gamma factor map statistics is even more promising with an average gamma over all fields of 0.61. This analysis also shows that 82% of the pixels from all fields had gamma values less than 1.0 indicating fulfillment of the dose and distance criteria.

Both percent dose difference and gamma factor analysis for the 7-field IMRT plan indicate poorer results when compared to the simple square field and dynamic wedged fields verified during previous system testing in Chapter 4. The discrepancies observed in the IMRT fields are consistent with the previously discussed conclusions of Chapter 4 indicating problems with high frequency noise in the scintillator data and imperfections in the deconvolution kernel used to remove optical photon blurring from the acquired images. While the deviation in the penumbral shape in the profiles in Figure 5.1 and Figure 5.2 is not as apparent as in previously observed profiles, the inadequacy of the deconvolution kernel is clearly observed in the scintillator system's underestimation of dose in high spatial frequency regions (i.e. narrow peaks in the profiles) such as those found in the horizontal profile in Figure 5.2(c) and in several of the other field profiles in the appendix. It is the prevalence of high spatial frequency regions and high dose gradients in individual IMRT fields that causes increased discrepancies compared to the simple square field and dynamic wedged fields previously tested.

5.3.2 System Efficiency

The true benefit of the scintillator based dosimetry system is revealed by the system efficiency results. Using the current prototype scintillator system to verify the 7-field IMRT plan resulted in a 30% time savings over film dosimetry as shown in Table 5.2. While this is already a considerable decrease in the time taken for a field-by-field IMRT verification, it does not truly represent the full potential of the scintillator system. The current prototype scintillator system used in the comparison has not yet been optimized for efficiency. In contrast, the film dosimetry was carried out using a commercial phantom. Of the tasks listed in Table 5.2, system setup is the most heavily affected by the prototype nature of the scintillator system. The sub-tasks involved in setup of the scintillator system are listed in Table 5.3. These sub-tasks include: blocking all

extraneous light sources in the treatment room; setting up and aligning the phantom and CCD camera using the setup board (includes placing lead shielding around camera); setting up the control and capture computer (including monitor, mouse, and keyboard) inside the treatment room and shielding the central processing unit (CPU) with lead lined vests; final system alignment and light-field acquisition from inside treatment room; polishing of system optics and positioning of reflective sheet adjacent to scintillator sheet; re-location of computer monitor, mouse, and keyboard outside treatment room; and finally acquisition of background and flood field images. Several of these sub-tasks would likely be eliminated following construction of a commercial scintillator based dosimetry system. A commercial implementation would likely include a light tight cover thus eliminating the need for blocking light sources in the treatment room. Inside this light tight cover, both the phantom and CCD camera would be fixed relative to one another with camera shielding permanently in place thus eliminating the second sub-task in Table 5.3. A commercial version would also feature a dedicated and shielded CPU thus simplifying the computer setup. Finally, the polishing of system optics would not be necessary in a sealed commercial system and re-location of the computer monitor, mouse, and keyboard outside the treatment room would be eliminated since the fixed setup of the camera and phantom (along with external crosshairs indicating scintillator position for setup) would allow final setup alignment and light field acquisition to be performed from outside the treatment room. Accounting for these improvements, the setup sub-tasks would be greatly simplified. Essentially setup would only involve placing the enclosed system on the treatment couch, aligning it to room lasers, connecting and starting up the CPU, and finally acquiring light-field, background, and flood field images. The time required for these sub-tasks alone have been shaded in Table 5.3 along with their total (estimated time for setup of a non-prototype implementation) indicating an additional savings of almost 30 minutes. The subsequent predicted time requirements for a 7-field IMRT field-by-field dose verification (shown in Table 5.4) indicate a 50% reduction in time for a commercial scintillator dosimetry system compared to film dosimetry shortening the time for verification from over 2 hours to just over 1 hour.

Examination of the timing results in Table 5.2 also reveal the scintillator based system's potential for being more forgiving to experimenter errors made during

verification procedures. One common example of a typical experimenter error is the setting of incorrect collimator jaw sizes before delivery of an IMRT field. If the experimenter is lucky enough to realize the error during or immediately after delivery, film dosimetry requires an extra trip to the dark room (approximately 7 minutes). If the experimenter does not realize the error until examination of the digitized films, it will be necessary to re-perform the film dosimetry for that field together with the necessary calibration films. In the case of the scintillator dosimetry system, the experimenter who realizes the error during or immediately after delivery simply has to change the collimator sizes and run the delivery again (approximately 1 minute). For errors which are not immediately recognized, the digital nature of the data acquired by the scintillator system has the potential to provide immediate visualization of the dose distributions following acquisition. This would enable the experimenter to perform a quick analysis of each field prior to takedown of the apparatus thereby decreasing the likelihood of having to re-perform the entire setup and acquisition procedure.

5.3.3 High Spatial Frequency IMRT Field

Results from the dosimetric comparison for the high spatial frequency IMRT field revealed discrepancies consistent with those found in verification of the 7-field IMRT treatment plan. The scintillator system was found to underestimate the dose in the high spatial frequency regions by approximately 5% to 7 % as is evident from the profiles in Figure 5.4. Also evident in this figure, and in the percent dose difference (Figure 5.5) and gamma factor maps (Figure 5.6), are the similarities of the scintillator distribution to the Eclipse distribution especially in the high dose gradient regions where the dose drops off. These similarities are to be expected given the use of an Eclipse treatment planning system distribution in the optimization of the deconvolution kernel used to remove optical photon blurring. As previously discussed, use of this treatment planning system calculated distribution underestimates the spread of the deconvolution kernel thereby causing the dose at the edges of high dose regions to have a less sharp fall off. Results from the profiles in Figure 5.4 are consistent with previous observations (section 4.3.6) where the fall off at the edge of high dose regions for film distributions was sharper than scintillator distributions which was in turn sharper than Eclipse calculated distributions.

While the dose indicated by the scintillator distribution is still lower than that indicated by the film distribution, it is not as low as that indicated by the Eclipse distribution. Furthermore, in Figure 5.4(d), the scintillator system is able to resolve the two small peaks on the left side of the profile while the Eclipse system is not.

Chapter 6

CONCLUSION

6.1 Conclusion

The primary objective of this thesis has been the development and implementation of a novel and advantageous method for the dosimetric verification of IMRT treatment fields. This work was motivated by an initial study which compared two IMRT treatment planning systems. This study, presented in detail in the first part of thesis, compared the clinical functionality of BrainLAB's BrainSCAN and Varian's Helios IMRT treatment planning systems with the aim of identifying practical and technical issues. The study considered implementation and commissioning, dose optimization, and plan assessment. Following commissioning of both treatment planning systems for the same 6 MV photon beam equipped with a high resolution multileaf collimator, both systems were applied to three test plans having identical imaging and contour data. Analysis considered three dimensional axial dose distributions, dose volume histograms and monitor unit calculations. Implementation and commissioning of the systems revealed that each requires somewhat different input data to characterize the beam prior to use. As a result, the same data cannot be used for commissioning of both systems. Also, whereas measured beam data was entered directly into Helios with minimal data processing, the BrainSCAN system required configured beam data to be sent to BrainLAB before clinical use. One key difference with respect to system commissioning was that BrainSCAN required high resolution data which necessitated the use of detectors with small active volumes. This difference was found to impact on the ability of the systems to accurately calculate dose for highly modulated fields, with BrainSCAN being more successful than Helios. For a selected high spatial frequency IMRT field, discrepancies of up to 13% were observed between film measured distributions and Helios calculated distributions. For the same field, BrainSCAN calculated distributions were found to deviate from film

by less than 3%. In terms of functionality, the BrainSCAN system uses a dynamically penalized likelihood inverse planning algorithm and calculates 4 plans at once with various relative weighting of the planning target and organ-at-risk volumes. Helios uses a gradient algorithm which allows the user to make changes to some of the input parameters during optimization. An analysis of the dosimetry output shows that, although the systems are different in many respects, they are each capable of producing substantially equivalent dose plans in terms of target coverage and normal tissue sparing. The extensive use of IMRT verification techniques during this comparison study served as motivation for the primary objective of this thesis, namely the design, development, and implementation of a novel IMRT dosimetric verification system that has several advantages over current techniques.

The development, characterization, and testing of a novel tissue equivalent plastic scintillator dose verification system were presented throughout the remainder of the thesis. During development of the system, several aspects of system design were investigated. These investigations included: determination of the optimal grit for scintillator sanding in order to maximize light output from the scintillator sheet; minimization/elimination of the cross talk signal caused by the multiple reflections of optical photons between the mirror and the scintillator; minimization of noise caused by video signal degradation over long distance cables; and determination of the optimal optical photon blurring kernel for deblurring of the acquired images. The optimal grit for scintillator sanding was determined to be 220. This grit was determined to maximize the light output with little effect on the spatial spread of the optical photons exiting the scintillator sheet. A micro-louvre optical collimator was used to eliminate the cross talk signal in the system. While successful in this endeavour, this solution was also found to lower the scintillator signal intensity considerably. Minimization of the noise due to video signal degradation was carried out by placing the CCD camera control and capture CPU local to the CCD camera and using a short coaxial cable. Optimization of the optical photon blurring kernel revealed an elliptical Gaussian shaped spread consistent with the use of the one-dimensional collimator used to eliminate the cross talk signal.

Characterization and testing of the new scintillator system indicate excellent dose response linearity and spatial linearity, high spatial resolution and good signal uniformity

and reproducibility. Dosimetric results from simple square fields and dynamic wedged fields indicate agreement with film dosimetry distributions within 8% inside the field edges. Gamma factor results for a 7-field head and neck IMRT treatment plan indicate fulfillment of a 3% dose and 3 mm distance criteria for 82% of the pixels over all 7 fields. Discrepancies between scintillator distributions and film distributions are mainly the result of inadequacies in the optimized optical photon blurring kernel. These inadequacies most likely stem from the optimization procedure's use of an Eclipse calculated dose distribution and the use of summed dose difference values as a cost function. Analysis of the efficiency of the scintillator system compared to film dosimetry revealed considerable benefits with a 50% reduction in time requirements for field-by-field verification of a 7-field IMRT treatment plan. Additional benefits of the scintillator system over film dosimetry include the elimination of the artifact-prone film processing step and the fact that the scintillator system is more forgiving to experimenter errors made during verification measurements.

In summary, the novel scintillator dosimetry system developed throughout this thesis shows a great deal of potential to become a commercial IMRT verification system. This technology promises to provide a truly tissue equivalent measurement medium dosimetry system capable of efficiently and accurately measuring dose in a 2D plane. The success of the prototype system in demonstrating the clear advantages of this technology over current IMRT verification systems has lead to the filing of a PCT international patent [120].

6.2 Future Work

This thesis having dealt with the design, development, and implementation of a prototype system, there are several areas in which further research of this technology could be conducted. The most obvious further investigation would be exploring the effects of different optimization procedures on the optical photon blurring kernel used to deconvolve the acquired images. As previously discussed, these investigations could make use of more robust dose distributions (film measured or Monte Carlo-derived) for comparison during the optimization. Improvements may also be realized by changing the

comparison technique from a dose difference comparison to a gamma factor comparison and by including several different sized fields in the optimization.

Further investigation could also be carried out to study the effect of using a more expensive, high-speed CCD camera matched more closely to the maximum emission wavelength of the scintillator sheet. As previously discussed, use of such a camera would increase system signal-to-noise and allow for verification of IMRT fields using the same number of monitor units as used in the actual treatment scenario.

Another possible investigation would be to study the potential of the current prototype system to be used for cumulative dosimetry of IMRT treatment plans. As discussed in section 1.6, verification of IMRT treatment plans typically also include the measurement of a cumulative dose distribution from all the treatment fields. Extending the current prototype scintillator system to enable cumulative measurements would necessitate the construction of an anthropomorphic tissue equivalent shell to fit around the current system. Figure 6.1 shows a schematic diagram of such a shell along with the placement of the current system inside for acquiring cumulative IMRT dose measurements. As illustrated, the current prototype phantom fits inside the shell and the entire apparatus is placed in the treatment room such that isocenter is located in the center of the scintillator sheet. The treatment is then delivered using all fields with multiple gantry angles and the cumulative dose distribution is acquired. Several problems would have to be overcome using such a setup. Due to the angular dependence of Čerenkov radiation, the Čerenkov component of the scintillator signal would change as the angle of incident radiation changes with gantry angle. This variation would have to be accounted for possibly by using previously documented methods of eliminating Čerenkov contamination [115, 117]. Another problem with the setup proposed in Figure 6.1 is the large size required of the tissue equivalent shell to fit the current prototype phantom. Taking into account the dimensions of the current prototype phantom (dictated by the size of the field of view), the diameter of the anthropomorphic shell would have to be approximately 38 cm. A phantom of this size is not representative of the size of a typical patient and may pose difficulties in transferring to and from treatment couches. In order to decrease the required size of the shell, the prototype would likely have to be re-designed to be more compact.

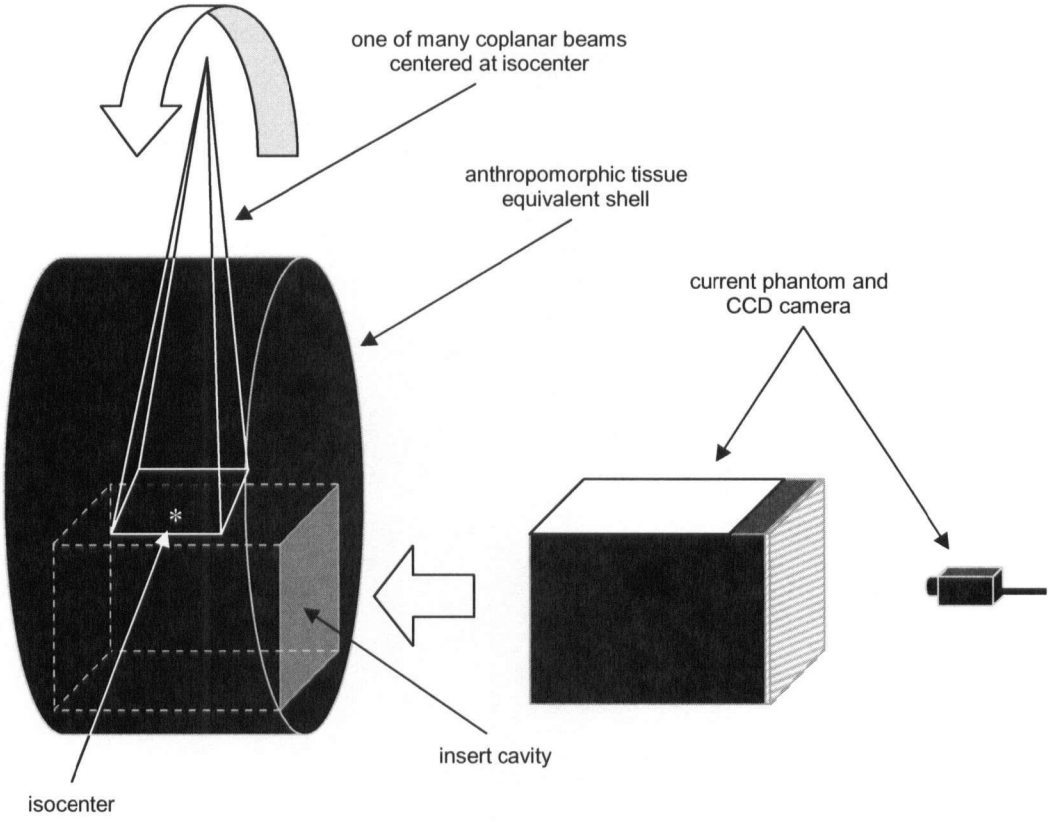

Figure 6.1: Schematic representation of an anthropomorphic cumulative dosimetry phantom using the prototype IMRT verification system described in this work.

Finally, an investigation could be carried out to study the effect of placing the reflecting mirror outside of the water filled cavity. A schematic diagram of such a setup is shown in Figure 6.2. In this setup, a water cavity approximately 10 cm in depth is used to provide scatter for the measurement plane and the mirror is located outside. As such, the scintillation photons traverse the water and exit into air before being reflected towards the CCD camera. This design has several possible advantages over the current prototype design. By increasing the separation between the scintillator sheet and the mirror the cross talk signal should decrease dramatically. This decrease in cross talk may be sufficient enough to negate use of the micro-louvre optical collimator thereby increasing the signal-to-noise of the system. In this setup the scintillation photons traverse a constant depth of water before exiting into air thereby completely eliminating the position dependent Čerenkov signal contribution observed in section 4.2.4. The depth of water

traversed by the scintillation photons in this setup (~ 10 cm) is also considerably less than that traversed in the current phantom (~ 20 cm). Theoretically, this decrease should lead to decreased optical photon spread in the acquired images. This setup also further removes the CCD camera from the primary treatment beam since it is positioned lower relative to the scintillation sheet.

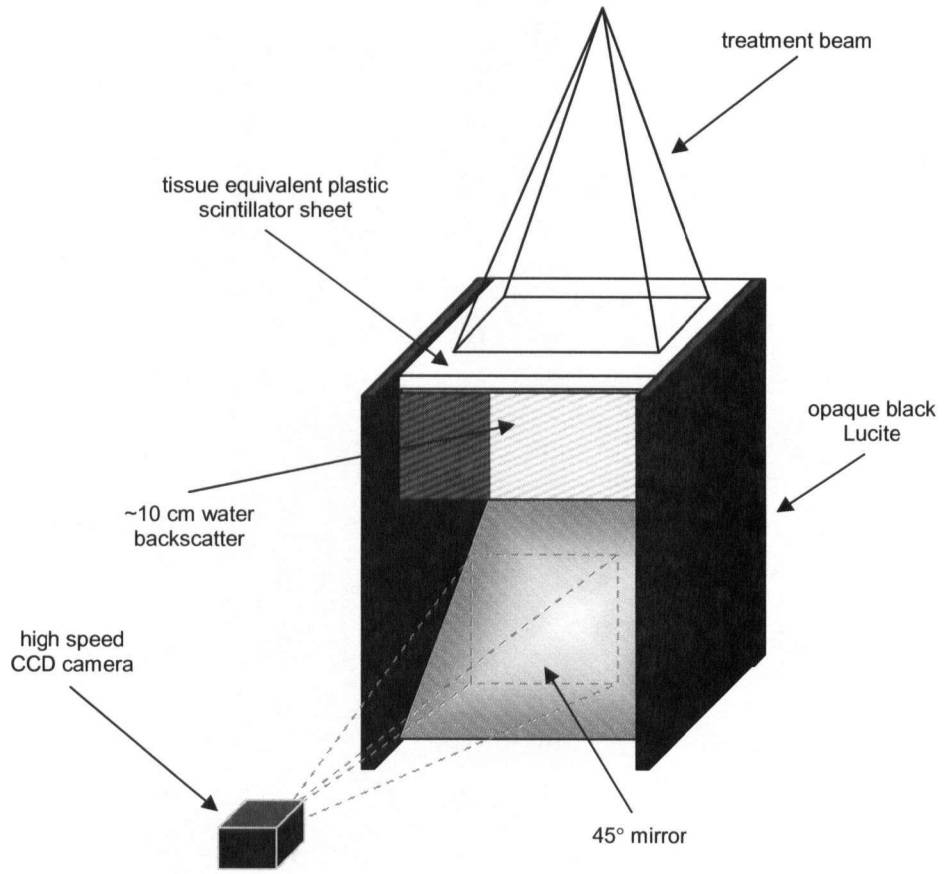

Figure 6.2: Schematic diagram of alternative tissue equivalent plastic scintillator dosimetry system with reflecting mirror placed outside of water cavity.

Finally, this setup also allows for construction of an anthropomorphic measurement volume for acquiring cumulative dose distributions without being constrained by the size of the measurement field of view. A schematic diagram of such a cumulative dosimetry system is shown in Figure 6.3. In this case, an anthropomorphic shape has been achieved by rounding the edges of the phantom. This setup also features a removable top buildup/scatter piece that allows for stacking of varying thicknesses of buildup on top of

the scintillator sheet thus enabling use for field-by-field and cumulative verification of IMRT treatment plans.

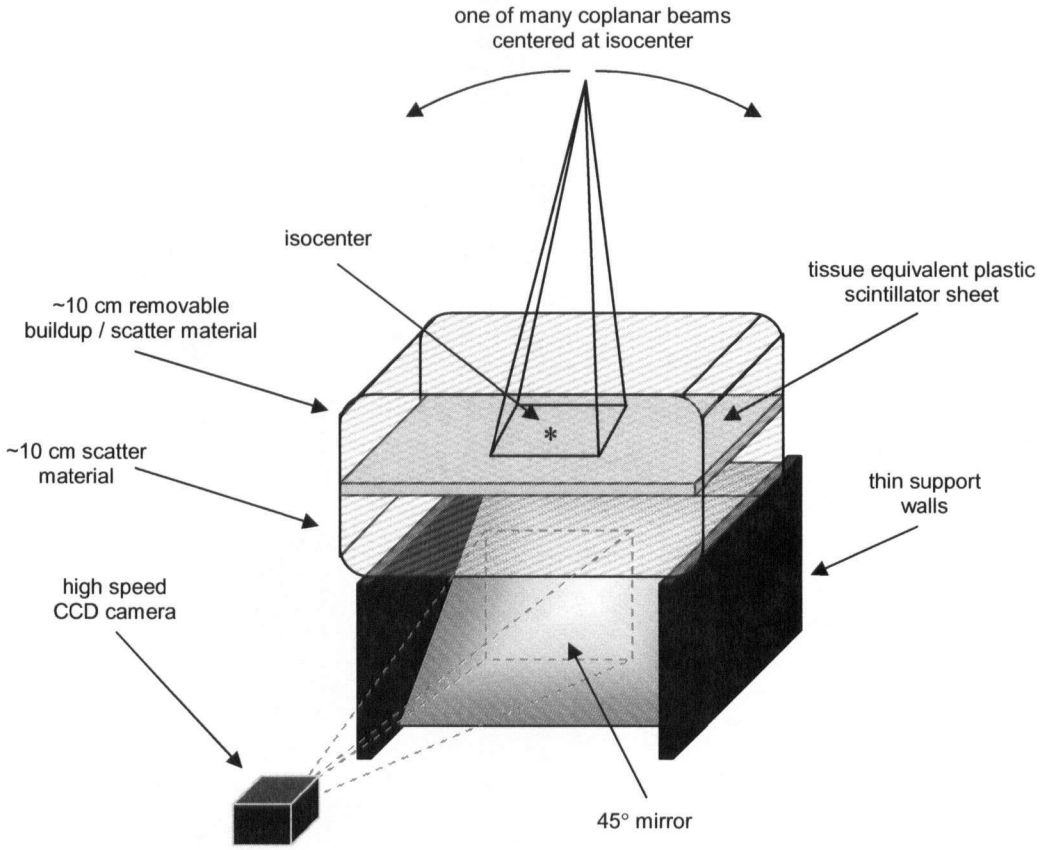

Figure 6.3: Anthropomorphic, cumulative version of alternative tissue equivalent plastic scintillator dosimetry system.

Bibliography

1. Canadian Cancer Society / National Cancer Institute of Canada, "Canadian Cancer Statistics 2005," Toronto, Canada, 2005.
2. U.S. National Institutes of Health, "National Cancer Institute Factsheet: Radiation therapy for cancer," www.cancer.gov/cancertopics/factsheet/Therapy/radiation, 2005.
3. E.J. Hall, *Radiobiology for the Radiologist*, J.B. Lippincott Company, Philadelphia, 1994.
4. H.D. Kogelnik, "The history and evolution of radiotherapy and radiation oncology in Austria," Int J Radiat Oncol Biol Phys **35**, 219-226 (1996).
5. C.A. Perez, L.W. Brady, and J.L. Roti, "Overview," in *Principles and Practice of Radiation Oncology*, C. A. Perez and L. W. Brady, pp. 1-78, Lippincott-Raven, Philadelphia, 1998.
6. F.M. Kahn, *The Physics of Radiation Therapy*, 2nd ed., Williams and Wilkins, Baltimore, 1984.
7. E.J. Hall and J.D. Cox, "Physical and Biological Basis of Radiation Therapy," in *Radiation Oncology: Rationale, Technique, Results*, 8th ed., edited by J. D. Cox and K. K. Ang, pp. 3-62, Mosby Inc., St. Louis, 2003.
8. G.P. Glasgow, "Cobalt-60 Teletherapy," in *The Modern Technology of Radiation Oncology*, J. Van Dyk, pp. 313-348, Medical Physics Publishing, Madison, 1999.
9. H.E. Johns and J.R. Cunningham, *The Physics of Radiology*, 4th ed., Charles C. Thomas, Springfield, 1983.
10. G.N. Hounsfield, "Computerized transverse axial scanning (tomography). 1. Description of system," Br J Radiol **46**, 1016-1022 (1973).
11. R.D. Evans, *The Atomic Nucleus*, McGraw-Hill, New York, 1955.
12. J. Van Dyk, R.B. Barnett, and J.J. Battista, "Computerized Radiation Treatment-Planning Systems," in *The Modern Technology of Radiation Oncology*, J. Van Dyk, pp. 231-286, Medical Physics Publishing, Madison, 1999.

13. R. Mohan and C.S. Chui, "Use of fast Fourier transforms in calculating dose distributions for irregularly shaped fields for three-dimensional treatment planning," Med Phys **14**, 70-77 (1987).

14. A. Ahnesjo, M. Saxner, and A. Trepp, "A pencil beam model for photon dose calculation," Med Phys **19**, 263-273 (1992).

15. P. Storchi and E. Woudstra, "Calculation of the absorbed dose distribution due to irregularly shaped photon beams using pencil beam kernels derived form basic beam data," Phys Med Biol **41**, 637-656 (1996).

16. P.R. Storchi, L.J. van Battum, and E. Woudstra, "Calculation of a pencil beam kernel from measured photon beam data," Phys Med Biol **44**, 2917-2928 (1999).

17. A.B. Pugachev, A.L. Boyer, and L. Xing, "Beam orientation optimization in intensity-modulated radiation treatment planning," Med Phys **27**, 1238-1245 (2000).

18. A. Pugachev, J.G. Li, A.L. Boyer, S.L. Hancock, Q.T. Le, S.S. Donaldson, and L. Xing, "Role of beam orientation optimization in intensity-modulated radiation therapy," Int J Radiat Oncol Biol Phys **50**, 551-560 (2001).

19. A.L. Boyer, L. Xing, and P. Xia, "Beam Shaping and Intensity Modulation," in *The Modern Technology of Radiation Oncology*, J. Van Dyk, pp. 437-479, Medical Physics Publishing, Madison, 1999.

20. J.D. Bourland, "Radiation Oncology Physics," in *Clinical Radiation Oncology*, L. L. Gunderson and Tepper J. E., pp. 64-118, Churchill Livingstone, Philadelphia, 2000.

21. J.M. Galvin, G. Ezzell, A. Eisbrauch, C. Yu, B. Butler, Y. Xiao, I. Rosen, J. Rosenman, M. Sharpe, L. Xing, P. Xia, T. Lomax, D.A. Low, and J. Palta, "Implementing IMRT in clinical practice: a joint document of the American Society for Therapeutic Radiology and Oncology and the American Association of Physicists in Medicine," Int J Radiat Oncol Biol Phys **58**, 1616-1634 (2004).

22. C. Nutting, D.P. Dearnaley, and S. Webb, "Intensity modulated radiation therapy: a clinical review," Br J Radiol **73**, 459-469 (2000).

23. T.W. Holmes, T.R. Mackie, and P. Reckwerdt, "An iterative filtered backprojection inverse treatment planning algorithm for tomotherapy," Int J Radiat Oncol Biol Phys **32**, 1215-1225 (1995).

24. J. Llacer, "Inverse radiation treatment planning using the Dynamically Penalized Likelihood method," Med Phys **24**, 1751-1764 (1997).

25. O.A. Sauer, D.M. Shepard, and T.R. Mackie, "Application of constrained optimization to radiotherapy planning," Med Phys **26**, 2359-2366 (1999).

26. S.V. Spirou and C.S. Chui, "A gradient inverse planning algorithm with dose-volume constraints," Med Phys **25**, 321-333 (1998).

27. S. Webb, "Optimization by simulated annealing of three-dimensional, conformal treatment planning for radiation fields defined by a multileaf collimator: II. Inclusion of two-dimensional modulation of the x-ray intensity," Phys Med Biol **37**, 1689-1704 (1992).

28. J.M. Galvin, X.G. Chen, and R.M. Smith, "Combining multileaf fields to modulate fluence distributions," Int J Radiat Oncol Biol Phys **27**, 697-705 (1993).

29. T.R. Bortfeld, D.L. Kahler, T.J. Waldron, and A.L. Boyer, "X-ray field compensation with multileaf collimators," Int J Radiat Oncol Biol Phys **28**, 723-730 (1994).

30. C.X. Yu, M.J. Symons, M.N. Du, A.A. Martinez, and J.W. Wong, "A method for implementing dynamic photon beam intensity modulation using independent jaws and a multileaf collimator," Phys Med Biol **40**, 769-787 (1995).

31. C.S. Chui, T. LoSasso, and S. Spirou, "Dose calculation for photon beams with intensity modulation generated by dynamic jaw or multileaf collimations," Med Phys **21**, 1237-1244 (1994).

32. G.A. Ezzell, J.M. Galvin, D. Low, J.R. Palta, I. Rosen, M.B. Sharpe, P. Xia, Y. Xiao, L. Xing, and C.X. Yu, "Guidance document on delivery, treatment planning, and clinical implementation of IMRT: report of the IMRT Subcommittee of the AAPM Radiation Therapy Committee," Med Phys **30**, 2089-2115 (2003).

33. M.R. Arnfield, Q. Wu, S. Tong, and R. Mohan, "Dosimetric validation for multileaf collimator-based intensity-modulated radiotherapy: a review," Med. Dosim. **26**, 179-188 (2001).

34. D.A. Low, R.L. Gerber, S. Mutic, and J.A. Purdy, "Phantoms for IMRT dose distribution measurement and treatment verification," Int J Radiat Oncol Biol Phys **40**, 1231-1235 (1998).

35. D.A. Low, W.B. Harms, S. Mutic, and J.A. Purdy, "A technique for the quantitative evaluation of dose distributions," Med Phys **25**, 656-661 (1998).

36. C. Constantinou, F.H. Attix, and B.R. Paliwal, "A solid water phantom material for radiotherapy x-ray and gamma-ray beam calibrations," Med Phys **9**, 436-441 (1982).

37. D.I. Thwaites, "Measurements of ionisation in water, polystyrene and a 'solid water' phantom material for electron beams," Phys Med Biol **30**, 41-53 (1985).

38. S. Amerio, A. Boriano, F. Bourhaleb, R. Cirio, M. Donetti, A. Fidanzio, E. Garelli, S. Giordanengo, E. Madon, F. Marchetto, U. Nastasi, C. Peroni, A. Piermattei, C.J. Sanz Freire, A. Sardo, and E. Trevisiol, "Dosimetric characterization of a large area pixel-segmented ionization chamber," Med Phys **31**, 414-420 (2004).

39. E. Spezi, A.L. Angelini, F. Romani, and A. Ferri, "Characterization of a 2D ion chamber array for the verification of radiotherapy treatments," Phys Med Biol **50**, 3361-3373 (2005).

40. P.A. Jursinic and B.E. Nelms, "A 2-D diode array and analysis software for verification of intensity modulated radiation therapy delivery," Med Phys **30**, 870-879 (2003).

41. D. Letourneau, M. Gulam, D. Yan, M. Oldham, and J.W. Wong, "Evaluation of a 2D diode array for IMRT quality assurance," Radiother Oncol **70**, 199-206 (2004).

42. G.F. Knoll, *Radiation Detection and Measurement*, 2nd ed., John Wiley and Sons, Toronto, 1989.

43. N.D. MacDougall, W.G. Pitchford, and M.A. Smith, "A systematic review of the precision and accuracy of dose measurements in photon radiotherapy using polymer and Fricke MRI gel dosimetry," Phys Med Biol **47**, R107-121 (2002).

44. A.I. Jirasek, C. Duzenli, C. Audet, and J. Eldridge, "Characterization of monomer/crosslinker consumption and polymer formation observed in FT-Raman spectra of irradiated polyacrylamide gels," Phys Med Biol **46**, 151-165 (2001).

45. M.J. Maryanski, G.S. Ibbott, P. Eastman, R.J. Schulz, and J.C. Gore, "Radiation therapy dosimetry using magnetic resonance imaging of polymer gels," Med Phys **23**, 699-705 (1996).

46. D.A. Low, J.F. Dempsey, R. Venkatesan, S. Mutic, J. Markman, E. Mark Haacke, and J.A. Purdy, "Evaluation of polymer gels and MRI as a 3-D dosimeter for intensity-modulated radiation therapy," Med Phys **26**, 1542-1551 (1999).

47. M. Hilts, C. Audet, C. Duzenli, and A. Jirasek, "Polymer gel dosimetry using x-ray computed tomography: a feasibility study," Phys Med Biol **45**, 2559-2571 (2000).

48. J.C. Gore, M. Ranade, M.J. Maryanski, and R.J. Schulz, "Radiation dose distributions in three dimensions from tomographic optical density scanning of polymer gels: I. Development of an optical scanner," Phys Med Biol **41**, 2695-2704 (1996).

49. H.H. Barrett and W. Swindell, *Radiological Imaging*, Academic Press, Toronto, 1981.

50. X.R. Zhu, S. Yoo, P.A. Jursinic, D.F. Grimm, F. Lopez, J.J. Rownd, and M.T. Gillin, "Characteristics of sensitometric curves of radiographic films," Med Phys **30**, 912-919 (2003).

51. P. Cadman, R. Bassalow, N.P. Sidhu, G. Ibbott, and A. Nelson, "Dosimetric considerations for validation of a sequential IMRT process with a commercial treatment planning system," Phys Med Biol **47**, 3001-3010 (2002).

52. N. Dogan, L.B. Leybovich, A. Sethi, and B. Emami, "Automatic feathering of split fields for step-and-shoot intensity modulated radiation therapy," Phys Med Biol **48**, 1133-1140 (2003).

53. A. Kapulsky, E. Mullokandov, and G. Gejerman, "An automated phantom-film QA procedure for intensity-modulated radiation therapy," Med Dosim **27**, 201-207 (2002).

54. J.L. Robar, M.P. Petric, and B.G. Clark, "Verification of three-dimensional dose surfaces for IMRS/IMRT with micro-multileaf collimation," Proceedings of the 44th Annual Meeting of the American Association of Physicists in Medicine, Montreal, Quebec, Canada, 1251 (2002).

55. J.L. Robar and B.G. Clark, "A practical technique for verification of three-dimensional conformal dose distributions in stereotactic radiosurgery," Med Phys **27**, 978-987 (2000).

56. N. Suchowerska, P. Hoban, A. Davison, and P. Metcalfe, "Perturbation of radiotherapy beams by radiographic film: measurements and Monte Carlo simulations," Phys Med Biol **44**, 1755-1765 (1999).

57. J. Esthappan, S. Mutic, W.B. Harms, J.F. Dempsey, and D.A. Low, "Dosimetry of therapeutic photon beams using an extended dose range film," Med Phys **29**, 2438-2445 (2002).

58. B. Paliwal, W. Tome, S. Richardson, and T.R. Makie, "A spiral phantom for IMRT and tomotherapy treatment delivery verification," Med Phys **27**, 2503-2507 (2000).

59. A.G. Haus and S.M. Jaskulski, *The Basics of Film Processing in Medical Imaging*, Medical Physics Publishing, Madison, 1997.

60. H. Meertens, M. van Herk, and J. Weeda, "A liquid ionisation detector for digital radiography of therapeutic megavoltage photon beams," Phys Med Biol **30**, 313-321 (1985).

61. P. Munro, "Megavoltage Radiography for Treatment Verification," in *The Modern Technology of Radiation Oncology*, J. Van Dyk, pp. 481-508, Medical Physics Publishing, Madison, 1999.

62. B.M. McCurdy, K. Luchka, and S. Pistorius, "Dosimetric investigation and portal dose image prediction using an amorphous silicon electronic portal imaging device," Med Phys **28**, 911-924 (2001).

63. B. Warkentin, S. Steciw, S. Rathee, and B.G. Fallone, "Dosimetric IMRT verification with a flat-panel EPID," Med Phys **30**, 3143-3155 (2003).

64. K.L. Pasma, M.L. Dirkx, M. Kroonwijk, A.G. Visser, and B.J. Heijmen, "Dosimetric verification of intensity modulated beams produced with dynamic multileaf collimation using an electronic portal imaging device," Med Phys **26**, 2373-2378 (1999).

65. S.C. Vieira, M.L. Dirkx, K.L. Pasma, and B.J. Heijmen, "Dosimetric verification of x-ray fields with steep dose gradients using an electronic portal imaging device," Phys Med Biol **48**, 157-166 (2003).

66. C. Yeboah and S. Pistorius, "Monte Carlo studies of the exit photon spectra and dose to a metal/phosphor portal imaging screen," Med. Phys. **27**, 330-339 (2000).

67. C.S. Chui and S.V. Spirou, "Inverse planning algorithms for external beam radiation therapy," Med Dosim **26**, 189-197 (2001).

68. T. Holmes and T.R. Mackie, "A comparison of three inverse treatment planning algorithms," Phys Med Biol **39**, 91-106 (1994).

69. J. Llacer, T.D. Solberg, and C. Promberger, "Comparative behaviour of the dynamically penalized likelihood algorithm in inverse radiation therapy planning," Phys Med Biol **46**, 2637-2663 (2001).

70. A. Fogliata, A. Bolsi, and L. Cozzi, "Comparative analysis of intensity modulation inverse planning modules of three commercial treatment planning systems applied to head and neck tumour model," Radiother Oncol **66**, 29-40. (2003).

71. C.S. Mayo and M.M. Urie, "A systematic benchmark method for analysis and comparison of IMRT treatment planning algorithms," Med Dosim **28**, 235-242 (2003).

72. M.P. Petric, B.G. Clark, and J.L. Robar, "A comparison of two commercial treatment-planning systems to IMRT," J Appl Clin Med Phys **6**, 63-80 (2005).

73. M.P. Petric, J.L. Robar, and B.G. Clark, "A comparison of two commercial treatment planning systems for IMRT," Proceedings of the 49th Annual Scientific Meeting of the Canadian Organisation of Physicists in Medicine, Edmonton, Alberta, Canada, 90-92 (2003).

74. M.P. Petric, J.L. Robar, and B.G. Clark, "Clinical functionality of two commercial IMRT treatment planning systems," Proceedings of the 7th Biennial European Society for Therapeutic Radiology and Oncology Meeting on Physics and Radiation Technology for Clinical Radiotherapy, Geneva, Switzerland, S98 (2003).

75. P.R. Almond, P.J. Biggs, B.M. Coursey, W.F. Hanson, M.S. Huq, R. Nath, and D.W. Rogers, "AAPM's TG-51 protocol for clinical reference dosimetry of high-energy photon and electron beams," Med Phys **26**, 1847-1870 (1999).

76. T. LoSasso, C.S. Chui, and C.C. Ling, "Physical and dosimetric aspects of a multileaf collimation system used in the dynamic mode for implementing intensity modulated radiotherapy," Med Phys **25**, 1919-1927 (1998).

77. M.R. Arnfield, K. Otto, V.R. Aroumougame, and R.D. Alkins, "The use of film dosimetry of the penumbra region to improve the accuracy of intensity modulated radiotherapy," Med Phys **32**, 12-18 (2005).

78. N.L. Childress and Rosen, II, "Effect of processing time delay on the dose response of Kodak EDR2 film," Med Phys **31**, 2284-2288 (2004).

79. P. Charland and E. El-Khatib, "Accounting for detector and source size effects on photon beam penumbra.," Proceedings of the 44th Annual Scientific Meeting of the Canadian Organisation of Physicists in Medicine, London, Ontario, Canada, 58-60 (1998).

80. C.R. Ramsey, I.L. Cordrey, K.M. Spencer, and A.L. Oliver, "Dosimetric verification of two commercially available three-dimensional treatment planning systems using the TG 23 test package," Med Phys **26**, 1188-1195 (1999).

81. A.M. Bergman, K. Otto, and C. Duzenli, "The use of modified single pencil beam dose kernels to improve IMRT dose calculation accuracy," Med Phys **31**, 3279-3287 (2004).

82. J.H. Hubbell, "Photon mass attenuation and energy-absorption coefficients from 1 keV to 20 MeV," Int J Appl Radiat Isotope **33**, 1269-1290 (1982).

83. International Commission on Radiation Units and Measurements Report No. 37: Stopping powers for electrons and positrons. Report prepared by ICRU, Bethesda, MD, 1984.

84. A.S. Beddar, T.R. Mackie, and F.H. Attix, "Water-equivalent plastic scintillation detectors for high-energy beam dosimetry: I. Physical characteristics and theoretical consideration," Phys Med Biol **37**, 1883-1900 (1992).

85. A.S. Beddar, T.J. Kinsella, A. Ikhlef, and C.H. Sibata, "A miniature "scintillation-fiberoptic-PMT" detector system for the dosimetry of small fields in stereotactic radiosurgery," IEEE Trans Nucl Sci **48**, 924-928 (2001).

86. D. Letourneau, J. Pouliot, and R. Roy, "Miniature scintillating detector for small field radiation therapy," Med Phys **26**, 2555-2561 (1999).

87. J.W. Wong, S.P. Monthofer, W.R. Binns, J. Klarmann, and G.L. Fuller, "Rapid areal radiotherapy dosimetry using a sheet of plastic scintillator," Proceedings of the World Congress on Medical Physics and Biomedical Engineering, Kyoto, Japan, OP-3-B1-1-02 (1991).

88. H. Perera, J.F. Williamson, S.P. Monthofer, W.R. Binns, J. Klarmann, G.L. Fuller, and J.W. Wong, "Rapid two-dimensional dose measurement in brachytherapy using plastic scintillator sheet: linearity, signal-to-noise ratio, and energy response characteristics," Int J Radiat Oncol Biol Phys **23**, 1059-1069 (1992).

89. J.S. Li, A.L. Boyer, and C.M. Ma, "Verification of IMRT dose distributions using a water beam imaging system," Med Phys **28**, 2466-2474 (2001).

90. L. Archambault, L. Gingras, A.S. Beddar, R. Roy, and L. Beaulieu, "Small volume dosimetry with multiple scintillation probes," Proceedings of the 47th Annual Meeting of the American Association of Physicists in Medicine, Seattle, Washington, USA, SU-FF-T-251 (2005).

91. K. Murthy, C.J. Thompson, C. Liu-Hinz, and D. Jolly, "A study of the light output and energy resolution of small BGO crystals," IEEE Nuclear Science Symposium and Medical Imaging Conference **3**, 1352-1356 (1994).

92. C. Moisan, A. Levin, and H. Laman, "Testing scintillation transport models with photoelectron yields measured under different surface finishes," IEEE Nuclear Science Symposium **1**, 824-828 (1997).

93. A. Saoudi, C.M. Pepin, and R. Lecompte, "Study of light collection in multi-crystal detectors," IEEE Trans Nucl Sci **47**, 1634-1639 (2000).

94. C. Hurlbut, Eljen Technology, Sweetwater, Texas, USA, (personal communication, April 11, 2003).

95. M. Partridge, P.M. Evans, and J.R. Symonds-Tayler, "Optical scattering in camera-based electronic portal imaging," Phys. Med. Biol. **44**, 2381-2396 (1999).

96. J.G. Nagy and D.P. O'Leary, "Restoring images degraded by spatially-variant blur," SIAM J Sci Comput **19**, 1063-1082 (1998).

97. E.S. Angel and A.K. Jain, "Restoration of images degraded by spatially varying pointspread functions by a conjugate gradient method," Appl Opt **17**, 2186-2190 (1978).

98. H.J. Trussell and B.R. Hunt, "Image restoration of space-variant blurs by sectioned methods," IEEE Trans Acoust Speech Signal Processing **26**, 608-609 (1978).

99. Hitachi Denshi Service Net, "CCD Camera Specifications: Hitachi KP-M1 E/K," www.hitachi-service.net/kp-m1/kpm1.htm, 2001.

100. T. Nuns, J.-P. David, J.-G. Loquet, F. Gardillou, M. Lescure, and S. Barde, "Radiation effects on commercial CCDs," 6th European Conference on Radiation and Its Effects on Components and Systems 481-487 (2001).

101. J. Janesick, T. Elliott, and F. Pool, "Radiation damage in scientific charge-coupled devices," IEEE Trans Nucl Sci **36**, 572-578 (1989).

102. K.J. Kerpez, T.E. Chapuran, R.C. Menendez, and S.S. Wagner, "Digital transmission over in-home coaxial wiring," IEEE Trans on Broadcasting **43**, 136-144 (1997).

103. J.C. Lagarias, J.A. Reeds, M.H. Wright, and P.E. Wright, "Convergence properties of the Nelder-Mead simplex method in low dimensions," SIAM J Optim **9**, 112-147 (1998).

104. M.P. Petric, J.L. Robar, and B.G. Clark, "Characterization of a tissue equivalent plastic scintillator dosimetry system," Proceedings of the 51st Annual Scientific Meeting of the Canadian Organisation of Physicists in Medicine, Hamilton, Ontario, Canada, 254-256 (2005).

105. M.P. Petric, J.L. Robar, and B.G. Clark, "A tissue equivalent plastic scintillator based dosimetry system for verification of IMRT dose distributions," Proceedings

of the 59th Annual Joint Congress of the Canadian Association of Physicists, Winnipeg, Manitoba, Canada, 114 (2004).

106. M.P. Petric, J.L. Robar, and B.G. Clark, "Development and characterization of a tissue equivalent plastic scintillator based dosimetry system," Med Phys **33**, 96-105 (2006).

107. L. Ma, P.B. Geis, and A.L. Boyer, "Quality assurance for dynamic multileaf collimator modulated fields using a fast beam imaging system," Med Phys **24**, 1213-1220 (1997).

108. American Association of Physicists in Medicine Report No. 13: Physical aspects of quality assurance in radiation therapy. Report prepared by Task Group 24 with contribution by Task Group 22, AAPM Radiation Therapy Committee, 1984.

109. A.S. Beddar, T.R. Mackie, and F.H. Attix, "Water-equivalent plastic scintillation detectors for high-energy beam dosimetry: II. Properties and measurements," Phys Med Biol **37**, 1901-1913 (1992).

110. B.J. Heijmen, K.L. Pasma, M. Kroonwijk, V.G. Althof, J.C. de Boer, A.G. Visser, and H. Huizenga, "Portal dose measurement in radiotherapy using an electronic portal imaging device (EPID)," Phys Med Biol **40**, 1943-1955 (1995).

111. O.A. Zeidan, J.G. Li, M. Ranade, A.M. Stell, and J.F. Dempsey, "Verification of step-and-shoot IMRT delivery using a fast video-based electronic portal imaging device," Med Phys **31**, 463-476 (2004).

112. M. Partridge, P.M. Evans, and M.A. Mosleh-Shirazi, "Linear accelerator output variations and their consequences for megavoltage imaging," Med Phys **25**, 1443-1452 (1998).

113. L. Archambault, A.S. Beddar, L. Gingras, R. Roy, and L. Beaulieu, "Measurement accuracy and Cerenkov removal for high performance, high spatial resolution scintillation dosimetry," Med Phys **33**, 128-135 (2006).

114. L. Archambault, J. Arsenault, L. Gingras, A.S. Beddar, R. Roy, and L. Beaulieu, "Plastic scintillation dosimetry: optimal selection of scintillating fibers and scintillators," Med Phys **32**, 2271-2278 (2005).

115. M.A. Clift, P.N. Johnston, and D.V. Webb, "A temporal method of avoiding the Cerenkov radiation generated in organic scintillator dosimeters by pulsed mega-voltage electron and photon beams," Phys Med Biol **47**, 1421-1433 (2002).

116. A.S. Beddar, N. Suchowerska, and S.H. Law, "Plastic scintillation dosimetry for radiation therapy: minimizing capture of Cerenkov radiation noise," Phys Med Biol **49**, 783-790 (2004).

117. A.M. Frelin, J.M. Fontbonne, G. Ban, J. Colin, M. Labalme, A. Batalla, A. Isambert, A. Vela, and T. Leroux, "Spectral discrimination of Cerenkov radiation in scintillating dosimeters," Med Phys **32**, 3000-3006 (2005).

118. M.P. Petric, J.L. Robar, and B.G. Clark, "Verification of IMRT dose distributions using a tissue equivalent plastic scintillator based dosimetry system," Proceedings of the 47th Annual Meeting of the American Association of Physicists in Medicine, Seattle, Washington, Canada, 1891 (2005).

119. M.P. Petric, J.L. Robar, and B.G. Clark, "Verification of IMRT dose distributions using a tissue equivalent plastic scintillator dosimetry system," *In manuscript* (2006).

120. M.P. Petric, J.L. Robar, and B.G. Clark, "Method and apparatus for verifying radiation dose distributions," PCT Patent International Publication Number WO 2005/119295 (December 15, 2005).

Appendix A: 7-Field IMRT Results

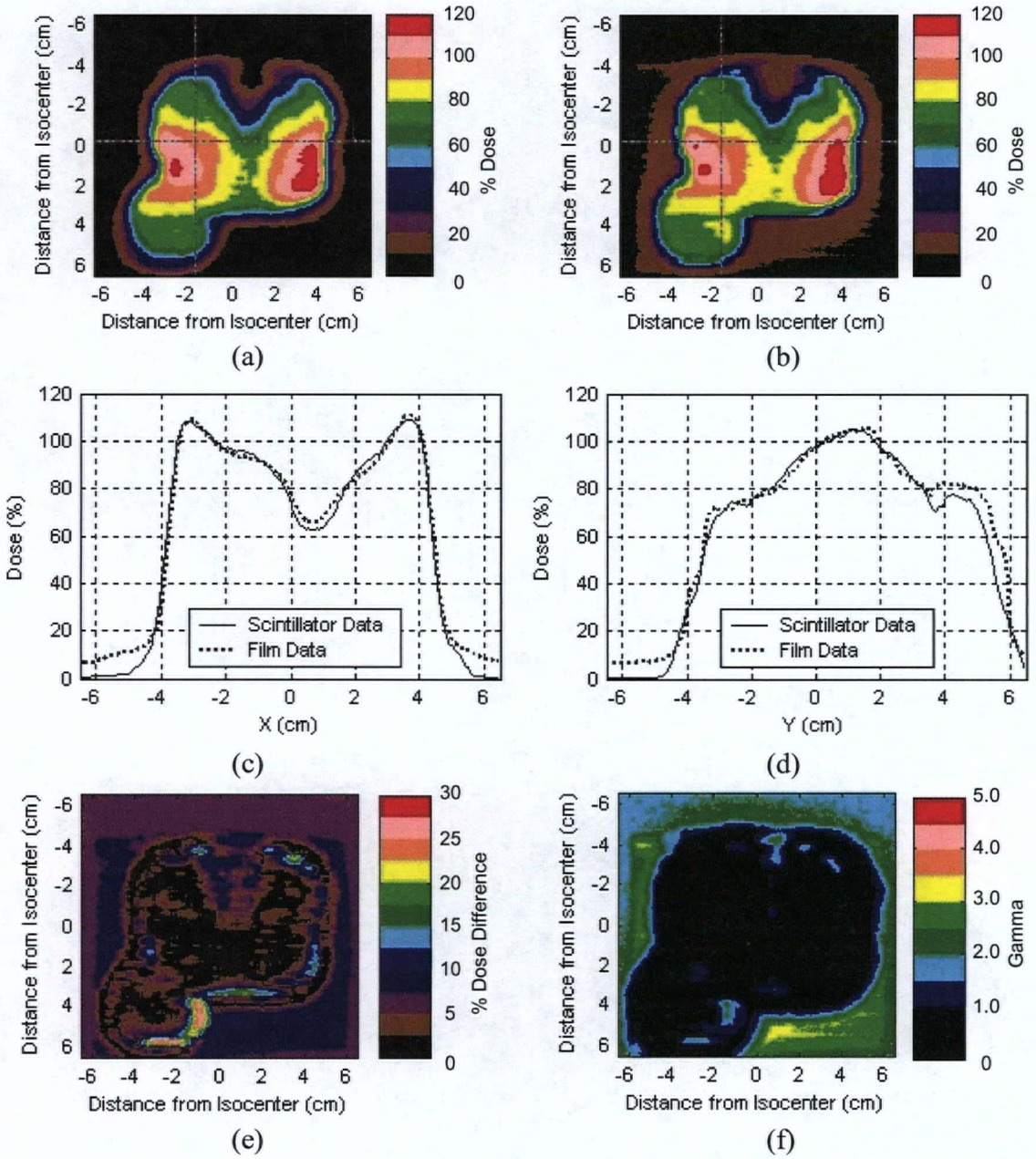

Figure A.1: Dosimetric comparison results for field number 1 of the 7-field IMRT treatment plan. Dose distributions measured using (a) scintillator dosimetry system and (b) film dosimetry are shown with crosshairs indicating positions of 1-D profiles. Profiles in the x- and y-directions are shown in (c) and (d) respectively. Percent dose difference (e) and gamma factor (f) maps are also shown for these dose distributions.

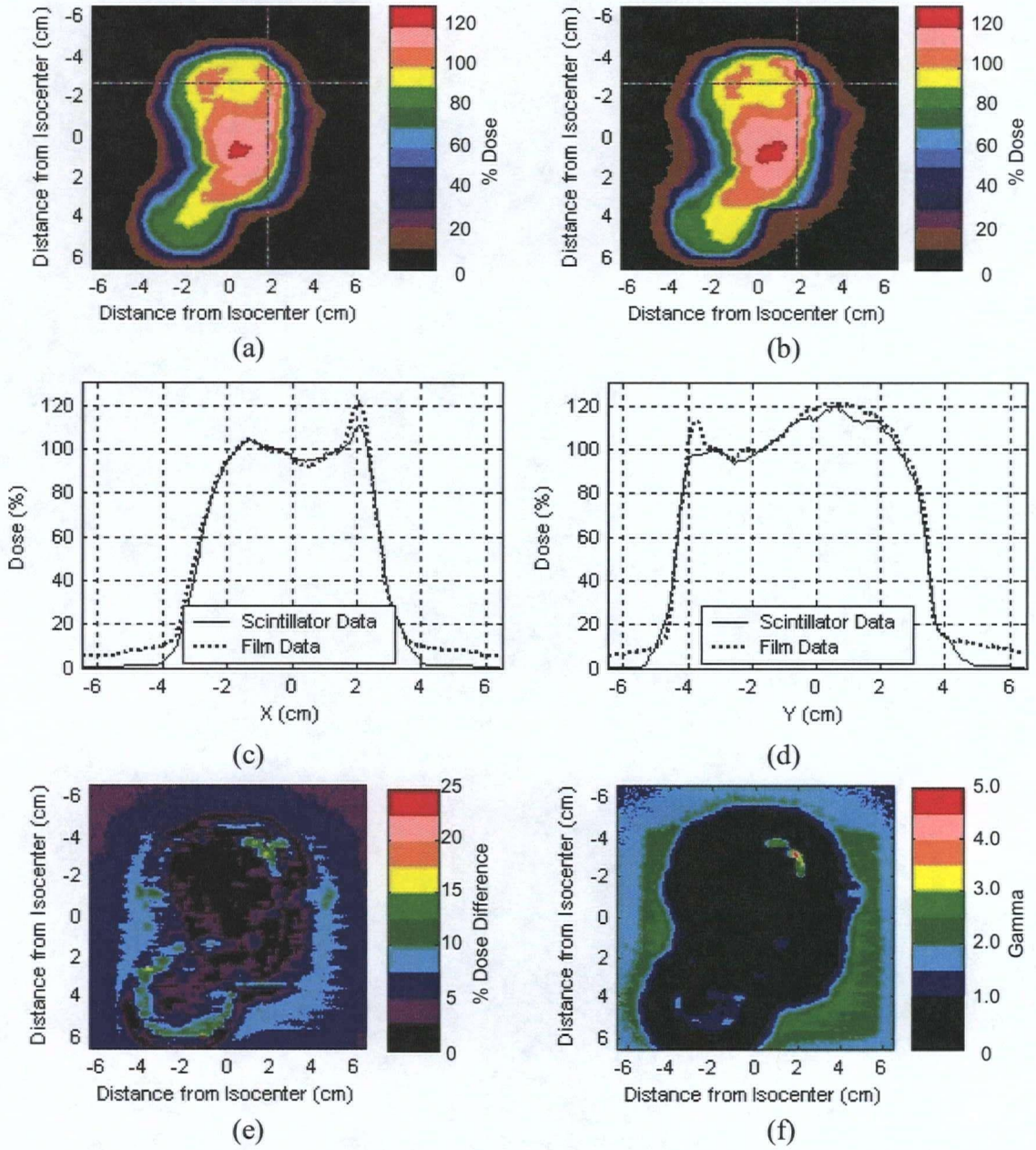

Figure A.2: Dosimetric comparison results for field number 2 of the 7-field IMRT treatment plan. Dose distributions measured using (a) scintillator dosimetry system and (b) film dosimetry are shown with crosshairs indicating positions of 1-D profiles. Profiles in the x- and y-directions are shown in (c) and (d) respectively. Percent dose difference (e) and gamma factor (f) maps are also shown for these dose distributions.

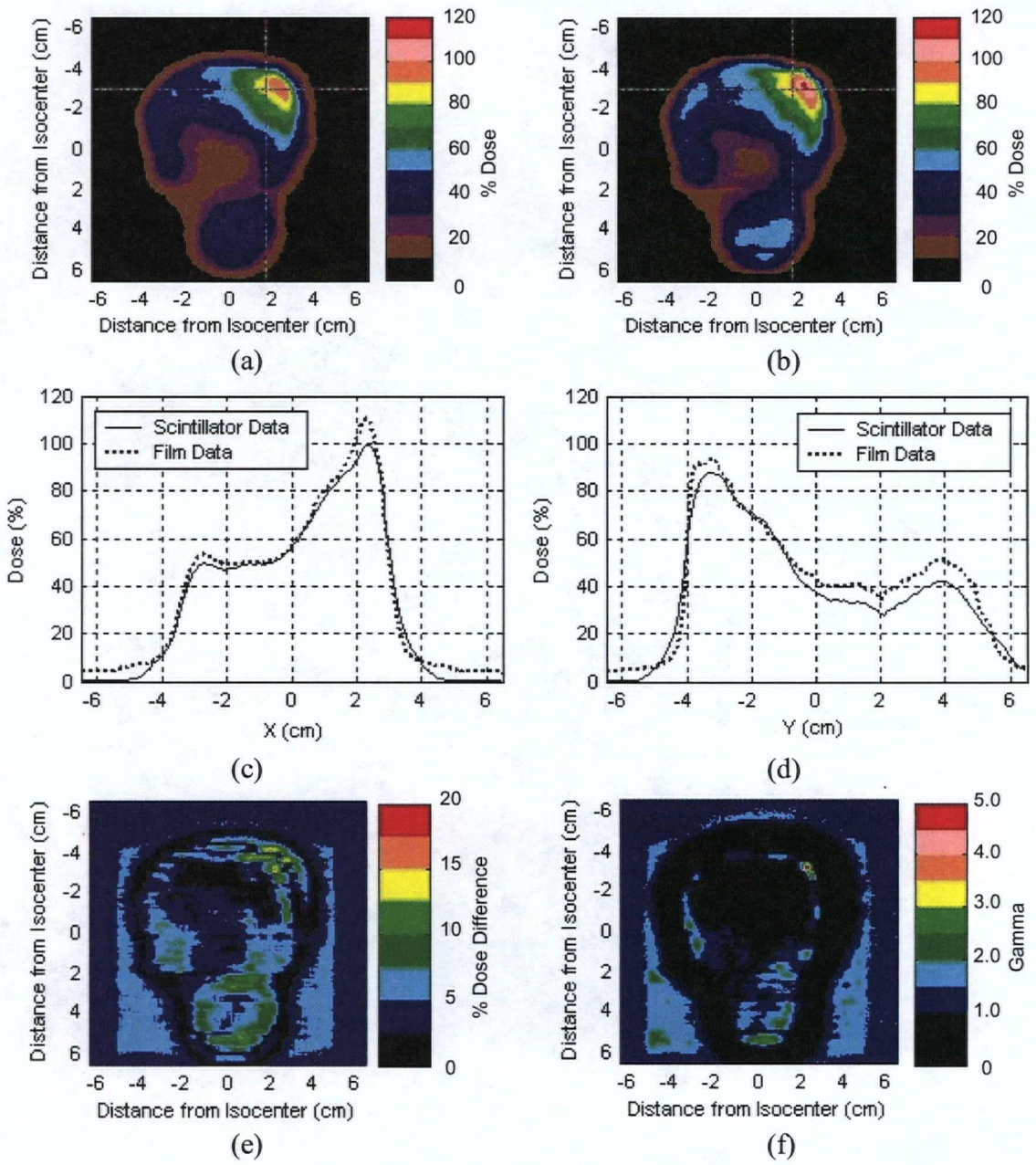

Figure A.3: Dosimetric comparison results for field number 3 of the 7-field IMRT treatment plan. Dose distributions measured using (a) scintillator dosimetry system and (b) film dosimetry are shown with crosshairs indicating positions of 1-D profiles. Profiles in the x- and y-directions are shown in (c) and (d) respectively. Percent dose difference (e) and gamma factor (f) maps are also shown for these dose distributions.

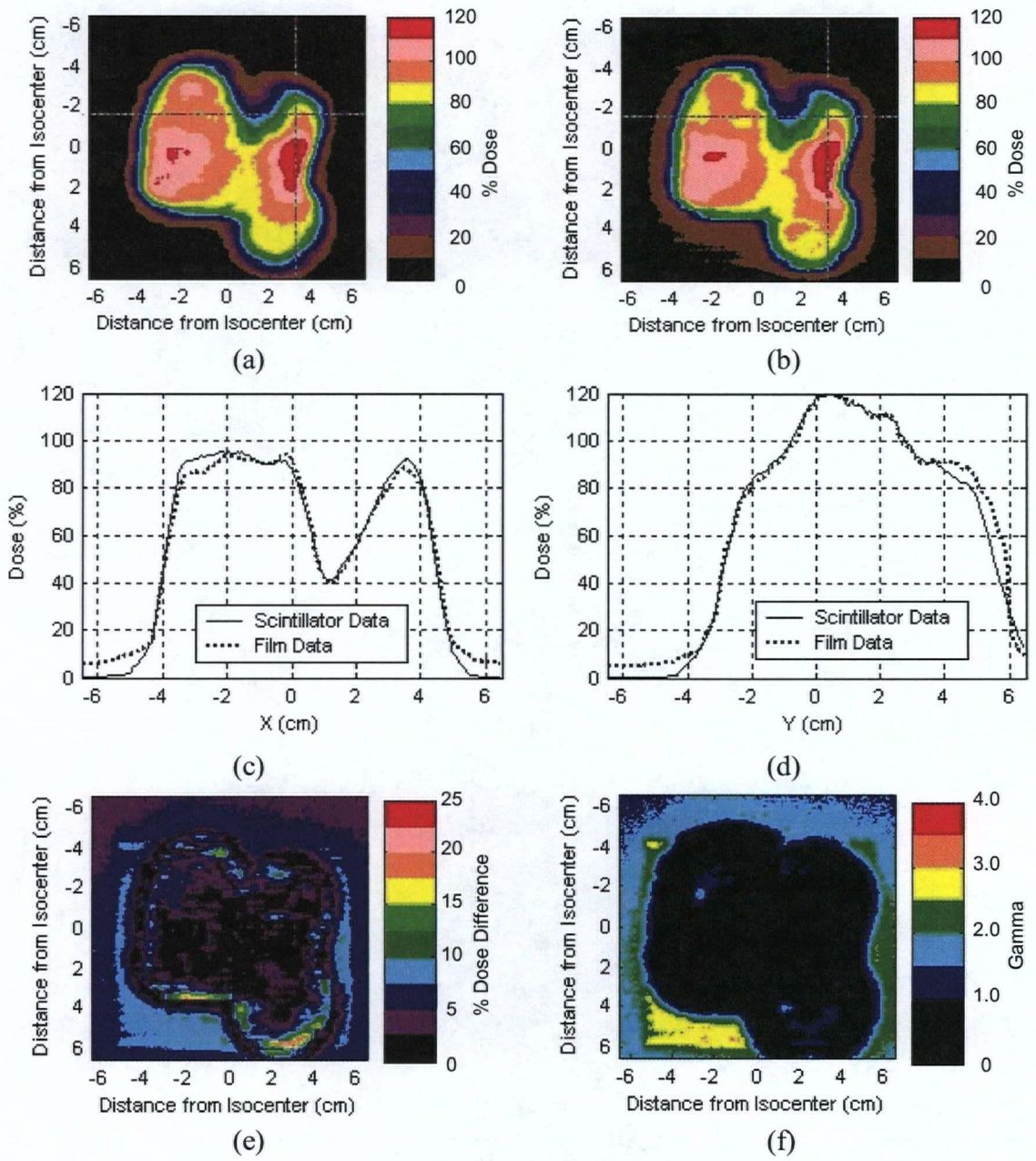

Figure A.4: Dosimetric comparison results for field number 4 of the 7-field IMRT treatment plan. Dose distributions measured using (a) scintillator dosimetry system and (b) film dosimetry are shown with crosshairs indicating positions of 1-D profiles. Profiles in the x- and y-directions are shown in (c) and (d) respectively. Percent dose difference (e) and gamma factor (f) maps are also shown for these dose distributions.

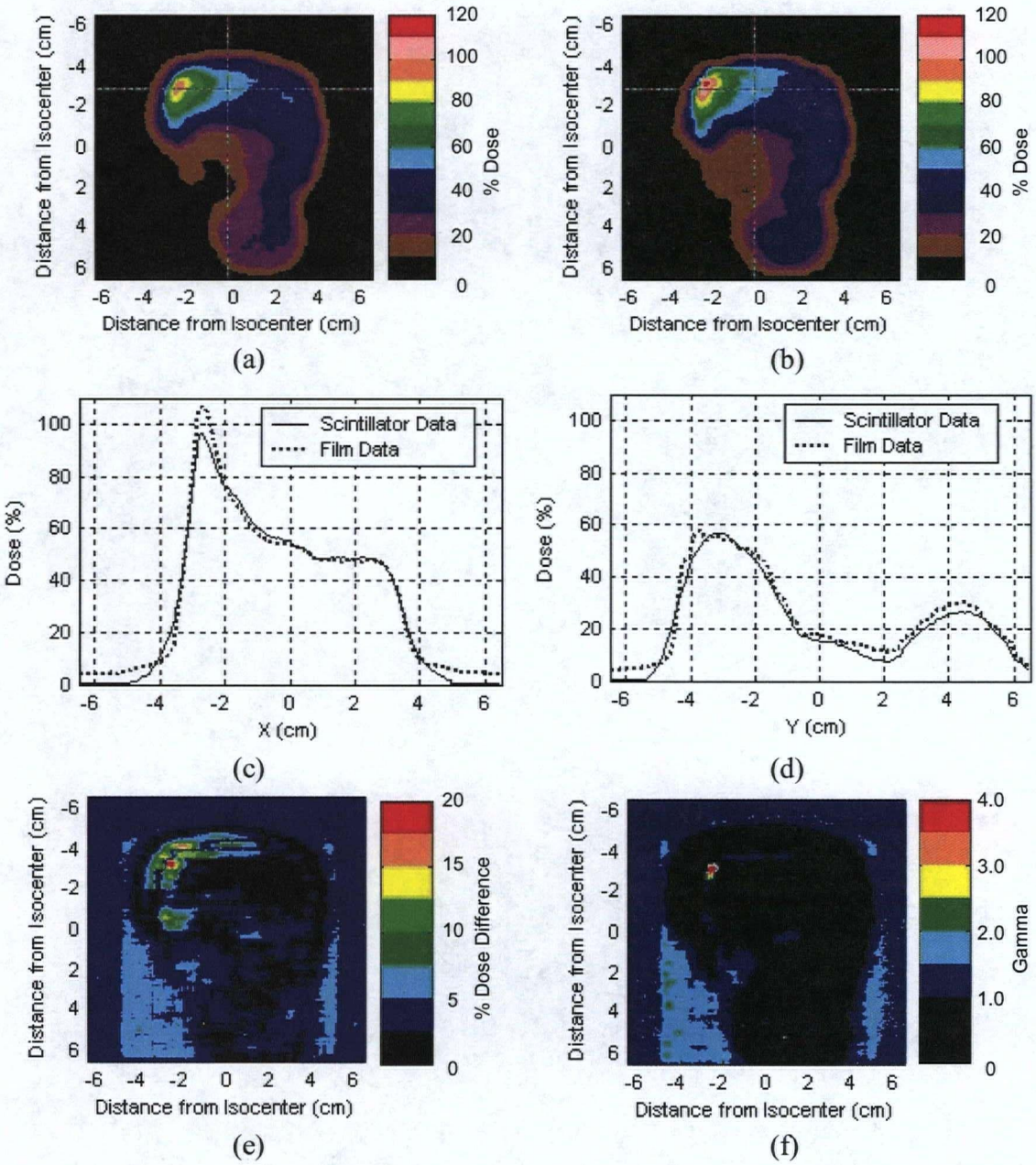

Figure A.5: Dosimetric comparison results for field number 6 of the 7-field IMRT treatment plan. Dose distributions measured using (a) scintillator dosimetry system and (b) film dosimetry are shown with crosshairs indicating positions of 1-D profiles. Profiles in the x- and y-directions are shown in (c) and (d) respectively. Percent dose difference (e) and gamma factor (f) maps are also shown for these dose distributions.